Observable jets in deep inelastic scattering as a probe of small x dynamics

Claire Anne Lewis

Observable Jets in Deep Inelastic Scattering as a Probe of Small x Dynamics

A thesis presented for the degree of
Doctor of Philosophy
by

Claire Anne Lewis

August 1997

University of Durham
Department of Physics

Abstract

The observation of the underlying small x dynamics arising from the resummation of large terms in $\ln 1/x$ in QCD descriptions of the gluon distribution have been searched for in deep inelastic scattering experiments at the electron proton collider HERA since the early 1990's. It has been recognized that the first fully inclusive measurements of the proton structure function F_2 are too inclusive to identify underlying dynamics. Less inclusive quantities need to be considered.

In this thesis a modified form of the BFKL equation is derived which enables the structure of the gluon emissions to be studied in small x deep inelastic scattering. The equation incorporates the resummation of the virtual and unresolved real gluon emissions and is solved to calculate the number of small x deep-inelastic events containing 0, 1, 2 ... resolved gluon jets, that is jets with transverse momenta $q_T > \mu$. We study the jet decomposition for different choices of the jet resolution parameter μ to look for possible signatures of BFKL dynamics in the x dependence of the exclusive observable quantities of the $n-$jet contributions to F_2.

We also study the application of the BFKL equation to forward jet events at HERA. We calculate the rate of deep inelastic scattering events containing two forward jets adjacent to the proton remnants and compare with the production rate of only one forward jet - the so-called Mueller process. We obtain a stable prediction for this two to one jet ratio, which may serve as a measure of the BFKL vertex function.

Declaration

I declare that no material in this thesis has previously been submitted for a degree at this or any other university.

The work in this thesis has been carried out in collaboration with Professors A.D. Martin and J. Kwieciński. The material in chapters 1 and 2 is a summary of the deep inelastic scattering process and small-x physics and as such is not original. The contents of chapters 3 and 4 are based on the publications:

- J. Kwieciński, C.A.M. Lewis and A.D. Martin, Phys. Rev. **D54** (1996) 6664.
- J. Kwieciński, C.A.M. Lewis and A.D. Martin, Durham university preprint DTP/97/58, July 1997 (hep-ph/9707375).

Acknowledgements

First, my deepest gratitude goes to Professors Alan Martin and Jan Kwieciński for their patience and kindness throughout the years of my PhD study and for giving me the opportunity to work in a very interesting and exciting field of study. Jan thank you for taking the time to explain the concepts of small x physics clearly and repeatedly - without our discussions my knowledge of the BFKL equation would be greatly reduced. Thanks also for your friendship and for making my stay in Poland very interesting and enjoyable.

Thanks to Dr. Krzysztof Golec-Biernat, whose questions and discussions have helped me enormously in the understanding of my subject and in giving me an insight into the experimental viewpoint of DIS experiments at HERA. Thanks for your time and interest in my work. Thanks also to Albert De-Roeck and Ewelina Mroczko for useful discussions relating to the experimental measurement of forward jets.

Sabine - so we made it! Thanks for sharing a supervisor, office and house for so many years ... thank you for your friendship, although after competing for computer time for so long I don´t know how we survived. Keep in touch.

On the "not so academic" side of things I would like to thank my friends and colleagues on the top floor of the physics department who have frozen with me in winter and fried in summer - to Andy, Anna, Darrell, David, Elena, John O., Kirsten, Matthias, Matt C., Matt S., Peter, Ricardo and Tom; thanks for keeping me sane throughout my time in Durham. We had some laughs. I wish you all the best for the future.Thanks especially to John for our early morning discussions on everything except physics - oops I just dispelled the myth that we actually do some work! You´ve been a good friend. Good luck.

Particular thanks go to my family (mum, Robin, Lynne and James) for their support during these last few years of study.

Lastly, my deepest thanks and love to Hans, whose love and support I could not have done without. Thank you for putting up with me; especially when the numerics were not working quite right! I don't know how you managed to survive my problems.

Dedicated to

Hans,

mum, Robin, Lynne & James

With Love.

Contents

Chapter 1

Deep Inelastic Scattering at HERA

1.1 The structure of matter - an historical note

In todays world the question "what constitutes the structure of matter that we see around us?" would receive a somewhat different answer than if asked only one century ago. Today an answer would involve words such as: protons, neutrons, quarks and gluons, one hundred years ago even the proton was unheard of!

The structure of matter as we understand it has undergone radical changes over this last century. Then, matter was considered to be made from discrete ("fundamental") building blocks called *atoms*. However, with the discovery of the *electron* in 1897, the revolution leading to todays understanding of the structure of matter began. The atom was no longer the fundamental building block - the negative charge carried by the electrons had to be balanced by something of positive charge to produce an overall neutrally charged atom. But, how were these charges distributed? The answer to this question came in 1911 when Rutherford and his collaborators performed his famous alpha particle scattering experiment showing that the atom consists of a *very* small positively charged nucleus surrounded by negatively charged electrons at some distance. This leads to the amazing discovery that the atom consists mainly of "space"! Consequently, the advent of the quantum theory of the atom arose, in which the picture of a tiny, compact nucleus surrounded by electrons held together by the electromagnetic force, essentially remains the same over 85 years later. These nuclei were subsequently found to consist of discrete particles; protons (1919) and neutrons (1932) and it is the structure of these spin 1/2 nucleons which we are interested in understanding today.

1.2 Experimental picture of the proton

So what is the structure of the proton? Is it an elementary particle and thus structureless, or, is there a more fundamental substructure?

Already by 1933, the discovery by Frisch and Stern that the proton magnetic moment differed from that of the Dirac magnetic moment for a spin 1/2 particle, provided the first experimental hints that the proton was not a point like elementary particle. After the war, the invention of new photographic emulsions gave physicists the means to discover new types of particles not present in ordinary matter; muons (a heavier relative of the electron with mass $m_\mu = 207m_e$) and pions (mediators of the strong nuclear force) were discovered in cosmic ray showers. As intense beams of particles of increasingly high energies became available at accelerators, more and more hadrons were discovered. In 1964, one explanation for this proliferation of particles was proposed by Gell-Mann and also by Zweig [1]. They found that all these new observed hadrons (which include the proton and neutron with the proton having the distinction of being the lightest baryon) could be interpreted as bound states of just three fundamental spin 1/2 particles, or bound states of a particle-antiparticle pair, assuming these "quarks" were allowed to have fractional electric charge. This provided additional theoretical motivation for the existence of something more elementary than the proton, although, as no free quarks were observed directly, the quark model became a useful tool in describing the properties of many new hadrons which were later found, but at the time was not considered a viable fundamental theory.

In the late 1960´s the second revolution leading to our present understanding of matter occured. High energy scattering experiments analogous to Rutherford´s scattering of alpha particles from a fixed target were repeated, this time using energies a thousand times higher in which the dynamical effects of the partons inside the proton were observed. In 1968 at Stanford the scattering of electrons from a proton target proved that the proton does indeed have a structure - it is not a point like object but is built up from smaller partons. The proton (and neutron) are now known to be built from two types of quark, the up and down. Indeed, almost everything we observe in the visible world around us can be ultimately decomposed into up and down quark constituents and electrons.

Today, the idea that the proton is composed of quarks (fermions carrying spin = 1/2

and fractional electric charge) is a well established idea, even though none have, or can, be observed freely in nature. Potentially we do have an explanation for this confinement of the quarks to bound states, given by the theory of Quantum Chromodynamics (QCD) describing the quarks and their interactions, although there is still a long way to go to understand the origin of this confinement.

With the advent of collider technology, huge increases in the experimental invariant energy available for the creation of new particles, from the GeV (10^9 eV) to the TeV (10^{12} eV) scales have been achieved, resulting in the discovery of many new particles. Although the physical world around us can be described in terms of two quark components, the up and down, and one lepton family (the electron), experiment shows that nature provides us with two more (identical except for mass) replica sets. During the 70´s, heavier quarks (charm and bottom) were discovered, and also the heaviest relative of the electron (tau lepton), at electron-positron colliders. In 1983 heavy bosons ($W^{\pm}$, Z^0), the mediators of the weak forces between particles, were found in $p\bar{p}$ collisions at CERN. Thus, by the early 90´s the quark contents of the world around us could be divided into three families, with the postulation of the existence of a *top* quark to fill the gap in the third family,

$$\begin{pmatrix} \text{up } (u) \\ \text{down } (d) \end{pmatrix} \begin{pmatrix} \text{charm } (c) \\ \text{strange } (s) \end{pmatrix} \begin{pmatrix} \text{top } (t) \\ \text{bottom } (b) \end{pmatrix}$$

with the quarks increasing in mass as we go to higher generations. Only the postulated top quark remained to be discovered.

The culmination of these discoveries came as recently as 1995 when the heaviest top quark was finally observed with a mass of 175 GeV at the $p\bar{p}$ collider at Fermilab.

So far with the energies (TeV) reached by modern day experiments no further sub-structure of matter, i.e. of quarks, has been observed. However, it still remains to be seen, as experiments with larger and larger energies are built, such as the Large Hadron pp Collider (LHC) which will begin taking data in the early part of the next century, whether the quark remains the fundamental building block of matter or whether, as in the case of the atom and proton before it, it is observed to have its own structure.

For reviews of the history of modern particle physics, see for example references [2, 3, 4] and others therein.

The basic interactions of matter

As well as the basic constituents of matter, there exist particles which act as carriers of the forces which bind hadrons and leptons together.

On the macroscopic scale, gravity is the dominant force which holds masses (e.g. planets, the solar system, galaxies) together, however, it is negligible at scales of atomic and nuclear size. Subatomically, it is the electromagnetic interaction which is responsible for the formation of atoms, in which the exchange of virtual photons between the electrons and nuclei constitutes a force which binds them together. A similar picture holds at smaller scales in which the protons and neutrons are bound together in the nucleus via the exchange of particles known as mesons (e.g. the pion). This "strong" nuclear force was later to be understood to arise from a more fundamental particle exchange in which the quarks of the protons and neutrons are held together by the exchange of spin 1 gauge bosons called *gluons*, analogous to the exchange of spin 1 photons for the electromagnetic force. This is the true strong force of nature.

As well as these, there is a fourth force - the weak interaction, which is mediated by the exchange of heavy $W^{\pm}$ (and Z) bosons, responsible for the decay of particles through β-emission.

So what now? Experiments over the last two decades have left us with a proliferation of partons - six quarks, together with six leptons, as well as the particles responsible for the mediation of forces, constituting the elements of matter we see in the universe today. One of the puzzles we face is, why two duplicate families of quarks and leptons, when the world around us is adequately described by the first family $(u, d; e^-, \nu_e)$? However they exist, and the question remains as to how do these "extra" constituents fit into the simple quark picture we have of the proton - what is the structure of the proton?

1.2.1 Deep Inelastic Scattering at HERA

To answer this question, the electron (positron) - proton collider HERA[1] (Hadron Electron Ring Accelerator) was designed and built in which $\sim$ 30 GeV electrons (or positrons)

[1] An overview of HERA physics (experimental and theoretical) and the relevant kinematics can be found, for example, in [5, 6, 7, 8].

collide with 820 GeV protons giving an invariant centre of mass energy

$$\sqrt{s} \sim 300\text{GeV} ,$$

which gives $s \sim 10^5$ GeV^2, much larger than energies available at fixed target experiments for the production of new particles. This international, high energy physics program consists of four experimental detectors; two taking fixed target data, HERMES and HERA-B, and two situated at collision points of the electron and proton beams, H1 and ZEUS. Operation began earlier this decade in 1992 and for the first time new kinematic regimes were opened, never before probed experimentally. From the outset, results from H1 and ZEUS showed many interesting features in the observables, such as strong rises of the measured structure functions, throwing down the gauntlet to theoreticians and phenomenologists to explain these novel effects.

In this chapter, an overview of the deep inelastic scattering (DIS) process as observed experimentally will be presented with a discussion of the kinematics and variables used. The novel results observed by HERA are shown, leading to the theoretical view of the proton as we understand it today - primarily we will discuss the evolution equations used to describe experimental observables. The focus will then be shifted to small x BFKL dynamics (chapter 2), expected to be important in the HERA kinematic regime, and a closer look taken at exclusive jet production to provide a deeper insight into the structure of the BFKL formalism. This will be discussed in the later chapters (3 & 4) of this thesis.

The basic lepton-proton scattering process, $l + p \rightarrow l + X$, relevant for the collisions at HERA, is shown in Figure 1.1. An incoming lepton (electron or neutrino), with four momentum k^μ, is scattered from the incoming proton which carries a momentum p^μ, via the exchange of a (virtual) boson. There are two types of process that can occur - neutral current (NC) and charged current (CC) interactions. The former is mediated by the exchange of a neutral photon or Z^0 boson, characterized by no flow of charge at the leptonic vertex; the incoming and outgoing lepton are the same except for a change in the outgoing lepton energy. Through charge conservation at the upper vertex, in CC interactions the emission of an electrically charged, heavy $W^\pm$ boson requires that the incoming lepton be different from that in the final state. Either $\nu_e \rightarrow e^-$, or, $e^- \rightarrow \nu_e$ through the exchange of a W^-. For the antiparticles, we would have the exchange of the W^+.

Experimentally, the DIS process is observed through the presence of the scattered

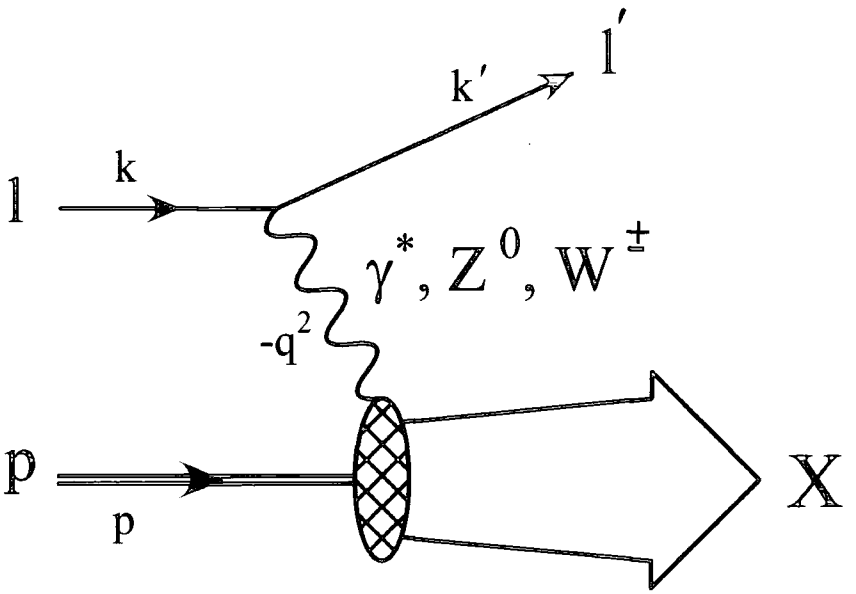

Figure 1.1: Basic lepton-proton scattering in which the interaction takes place via the exchange of a virtual photon, Z^0 boson (neutral current) or $W^{\pm}$ (charged current). The scattered lepton exchanges momentum $-q^2$ which determines the resolution with which the probe sees the proton. The proton is broken up, its remnants X passing down, or close to, the beam pipe.

electron in the detectors accompanied by hadronic jets, either 1 or more, resulting from the interaction of the photon with the proton. The proton itself is broken up during the scattering process, and its remnants are emitted in the original direction of the proton, with the majority of the remnant jet passing down the beam pipe.

We are interested in processes of electron scattering through the exchange of a highly virtual (large $-q^2$) photon with the proton, that is, the restriction $-q^2 \ll M_Z^2$, where M_Z is the mass of the Z^0 boson, will ensure that the dominant scattering process is via photon exchange and production of the Z^0 can be neglected. There are two important regions probed by the HERA collider experiments: the photoproduction region ($-q^2 = 0$) in which the scattering occurs via the exchange of a real photon, and the deep inelastic region where the virtual photon has a high virtuality ($-q^2 \gg 0$). Because such a wide q^2 range is covered, previous gaps in the kinematic range between fixed target (low energy) and collider experiments (higher energies) have been filled. Cross sectional data now covers the entire energy region from the real, photoproduction regime described by non-

perturbative physics, to the DIS region in which perturbative calculations can be made. This provides important information on the transition region between the two extremes.

Kinematic variables of deep inelastic scattering

Other than the energy variables, $E_{e,(e')}$ of the electron (scattered electron) and the proton, E_p, using the notation k, p & q for the four momentum vectors of the electron, proton and photon respectively, then the relevant kinematic variables of the inclusive DIS process are [5, 7]

$$\begin{aligned} s &= (k+p)^2 \simeq 4E_eE_p \\ Q^2 &= -q^2 \simeq 4E_eE_{e'}\cos^2(\theta/2) \\ y &= (p\cdot q)/(p\cdot k) \simeq 1 - E_e\sin^2(\theta/2)/E_{e'} \\ x &= Q^2/(2p\cdot q) \simeq Q^2/ys \\ W &= (q+p)^2 \simeq -Q^2 + ys\ , \end{aligned} \tag{1.1}$$

where s is the centre of mass energy squared of the process, Q^2 the negative squared momentum transfer $-q^2$, i.e. Q^2 is positive, y the fraction of energy carried by the virtual photon in the proton rest frame, x the famous Bjorken x variable (discussed below) and W the hadronic invariant mass of the system X. The angle θ is that of the scattered electron defined in the HERA laboratory frame with respect to the proton direction. In reality, the process of ep scattering is given by the subprocess of γ^*p scattering in which the incoming photon is not exactly parallel to the incoming electron. This defines the γ^*p collinear frame and care needs to be taken which angular definitions are used when applying experimental cuts on θ to obtain theoretical predictions. In the above, particle masses have been ignored, although for future reference the protons mass will be denoted by M_p and the electron mass m_e.

The two most important Lorentz invariant variables required for discussion of deep ($Q^2 \gg M_p^2$) inelastic ($W^2 \gg M_p^2$) scattering at HERA are Q^2 and x defined in (1.1).

Q^2 is directly measured from the kinematics of the scattered electron. For $E \gg m_e$, defining the x-axis to lie along the electron direction and the outgoing electron scattering to lie in the xy plane, then the four momentum of the incoming electron can be written as

$$k^\mu = (E_e, E_e, 0, 0)\ . \tag{1.2}$$

Letting $\hat{\theta}$ be the angle between the scattered electron and the incoming electron direction, then the four momentum of the scattered electron is

$$k'^{\mu} = (E_{e'}, E_{e'} \cos\hat{\theta}, E_{e'} \sin\hat{\theta}, 0) \; . \tag{1.3}$$

The virtuality of the photon γ^* is given by the change in energy of the initial and final state electrons, thus,

$$\begin{aligned} -q^2 &= -(k - k')^2 \\ &= -k^2 - k'^2 + 2k \cdot k' \; . \end{aligned} \tag{1.4}$$

From (1.2) and (1.3) we have $k^2 = k'^2 = 0$ in (1.4) giving

$$\begin{aligned} -q^2 &= 2k^{\mu}k'_{\mu} \\ &= 2(E_e E_{e'} - E_e E_{e'} \cos\hat{\theta}) \\ &= 2E_e E_{e'}(1 + \cos\theta) \\ &= 4E_e E_{e'} \cos^2(\theta/2) \end{aligned}$$

as quoted in (1.1) where we note $\cos\theta = -\cos\hat{\theta}$. It is this value of Q^2 which sets the resolution scale at which the constituents of the proton are viewed. The larger the virtuality, the smaller the wavelength of the photon which allows us to "see" scales much smaller than the size of the proton - for small enough wavelengths the dynamical effects of the individual quarks are observed. Repeating the principles of earlier scattering experiments which discovered the nucleus within the atom, and quarks within the proton, if there is another layer of substructure such as "preons" inside the quarks, then taking DIS experiments to higher Q^2 energies, would be the logical step required to reveal any underlying picture that might be there - so far, none has been observed.

The second important variable required is the dimensionless quantity Bjorken x, usually denoted by x_B. For simplicity, the notation $x_B = x$ will be used.

Later we shall see that the physical cross section is dependent on dimensionless quantities called structure functions. The Lorentz invariant quantities of Figure 1.1 are given by q^{μ} of the photon and p^{μ} of the proton in the combinations: $q^2, q \cdot p$ and p^2. However, the proton is on mass shell and $p^2 = M_p^2$ and so is not a variable of the process. The relevant dimensionless quantities used to describe the scattering process are given by the

ratios

$$\frac{Q^2}{2q \cdot p} \text{ and } \frac{Q^2}{M_p^2} ,$$

the former defining Bjorken x. In general the structure functions (F) depend on both these ratios, but for $Q^2 \gg M_p^2$ as for DIS, in which the photon probes scales much smaller than the size of the proton, it no longer cares about the proton size and we get scaling [9]. That is $F(x, Q^2/M_p^2) \rightarrow F(x)$ only (see sections (1.2.2) & (1.3.1) for discussion of structure functions).

A useful physical interpretation of x can be obtained if we consider the scattering of a virtual photon from a constituent in the proton where we restrict ourselves to the infinite momentum frame of the proton (i.e. $v_p \sim c$). In this frame $\mid \boldsymbol{p} \mid \gg m, M_p$ thus we can neglect all parton masses and the proton can be imagined to be made of partons all travelling together in the direction of the proton. Defining the z-axis to lie in the direction of the proton, and the four momenta of one of the incoming partons and photon as $p^\mu = (p, 0, 0, p)$, $q^\mu = (0, 0, 0, -Q)$ respectively, such that $-q^2 = Q^2$ and p is the longitudinal momentum of the parton, then for a photon of very small wavelength λ ($\lambda = h/p$), only one parton will be struck and subsequently reflected through 180°. This allows us to define the momentum of the scattered parton, $p'^\mu = (p, 0, 0, -p)$ and from momentum conservation determine that $p = Q/2$. Letting ξ be the fraction of the protons momentum (P) carried by the parton then

$$p = \xi P = \frac{Q}{2} .$$

Taking the product of q^μ and P^μ gives

$$q \cdot P = \frac{Q^2}{2\xi}$$

and recalling that the definition of x is

$$x = \frac{Q^2}{2q \cdot P} , \tag{1.5}$$

we obtain the relation

$$x = \xi .$$

Thus for the infinite momentum frame, the physical interpretation of x is that it defines the fraction of the protons momentum carried by the struck parton in the DIS process.

This is the picture that will be used throughout the discussions for the observables studied at HERA in the remainder of this thesis.

Experimentally, x is calculated from Q^2 and y, see (1.1), and the accuracy with which it is known is dependent on the experimental resolution of the variable y.

x,Q^2 phase space at HERA

Before we take a look at the experimental results obtained at HERA, it is useful to make a small deviation and consider the x, Q^2 phase space available. This will be helpful in later discussions, chapters 3 & 4, in which we will calculate physical cross sections theoretically for the DIS process. Due to experimental and detector practicalities, the available x, Q^2 phase space is constrained by cuts on the measured variables. As this thesis will deal with the theoretical aspects of DIS (section 1.3 onwards), in this introduction the aim is to give a brief summary of the experimental limitations and a physical explanation of the origin of the cuts used. More detailed cuts will be discussed as required in the relevant sections.

Experimentally the kinematic variables of (1.1) are reconstructed through measurements of the angles and energies of the scattered electron and hadronic jets. The definitions are shown in Figure 1.2. Angles are measured with respect to the proton direction in the HERA frame. Note, here $\theta_e \equiv \theta$ of (1.1).

The x, Q^2 range at HERA is large. Q^2 theoretically covers the range from 1 GeV^2 to s, whilst x lies in the approximate range $10^{-5} - 1$. In reality, the upper limit of x is restricted to $x \lesssim 0.7$ because for very large x, reconstruction can only be made using hadronic measurements which are smeared due to inaccuracies in the resolution of the jet angles and energies.

The most stringent limits on the kinematic plane are determined by the beam pipe cuts. These set the restrictions on the angular emission of the electron (θ_e) and jets (θ_j) thus determining the low Q^2 limit for detection of the electron and the highest x values that can be reached. In practice, this means that the limits of Q^2 are dependent on which x bin is being studied, i.e. we have $Q^2(x)$ which can be calculated from [7]

$$Q^2(x, \theta_e) = \frac{sx}{1 + xE_p \tan^2(\theta_e/2)/E_e}\,, \tag{1.6}$$

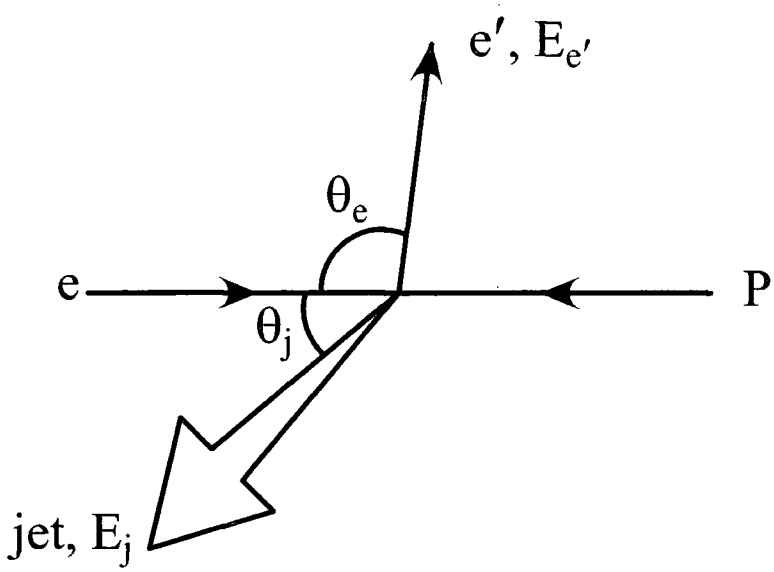

Figure 1.2: Schematic diagram of HERA final state kinematics. The beam pipe lies in the direction of the proton. Definitions of electron and jet angles are shown with respect to the proton direction.

and

$$Q^2(x,\theta_j) = \frac{sx}{1 + E_e \cot^2(\theta_j/2)/xE_p} \,. \tag{1.7}$$

The two equations above determine the electron acceptance region $Q^2(\theta_e)$, and the jet acceptance region $Q^2(\theta_j)$ respectively. Both the electron and jet regions are also restricted by the electron ($E_{e'}$) and hadronic (E_j) energy resolutions of the detectors.

There is one other important cut to consider - a cut on the variable y. Practically this is restricted to the range $0.1 \lesssim y \lesssim 0.9$. The upper cut is to remove uncertainties arising from background, radiative corrections, electron resolution etc, whereas the lower cut is not so well defined. The conservative (lower) cut quoted above is applied when reconstruction of y is obtained only from the scattered electron kinematics. If extra information is included from the hadronic sector, this cut can be lowered to $y \sim 0.01 - 0.05$.

In summary, the accessible kinematic range at HERA for electrons with energy $E_e = 27.5$ GeV, and protons with $E_p = 820$ GeV is determined by the cuts.

$$\begin{aligned} \theta_j &\gtrsim 5^\circ \\ 8^\circ &\lesssim \theta_e \lesssim 175^\circ \\ E_j &\gtrsim 5\text{GeV} \,. \end{aligned}$$

$$\begin{aligned} E_{e'} &\gtrsim 5\text{GeV} \\ 0.1 &\lesssim y \lesssim 0.9 \\ 10^{-5} &\lesssim x \lesssim 0.7 \end{aligned} \tag{1.8}$$

and is shown in Figure 1.3. It is important to remember that this shows only approximately the phase space available; different processes measured at the different detectors will have slightly different cuts on the above variables.

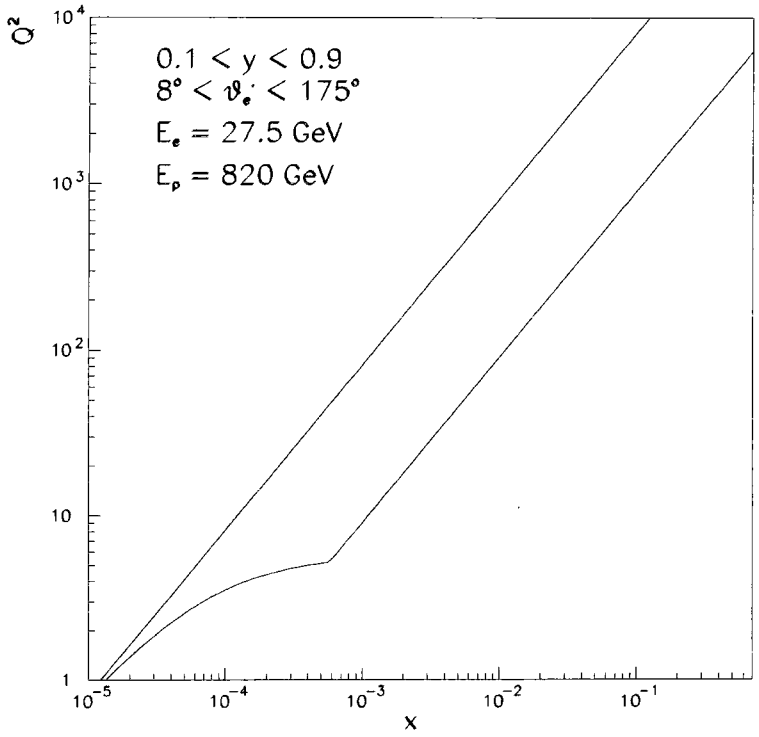

Figure 1.3: x, Q^2 phase space available at HERA.

1.2.2 The structure of the proton as seen at HERA

The scattering process of Figure 1.1 is mathematically described[2] by two terms; a leptonic term which describes the lepton-photon vertex in the upper part of the diagram, and a hadronic term which describes the hard scattering of the photon-proton system. The leptonic contribution is fully determined by Quantum Electrodynamics, (QED), the theory

[2]The full description of Figure 1.1 is obtained when we include W,Z mediated processes which are described by the electroweak theory.

describing electromagnetic interactions of charged leptons and photons. However, the hadronic part is not fully understood. Our ignorance of this lower vertex (represented by the hatched blob) and how the proton is broken up through interaction with the photon, is parameterized by the dimensionless structure functions F_1 and F_2. These are functions of the independent kinematic variables x and Q^2 discussed previously, i.e. we have $F_1(x, Q^2)$ and $F_2(x, Q^2)$ which are measured experimentally. The proton is described by two structure functions as it is a spin 1/2 particle. However, if the quarks of the proton were not spin 1/2 objects then F_1 would be given by $F_1 = 0$ which is not observed experimentally.

The high energy differential cross section is related to these structure functions by [2, 10]

$$\frac{d\sigma}{dxdQ^2} = \frac{4\pi\alpha^2}{xQ^4}\left\{y^2 xF_1(x,Q^2) + (1-y)F_2(x,Q^2)\right\} \tag{1.9}$$

where y is defined as $y = Q^2/xs$ from (1.1). The fine structure constant α is due to the coupling of the virtual photon to the quarks and leptons and the suppression $d\sigma/dxdQ^2 \propto 1/Q^4$ arises through the exchange of the photon with virtuality Q^2 (see section (1.3.1)). Because the probe is a virtual photon, it possesses both longitudinal and transverse polarizations which define the longitudinal and transverse components of the proton structure functions F_L and F_T respectively. These are related to F_1 and F_2 through the relations

$$\begin{aligned} F_T &= 2xF_1 \\ F_L &= F_2 - 2xF_1 \,. \end{aligned} \tag{1.10}$$

Thus, we can rewrite (1.9) as

$$\frac{d\sigma}{dxdQ^2} = \frac{4\pi\alpha^2}{xQ^4}\left\{(1-y)F_2(x,Q^2) + \frac{1}{2}y^2 F_T(x,Q^2)\right\} \,. \tag{1.11}$$

The above is for the electron-proton scattering process via interaction of a massless photon with the proton. If we instead were to look at lepton-nucleon scattering of $\nu N \rightarrow \mu^- N$ or $\overline{\nu} N \rightarrow \mu^+ N$ mediated by the heavy W bosons, (1.9) would be modified by the addition of a third structure function, $F_3(x, Q^2)$, which is a parity violating term due to effects of the weak interaction. It would become

$$\frac{d\sigma^{\nu\overline{\nu}}}{dxdQ^2} = \frac{G_F^2}{x\pi}\left(\frac{M_W^2}{Q^2+M_W^2}\right)^2\left\{y^2 xF_1^{\nu}(x,Q^2) + (1-y)F_2^{\nu}(x,Q^2) \pm y\left(1-\frac{y}{2}\right)xF_3^{\nu}(x,Q^2)\right\} \tag{1.12}$$

where the α^2 of (1.9) $\rightarrow G_F^2$, the Fermi coupling constant specifying the strength of the weak interaction. The $1/Q^4$ dependence for the heavy W propagator becomes

$$\frac{1}{(Q^2 + M_W^2)^2} \tag{1.13}$$

with $M_W \sim 80$ GeV the mass of the W boson. A similar propagator would be used for the neutral current Z_0 contribution with $M_W \rightarrow M_Z (\sim 91.2\text{GeV})$ in (1.13).

In (1.9), F_1 and F_2 can only be distinguished if the cross section is measured at different values of y (i.e. $\sqrt{s}$). In practice, the quantity $F_L = F_2 - 2xF_1$ is small, which in measurements at fixed energy is often taken from the theoretical (i.e. QCD) estimates.

Previous measurements of the proton structure functions from fixed target experiments, such as muon beams incident on stationary proton targets, had energies of the order

$$s \equiv (p_\mu + p_p)^2 \simeq 2M_p E_\mu \tag{1.14}$$

which for a muon beam with $E_\mu \sim 400$ GeV gives $s \sim 750$ GeV^2. This is orders of magnitude lower than for collider energies

$$\begin{aligned} s \equiv (p_e + p_p)^2 &\simeq (E_e + E_p)^2 - (E_e - E_p)^2 \\ &= 4E_e E_p \end{aligned} \tag{1.15}$$

as given in (1.1), which for HERA is $\sim 10^5$ GeV^2. Thus, these fixed target experiments could only probe the region $x \gtrsim 10^{-2}$ and the results showed that after an initial rise of the structure functions to $x \sim 10^{-1}$ the x dependence flattened. What happened afterwards at small x was a question theorists were trying to predict.

The first results of the proton structure functions measured at HERA probed the region $x < 10^{-2}$ and immediately showed a dramatic increase of F_2 (and thus the cross section) with decreasing x which is shown in Figure 1.4. It is this dramatic rise of the structure functions we wish to describe in the next section in the framework of perturbative QCD. It should be noted that the recent data plotted below for F_2^{ep} is that of e^+p scattering as, in 1994, HERA began running with positron beams to increase luminosity.

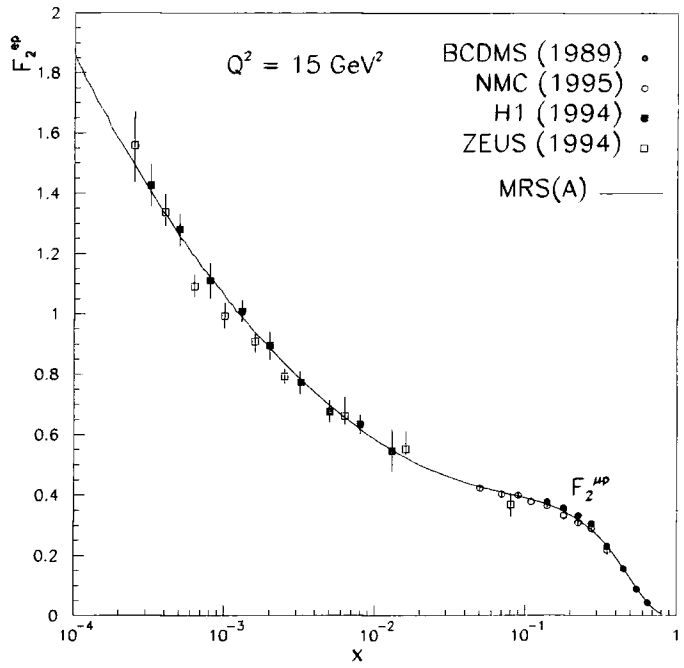

Figure 1.4: Rise of the proton structure function F_2 [11] with x measured at HERA for $Q^2 = 15$ GeV^2. Earlier fixed target data (BCDMS, NMC) using μp scattering showed flattening of structure functions at $x \sim 10^{-1}$. The data plotted is for the most recent published data from the respective collaborations. The data errors are combined systematic and statistical. The solid line shows the QCD prediction of F_2^{ep} using MRS(A), $\Lambda_{QCD} =$ 230 MeV [12], parton distributions fitted at large x.

1.3 Structure of the proton in Quantum Chromodynamics

We have seen in the previous section that in ep scattering the proton is described by two structure functions F_1 and F_2, and that $F_2(x, Q^2)$ shows a dramatic rise, Figure 1.4, as we move into the kinematic region $x \sim 10^{-2} \rightarrow 10^{-4}$. In this section we will consider how the proton is described by the field theory of Quantum Chromodynamics (QCD), in which the strong rise of the structure function F_2 can be reproduced theoretically through careful choice of input to the DGLAP evolution equation (Eq. (1.29)), or, through BFKL ($\ln 1/x$) evolution (Eq. 2.3). In Figure 1.4, the rise of the structure function F_2 is predicted through DGLAP evolution of the variable Q^2 (solid line) using MRS(A) parton distributions.

QCD is the theory of quarks and their interactions. In this framework the proton (and observed baryons) are interpreted as bound states of three quarks, whilst the mesons consist of a quark-antiquark pair. The proton is a *uud* state with all quarks carrying fractional charges, $e_u = 2/3$ and $e_d = -1/3$. These quarks are held together in the proton by the strong force mediated by the exchange of spin 1 bosons - gluons. This is analogous to the origin of the electromagnetic force arising through the exchange of neutrally charged spin 1 photons.

A colourful theory

Fermi-Dirac statistics require that the baryon wavefunction be antisymmetric, which introduces the important constituent of QCD - each quark carries, as well as an electric charge, a colour charge quantum number which can have one of three values; red (r), green (g) or blue (b). The anti-quarks carry anti-colour, $\overline{r}, \overline{g}$ and $\overline{b}$. So as to prevent all combinations of $q, \overline{q}$ states occuring in nature, QCD has a very important restriction, only combinations of quarks and antiquarks forming colour singlet states can exist in nature. This is termed *colour confinement* which prevents states such as $qqqq$ or $qq\overline{q}$ for example forming and theoretically predicting the existence of particles which we do not observe.

The importance of glue in the proton

One other important aspect of the colour charge in QCD is that it is also carried by the gluons. Unlike neutrally charged photons in QED which do not interact with each other, in QCD, the gluons do, allowing the existence of the three (ggg) and four ($gggg$) gluon vertices. The result is, the simple quark structure of the proton is inadequate - it is no longer described by the simple *uud* model. The quarks of the proton can radiate gluons, which in turn can radiate more gluons or a $q\overline{q}$ pair. It is the presence of these gluons (and other "sea" quark constituents) in the proton which produce the Q^2 dependence of the structure functions. If they were not present then $F_2(x, Q^2) \rightarrow F_2(x)$ only, and we would observe scaling in the variable x. For the small-x, moderate Q^2 range of HERA these gluon distributions are important, with the gluon providing the dominant parton density contribution in the proton. It is these gluon distributions which we will be considering in more detail in the following chapters. Thus, we should convince ourselves that this "glue" does actually exist.

The first indirect evidence for gluons was observed in the measurements of the momentum distributions for the quarks in the proton. The known quarks only accounted for approximately half the protons momentum, i.e.

$$\int xq(x)\,dx = \int dx\; x(u_v + d_v + u_s + \overline{u}_s + d_s + \overline{d}_s + s + \overline{s}_s + ...) \sim 0.5\,. \qquad (1.16)$$

Here, $q(x)$ is the probability distribution for finding a quark carrying fraction x of the protons momentum and ... represents the small component of momentum carried by the heavy quarks. Thus, approximately 50% of the momentum is carried by something else within the proton. After the first clear observation in 1979 at DESY [13] of three jet events arising from the process $e^+e^- \rightarrow qqg$, the existence of the gluon was established.

Scaling and scaling violations

As mentioned above, the presence of glue in the proton leads to an important feature of QCD - the observation of scaling violations in the structure functions of the proton. That is, F_2 is observed to be a function of x and Q^2 instead of just x. More formally, gluon bremsstrahlung introduces a $\ln Q^2/\mu^2$ term to the mathematical description of the parton distribution evolution equations (1.29) producing the result $F_2(x) \rightarrow F_2(x, Q^2)$.

For a photon probe of small enough wavelength then the individual quarks within the proton can be resolved. Naively the proton can be considered to be built from just three valence quarks; a combination of *uud* quarks. If these quarks were non-interacting then this would be signalled by the inelastic structure functions of the proton being independent of Q^2 at a given value of x - the structure functions would exhibit *scaling*. This is indeed observed experimentally for the Bjorken x values, $x \sim 0.2 - 0.3$. However, this x range is found to be a pivot point. For $x \lesssim 0.2$ the structure functions are observed to rise with increasing Q^2, whilst for $x \gtrsim 0.3$, the structure functions decrease with increasing Q^2; i.e. we see *scaling violations*. However, unlike the cases of the atom and nucleon in which scaling violations pointed to the existence of another layer of substructure, this scaling violation does not lead to the need for an underlying "preonic" substructure for the quarks. This variation of the structure function with Q^2 can be understood within the framework of QCD.

For increasing Q^2 we are viewing the proton with smaller and smaller wavelength photons and so are able to "see" more and more of the parton constituents making up the

proton. We see that the individual valence quarks are themselves surrounded by a cloud of other partons - gluons and sea quarks. These partons all share the total energy and momentum of the proton. For a quark (initially) carrying a large momentum fraction x there is a significant probability that its momentum will be degraded by the emission of a gluon. Thus, the momentum distributions of the quarks will be depleted in the high $x \to 1$ region, and weighted towards the smaller x values so producing an increase in the structure functions as we move to smaller x and conversely a decrease in the structure function at high x as we view the proton with greater resolution. In fact, these observed scaling violations are an experimental signature of the gluon emission in the proton.

Confinement of quarks to bound states

At short distances the quarks within the proton act as free particles. However, at large distances we know they are not as no free quarks are observed outside of the bound state producing nucleons. This is because the coupling constant α_s of QCD (analogous to the fine structure coupling α in QED between quarks and the photon) exhibits asymptotic freedom - that is, it runs as we vary the energy scale as shown in Figure 1.5.

At low Q^2, in the "soft" non-perturbative physics regime the coupling increases with $\alpha_s \to \infty$ as $Q^2 \to 0$. As we move to high Q^2, the coupling decreases and we have asymptotic freedom. In this region $\alpha_s(Q^2)$ is small (i.e. $\alpha_s \ll 1$), thus we can make a perturbative expansion in α_s which is the basis of calculations in perturbative theory. The DIS region is that of moderate to high Q^2 in which "hard" scattering interactions take place and we can use perturbative QCD (pQCD) to provide a mathematical interpretation of the F_2 structure functions. At the opposite end of the scale $Q^2 \to 0$, we observe infrared slavery. Here the force between the quarks is large. It is this behaviour of the coupling of the strong force, together with the condition of colour confinement (mentioned above) which prevent the existence of free quarks in nature. However, as confinment has its roots in the non-perturbative physics region which is not very well understood, the actual origin of the confinement of quarks and gluons to bound states is still not fully known - advances in lattice calculations are providing useful information and a method of calculation in this regime.

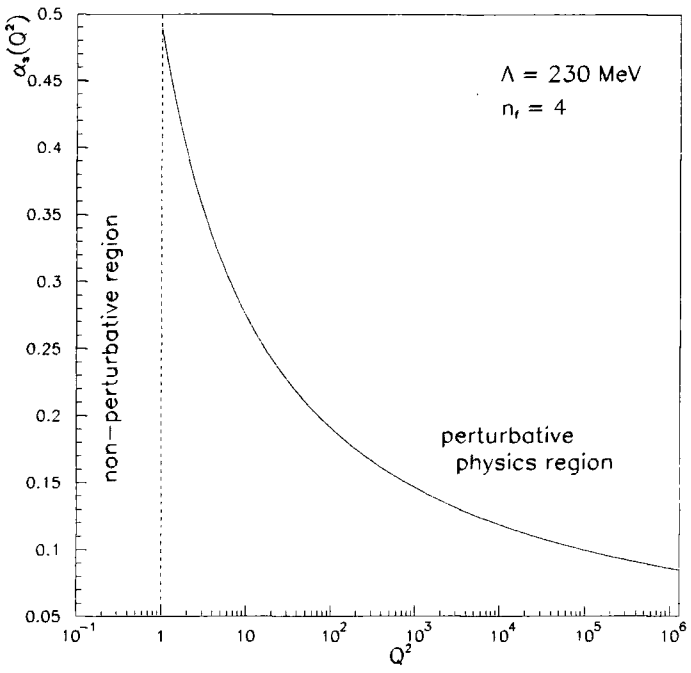

Figure 1.5: Running α_s with Q^2 for $n_f = 4$ and $\Lambda_{QCD} = 230$ MeV. Below the cut $Q^2 = 1$ GeV^2 we define the infrared region in which α_s "blows up" and perturbative theory no longer holds.

1.3.1 Theoretical description of DIS observables

We are now in a position which allows us to describe the DIS process theoretically. Now we know the proton is composed of quarks, gluons and sea quarks, the interaction of the photon (of small wavelength) with the proton in Figure 1.1 can be reinterpreted as the interaction of the photon with a constituent of the proton. For the present we will consider the hard process of $\gamma^* q$ scattering, but this can just as readily be taken as $\gamma^* g$ scattering which will be considered later. The "new" DIS process is shown in Figure 1.6. The kinematic variables are the same as discussed in section (1.2.1) where x is the fraction of momentum carried by the struck parton inside the proton. The label a runs over the quark, antiquark flavours. If we consider QCD α_s corrections to this process then a will also include the gluon with the modification that the gluon will couple to the photon through the fusion process $\gamma^* g \rightarrow q\overline{q}$.

To obtain a theoretical description of the scattering process $eP \rightarrow eX$, we work in the infinite momentum frame where the proton travels with $v_p \sim c$. Due to relativistic

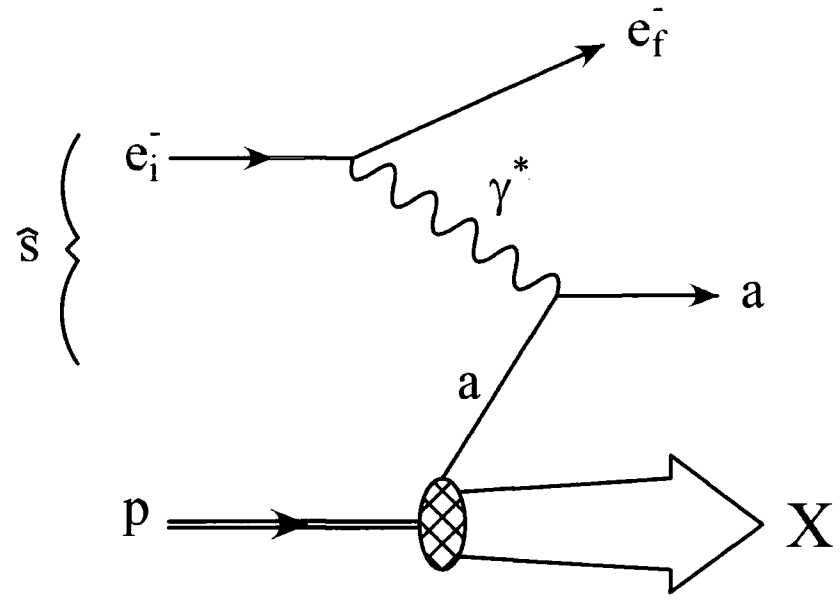

Figure 1.6: Theoretical view of DIS in which the photon of virtuality Q^2 interacts with a single parton carrying a momentum fraction x within the proton. The label a can be either q, or $\overline{q}$. This forms the hard scattering process which can be calculated perturbatively. Using the mass factorization theorem which separates the long and short distance effects, allows a mathematical description of the physical cross sections of the process. $\hat{s}$ is the energy of the subprocess $eq \rightarrow eq$.

time dilation the interaction time of the partons with each other inside the proton is much larger than the timescale $(1/\sqrt{Q^2})$ of the photon interaction with the parton. Thus, the eP scattering hard collision is considered to be the scattering of the photon from a free parton within the proton. In this frame the transverse momentum of the partons is governed by the uncertainty principle and so is small ($\sim$ MeV) in comparison to the longitudinal momentum component.

In later chapters we will be calculating the cross sections of jet production at HERA, so it is useful to first consider how these are calculated. The differential cross section for the process of Figure 1.6 is written[3] as the sum over all the contributing quarks q

$$\frac{d\sigma}{dxdQ^2} = \sum_q \int_0^1 d\xi \; f_q(\xi) \left(\frac{d^2\hat{\sigma}}{dxdQ^2} \right)_{eq \rightarrow eq} \tag{1.17}$$

where the hard scattering subprocess $eq \rightarrow eq$ in the brackets is described from Feynman rules of the scattering process $a + b \rightarrow c + d$. $f_q(\xi)$ describes the probability of finding

[3] A full description of the method of calculation of scattering cross sections can be found, for example, in [2, 14] and other text books on particle physics

a quark in the proton carrying a fraction ξ of the momentum. Using the Mandelstam variables of the eq subprocess

$$\begin{aligned} \hat{s} &= xs = 2xp \cdot k \\ \hat{t} &= t = -Q^2 = -xys \\ \hat{u} &= -\hat{s} - \hat{t} = -x(1-y)s \end{aligned} \tag{1.18}$$

then the subprocess $eq \to eq$ of (1.17) can be written as, [2, 10]

$$\left.\frac{d\hat{\sigma}}{d\hat{t}}\right|_{eq} = \frac{2\pi\alpha^2 e_q^2}{\hat{s}^2}\left(\frac{\hat{s}^2+\hat{u}^2}{\hat{t}^2}\right) \tag{1.19}$$

which from $t^2 = (-Q^2)^2$ gives the $1/Q^4$ behaviour typical of virtual photon mediated processes. Substitution of (1.18) into (1.19) then gives

$$\begin{aligned} \left.\frac{d^2\hat{\sigma}}{dxdQ^2}\right|_{eq\to eq} &= \frac{2\pi\alpha^2 e_q^2}{Q^4}\left(1+\frac{\hat{u}^2}{\hat{s}^2}\right)\,\delta(x-\xi) \\ &= \frac{2\pi\alpha^2 e_q^2}{Q^4}(1+(1-y)^2)\,\delta(x-\xi) \\ &= \frac{4\pi\alpha^2 e_q^2}{xQ^4}\,\frac{x}{2}\,(1+(1-y)^2)\,\delta(x-\xi). \end{aligned} \tag{1.20}$$

Thus the full differential cross section for $ep \to eX$ is obtained from substitution of (1.20) in (1.17) and performing the integration over ξ to give

$$\begin{aligned} \left.\frac{d\sigma}{dxdQ^2}\right|_{ep\to eX} &= \frac{4\pi\alpha^2}{xQ^4}\sum_q \int_0^1 d\xi\, f_q(\xi) e_q^2 \frac{x}{2}(1+(1-y)^2)\,\delta(x-\xi) \\ &= \frac{4\pi\alpha^2}{xQ^4}\sum_q f_q(x) e_q^2 \frac{x}{2}(1+(1-y)^2)\,. \end{aligned} \tag{1.21}$$

This gives the cross section dependence on the parton distribution $f_q(x)$ which should be compared with the alternative formalism stated in (1.9). The general formula of (1.9) is obtained from the standard calculation of cross sections from the matrix element given by

$$d\sigma = \frac{|\mathcal{M}|^2\, d\mathcal{P}}{\mathcal{F}} \tag{1.22}$$

where $\mathcal{F}$ is the incident flux factor, d$\mathcal{P}$ the Lorentz-invariant phase space term and $|\mathcal{M}|^2$ the matrix element of the general process $a+b \to c+d$ squared. For the DIS process $\mathcal{M}$ contains a leptonic (L) part and hadronic (W) part of the form

$$\mathcal{M} \propto L_{\mu\nu} W^{\mu\nu}\,.$$

The leptonic term

$$\begin{aligned} L^{\mu\nu} &= \frac{1}{2}\sum_{spin}[\overline{u}(k')\gamma_\mu u(k)][\overline{u}(k')\gamma_\nu u(k)]^* \\ &= \frac{1}{2}\mathrm{Tr}((\not{k}' + m_e)\gamma^\mu(\not{k} + m_e)\gamma^\nu) \\ &= 2(k_\mu k'_\nu + k'_\nu k_\mu - k'\cdot k g_{\mu\nu}) \end{aligned} \tag{1.23}$$

is calculated at the $e\gamma$ vertex in QED, where in the final result of (1.23) the electron mass m_e is neglected. The unknown hadronic vertex describing the γP interaction is written in the most general tensor form

$$W^{\mu\nu} = W_1\left(-g^{\mu\nu} + \frac{q^\mu q^\nu}{q^2}\right) + \frac{W_2}{M_p^2}\left(p^\mu - \frac{p\cdot q}{q^2}q^\mu\right)\left(p^\nu - \frac{p\cdot q}{q^2}q^\nu\right) \tag{1.24}$$

where the functions W_1 and W_2 are identified with the structure functions F_1 and F_2 via the relations

$$F_1 \equiv M_p W_1 \quad \& \quad F_2 \equiv \frac{p\cdot q}{M_p}W_2\,. \tag{1.25}$$

Combining (1.23), (1.24) and (1.25) in (1.22) leads to the general scattering cross section of (1.9)

$$\begin{aligned} \frac{d\sigma}{dxdQ^2} &= \frac{4\pi\alpha^2}{xQ^4}\left\{y^2 xF_1 + (1-y)F_2\right\} \\ &= \frac{4\pi\alpha^2}{xQ^4}\left\{y^2 xF_1 + (1-y)F_2 - \frac{y^2F_2}{2} + \frac{y^2F_2}{2}\right\} \\ &= \frac{4\pi\alpha^2}{xQ^4}\left\{\frac{1}{2}y^2(2xF_1 - F_2) + \frac{1}{2}(1+(1-y)^2)F_2\right\}\,. \end{aligned} \tag{1.26}$$

Thus, the form of the observable structure functions is apparent. On comparison of (1.26) with (1.21) we see that

$$\begin{aligned} F_2 = 2xF_1 &= \sum_q \int_0^1 d\xi\; e_q^2 x f_q(\xi)\delta(x-\xi) \\ &= \sum_q e_q^2 x f_q(x)\,, \end{aligned} \tag{1.27}$$

i.e. F_2 exhibits scaling in that it is a function of x only. In the above, e_q is the charge of the individual quarks and the sum is over all flavours.

1.3.2 Parton distributions and their evolution in Q^2

The term $f_q(x)$ in (1.27) is the parton distribution of the quarks, and describes the probability of finding a quark q inside the proton carrying a momentum fraction x. However,

QCD predicts corrections arising from the presence of glue in the proton. That is gluon emission from the quarks will lead to scaling violations of F_2 such that, $F_2(x) \rightarrow F_2(x, Q^2)$ through the Q^2 dependence of the parton distributions $f(x) \rightarrow f(x, Q^2)$. These are determined theoretically in pQCD.

The order α_s gluon corrections to the bare $\gamma^* q$ scattering process are shown in Figure 1.7. Diagrams (a) and (b) show the real gluon emission from the parton, whilst $(c)\rightarrow(e)$

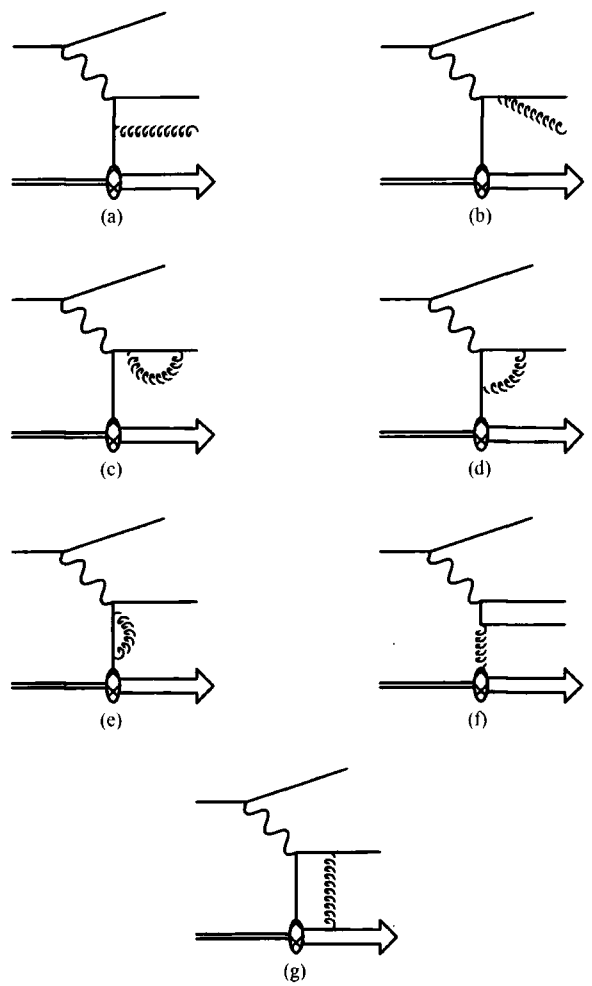

Figure 1.7: Real and virtual gluon emission contributions of the leading order corrections to the DIS scattering process $eq \rightarrow eq$.

show the virtual contributions. Diagram (f) is important as the photon is probing a gluon of the proton in which the $\gamma^* g$ interaction is through the process $\gamma^* g \rightarrow q\overline{q}$. This will be the focus of the next section and remainder of the thesis. Lastly, diagram (g) represents interactions between the struck quark and the other partons in the proton. However, this

is a higher twist effect and as such is suppressed by a factor α_s/Q^2 and can be neglected.

In the next chapter the formalism of these x, Q^2 dependent parton distributions will be discussed in detail for evolution of the variable x. Here a qualitative discussion will be made for the evolution in Q^2, concentrating on the solution of the evolution equation and the implications it has for the observed structure functions.

Including the contributions from gluon emission in Figure 1.7 to the structure function of (1.27), the mathematical formalism becomes,

$$\frac{F_2}{x} = \sum_q \int_x^1 \frac{dy}{y} f_q(y, M^2) e_q^2 \left[\delta\left(1 - \frac{x}{y}\right) + \frac{\alpha_s(M^2)}{2\pi} P\left(\frac{x}{y}\right) \int_{M^2}^{Q^2} \frac{dk_T^2}{k_T^2} \right] \tag{1.28}$$

where k_T^2 is the transverse momentum of the struck quark, $y \equiv \xi$ of (1.17) and $P(x/y)$ is the splitting function determining the probability of finding a parton with momentum fraction x inside a parton with momentum fraction y. The δ function term describes the "bare" process of Figure 1.6 in which there are no gluon corrections. The above equation (1.28) is finite because F_2 is a finite observable, but to achieve this, singularities arising from the inclusion of the QCD corrections have to be taken into account. The coupling α_s runs to remove the presence of UV singularities. The $1/k^2$ singularity arising from the $1/t$ pole of the Feynman calculation of the corrections of Figure 1.7 is regulated by the artificial cutoff M^2 defining the mass renormalization scale. Initial state collinear singularities have been swept into the the parton distribution $f_q(x)$ introducing the Q^2 dependence of $f_q(x) \rightarrow f_q(x, Q^2)$. The result is that we have a factorized form of the structure function equation, in which the long distance (non-perturbative) effects have been separated from the short distance physics which is calculated theoretically; the Q^2 dependence of the parton distributions is described by pQCD.

This Q^2 dependence of the parton densities means they can no longer be determined absolutely, only their behaviour with Q^2 which is described by the Dokshitzer-Gribov-Lipatov-Altarelli-Parisi (DGLAP) equation [15]

$$\frac{\partial f_q(x, Q^2)}{\partial \ln Q^2} = \frac{\alpha_s(Q^2)}{2\pi} \int_x^1 \frac{dy}{y} f_q(y, Q^2) P\left(\frac{x}{y}\right) . \tag{1.29}$$

Thus, the parton distributions can be calculated at any scale Q^2 provided we know the distribution at some input scale Q_0^2. This is determined experimentally at large values of x where the parton distributions can be measured accurately and are well known. The above evolution equation (1.29) is not the full story. There are contributions to the quark

parton density arising also from the process of $g \rightarrow q\overline{q}$ to be included. Glue is also produced through the processes $g \rightarrow gg$ and $q(\overline{q}) \rightarrow g\overline{q}(q)$. These determine the gluon distribution function $g(x,Q^2)$ and the full evolution equation becomes

$$\frac{\partial q(x,Q^2)}{\partial \ln Q^2} = \frac{\alpha_s(Q^2)}{2\pi}\int_x^1 \frac{dy}{y}\left[q(y,Q^2)P_{qq}\left(\frac{x}{y}\right) + g(y,Q^2)P_{qg}\left(\frac{x}{y}\right)\right] \tag{1.30}$$

for the quark distribution, and, for the gluon distribution

$$\frac{\partial g(x,Q^2)}{\partial \ln Q^2} = \frac{\alpha_s(Q^2)}{2\pi}\int_x^1 \frac{dy}{y}\left[g(y,Q^2)P_{gg}\left(\frac{x}{y}\right) + \sum_{i=1}^{2n_f} q_i(y,Q^2)P_{gq}\left(\frac{x}{y}\right)\right] . \tag{1.31}$$

Here the notation $f(x,Q^2) \equiv q(x,Q^2)$ is used with the summation i over all quark and antiquark flavours. As before the splitting functions P_{fi} give the probability of finding parton f with momentum fraction x inside an initial parton i $(i, f = q, g)$ with momentum fraction y.

1.3.3 Double Leading Logarithmic form of DGLAP equation

In the HERA DIS kinematic regime x is small and the gluon is the dominant constituent of the proton. Thus, we will concentrate on the form of the gluon distribution with Q^2 given by equation (1.31) and show that the DGLAP evolution equation is essentially a resummation of the $(\alpha_s \ln Q^2/Q_0^2)$ terms to all orders. However, at HERA x is also small so we will consider the region where $\ln(1/x)$ is large and obtain the double leading logarithmic (DLL) form of the DGLAP evolution equation.

In the HERA region the ratio x/y is small and the evolution equation of (1.31) can be approximated by the P_{gg} term only

$$\frac{\partial g(x,Q^2)}{\partial \ln Q^2} \simeq \frac{\alpha_s(Q^2)}{2\pi}\int_x^1 \frac{dy}{y}\, g(y,Q^2)\, P_{gg}\left(\frac{x}{y}\right) . \tag{1.32}$$

Equation (1.32) gives the contribution to the gluon distribution due to gluon emission from the probed gluon before interaction with the photon. For simplicity, if we consider fixed α_s then the solution can be obtained by taking moments, defined as

$$\tilde{g}(n,Q^2) = \int_0^1 dx\; x^{n-1} g(x,Q^2) , \tag{1.33}$$

of (1.32) giving

$$\begin{aligned}\frac{\partial \tilde{g}(n,Q^2)}{\partial \ln Q^2} &= \frac{\alpha_s}{2\pi}\int_0^1 dx\; x^{n-1}\int_x^1 \frac{dy}{y} P\left(\frac{x}{y}\right) g(y,Q^2) \\ &= \frac{\alpha_s}{2\pi}\int_0^1 dy\; y^{n-1} g(y,Q^2)\int_0^y \frac{dx}{y} P_{gg}\left(\frac{x}{y}\right)\frac{x^{n-1}}{y^{n-1}} .\end{aligned} \tag{1.34}$$

Letting $z = x/y$ then (1.34) becomes

$$\frac{\partial \tilde{g}(n,Q^2)}{\partial \ln Q^2} = \frac{\alpha_s}{2\pi}\tilde{g}(n,Q^2)\int_0^1 dz\ P_{gg}(z)z^{n-1}\ . \tag{1.35}$$

For small x, i.e. small z, the splitting function takes the approximate form

$$P_{gg} = 6\left(\frac{1-z}{z} + \frac{z}{1-z} + z(1-z)\right) \sim \frac{6}{z}\ ,$$

giving

$$\begin{aligned}\frac{\partial \tilde{g}(n,Q^2)}{\partial \ln Q^2} &= \frac{3\alpha_s}{\pi}\tilde{g}(n,Q^2)\int_0^1 dz\ z^{n-2} \\ &= \frac{3\alpha_s}{\pi}\frac{\tilde{g}(n,Q^2)}{n-1}\ .\end{aligned} \tag{1.36}$$

Rearrangement of (1.36) allows us to write

$$\int \frac{d\tilde{g}(n,Q^2)}{\tilde{g}(n,Q^2)} = \frac{3\alpha_s}{\pi(n-1)}\int_{Q_0^2}^{Q^2} d\ln Q^2$$

which has the solution, in moment space, of the form

$$\tilde{g}(n,Q^2) = A\exp\left[\frac{3\alpha_s}{\pi(n-1)}\ln\left(\frac{Q^2}{Q_0^2}\right)\right]\ . \tag{1.37}$$

Using the inverse transformation

$$xg(x,Q^2) = \frac{1}{2\pi i}\int_{-i\infty}^{i\infty} dn\ x^{-(n-1)}\tilde{g}(n,Q^2)\ , \tag{1.38}$$

the solution of the gluon distribution can be obtained in x, Q^2 space. Substituting the result of (1.37) into (1.38) and writing

$$x^{-(n-1)} = \exp\left[(n-1)\ln\left(\frac{1}{x}\right)\right],$$

we get

$$xg(x,Q^2) = \frac{1}{2\pi i}\int_{-i\infty}^{i\infty} dn\ \exp\left[(n-1)\ln\left(\frac{1}{x}\right) + \frac{3\alpha_s t}{\pi(n-1)}\right]\tilde{g}(n,Q_0^2) \tag{1.39}$$

where we define $t = \ln(Q^2/Q_0^2)$. For small x and large Q^2, as in the HERA kinematic regime, then the $\ln(1/x)$ and $\alpha_s \ln(Q^2/Q_0^2)$ terms are large and have to be resummed, i.e. we require the solution to (1.39). The integration of (1.39) can be performed approximately using the saddle point method of integration giving the result

$$\begin{aligned}xg(x,Q^2) &\simeq \exp\left[\ln\left(\frac{1}{x}\right)\left(\frac{3\alpha_s t}{\pi\ln(1/x)}\right)^{1/2} + \frac{3\alpha_s t}{\pi}\left(\frac{3\alpha_s t}{\pi\ln(1/x)}\right)^{-1/2}\right] \\ &\simeq \exp\left[2\left(\frac{3\alpha_s}{\pi}\ln\left(\frac{1}{x}\right)\ln\left(\frac{Q^2}{Q_0^2}\right)\right)^{\frac{1}{2}}\right]\ .\end{aligned} \tag{1.40}$$

This is the DLL solution of the DGLAP equation for fixed α_s. The above DLL approximation can also be performed analytically for running coupling $\alpha_s(Q^2)$ in (1.32). The form of the solution for the $\ln Q^2$ terms is the same as that above after the simple substitution

$$\alpha_s \ln\left(\frac{Q^2}{Q_0^2}\right) \rightarrow \int_{Q_0^2}^{Q^2} \frac{dq^2}{q^2}\alpha_s(q^2)$$

in (1.37).

For a constant starting distribution, $xg(x,Q_0^2) = G_0$, then (1.40) predicts that the gluon distribution will grow faster than any power $\ln(1/x)$ as $x \rightarrow 0$; the structure functions will rise with decreasing x.

Q^2 evolution in ladder form

Theoretically we can have multiple gluon emission and allow n gluons to be emitted from the probed gluon before interaction with the photon. The DGLAP equation can then be considered to be built up from n gluon emissions forming "rungs" of a ladder diagram [16] as shown in Figure 1.8. It is important to remember this picture only holds in an axial gauge where the gluon has two physical polarizations.

The important feature of LO DGLAP evolution is that the leading log contribution comes from the strong ordering configuration of the gluon emission along the chain as we move from the hard scale Q^2, determined by the virtuality of the photon, to the hadronic scale

$$Q^2 \gg k_n^2 \gg k_{n-1}^2 \gg \ldots \gg k_1^2 \,. \tag{1.41}$$

In the DLL region, we also have strong ordering of the longitudinal momentum xP such that

$$x \ll x_{n-1} \ll \ldots \ll y \,. \tag{1.42}$$

The emission of n gluons is calculated from the modified "1 rung" integral equation form of (1.29)

$$xg(x,Q^2) = \int_{Q_0^2}^{Q^2} \frac{dk^2}{k^2}\,\frac{3\alpha_s}{\pi}\int_x^1 dy\; yg(y)$$

by the inclusion of n nested integrals

$$\begin{aligned} xg^n(x,Q^2) &= \left(\frac{3\alpha_s}{\pi}\right)^n \int^{Q^2}\frac{dk_n^2}{k_n^2}\ldots\int^{k_2^2}\frac{dk_1^2}{k_1^2}\int_x^1\frac{dx_{n-1}}{x_{n-1}}\ldots\int_{x_2}^1\frac{dx_1}{x_1}\int_{x_1}^1\frac{dy}{y}\;yg(y) \\ &= \frac{1}{n!}\left[\frac{3\alpha_s}{\pi}\ln\left(\frac{Q^2}{Q_0^2}\right)\right]^n \frac{1}{n!}\left[\ln\left(\frac{1}{x}\right)\right]^n G_0 \end{aligned} \tag{1.43}$$

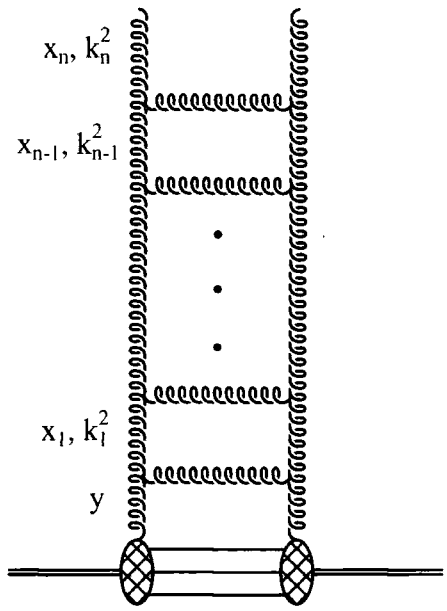

Figure 1.8: Ladder diagram of DGLAP evolution of the gluon distribution of the proton. The transverse momenta of the emitted gluons are strongly ordered along the chain. This shows the DLL approximation where we also include strong ordering of the longitudinal momentum x. For the DGLAP evolution which resums $\ln Q^2/Q_0^2$ terms there is only a soft, kinematical ordering of the $x's$; $x < x_{n-1} < ... < x_1$. The "ladder" diagram is representative only in an axial gauge. The symmetry of the diagram is to indicate that the cross sections are obtained by taking the matrix element squared of the process.

where the starting input $G_0 = yg(y)$. This is using the small z approximation of P_{gg}. Thus, the DGLAP equation for the gluon distribution $xg(x, Q^2)$ is given by the summation over n gluon rungs of the ladder diagram

$$xg(x, Q^2) = \sum_n xg^n(x, Q^2) \, . \tag{1.44}$$

From (1.43) and (1.44) we see that the leading logarithmic equation is effectively the resummation of the $[\alpha_s \ln(Q^2/Q_0^2)]^n$ terms. By relaxing the strong ordering of one pair of momenta in the gluon chain such that $k_j \sim k_{j-1}$, we would lose one power of $\ln(Q^2/Q_0^2)$ giving the next-to-leading logarithmic (NLL) DGLAP equation.

For completeness, using the identity of the modified Bessel function[17]

$$I_0(u) = \sum_n \left(\frac{1}{n!}\right)^2 \left(\frac{u^2}{4}\right)^n \sim \frac{e^u}{\sqrt{2\pi u}} \, , \tag{1.45}$$

and defining

$$\left(\frac{u^2}{4}\right)^n = \left[\frac{3\alpha_s}{\pi}\ln\left(\frac{1}{x}\right)\ln\left(\frac{Q^2}{Q_0^2}\right)\right]^n ,$$

then (1.43) gives the same result as obtained from taking the moments of (1.32). We have regained the result of (1.40) but from the treatment of the evolution equation as a sum over n gluon emissions.

The form of the input $G_0(x, Q_0^2)$ in (1.40) determines the form of the gluon distribution after evolution to higher Q^2. A flat input at the scale Q_0^2 will result in the form of the DLL result of (1.40).

The observables are now obtained using the parton distribution of (1.40) to give the structure function F_2 of (1.28) and hence the cross section. The success of the DGLAP evolution formalism in predicting the structure function F_2 of the proton at HERA can be seen in Figure 1.4 where the solid line is calculated using Q^2 evolution of the MRS(A) [12] parton distributions.

Chapter 2

The small x kinematic region

Experiments at HERA probe values of Bjorken x as low as $x \sim 10^{-4}$. For values this small logarithmic terms in $1/x$ become large indicating that the DGLAP formalism (1.32) which sums the leading[1] $\ln Q^2$ terms is not enough. These logarithms in $1/x$ need to be considered and resummed. As for the DGLAP equation, in which the LO behaviour arises from the strong ordering of transverse momenta k_T, the leading behaviour $[\ln 1/x]^n$ terms arise from a strongly ordered kinematic region, but this time of the longitudinal momenta i.e.

$$x \ll x_n \ll x_{n-1} \ldots \ll x_1 \,. \tag{2.1}$$

This leading logarithmic resummation (LL($1/x$)) is performed by the Balitskii-Fadin - Kuraev-Lipatov (BFKL) equation which effectively resums the leading $[\alpha_s \ln(1/x)]^n$ terms.

The aim of this thesis is to study the BFKL equation and its application in making predictions for observable quantities at HERA. Because at present the BFKL equation is known only, for practical purposes, to LO (see section 2.4), modifications will be made to the standard equation (2.3) to incorporate some effects of subleading contributions. At LO the BFKL equation corresponds to a fixed coupling α_s, however, at NLO running of the coupling is specified[19]. Also, one component of the full NLO BFKL calculation is a kinematic constraint on the longitudinal momenta of real emitted gluons[2]. These (incomplete) subleading effects can be included with the LO BFKL equation to give a more "realistic" solution for the gluon distribution. These modifications will be studied in greater detail in chapter 3 where we also make a further modification to the small q_T

[1]The coefficient functions and anomalous dimensions of DGLAP evolution are known at NLO. [14, 18]
[2]see section 3.5

region[3] to allow exclusive jet production to be calculated within the BFKL formalism. Here we split real gluon emission into two parts - gluons with very small transverse momenta q_T, and those with larger q_T. The low momentum real gluons will then be resummed with the virtual gluons before evolution in $\ln 1/x$ is performed. This approach is useful in the production of full BFKL Monte Carlo simulations which are required for experimental analysis[20, 21, 22]. Because the work in this thesis will apply these modifications, in this introductory chapter the aim is to present the BFKL equation and discuss its properties which should be observable experimentally. Thus, only a brief outline of the equation will be presented here. Detailed discussions of the origin and derivation of the BFKL equation can be found for example in [10, 14, 23, 24, 25]. The solution will be given in detail in appendix B and can also be found in the above references. Discussion of NLO improvements can be found in section 2.4 and chapter 3.

2.1 The BFKL equation

The BFKL equation is pictorially described by a ladder type diagram somewhat similar to that of the DGLAP evolution ladder of Figure 1.8, but, since we wish to sum only the leading $\ln 1/x$ terms which arise from strong ordering of the longitudinal momenta (2.1), we now need to consider the full transverse momentum dependence of the gluon distribution. That is, for a finite scale Q^2, we must keep the full Q^2 dependence of the gluon distribution $g(x, Q^2)$, not just the LLQ^2 terms. Thus, we unfold the k_T^2 integration over the last rung of the gluon ladder and we must now work with the unintegrated gluon distribution $f(x, k_T^2)$. The gluon distribution $g(x, Q^2)$, as discussed in chapter 1, is then obtained through integration of the transverse momenta up to the scale Q^2. That is,

$$g(x, Q^2) = \int^{Q^2} \frac{dk_T^2}{k_T^2} f(x, k_T^2) \, . \tag{2.2}$$

Figure 2.1 shows part of the BFKL ladder diagram. However, the diagram of Figure 2.1 is more complicated than that of Figure 1.8, as the BFKL ladder is only an effective diagram representing many different Feynman graph contributions from both real and virtual gluon emissions. Some of the gluon emission contributions to the BFKL ladder can be seen in Figure 2.2 which shows quark-quark scattering via t-channel gluon exchange.

[3] q_T refers to the transverse momenta of real emitted gluons from the BFKL gluon chain. See Figure 2.3

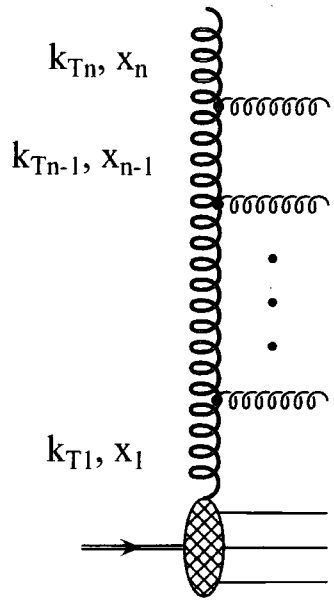

Figure 2.1: The unintegrated gluon distribution, $f(x, k_T^2)$, is effectively the sum of ladder diagrams formed by the modulus squared of such amplitudes. The leading $\alpha_s \ln 1/x$ resummation is performed by the BFKL equation incorporating strong ordering in the longitudinal momenta x_i as in (2.1). The k_{Ti}^2 are unordered along the chain. The vertical gluon is reggeized as indicated by the thicker gluon line than the real emitted (horizontal) gluons (see Figure 2.3).

The tree level contribution is shown in Figure 2.2(a) and leads to the delta function driving term for the integrated BFKL equation discussed in chapter 4. Diagrams 2.2(b)-(f) show corrections to the tree level process arising from real gluon emission. On calculation of these graphs the results can be written as an effective vertex factor[10, 24]

$$\Gamma_R = \frac{3\alpha_s}{\pi} \frac{k_T^2}{k_T'^2 q_T^2} .$$

Here k_T and k_T' refer to the momenta of the vertical propagators below and above the emitted gluon which carries a transverse momentum q_T. Thus the real gluon corrections can be described by a single *effective* diagram which is shown in Figure 2.3(a).

The virtual gluon corrections (at the same order as the real corrections) are shown in diagrams (g)-(j) of Figure 2.2. The overall effect of including these diagrams is to modify the real gluon emission effective diagram of Figure 2.3(a) by *reggeizing* the t-channel gluon propagator, see Figure 2.3(b). That is, the leading $\ln s$ behaviour of the amplitude for

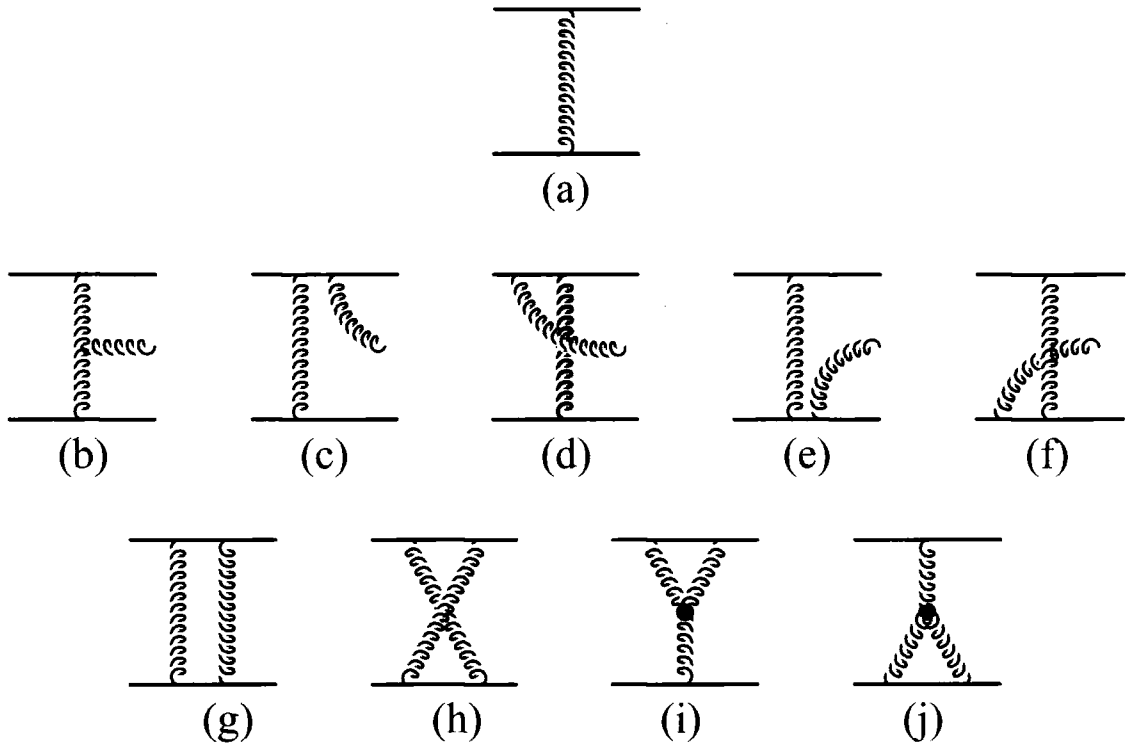

Figure 2.2: (a) Parton-parton scattering via gluon exchange in the t-channel. (b)-(f) Order α_s^2 corrections to the tree level amplitude (a) i.e. $qq \to qq + g$. (g)-(j) Virtual corrections to the tree level amplitude (a).

quark-quark scattering in the high energy Regge limit (i.e. $s \gg -t$) has the form

$$\left(\frac{s}{k_T^2}\right)^{\alpha_g(k_T^2)},$$

where $s = (p_A + p_B)^2$ and $t = (p_A - p_C)^2$ are the Mandelstam variables of the scattering process $A(p_A) + B(p_B) \to C(p_C) + D(p_D)$ (see section 4.2 for a full description of these variables), with $\alpha_g(k_T^2 = t)$ the Regge trajectory of the gluon. The BFKL gluon ladder is then built up from multiple gluon emissions of the type shown in Figure 2.3(b) in which the vertical propagator is described by a reggeized gluon with the rungs of the ladder corresponding to real gluon emission with an effective vertex Γ_R. Both the effective vertex term and the virtual corrections have the correct colour structure.

Full calculation of Figure 2.2, keeping only the leading $\ln s$ factors, leads to the famous

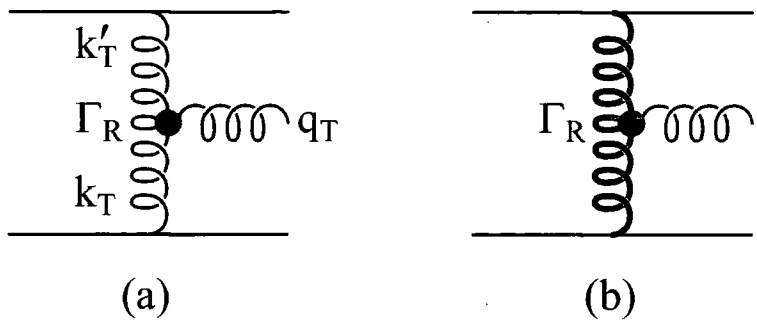

Figure 2.3: (a) Effective diagram for real gluon emission from the exchanged gluon propagator. This contains contributions from diagrams (a)-(f) of Figure 2.2 which are described by the vertex term Γ_R as indicated by the black dot. (b) Modification of the effective real gluon diagram 2.3(a) in which the virtual contributions (Figure 2.2(g)-(j)) *reggeize* the vertical gluon as indicated by the thicker line.

BFKL equation[23]

$$f(x,k_T^2) = f^{(0)}(x_0,k_T^2) + \frac{3\alpha_s}{\pi}k_T^2\int_x^{x_0}\frac{dx'}{x'}\int\frac{dk_T'^2}{k_T'^2}\left[\frac{f(x',k_T'^2)-f(x',k_T^2)}{\mid k_T^2-k_T'^2\mid} + \frac{f(x',k_T^2)}{(4k_T'^4+k_T^4)^{1/2}}\right]. \tag{2.3}$$

Equation (2.3) gives the $n = 0$ form of the LO integral evolution equation for the unintegrated gluon distribution $f(x,k_T^2)$ where n refers to the azimuthal projection $\exp(in\varphi)$. It has the boundary conditon

$$f(x,k_T^2) = f^{(0)}(x,k_T^2) \tag{2.4}$$

at $x = x_0$. For recursive computation of the solution f, $f^{(0)}(x,k_T^2)$ is a suitable inhomogeneous driving term from which the BFKL $\ln 1/x$ evolution is started at the input scale $x = x_0$. In the next chapter $f^{(0)}(x,k_T^2)$ will describe the proton gluon distribution, whilst in chapter 4, in which DIS including forward jet events will be discussed, the driving term will be considered to be the fusion process $\gamma^* g \to q\overline{q}$ which can be calculated from the quark box (and crossed box) diagrams shown in Figure 3.11. One important feature to note for this equation is that the infrared divergence of the integral as $k_T'^2 \to 0$ cancels between the real and virtual contributions. The factor $3\alpha_s/\pi$ arises from the real emission vertex Γ_R.

For future reference, it is useful to write the BFKL equation of (2.3) in symbolic form

$$f = f^{(0)} + K \otimes f\ , \tag{2.5}$$

in which K is known as the BFKL kernel. (2.5) is solved subject to the boundary condition (2.4) with the convolution $\otimes$ referring to integration in $\ln 1/x$. Comparing (2.3) with (2.5) we observe that the explicit form for $K \otimes f$ is

$$K \otimes f = \frac{3\alpha_s}{\pi} k_T^2 \int_x^{x_0} \frac{dx'}{x'} \int \frac{dk_T'^2}{k_T'^2} \left[\frac{f(x', k_T'^2)}{| k_T^2 - k_T'^2 |} - \frac{f(x', k_T^2)}{| k_T^2 - k_T'^2 |} + \frac{f(x', k_T^2)}{(4k_T'^4 + k_T^4)^{1/2}} \right] . \quad (2.6)$$

Here the real gluon emission is described by the first term of (2.6) whilst the second and third terms give the virtual contributions. The cancellation of infrared divergences between the real and virtual terms can be seen between the first and second terms of 2.6.

Expected small x behaviour of the gluon distribution from BFKL dynamics

Before studying the solution of the BFKL equation in more detail, it is instructive to look at the expected form of the solution of (2.3).

Let λ be the leading eigenvalue of the kernel K, then

$$\frac{\partial f}{\partial \ln(1/x)} = Kf = \lambda f ,$$

from which we see that f has the solution of the form

$$f \sim e^{\lambda \ln 1/x} \sim x^{-\lambda} .$$

Indeed, this $x^{-\lambda}$ behaviour obtained from the simple calculation above is the x dependence we will observe when a more rigorous calculation of (2.3) is made in section 2.2.

n-rung decomposition of the BFKL gluon $f(x, k_T^2)$

Similar to the picture of DGLAP evolution in which the total gluon distribution $g(x, Q^2)$ is made up from the sum of n gluon rung contributions to the gluon ladder chain(section 1.3.3), the total BFKL unintegrated distribution, $f(x, k_T^2)$, is also composed of the summation over the n rungs of the BFKL effective ladder, i.e.

$$f(x, k_T^2) = \sum_n f^n(x, k_T^2) . \quad (2.7)$$

This decomposition into the individual n rung components will be used as the basis for the exclusive jet cross section calculation of chapter 3.

2.1.1 Double Leading Logarithmic form of the BFKL equation

Both the BFKL and DGLAP equations describe the evolution of a gluon through emission of real and virtual gluons. The DGLAP equation performs a resummation of the $\mathrm{LL}Q^2$ terms whilst the BFKL equation resums the $\mathrm{LL}(1/x)$ terms. How do these approaches compare in the DLL phase space region where $\ln(1/x)\ln Q^2$ is large? The DLL result for the DGLAP equation was presented in section 1.3.3 (Eq. 1.40).

If we consider the limit $k_T^2 \gg k_T'^2$, then the BFKL kernel K of (2.6) becomes

$$K(k_T, k_T') \simeq \frac{3\alpha_s}{\pi}\frac{1}{k_T'^2} . \tag{2.8}$$

Substituting (2.8) into the recursive form of the BFKL equation (2.5), i.e. the n^{th} rung contribution to the gluon distribution is obtained from the $(n-1)^{\text{th}}$ rung, then we have

$$\begin{aligned} f_n(x,k_T^2) &= \int_x^1 \frac{dx'}{x'}\int dk_T'^2\; K(k_T,k_T')f_{n-1}(x',k_T'^2) \\ &\simeq \int_x^1 \frac{dx'}{x'}\int^{k_T^2} dk_T'^2\;\frac{3\alpha_s}{\pi}\frac{1}{k_T'^2}f_{n-1}(x',k_T'^2) \\ &\simeq \frac{3\alpha_s}{\pi}\frac{1}{n}\ln\left(\frac{1}{x}\right)\frac{1}{n}\ln\left(\frac{k_T^2}{\mu^2}\right)f_{n-1}(x,k_T^2) . \end{aligned}$$

Using (2.7) then the total unintegrated gluon distribution is

$$\begin{aligned} f(x,k_T^2) &= \sum_n \frac{3\alpha_s}{\pi}\left(\frac{1}{n}\right)^2\ln\left(\frac{1}{x}\right)\ln\left(\frac{k_T^2}{\mu^2}\right)f_{n-1}(x,k_T^2) \\ &= \sum_n \left(\frac{1}{n!}\right)^2\left[\frac{3\alpha_s}{\pi}\ln\left(\frac{1}{x}\right)\ln\left(\frac{k_T^2}{\mu^2}\right)\right]^n . \end{aligned} \tag{2.9}$$

Thus, after substitution of

$$\frac{u^2}{4} = \frac{3\alpha_s}{\pi}\ln\left(\frac{1}{x}\right)\ln\left(\frac{k_T^2}{\mu^2}\right)$$

into the modified Bessel function of (1.45), Eq.(2.9) gives the result

$$f(x,k_T^2) \simeq \exp\left[2\left(\frac{3\alpha_s}{\pi}\ln\left(\frac{1}{x}\right)\ln\left(\frac{k_T^2}{\mu^2}\right)\right)^{\frac{1}{2}}\right] , \tag{2.10}$$

which on integration of k_T^2 up to the scale Q^2 reproduces the DLL approximation of the gluon distribution $g(x,Q^2)$ as obtained in chapter 1.

2.2 Solving the BFKL equation for fixed α_s

For the BFKL equation with fixed coupling α_s, then (2.3) can be solved analytically. For completeness the solution of the BFKL equation and the kernel K can be found in appendices A & B. Here a quick outline of the solution will be presented[10].

Defining the moment equation

$$\tilde{f}(x,\omega) \equiv \int_o^\infty (k^2)^{-\omega-1} f(x,k^2) dk^2 \tag{2.11}$$

where for simplicity of notation we take $k^2 = k_T^2$, and applying (2.11) to (2.5), then the BFKL equation factorizes and the differential equation in moment space is

$$\frac{\partial \tilde{f}(x,\omega)}{\partial \ln(1/x)} = \tilde{K}(\omega)\tilde{f}(x,\omega) \; . \tag{2.12}$$

$\tilde{K}(\omega)$ is the kernel written in moment space which has the solution (see appendix A)

$$\tilde{K}(\omega) = \frac{3\alpha_s}{\pi}[2\Psi(1) - \Psi(\omega) - \Psi(1-\omega)] \; . \tag{2.13}$$

Ψ is defined by the gamma functions $\Psi(\omega) = \Gamma'(\omega)/\Gamma(\omega)$, with $\Psi(1) = -\gamma_E = 0.5772...$ the Euler-Mascheroni constant.

Knowing the solution for the kernel (Eq. 2.13), we can now solve the BFKL equation in moment space to give

$$\tilde{f}(x,\omega) = \tilde{f}(x_0,\omega)\left(\frac{x}{x_0}\right)^{-\tilde{K}(\omega)} \; . \tag{2.14}$$

Performing the inverse Mellin transformation of (2.14) and using saddle point integration gives (eventually) the result

$$f(x,k^2) = \left(\frac{x}{x_0}\right)^{-\lambda} \frac{\tilde{f}(x_0,1/2)(k^2)^{\frac{1}{2}}}{\left[2\pi\left(\lambda'' \ln(x_0/x) + A\right)^{\frac{1}{2}}\right]} \exp\left(\frac{-\ln^2(k^2/\overline{k}^2)}{2\lambda'' \ln(x_0/x) + 2A}\right) \tag{2.15}$$

where λ is the maximum eigenvalue of the kernel K, and is given by

$$\lambda = \frac{3\alpha_s}{\pi} 4 \ln 2 \; . \tag{2.16}$$

Also

$$\lambda'' = \frac{3\alpha_s}{\pi} 28\zeta(3) \; . \tag{2.17}$$

$\zeta(3)$ is the Riemann zeta function with a value 1.202. A is defined as $1/\tilde{f} d^2\tilde{f}/d\omega^2$, and $\overline{k}$ is an arbitrary scale to make the argument of the logarithm dimensionless. This calculation can be found in more detail in Appendix B.

2.2.1 Dynamical properties of the BFKL solution

Let us now look at the properties of the BFKL solution for $f(x, k_T^2)$ to determine what small x behaviour should be observable at HERA.

To recap, the solution of the BFKL equation (for fixed coupling) is

$$\frac{f(x,k^2)}{(k^2)^{\frac{1}{2}}} \sim \left(\frac{x}{x_0}\right)^{-\lambda} \frac{\exp\left(\frac{-\ln^2(k^2/\bar{k}^2)}{2(\lambda''\ln(x_0/x)+A)}\right)}{\left[2\pi\left(\lambda''\ln(x_0/x)+A\right)^{\frac{1}{2}}\right]},$$

thus as $x \to 0$ we would expect to see an $x^{-\lambda}$ behaviour of the gluon distribution f, where λ, the maximum eigenvalue of the kernel, is defined in (2.16). This behaviour of the gluon distribution at small x (an unobservable quantity), will feed through to the observable structure functions and cross sections measurable at HERA. For fixed α_s, then from (2.16) we see that the value of λ is fixed but is dependent on the scale at which α_s is set. For reasonable values of $\alpha_s \sim 0.2$, then we find $\lambda \sim 0.5$. Thus, we would expect an increase in the unintegrated gluon distribution $f(x, k_T^2)$, and also the structure function F_2, as we move to smaller x values if BFKL dynamics are obeyed. This is to be compared with the expected rise of the gluon distribution $g(x, Q^2)$ obtained from DGLAP evolution which for suitable input $g^{(0)}(x, Q^2)$ can reproduce the rise of the structure functions obtained by evolution in $\ln 1/x$. The following chapters will address processes which neutralize (unwanted) evolution in Q^2 and allow us to concentrate on the small x behaviour of the gluon distributions in order to try to observe this expected $x^{-\lambda}$ rise characteristic of BFKL dynamics.

One other important feature to notice in the result of (2.15) is the exponential term in k^2. This is of Gaussian form and as such has a width Γ_g equal to

$$\Gamma_g = \sqrt{(\lambda''\ln(x_0/x) + A)}$$

with λ'' of (2.17) and A defined above in section 2.2. The consequence of this is we observe a diffusion in $\ln k^2$ as we evolve from a starting scale x_0 down to some smaller value x. This diffusion in fact causes problems - the integral over k^2 can now enter the non-perturbative infrared region of low k^2 where the physics is not completely understood. This introduces uncertainties into the validity of results calculated using the BFKL equation. The most simple (and crude) way of removing this problem is to impose an infrared cutoff k_0^2 on the lower limit of integration[26, 27]. This problem will be addressed further in chapter 4.

Thus to summarize, the characteristic features arising from BFKL small x dynamics are

(i) a strong increase of the gluon distribution $f(x, k_T^2)$ as $x \to 0$, of the form $x^{-\lambda}$. The rate of increase is determined by the value of λ, the maximum eigenvalue of the BFKL kernel, which for fixed α_s is $\lambda = 3\alpha_s 4 \ln 2/\pi \sim 0.5$ (for relevant values of α_s)

(ii) a diffusion in the transverse momenta, the rate of which is determined by the initial conditions and the value of λ'' giving the curvature of K at the point $\omega = 1/2$. This arises directly from the lack of strong ordering in k^2 of the emitted gluons.

2.2.2 BFKL equation incorporating running α_s

The above discussion of the BFKL equation and solution has been for fixed α_s. However, NLO corrections will introduce running coupling [19] such that we now require $\alpha_s(k_T^2)$. This can be incorporated into the BFKL equation without actually knowing the full NLO corrections, to attempt to include some of the subleading effects. By including running coupling into (2.3), then the equation becomes

$$f(x,k_T^2) = f^{(0)}(x,k_T^2) + \frac{3\alpha_s(k_T^2)}{\pi} k_T^2 \int \frac{dk_T'^2}{k_T'^2} \left[\frac{f(x,k_T'^2) - f(x,k_T^2)}{\mid k_T^2 - k_T'^2 \mid} + \frac{f(x,k_T^2)}{(4k_T'^4 + k_T^4)^{1/2}} \right] \quad (2.18)$$

and we can no longer solve for f analytically. We must numerically solve (2.18) using the recursive nature $f_n = K \otimes f_{n-1}$ starting from a suitable input $f^{(0)}$. Thus, we explicitly solve the BFKL equation of the form

$$\frac{\partial f(x,k_T^2)}{\partial \ln 1/x} = \int_{k_0^2} dk_T'^2 \; K(k_T^2, k_T'^2) f(x, k_T'^2) \quad (2.19)$$

where the input $f^{(0)}(x_0, k_T^2)$, with $x_0 \sim 0.01$, can be determined (for example) from the MRS parton distributions[12] for the proton. Also, we must now explicitly include an IR cutoff, k_0^2, on the momentum integral to prevent the solution from entering the non-perturbative region for large α_s, (i.e. $\alpha_s(k^2 \to 0) \to \infty$, see Figure 1.5).

Numerical computation of (2.19) gives the solution

$$f(x,k_T^2) \to C x^{-\lambda} ,$$

the form of which is achieved very quickly as we evolve downwards in x. It is found [26] that λ has the effective value

$$\lambda \sim 0.4 - 0.5$$

which is weakly dependent on the cutoff k_0^2[26, 27]. More disconcerting though is the stronger dependence of the normalization C on k_0^2. Due to this ambiguity, numerical computations of the gluon distribution using BFKL dynamics will concentrate on the x dependence of observables, rather than the normalization (see chapters 3 & 4).

Recall, $f(x, k_T^2)$ is the unintegrated gluon distribution, then

$$xg(x, Q^2) = \int^{Q^2} \frac{dk_T^2}{k_T^2} f(x, k_T^2) \sim x^{-\lambda} ,$$

that is the $x^{-\lambda}$ behaviour feeds into the fully integrated gluon distribution and also to the observable quantities such as F_2.

Thus we see the numerical solution of the BFKL equation incorporating running coupling $\alpha_s(k_T^2)$ is successfully consistent with the analytic solution for fixed coupling. It is this numerical form which will be used throughout the remainder of this thesis.

2.3 Alternative formalism of the BFKL equation

The above discussion has considered the general properties of the BFKL equation as given by (2.3), where we have integration over $k_T'^2$ relating to the momentum of the vertical gluon propagator. In the following chapters we wish to use the BFKL formalism, which sums real and virtual gluon emissions, to provide an estimate of exclusive jet production, i.e. we will identify the real gluon rungs of the ladder as individual jets in the final state (subject to resolution cuts). Thus, it is more convienient to have a form of (2.3) in which the explicit momentum dependence, q_T^2, of the emitted gluons is displayed. Below it will be shown that (2.3) can be written equivalently as

$$f(x, k_T^2) = f^{(0)}(x, k_T^2) + \frac{3\alpha_S}{\pi} \int_x^1 \frac{dx'}{x'} \int \frac{d^2\boldsymbol{q}_T}{\pi q_T^2} \left[\frac{k_T^2}{k_T'^2} f(x', k_T'^2) - f(x', k_T^2)\, \Theta(k_T^2 - q_T^2) \right] . \tag{2.20}$$

This is the form of the BFKL equation that will be used throughout the remainder of the thesis.

The proof of the equivalence[28] of the two forms (2.3) and (2.20) of the BFKL equation is non-trivial and since we will be using the form of (2.20) it is worth while to show the proof here. This is in two parts,

(i) we will first quote the two dimensional form of (2.3) when we undo the azimuthal φ integration and show the equivalence with the fully integrated form, and

(ii) the integration over $k_T'^2$ will be performed using the Feynman parameter λ which will allow us to rewrite the equation in terms of q_T^2.

Performing the azimuthal integration

The BFKL equation (2.3) written in the azimuthal unintegrated form is

$$F(x,k_T^2) = F^0(x,k_T^2) + \lim_{\delta\to 0}\frac{3\alpha_s}{\pi}\int\frac{dx'}{x'}\int_{k_0^2=0}\frac{d^2\boldsymbol{k}_T'}{\pi}\frac{1}{|\,\boldsymbol{k}_T'-\boldsymbol{k}_T\,|^2+\delta^2} \times\left\{F(x',k_T'^2)-\frac{k_T^2\,F(x',k_T^2)}{(k_T'^2+|\,\boldsymbol{k}_T'-\boldsymbol{k}_T\,|^2+\delta^2)}\right\}, \tag{2.21}$$

where we have chosen to work with the distribution $F = f/k^2$ as it is slightly easier to keep track of k^2 factors. Equation (2.21) is equivalent to (2.3) under integration over azimuth φ between the vectors $\boldsymbol{k}_T'$ and $\boldsymbol{k}_T$. The regulator δ is included to remove any divergence problems under the integration over $k_T'^2$ as we take the lower integration limit $k_0^2 \to 0$.

By displaying the explicit azimuthal dependence of (2.21) we have, for the real emission terms

$$I_R = \int\frac{d^2\boldsymbol{k}_T'}{\pi}\frac{F(x',k_T'^2)}{|\,\boldsymbol{k}_T'-\boldsymbol{k}_T\,|^2+\delta^2} = \frac{1}{2\pi}\int dk_T'^2\int_0^{2\pi}d\varphi\,\frac{F(x',k_T'^2)}{k_T'^2+k_T^2-2k_T'k_T\cos\varphi+\delta^2} \tag{2.22}$$

and virtual terms,

$$I_V = \frac{1}{2\pi}\int dk_T'^2\int_0^{2\pi}d\varphi \times\left[\frac{-k_T^2\,F(x',k_T^2)}{(k_T'^2+k_T^2-2k_T'k_T\cos\varphi+\delta^2)(k_T'^2+k_T'^2+k_T^2-2k_T'k_T\cos\varphi+\delta^2)}\right]. \tag{2.23}$$

The φ integration in (2.22) can be performed using the standard integral[4]

$$I_R = \int_0^{2\pi}d\varphi\,\frac{1}{[x^2+y^2-2xy\cos\varphi+\delta^2]}$$

[4]integration performed using Mathematica

$$= \frac{2\pi}{\sqrt{[(\delta^2 + x^2 + y^2 - 2xy)(\delta^2 + x^2 + y^2 + 2xy)]}} .$$

Taking the limit $\delta \to 0$ and setting $a = x^2/y^2$ we obtain,

$$I_R = \frac{2\pi a}{x^2(1-a)},$$

which gives us the solution for the integrated real emission terms of (2.21) as

$$I_R = \frac{1}{2\pi} \int dk_T'^2 \, 2\pi \, \frac{k_T'^2 \, F(x', k_T'^2)}{k_T'^2 \mid k_T'^2 - k_T^2 \mid} . \tag{2.24}$$

Similarly we can perform the φ integration in (2.23) using[4]

$$I_V = \int_0^{2\pi} \frac{d\varphi}{(x^2 + y^2 - 2xy\cos\varphi + \delta^2)(x^2 + y^2 - 2xy\cos\varphi + x^2 + \delta^2)}$$

$$= 2\pi \left[\frac{1}{D_1} - \frac{1}{D_2}\right]$$

where,

$$D_1 = x^4 \left|\frac{x^2 - y^2}{x^2}\right|$$

$$D_2 = x^2\sqrt{(4x^4 + y^4)} .$$

Here we have set $\delta^2 = 0$.

This gives,

$$I_V = \int dk_T'^2 \, \frac{-k_T^2 \, F(x', k_T^2)}{k_T'^2 \mid k_T'^2 - k_T^2 \mid} + \int dk_T'^2 \, \frac{k_T^2 \, F(x', k_T^2)}{k_T'^2\sqrt{(4k_T'^4 + k_T^4)}}. \tag{2.25}$$

Thus, combining (2.24) and (2.25) and changing variables back to $f = k^2 F$ we obtain the azimuthal integrated form equation (2.3).

Feynman integration over λ to give q_T^2 integral form

Returning now to equation (2.21), we wish to show this can be written equivalently in terms of the momenta of the emitted gluon $\boldsymbol{q}_T$. To do this we introduce the Feynman parameter λ, so we can rewrite the virtual contributions in the form

$$I_V = \int \frac{d^2\boldsymbol{k}_T'}{\pi} \, \frac{k_T^2 \, F(x', k_T^2)}{[\mid \boldsymbol{k}_T' - \boldsymbol{k}_T \mid^2 + \delta^2][k_T'^2 + \mid \boldsymbol{k}_T' - \boldsymbol{k}_T \mid^2 + \delta^2]}$$

$$= \int_0^1 d\lambda \int \frac{d^2\boldsymbol{k}'_T}{\pi} \frac{k_T^2\, F(x', k_T^2)}{[(1-\lambda)[\mid \boldsymbol{k}'_T - \boldsymbol{k}_T \mid^2 + \delta^2] + \lambda[k_T'^2 + \mid \boldsymbol{k}'_T - \boldsymbol{k}_T \mid^2 + \delta^2]]^2}$$

$$= \int_0^1 d\lambda \int \frac{d^2\boldsymbol{k}'_T}{\pi} \frac{k_T^2\, F(x', k_T^2)}{[\lambda k_T'^2 + \mid \boldsymbol{k}'_T - \boldsymbol{k}_T \mid^2 + \delta^2]^2} \,. \tag{2.26}$$

Writing

$$d^2k'_T = \frac{1}{2}\, dk_T'^2\, d\varphi$$

and making the substitution

$$k'_T = \kappa + \frac{k_T}{\lambda + 1} \tag{2.27}$$

then we have

$$d^2k'_T = d^2\kappa = \frac{1}{2} d\kappa^2 d\varphi \,. \tag{2.28}$$

Considering the denominator of I_V then we have, making the above substitutions of (2.27) and (2.28),

$$\begin{aligned} \mid \boldsymbol{k}'_T - \boldsymbol{k}_T \mid^2 &= \kappa^2 + k_T^2 \left(\frac{1}{(1+\lambda)^2} + 1 - \frac{2}{(1+\lambda)} \right) + \boldsymbol{\kappa} \cdot \boldsymbol{k}_T \left(\frac{2}{(1+\lambda)} - 2 \right) \\ &= \kappa^2 + k_T^2 \left(\frac{1}{(1+\lambda)} - 1 \right)^2 + 2\boldsymbol{\kappa} \cdot \boldsymbol{k}_T \left(\frac{1}{(1+\lambda)} - 1 \right) \\ &= \kappa^2 + \frac{\lambda^2}{(1+\lambda)^2} k_T^2 - \frac{2\lambda}{(1+\lambda)} \boldsymbol{\kappa} \cdot \boldsymbol{k}_T \,, \end{aligned}$$

which gives

$$\begin{aligned} \lambda k_T'^2 + \mid \boldsymbol{k}'_T - \boldsymbol{k}_T \mid^2 &= \kappa^2(1+\lambda) + k_T^2 \left(\frac{\lambda}{(1+\lambda)^2} + \frac{\lambda^2}{(1+\lambda)^2} \right) \\ &= \kappa^2(1+\lambda) + \frac{\lambda}{(1+\lambda)^2} k_T^2 (1+\lambda) \\ &= \kappa^2(1+\lambda) + \frac{\lambda}{(1+\lambda)} k_T^2 \,, \end{aligned}$$

i.e. there is no longer azimuthal dependence in the denominator. Thus, the virtual contributions can be written as

$$I_V = k_T^2 \int_0^1 d\lambda \int_0^\infty d\kappa^2 \frac{1}{2\pi} \int_0^{2\pi} d\varphi \, \frac{F(x', k_T^2)}{\left((1+\lambda)\kappa^2 + \frac{\lambda}{(1+\lambda)} k_T^2 + \delta^2 \right)^2} \tag{2.29}$$

which on performing the integrations over $d\kappa^2$ and $d\varphi$ gives

$$\begin{aligned} I_V &= -\frac{k_T^2}{(1+\lambda)}\int_0^1 d\lambda\ F(x',k_T^2)\left[\left((1+\lambda)\kappa^2+\frac{\lambda}{(1+\lambda)}k_T^2+\delta^2\right)^{-1}\right]_0^\infty \\ &= \frac{k_T^2}{(1+\lambda)}\int_0^1 d\lambda\ \frac{F(x',k_T^2)}{\frac{k_T^2}{(1+\lambda)}\left(\lambda+\frac{\delta^2}{k_T^2}(1+\lambda)\right)} \\ &= \int_0^1 d\lambda\ \frac{F(x',k_T^2)}{\left(\lambda+\frac{\delta^2}{k_T^2}(1+\lambda)\right)}\ . \end{aligned} \tag{2.30}$$

This leaves the integration over λ giving

$$I_V = \log\left(\frac{k_T^2}{\delta^2}\right)+\mathcal{O}\left(\frac{\delta^2}{k_T^2}\right)\ , \tag{2.31}$$

which we write as

$$I_V = \int_{\delta^2}^{k_T^2}\frac{d^2q_T}{\pi q_T^2}+\mathcal{O}\left(\frac{\delta^2}{k_T^2}\right)\ . \tag{2.32}$$

Thus, all we have to do now is substitute the virtual contribution I_V of (2.32) back into (2.21) and change the variable of integration of the real emission contribution to

$$\boldsymbol{q}_T = \boldsymbol{k}_T' - \boldsymbol{k}_T\ ,$$

to obtain the BFKL equation as shown in (2.20).

2.4 Higher order corrections to the BFKL equation

The equivalent BFKL equations of (2.3) and (2.20) are a resummation of the $\mathcal{O}(\alpha_s \ln 1/x)^n$ terms which describe the evolution of the gluon propagator in transverse momentum in the t-channel. However, the equations presented above are only to leading order i.e. the BFKL equation only resums the region in which *all* gluon emissions are strongly ordered in rapidity, related to the strong ordering of the longitudinal momenta

$$x \ll x_n \ll x_{n-1} \ldots \ll x_1\ . \tag{2.33}$$

The LO BFKL formalism has a few drawbacks. First, it does not conserve energy (E) and longitudinal momentum (xP) which are desirable for a working theory[29]; the terms producing the violation being subleading. But obviously this could be very important phenomenologically for application of the BFKL formalism to real processes. A

method of removing this problem is to explicitly include energy/momentum conservation in Monte Carlo programs using the BFKL equation. Secondly, (2.3) and (2.20) have fixed α_s. We know scale variations of the coupling constant are important, but change of scale effects appear only in NLO logarithmic terms. The practical inclusion of running coupling into the LO equation has been discussed briefly in section 2.2.2, and will be considered throughout the remaining chapters of this thesis. Another problem is that perturbative QCD tells us that the high energy behaviour of the total cross section for parton-parton scattering is $\sim s^{0.5}$. That is, the cross section increases with increasing centre of mass energy. However, the Froissart-Martin bound imposes the constraint that the cross section cannot grow faster than $\ln^2 s$, where s is the squared centre of mass energy. Evidently, if this $s^{0.5}$ behaviour continues without slowing down, this parameterization will eventually violate the bound. The required deceleration of the growth of the cross section as we move to higher energies is also linked to subleading effects such as parton saturation. This describes the situation when the gluon density becomes so large the partons (inside the proton) are no longer free objects and their interactions must also be considered. One model that describes these shadowing effects i.e. the inclusion of interactions between the gluons, is treated through multiple exchanges of BFKL ladders in the same scattering process[30, 31]. In fact, unitarity requires that such contributions exist. The good news appears to be, that for the present energies reached by HERA, these shadowing corrections are not observed in the data. However, this is a hot topic of debate with recent studies of the unitarity and Froissart bound limits applicable in BFKL calculations of F_2 and the gluon density, showing that the saturation region of gluons *is* reached for HERA energies[32] - there still remains a lot of work to be done in this area before absolute conclusions can be drawn as to whether shadowing corrections are necessary in the kinematic regimes probed by todays experiments HERA and the TEVATRON. However, for the next generation of high energy colliders, e.g. the LHC which will have $\sqrt{s} \sim 14$ TeV, then parton densities will be very large and we would expect these corrections to become necessary. Thus, it is very important that the full NLO corrections be known before an accurate description of the gluon density using BFKL dynamics will be achieved.

NLO corrections to the BFKL equation have been considered for a long time from two viewpoints: i) the need for the BFKL theory to obey unitarity[30, 33] (Bartels, Gribov, Levin, Lipatov, Wüsthoff) and ii) the full computation of the NLO corrections to the BFKL gluon[19, 34]. This calculation was begun in 1989 by Fadin & Lipatov (et al.),

and has recently been completed at the end of last year (1996) / beginning of this year (1997). However, the form of the answer is such that it is not easily incorporated into practical calculations of the BFKL gluon as yet[35, 36]. The first calculations of the size of these subleading effects indicate the NLO corrections produce a dramatic decrease in the exponent λ of the BFKL solution [36]; the decrease being from $\lambda_{LO} \sim 0.5$ to $\lambda_{NLO} \sim 0.2$, which will result in a (very) large suppression of the strong rise of the LO BFKL gluon $f(x, k_T^2)$ as $x \to 0$.

The message is clear though - as the NLO correction is so large, we will have to include even higher order corrections to obtain an accurate description of the gluon density f using the BFKL formalism.

In comparison, the LO ([23] & appendix B) and NLO[19, 35, 36] calculations of the eigenvalue λ of the BFKL kernel give

$$\lambda_{LO} = \overline{\alpha}_s 4 \ln 2 \tag{2.34}$$

$$\lambda_{NLO} = \overline{\alpha}_s 4 \ln 2 \left(1 - 3.4\overline{\alpha}_s - 0.15\frac{N_f \alpha_s}{\pi}\right) \tag{2.35}$$

where in (2.35) the result is the *full* NLO calculation of the corrections by Fadin & Lipatov[19] and Caminci & Ciafaloni[36]. $\overline{\alpha}_s = N_c \alpha_s / \pi$, where N_c is the number of colours. We note that the NLO result is dependent on the number of flavours N_f. Also, the NLO corrections appear with "-ve" sign; since all other quantities $(\alpha_s, N_c, N_f, \pi)$ are "+ve", then the NLO corrections obviously have the effect of reducing the value of λ.

One contribution to the full NLO calculation is described by a kinematic constraint (kc) on the longitudinal momentum of real emitted gluons. This requires that the virtuality of the exchanged gluons along the chain be dominated by the transverse momentum component, $\mid k' \mid^2 \simeq k_T'^2$. Defining the variable z as $x' = x/z$ then the constraint can be written as[37]

$$k_T^2 > z q_T^2 \, .$$

At NLO the kinematic constraint has the effect of reducing the BFKL exponent λ to

$$\lambda_{kc} = \overline{\alpha}_s 4 \ln 2 (1 - 4.2\overline{\alpha}_s \ldots) . \tag{2.36}$$

So in comparing (2.35) and (2.36), it "appears" the kinematic constraint is a major part [38] of the NLO corrections. The effect of this constraint on the BFKL equation has been studied in detail by Kwieciński et al. [37, 39], and will be discussed further in section 3.5.

Since the kinematic constraint appears to be a very large part of the NLO corrections, we will just consider the effect of applying it to the BFKL equation to obtain an idea of the behaviour of the solution for λ at higher orders. An important feature of the calculation of the BFKL gluon including the kinematical constraint is that it *can* be done to *all* orders. Full details of this calculation can be found in [37]. A summary of the results is shown in Figure 2.4.

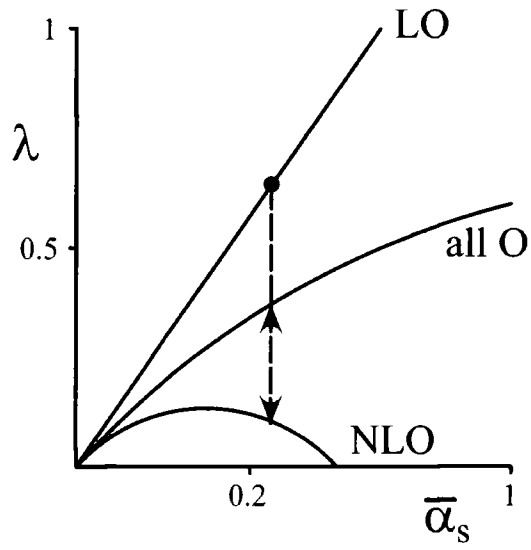

Figure 2.4: Sketch of the exponent λ of the $x^{-\lambda}$ behaviour for the BFKL gluon. λ is shown as a function of fixed $\overline{\alpha}_s = 3\alpha_s/\pi$. The curve (LO) shows the solution $\lambda = \overline{\alpha}_s 4 \ln 2$ for the BFKL equation of (2.3). Applying the kinematic constraint to the LO BFKL equation and keeping only the NLO contribution, (2.36), produces the curve denoted (NLO). Also sketched is the curve (all O) showing the solution of λ when the kinematic constraint is done to all orders[37].

As we can see, the NLO effect is very dramatic and only agrees with the LO behaviour for very small values of α_s. Taking an arbitrary value of α_s, then at LO the solution is a specific value λ_{LO}. Let us consider the point marked by the black dot on the (LO) curve in Figure 2.4. If we now include just the NLO correction to the BFKL equation with the kinematic constraint then, following the dotted line downwards to the curve marked (NLO), we obtain the corrected value, λ_{NLO}, which is *much* smaller than λ_{LO}. This decrease is very large indicating that higher order corrections are still very important. However, as mentioned above, the kinematic constraint calculation can be performed to

all orders. If we include the all order calculation, then the effect on the exponent λ is to increase its value again (following the dotted line upwards to the value given by the curve (all O)). The important point to notice about the "all orders" calculation is that the exponent λ_{allO} still lies below the LO value λ_{LO}. This has the effect of decreasing the steep $\lambda_{LO} \sim 0.5$ rise of the BFKL gluon (which we would like) and gives a much better result than performing just the NLO corrections.

In this chapter the BFKL formalism for resumming the large $\ln 1/x$ terms has been discussed briefly to give an overview focussing on the points important for phenomenological applications to physics at HERA. The BFKL equation (Eq.(2.3) and Eq.(2.20)) presented in sections 2.1 and 2.3 is only a leading order resummation of the $[\alpha_s \ln 1/x]^n$ terms and, as has been discussed in this section, we realize that this LO equation can only be considered as an approximation - it is very important to know higher order corrections to the BFKL kernel of Eq.(2.6) before a completely accurate description can be obtained for the gluon distribution f. In the following work, we will look at modifications to Eq.(2.20) which will include some of the subleading effects in an attempt to obtain a more physically accurate description of $f(x, k_T^2)$ and use the equation to obtain predictions for observable quantities at HERA to search for signatures of the small x BFKL dynamics.

Chapter 3

Jet structure at HERA as a probe of BFKL dynamics

3.1 Introduction

With the advent of the DESY electron (positron) - proton collider HERA, tests of QCD in the small x regime have now become possible. The HERA measurements of the proton structure function $F_2(x, Q^2)$ show a striking rise with decreasing x, which with the latest data is now known with considerable precision [40, 41]. Theoretically, as discussed in chapter 2, we know that for sufficiently small x, such that $\alpha_S \ln(1/x) \sim 1$, that it is necessary to resum the $(\alpha_S \ln 1/x)^n$ contributions in order to obtain reliable perturbative QCD predictions. At leading order this is accomplished by the BFKL equation Eq.(2.20) [23] which effectively corresponds to the sum of gluon ladder diagrams of the type shown in Figure 2.1 in which the transverse momenta q_T are unordered along the chain. This should be contrasted with DGLAP evolution (see chapter 1) where, in the leading $\ln Q^2$ approximation, the transverse momenta are strongly ordered from the hadronic to the hard scale Q^2 which in deep-inelastic lepton scattering is provided by the virtuality of the photon, namely

$$Q^2 \gg k_T^2 \gg k_{nT}^2 \gg \ldots \quad . \tag{3.1}$$

Both BFKL and DGLAP evolution lead to an increase of the deep-inelastic scattering structure functions with decreasing x and it is possible to obtain a satisfactory description of the observed rise using both approaches, on their own, or with unified treatment [12, 42, 43]. The ambiguity lies in the inclusive nature of the structure function F_2 which makes it extremely difficult, even with the precise HERA data, to use the observed x behaviour

to reveal the underlying dynamics at small x. This is not surprising as the leading behaviour obtained from BFKL is an $x^{-\lambda}$ growth, whereas DGLAP evolution predicts an increase of the double logarithmic form $\exp\left(A[\ln(t/t_0)\ \ln(1/x)]^{\frac{1}{2}}\right)$ where $t = \ln(Q^2/\Lambda^2)$ (1.40). However, these are asymptotic predictions. For instance subleading $\ln(1/x)$ effects will weaken the BFKL growth in the HERA regime [37, 44] and moreover, the DGLAP behaviour is dependent on the choice of a non-perturbative input form at some scale $Q^2 = Q_0^2$; the steepness of the rise of F_2 can be controlled by varying the starting scale Q_0^2 or the input distribution $g^{(0)}(x, Q_0^2)$. Because we are concerned with the small x region, we are interested in looking for signatures of BFKL dynamics which will enable us to distinguish them from those produced by DGLAP evolution. It has been realized that the intimate relation between the increase of the cross sections with decreasing x and the absence of transverse momentum ordering, which is the basic property of the BFKL dynamics(section 2.2.1), should reflect itself in the properties of the final states in deep-inelastic lepton scattering. The solution is thus to look for a less inclusive quantity than F_2 in which we can observe the BFKL behaviour, and in which contributions from DGLAP evolution will be neutralized. To this aim several dedicated measurements have already been proposed and are being experimentally studied at HERA; such as, deep inelastic events in which an energetic forward jet is observed [45], measurements of transverse momentum flow [46], azimuthal correlations [47] and the study of transverse momentum spectra of final state particles [48]. The first process of deep inelastic scattering events including forward jets will be discussed in more detail in chapter 4.

One less inclusive quantity that can be studied is exclusive jet production in deep inelastic scattering i.e. $F_2(x, Q^2)$ (and ultimately the total cross section σ) can be decomposed into components $F_2^n(x, Q^2)$ (σ_n), which will correspond to the production of a fixed number n of "resolved" gluon jets that is, jets each with a transverse momentum $q_T > \mu$ in the final state where μ is chosen sufficiently large that the jets can be experimentally identified. As seen in chapter 2, the BFKL equation can be pictured as a gluon ladder in which the rungs are formed via real gluon emission from a reggeized gluon in the t-channel. This leads naturally to the idea of multi-jet production in the final state from hadronization of these emitted gluons. In this chapter we will make a detailed study of the properties of the partonic final state produced by gluon emissions along the BFKL chain and in this way gain insight into the BFKL equation, as well as detailing observables with which to probe the underlying small x dynamics. In particular we will study the possible

jet configurations in the central region between the current jet and the proton remnants. One interesting feature resulting from BFKL dynamics, specifically the diffusion in k_T^2 with evolution in $\ln(1/x)$, is the possibility of producing jets even for $\mu > Q$ and one of the aims in this work is to quantify the yield of such jet configurations.

The BFKL equation of (2.20) resums all gluon emissions, real and virtual, which allows us to make predictions for *inclusive* [49, 50] quantities. We wish to look deeper into this gluon production and identify the real emissions as jets. But what is the definition of an observable jet? Theoretically we could define that *all* real gluon emission produce a jet in the final state, however, practically there must be some minimum transverse momentum carried by the gluon. To this end we introduced above the idea of a resolution parameter μ, that defines the minimum allowed transverse momentum of the real emitted gluon - practically this will be a reasonablly large cut of the order 5 GeV - such that we can split the real emission terms in the BFKL equation into two components, real *resolved* gluon emission which will be identified as a jet and real *unresolved* emission in which the gluon has a transverse momentum less than the required resolution.

As has been seen previously, there is a delicate cancellation between the real gluon emissions and the virtual contributions in the BFKL equation. Clearly this cancellation will be affected by the resolution $q_T > \mu$ that will be imposed. In particular we must ensure that the appropriate cancellation between the virtual contributions and the unresolved real gluon emissions with $q_T < \mu$ is maintained throughout the calculation. It is therefore necessary to first derive a modified form of the BFKL equation which will enable us to quantify the number of energetic *resolved* jets [1] produced along the gluon chain, but in which the virtual and unresolved contributions are treated on an equal footing and resummed.

Exclusive jet production in the CCFM formalism

The process of exclusive jet production has been addressed previously by Marchesini[51] using the theoretical framework of the CCFM (Catani-Ciafaloni-Fiorani-Marchesini) equation [52, 53] which provides a unified treatment of the x, Q^2 kinematic phase space. The important feature of the CCFM formalism is that it is based on the coherent radiation of

[1] Here the word *resolved* applies only to q_T. In particular there are no criteria imposed to ensure that the jets can be sufficiently kinematically separated so that they could be individually identified experimentally.

gluons. This leads to an angular ordering in their emissions. It reduces to the BFKL equation in the leading $\ln(1/x)$ limit and the DGLAP equation in the leading $\ln Q^2$ limit. It has been recognized in this formalism that the multi-regge kinematic region is unsuitable for calculation of exclusive jet rates due to the presence of double logarithms in $\ln(1/z)$ which only cancel between the real gluon emission and virtual corrections for inclusive quantities - they remain explicit in the exclusive case. The origin of these double logs arises due to the presence of coherence and angular ordering which imposes a z' dependent infrared cutoff on the logarithmic integration over the transverse momentum. However, if one introduces a finite resolution μ on the transverse momentum of the emitted gluons and makes a resummation (see [28] & section 3.2) beforehand of the unresolved real radiation and virtual corrections, then the problem of explicit double logarithms disappears. Specifically, the infrared cutoff on the real gluon transverse momentum is now given by μ and is independent of the z's. Within the CCFM formalism this requires that the non-Sudakov form factor be modified by the introduction of an extra $\Theta(k_T^2 - \mu^2)$ function. The application of the resolution cut μ and the resummation of the unresolved and virtual corrections in the CCFM equation has been discussed previously by Kwieciński et al. and can be found in detail in [28].

In summary, for the CCFM equation, if one introduces a finite resolution and resums the unresolved radiation and virtual corrections beforehand then the infrared cutoff on the transverse momentum integrals becomes $\max[qz', \mu]$. For finite μ then this becomes independent of z and we do not get enhancement of the exclusive rates by powers of logarithms. It should be stressed that in the following analysis we will be working with finite $\mu \sim$ few GeV, thus, by ensuring that we resum the unresolved radiation and virtual corrections first to control the problems in the infrared region then we can safely work within the *modified* BFKL formalism to calculate exclusive jet quantities. We will now discuss the required modifications to the naive BFKL equation which will ensure the infrared problems are kept under control.

3.2 The BFKL equation incorporating jet resolution $q_t > \mu$

The concept of using gluon emission from the BFKL ladder to describe the production of jets is not new and it provides a natural starting point for calculations of jet production

using Monte Carlo methods for solving the BFKL equation which are presently being studied (see for example Refs. [20, 21, 22]). Problems arise when we wish to study *exclusive* jet production as it is important to ensure that cancellation of infinities between the real and virtual gluon emission remains intact. The introduction of the arbitrary parameter μ does not necessarily ensure that this cancellation will remain explicit in the numerical integration of the real and virtual parts individually - especially for larger values of the cut μ which are necessary in the definition of physical observable jets. Thus, it is important to modify the BFKL kernel to include this jet resolution parameter in which the contributions from the unresolved real gluon emission and the virtual gluons are treated on an equal footing.

In the small x regime the dominant parton is the gluon. Since there is no longer strong-ordering in the transverse momenta along the gluon chain in Figure 2.1 it is necessary to work in terms of the gluon distribution $f(x, k_T^2)$ unintegrated over its transverse momentum k_T. The relation of the unintegrated distribution f to the conventional gluon distribution is

$$xg(x, Q^2) \;=\; \int^{Q^2} \frac{dk_T^2}{k_T^2}\, f(x, k_T^2). \tag{3.2}$$

Choosing to use the rapidity variable $y = \ln(1/x)$ instead of x, then the unintegrated gluon distribution which satisfies the BFKL equation (2.20) may be written [52, 53]

$$f(y, k_T^2) \;=\; f^{(0)}(y, k_T^2) + \overline{\alpha}_S \int_0^y dy' \int \frac{d^2q_T}{\pi q_T^2} \left[\frac{k_T^2}{k_T'^2}\, f(y', k_T'^2) \;-\; f(y', k_T^2)\, \Theta(k_T^2 - q_T^2) \right], \tag{3.3}$$

with $\overline{\alpha}_S \equiv N_c \alpha_S/\pi$. The integration in (3.3) has come from the replacement

$$\int_x^1 \frac{dx'}{x'} \;\to\; \int_0^y dy'.$$

The notation

$$k_T'^2 \;\equiv\; |\boldsymbol{q}_T \,+\, \boldsymbol{k}_T|^2 \tag{3.4}$$

has been introduced for convenience. It is important to note that the dependence on $k_T'^2$ makes the angular integration in d^2q_T nontrivial. The term $f^{(0)}$ in (3.3) is the inhomogeneous driving term of the BFKL equation and corresponds to the "no-rung" contribution of Figure 2.1. This non-perturbative term has to be input in order to solve (3.3) numerically and the form [54]

$$f^{(0)}(y) = \; 3N(1 - e^{-y})^5 \, \exp(-k_T^2/Q_0^2) \tag{3.5}$$

is taken where the normalization N is fixed so that the gluon, integrated over the region $k_T^2 > Q_0^2$, carries half the momentum of the proton (see Eq. (3.11)). In the following Q_0^2 is set to $Q_0^2 = 1$ GeV^2. The k_T^2 dependence of $f^{(0)}$ reflects the usual non-perturbative fall-off with increasing k_T^2 and this guarantees that the non-perturbative integrated gluon distribution $g^{(0)}$ exhibits Bjorken scaling for sufficiently large Q^2. Also, the product of theta functions

$$\Theta(Q_f^2 - k_T'^2)\,\Theta(k_T'^2 - Q_0^2) \tag{3.6}$$

is implicitly included under the d^2q_T integral in (3.3) so that the emitted gluon is constrained to the domain $Q_0^2 < k_T'^2 < Q_f^2$. Essentially the integral over q^2 can extend to ∞ which we numerically limit by the term $Q_f^2 =$ large number. Q_0^2 is set as above and $Q_f^2 = 10^4$ GeV^2.

The dependence on x of the nonperturbative input f^0

The above shape of the input $f^{(0)}$ (Eq.(3.5)) in $y \equiv ln(1/x)$ is based on the conventional parameterization of the non-perturbative gluon distribution $g^{(0)}$ which is related to $f^{(0)}$ through (3.2); that is it is assumed to have a $1/x$ "soft" Pomeron behaviour as $x \to 0$ and to satisfy the spectator counting rules as $x \to 1$.

The standard parameterization [12, 54, 55] of the parton distributions f_i, where $i = q, \overline{q}$, or g, are given by the form

$$x f_i(x, Q^2) \propto x^{-\lambda_i}\,(1-x)^{\beta_i}\,(\textit{polynomial in } x) \tag{3.7}$$

where the terms containing the parameters λ_i and β_i describe the parton distribution behaviour as $x \to 0, 1$ respectively. It is this behaviour we wish to incorporate in the driving term for the BFKL gluon.

Bjorken x is defined (1.5) as $x = Q^2/2p{\cdot}q$, thus for fixed Q^2, the kinematic region $x \to 0$ corresponds to $p \cdot q \to \infty$; we are dealing with the high energy limit ($s = (p+q)^2 \to \infty$) which is well described by Regge theory. This gives the high energy cross sections for the scattering process $\gamma(q) + P(p) \to \gamma + P$

$$\sigma \sim \beta_R s^{\alpha_R - 1} + \beta_{\wp} s^{\alpha_{\wp} - 1} \tag{3.8}$$

where the first term describes the leading high energy behaviour of the valence quark components and the second the gluon behaviour (and sea quarks which are driven by the

gluon through the process $g \to q\bar{q}$). The x behaviour of the valence quark distributions is controlled by the intercept of the Regge trajectory, α_R, in (3.8) which for the leading meson trajectory gives

$$\alpha_R(0) - 1 \simeq -0.5 \, .$$

This gives the result $\lambda_i = 0.5$. On the other hand, the gluon (and sea) distributions are controlled by the Pomeron trajectory ($\alpha_{I\!P}$) and have the form

$$\lambda_g = \lambda_{sea} \simeq \alpha_{I\!P}(0) - 1 = 0$$

predicting the behaviour of $xf_g(x,k^2) \to x^0$ (and ultimately $xg(x,Q^2)$) as $x \to 0$ which gives the "soft" Pomeron behaviour: $f(x,k^2) \to 1/x$. More precisely, experiment shows the effective pole to have a value of 0.08.

For the high x region ($x \to 1$) the parton distributions have the form

$$f_i(x) \sim (1-x)^{\beta_i}$$

where naive counting rules suggest $\beta_i \simeq 2n_s - 1$. n_s is the minimum number of spectator partons accompanying the probed parton, thus, for the gluon we have $n_s = 3$ (valence quarks of the proton) which gives the result $\beta_i = 5$ in (3.7).

Normalization of the BFKL gluon

One problem in applying the BFKL equation to obtain absolute predictions for magnitudes of cross sections and other physical observables is how to fix the normalization of the non-perturbative input. Here, a brief outline of the normalization N chosen in Eq.(3.5) is discussed which will be used throughout for the results presented in this chapter.

The normalization of the $f^{(0)}$ input is fixed such that upon integration over k_T^2 in Eq. (3.2), the input gluon distribution $g^{(0)}$ carries half the protons momentum

$$\int dx \int^{Q^2} \frac{dk_T^2}{k_T^2} \, f^{(0)}(x,k_T^2) = \int dx \; xg(x,Q^2) = \frac{1}{2} \tag{3.9}$$

with the initial unintegrated gluon distribution $f^{(0)}$ given by (3.5). Setting the lower cutoff at Q_0^2 in the momentum integration we have

$$\int_{Q_0^2}^{\infty} \frac{dk_T^2}{k_T^2} \, e^{-k_T^2/Q_0^2} \int_0^1 dx \; 3N(1-x)^5 = \frac{1}{2} \, , \tag{3.10}$$

which gives the normalization

$$N = e/Q_0^2. \tag{3.11}$$

3.2.1 Resummation of unresolved and virtual gluon emissions

Jet structure is embodied in the BFKL equation via real gluon emission from the gluon chain prior to its interaction with the photon probe (which takes place through the usual fusion subprocess $\gamma^* g \rightarrow q\overline{q}$ (see section 3.4.2)). An observed jet is defined by the resolution parameter μ which specifies the minimum transverse momentum that must be carried by the emitted gluon for it to be detected. For realistic observed jets in the experiments at HERA, the lowest choice for the resolution cutoff parameter is $\mu = 3.5$ GeV. In section 3.4 results will also be presented for $\mu = 6$ GeV and, so as to gain theoretical insight, for the low values of $\mu = 1$ and 2 GeV.

As discussed above we wish to obtain a modified form of (3.3) in which the unresolved radiation is treated at the same level as the virtual corrections to ensure that the singularities as $q_T^2 \rightarrow 0$ cancel in the q_T^2 integration. To do this the BFKL equation (3.3) is written in the symbolic form

$$f = f^{(0)} + \int_0^y dy' \, K \otimes f(y'), \tag{3.12}$$

where $\otimes$ denotes the convolution over q_T. The real resolved and unresolved gluon emission contributions are divided using the identity

$$\Theta(q_T^2 - \mu^2) + \Theta(\mu^2 - q_T^2) = 1, \tag{3.13}$$

where the first term denotes the real resolved (R) emission and the second the real unresolved (U) emission. This splits the BFKL kernel K of (3.12) into the components

$$K = K_R + K_U + K_V$$

where the subscript V denotes the (-ve) contributions from the virtual terms. The unresolved component is then combined with the virtual contribution [56] such that,

$$f = f^{(0)} + \int_0^y dy' \, (K_R + K_{UV}) \otimes f(y'), \tag{3.14}$$

where $K_{UV} = K_U + K_V$. By comparing (3.14) with (3.3) the identification of the kernel components can be made. The convolution of the kernel K_R for the *resolved* emissions with $q_T > \mu$, and gluon distribution $f(y)$ can be identified as

$$K_R \otimes f(y') = \overline{\alpha}_S(k_T^2) \, k_T^2 \int \frac{d^2 q_T}{\pi q_T^2} \, \Theta(q_T^2 - \mu^2) \, \frac{1}{k_T'^2} \, f(y', k_T'^2), \tag{3.15}$$

while K_{UV}, the combined *unresolved* and *virtual* part of the kernel, satisfies

$$K_{UV} \otimes f(y') = \overline{\alpha}_S(k_T^2) \int \frac{d^2q_T}{\pi q_T^2} \left[\frac{k_T^2}{k_T'^2} f(y', k_T'^2)\, \Theta(\mu^2 - q_T^2) - f(y', k_T^2)\, \Theta(k_T^2 - q_T^2) \right], \tag{3.16}$$

with $k_T'^2$ given by (3.4). The $q_T^2 \to 0$ singularity is now cancelled between the unresolved and virtual contributions of (3.16), and by working with the combined kernel K_{UV} ensures that the cancellation will remain intact throughout the numerical computation.

To obtain a BFKL equation for the real resolved emissions in which the unresolved and virtual contributions have been resummed, the BFKL equation (3.14) is first written in the differential form

$$\frac{\partial f}{\partial y} = \left(\frac{\partial f^{(0)}}{\partial y} + K_R \otimes f \right) + K_{UV} \otimes f, \tag{3.17}$$

where the expression in brackets is treated as the inhomogeneous contribution. The inhomogeneous equation can then be solved in the usual way by first finding a solution to the homogeneous equation and then obtaining the full solution via an integrating factor. The homogeneous version of (3.17) is

$$\frac{\partial \Delta}{\partial y} = K_{UV} \otimes \Delta \tag{3.18}$$

with solution

$$\Delta(y) = \exp(y\, K_{UV})\,. \tag{3.19}$$

It is important to note that (3.19) is an operator equation. Thus the integrating factor is $\Delta^{-1} = \exp(-y\, K_{UV})$ and the full solution of (3.17) is

$$\begin{aligned} f(y) &= \int_0^y dy'\, \Delta(y) \otimes \Delta^{-1}(y') \otimes \left(\frac{\partial f^{(0)}}{\partial y'} + K_R \otimes f(y') \right) \\ &= \int_0^y dy'\, e^{(y-y')K_{UV}} \otimes \left(\frac{\partial f^{(0)}}{\partial y'} + K_R \otimes f(y') \right). \end{aligned} \tag{3.20}$$

Equation (3.20) now provides us with the modified form of the BFKL equation for the gluon distribution f in which the unresolved and virtual terms have been resummed in the exponential factor. The equation is of the form

$$f(y) = \hat{f}^{(0)}(y) + \int_0^y dy'\, \hat{K} \otimes f(y') \tag{3.21}$$

where the driving term has become

$$\hat{f}^{(0)}(y) = \int_0^y dy'\, e^{(y-y')K_{UV}} \otimes \frac{\partial f^{(0)}}{\partial y'} \tag{3.22}$$

and the new kernel

$$\hat{K} \;=\; e^{(y-y')K_{UV}} \otimes K_R. \tag{3.23}$$

It is important to recall at this point that the original BFKL kernel, $K_R + K_{UV}$ of (3.3), has no y (i.e. x) dependence. However, the resummation of the unresolved and virtual radiation has generated an explicit y dependence which will be important when we come to solve for the modified BFKL kernel numerically. In fact the kernel $\hat{K}$ of (3.21) is a function of only the difference $y-y'$ (i.e. of $\ln x'/x$) and not y and y' individually, see (3.23).

3.2.2 Analytical solution at low μ

Before performing the full numerical calculation for the BFKL equation (3.3) which will be discussed in more detail in section (3.3), and by iteration determination made of the probability of the emission of n gluon jets with $q_T > \mu$, it is informative to derive an approximate form of the above equation which holds in the (theoretical) limit of small μ^2/k_T^2. In this limit it is possible to resum the unresolved and virtual contributions in a closed analytic form. The crucial observation is that for small μ^2/k_T^2 we may write

$$k_T'^2 \;\equiv\; |\boldsymbol{q}_T + \boldsymbol{k}_T|^2 \;\approx\; k_T^2 \tag{3.24}$$

in the integrand for the unresolved real emission term in (3.16). Equation (3.16) then simplifies to become

$$\begin{aligned} K_{UV} \otimes f(y') \;&=\; \overline{\alpha}_S(k_T^2)\, f(y') \int \frac{dq_T^2}{q_T^2} \left[\Theta(\mu^2 - q_T^2) \;-\; \Theta(k_T^2 - q_T^2)\right] \;+\; \mathcal{O}\left(\frac{\mu^2}{k_T^2}\right) \\ &=\; -\overline{\alpha}_S(k_T^2)\, \ln\left(\frac{k_T^2}{\mu^2}\right) f(y') \;+\; \mathcal{O}\left(\frac{\mu^2}{k_T^2}\right), \end{aligned} \tag{3.25}$$

where the "-ve" sign arises through inversion of the term $\ln(\mu^2/k_T^2)$. Thus through substitution of the solution to K_{UV} from (3.25) into (3.19), the homogeneous solution of the BFKL equation (3.17) is

$$\Delta(y) \;=\; \exp(y\, K_{UV}) \;=\; \exp\Big(-y\, \overline{\alpha}_S(k_T^2)\, \ln(k_T^2/\mu^2)\Big), \tag{3.26}$$

that is the resummation is given by a simple analytic form. As a consequence, in the small μ limit, the modified BFKL equation (3.21) becomes

$$f(y, k_T^2) \;=\; \hat{f}^{(0)}(y, k_T^2) + \overline{\alpha}_S(k_T^2) \int_0^y dy' \Delta(y-y', k_T^2) \int \frac{d^2 q_T}{\pi q_T^2} \Theta(q_T^2 - \mu^2) \frac{k_T^2}{k_T'^2} f(y', k_T'^2) \tag{3.27}$$

where here $k_T'^2 = |\boldsymbol{q}_T + \boldsymbol{k}_T|^2$, and the driving term is given by

$$\hat{f}^{(0)}(y, k_T^2) = \int_0^y dy' \, \Delta(y - y', k_T^2) \, \frac{\partial f^{(0)}(y', k_T^2)}{\partial y'}. \tag{3.28}$$

Let us now solve for $\hat{f}^{(0)}$ semi-analytically to obtain an insight into the structure we expect to see for the n resolved gluon emission contributions to $f(y, k_T^2)$ when we solve (3.21) using the full kernel of (3.23).

For small μ, then most gluon emission from the BFKL chain will be virtual, and effectively we are calculating the 0-jet contribution to f. The resummed BFKL kernel $\Delta(y)$ is now given by the effective kernel of Eq.(3.26). Substituting (3.5) and (3.26) into (3.28) gives

$$f^0(y, k_T^2) = \int_0^y dy' \; 15Ne^{-(k_T^2/Q_0^2)} \, (1 - e^{-y'})^4 \, e^{-y'} \, e^{-\overline{\alpha}_S(k_T^2) \ln(k_T^2/\mu^2)\,(y-y')} \tag{3.29}$$

where the normalization N is given by (3.11) with $Q_0^2 = 0$. For convenience of notation the 0-jet rate is denoted by $\hat{f}^{(0)} = f^{(0)}$. Defining

$$\begin{aligned} C &= 15Ne^{-k_T^2/Q_0^2} \\ \beta(k_T^2, \mu^2) &= \overline{\alpha}_s(k_T^2) \ln(k_T^2/\mu^2) \end{aligned} \tag{3.30}$$

then (3.29) becomes

$$f^{(0)}(y, k_T^2) = C \int_0^y dy' e^{-\beta(y-y')} e^{-y'} (1 - e^{-y'})^4. \tag{3.31}$$

By making a binomial expansion of the term $(1 - e^{-y'})^4$, we can solve the y' integration of (3.31) to give the analytic solution of (3.28) as

$$\begin{aligned} f^{(0)}(y, k_T^2) &= C \int_0^y dy' e^{-\beta(y-y')} \sum_{i=0}^{4} (-)^i \binom{4}{i} e^{-(i+1)y'} \\ &= Ce^{-\beta y} \sum_{i=0}^{4} (-)^i \binom{4}{i} \int_0^y dy' e^{[\beta-(i+1)]y'} \\ &= C \sum_{i=0}^{4} (-)^i \binom{4}{i} \frac{e^{-(i+1)y} - e^{-\beta y}}{\beta - (i+1)} \end{aligned} \tag{3.32}$$

where

$$\binom{n}{k} = \frac{n!}{k!(n-k)!}.$$

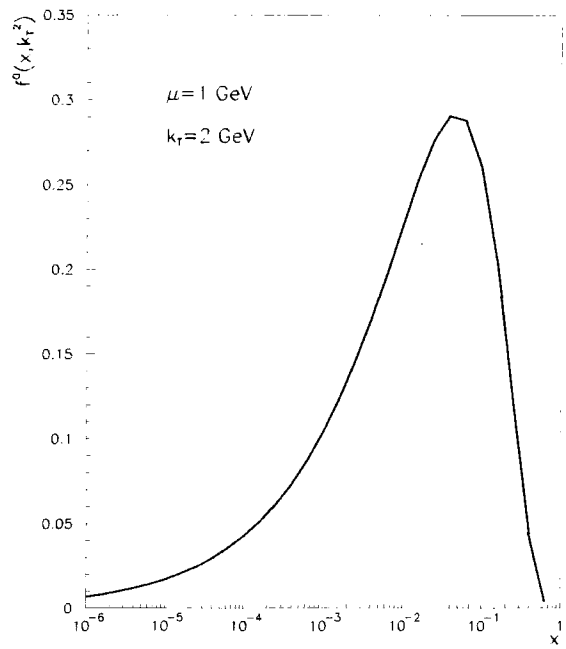

Figure 3.1: Analytical solution (Eq.(3.32)) of $f^0(x, k_T^2)$ for the approximation Eq.(3.24) in the limit of small μ^2/k_T^2, for resolution cutoff $\mu = 1$ GeV and $k_T = 2$ GeV.

Figure 3.1 shows the structure of the 0-jet contribution to the unintegrated gluon distribution for the analytical solution (3.32) with the low cutoff $\mu = 1$ GeV and $k_T = 2$ GeV. The prediction is that the 0^{th} jet (and as we shall see from numerical calculation, also the n^{th} jet) contribution will increase as we move to smaller values of Bjorken x, reach a maximum and then decrease as we continue moving down in x. This structure is seen in the numerical calculation when the results for the full input $\hat{f}^0$ of (3.22) are presented in section 3.4. Obviously, these results will not use the low μ approximation, although to gain insight the full prediction of (3.22) for $\hat{f}^{(0)}$ will be compared with the approximate $\mathcal{O}(\mu^2/k_T^2)$ result given in (3.28).

In this thesis we are interested in making predictions for physical jets which can be experimentally observed (i.e. large μ limit), thus, this comparison will provide an indication of how realistically the resummation of the unresolved and virtual gluon emission at small μ is in describing physical jet production using the approximation of (3.24).

The application of including a resolution parameter was introduced previously for

computational reasons [28], but only for the above approximation of μ very small, i.e. $\mu \sim 0.1$GeV. For very small values of μ, as discussed above, the form of the combined unresolved and virtual parts of the BFKL kernel simplify as in Eq.(3.25) which makes the numerical calculation for the full (recombined K_R and K_{UV}) kernel simpler. For larger values of the cutoff, the approximation $f(y, k_T'^2) \to f(y, k_T^2)$ cannot be made and no factorization occurs in (3.16). This leads, as we have seen, to the resummation of the unresolved and virtual terms of the kernel producing the exponential form of (3.23). Numerical methods need to be devised for obtaining the solution of (3.23) which as we shall see later are unstable for very low values of μ, ($\mu \lesssim 1$GeV) due to the difficulty of having to model the delta function numerically. This will be discussed in more detail in sections (3.4.1) and (4.3.5).

3.2.3 Jet decomposition of the BFKL gluon

The BFKL equation was expressed in the form (3.21) specifically in order to decompose the unintegrated gluon distribution f into the sum of contributions with different numbers of *resolved* gluon jets with transverse momenta $q_T > \mu$. That is

$$f(y) = \sum_{n=0}^{\infty} f^n(y\,;\mu^2) \tag{3.33}$$

where f^n denotes the contribution to the unintegrated gluon distribution f arising from n resolved jets in the chain, each with $q_T > \mu$, as shown in Fig. 3.2. This n-jet contribution f^n obviously depends on the resolution μ, whereas the sum f does not. Using (3.21) we can obtain an iterative equation for the n^{th} jet contribution in terms of the $(n-1)^{th}$ contributions

$$f^n(y) = \int_0^y dy'\, \hat{K} \otimes f^{n-1}(y') \tag{3.34}$$

which lends itself naturally to numerical computation. Here the 0-jet (starting term in (3.34)) contribution is just the modified non-perturbative input $f^0 = \hat{f}^{(0)}$ calculated in (3.22) and $\hat{K}$ the full resummed kernel of (3.23).

3.3 Numerical computation of the BFKL equation

In this section the numerical techniques required in the computation of the modified BFKL equation will be described. The equation we wish to solve is given by (3.21)

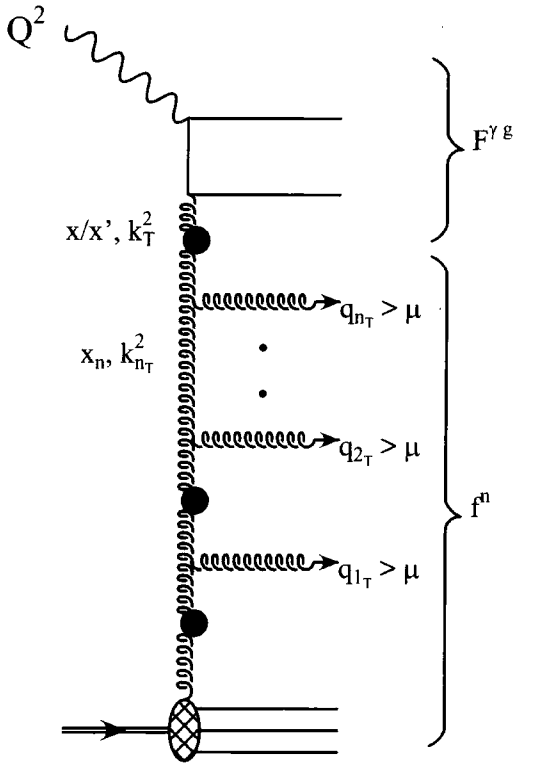

Figure 3.2: The n-jet contributions to the BFKL equation f are described by the lower part of the gluon ladder in which evolution in $\ln(1/x)$ is started from the proton. Each *resolved* gluon emission is identified as a jet in the final state. The black circles are to indicate the presence of both virtual and unresolved gluon emissions. The component F_i^n is calculated by the k_T-factorization theorem, which has the symbolic form $F_i^n = F_i^{\gamma g} \otimes f^n$, see (3.63) and (3.68).

in which the integration in the kernel $K = \hat{K}(y, k_T^2; K_{UV}, \mu^2)$ is over the momentum of the emitted gluon, q_T, subject to an extra restriction on the real emission terms by the introduction of the resolution parameter μ. The calculation of the *full* BFKL equation, i.e. all radiation from the reggeized gluon is soft and is resummed with the virtual contributions, corresponds to *all* gluon emissions in Figure 3.2 being unresolved - we set the resolution parameter to $\mu = \infty$. In practice, in the following the upper limit of the momentum integration will be set to a value $\mu^2 = Q_f^2 = 10^4$ GeV^2.

To solve for any arbitrary function, $f(x)$, the Chebyshev approximation [28, 57] can be made in which the function is discretized as a series polynomial of order n. The Chebyshev

polynomial is given by the explicit formula

$$T_n(x) = \cos(n \arccos(x)) \qquad n = 0, 1, 2... \tag{3.35}$$

which can be written in the recursive form

$$T_{n+1} = 2xT_n(x) - T_{n-1}(x) \qquad n \geq 1 \tag{3.36}$$

where $T_0(x) = 1$. The first five polynomials are shown in Figure 3.3 for the interval $[-1, 1]$. The important properties of these polynomials are that they are orthogonal over the interval $[-1, 1]$, and the zeros of the polynomial are located at the points

$$x_k = \cos\left(\frac{\pi(k - 1/2)}{n}\right) \qquad k = 1, 2...n \ . \tag{3.37}$$

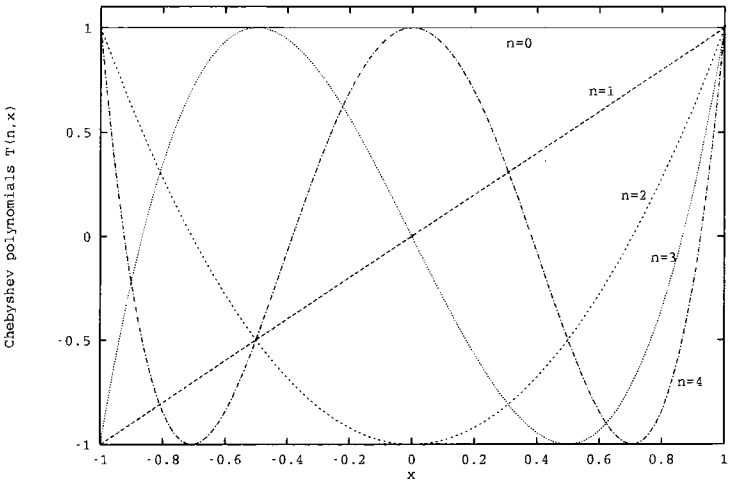

Figure 3.3: Chebyshev polynomials defined by Eq.(3.36) in the interval $[-1, 1]$ for T_0 to T_n. For $n = j$ there are j nodal points in the above range which are bounded by $\pm$ 1.

The formula from which we can now approximate any arbitrary function $f(x)$ in the interval $[-1, 1]$, where all the zeros of $T_n(x)$ are known, is given by

$$f(x) \simeq \left[\sum_{k=1}^{N} c_k \, T_{k-1}(x)\right] - \frac{1}{2}c_1 \tag{3.38}$$

where the coefficients c_j are defined as

$$c_j = \frac{2}{N} \sum_{k=1}^{N} f(x_k) T_{j-1}(x_k). \tag{3.39}$$

The values x_k are the zero nodes defined in (3.37). Equation (3.38) is exact for x equal to all the N nodes of $T_N(x)$.

We will now apply the Chebyshev approximation of (3.38) to the unintegrated gluon distribution of (3.21) to allow us to numerically solve for the BFKL equation.

3.3.1 Chebyshev approximation of the BFKL equation

We wish to make a practical application of the Chebyshev polynomial expansion to the unintegrated gluon distribution $f(y, k_T^2)$. The starting point is the mapping of the region $Q_0^2 < k_T^2 < Q_f^2$ into the interval $[-1, 1]$ in terms of the variable τ defined by

$$\tau(k_T^2) = 2 \ln \left(\frac{k_T^2}{Q_f Q_0} \right) \Big/ \ln \left(\frac{Q_f^2}{Q_0^2} \right). \tag{3.40}$$

The gluon distribution f is expanded in the polynomial form

$$f(y, k_T^2) = \sum_{i=1}^{N} C_i\Big(\tau(k_T^2)\Big) f_i(y) \tag{3.41}$$

where $f_i(y)$ are the values of $f(y, k_T^2)$ at the $(k_T^2)_i$ nodes obtained from

$$\frac{(k_T^2)_i}{Q_f Q_0} = \left(\frac{Q_f}{Q_0} \right)^{\tau_i}, \tag{3.42}$$

with τ_i defined by

$$\tau_i = \cos[(i - \tfrac{1}{2})\pi/N], \tag{3.43}$$

the zeros of the polynomial given in Eq.(3.37), and N the number of terms in the expansion. The k_T^2 dependent functions C_i are obtained from the Chebyshev polynomial functions of (3.35) and are given by

$$C_i(\tau) = \frac{2}{N} \sum_{n=1}^{N} \nu_n T_n(\tau)\, T_n(\tau_i), \tag{3.44}$$

where $\nu_n = 1$ for $n > 1$, and $\nu_1 = \frac{1}{2}$. A good approximation for the k_T^2 dependence of f is obtained with typically $N = 10 - 20$. For the results presented in this chapter we set $N = 20$.

The expansion (3.41) is then substituted into the BFKL equation (3.21) to give the discretized (symbolic) form

$$f_i(y) = f_i^{(0)}(y) + \int_0^y dy' \sum_{k=1}^{N} \hat{K}_{i,k}(y-y')\, f_k(y'), \tag{3.45}$$

where the full kernel (3.23) now becomes

$$\hat{K}_{i,k} = \sum_l [e^{(y-y')K_{UV}}]_{i,l}\, K^R_{l,k} \tag{3.46}$$

and the input distribution $\hat{f}_i^{(0)}(y)$ of (3.22) is

$$f_i^{(0)}(y) = \int_0^y dy' \sum_k [e^{(y-y')K_{UV}}]_{i,k} \frac{\partial f_k^{(0)}(y')}{\partial y'}. \tag{3.47}$$

The substitution of (3.41) into (3.15) and (3.16) gives the explicit form of the kernels K_R and K_{UV} respectively. The BFKL equation (3.45) is a Volterra-type integral equation which can now be solved iteratively for the $f_i(y)$'s. The gluon distribution $f(y, k_T^2)$ is then reconstructed from (3.41).

3.3.2 Calculating the exponentiated kernel: $\exp(K_{UV}Y)$

The discretized form (3.45) of the BFKL equation now includes a discretized version of the resummed unresolved and virtual contributions to the kernel K_{UV} (3.46) and is y (i.e. x) dependent. Recalling from section 2 that the original BFKL kernel is y independent, we now have to devise a method of including this new explicit y dependence in the exponential term of (3.46). The process of approximating the gluon distribution f with a Chebyshev polynomial produces the transformation that the convolutions over k_T^2 in the original equation now become nothing more than a matrix multiplication over the discrete elements of the exponential,

$$e^{(Y\,K_{UV})} \rightarrow \left[e^{(Y\,K_{UV})}\right]_{i,k}$$

with the functions $f_k(y)$. It should be noted that the discretization requires us to calculate the i, k^{th} nodes of the exponential term above which are not just defined by taking the exponential of the i, k^{th} nodes of the discrete form of the kernel $[K_{UV}]_{i,k}$ of (3.16).

The $Y \equiv y - y'$ dependence of the matrix elements of the exponential matrix in (3.46) and (3.47) is also calculated using Chebyshev interpolation. For convenience we denote

the matrix elements

$$[e^{Y K_{UV}}]_{i,k} \equiv M(Y)_{i,k} \tag{3.48}$$

and as before we expand in terms of Chebyshev polynomials

$$M(Y)_{i,k} = \sum_{j=1}^{J} C_j(\tau(Y))\, M^j_{i,k} \tag{3.49}$$

where M^j are the values of $M(Y)$ at the nodes Y_j. Here we take $J = 10$. We map the relevant region $0 < Y < Y_{\max}$, where $Y_{max} = \ln(1/x_{min})$, into the interval $-1 < \tau < 1$ by choosing

$$\tau(Y) = (2Y - Y_{\max})/Y_{\max}. \tag{3.50}$$

The C_j is given by (3.44) (together with (3.43) and (3.35)) with i replaced by j. It remains to calculate $M(Y)$ at the nodes $Y = Y_j$. We do this by solving

$$\frac{\partial M_{i,k}(Y)}{\partial y} = \sum_{j=1}^{J} (K_{UV})_{i,j}\, M_{j,k}(Y) \tag{3.51}$$

using the Runge-Kutta method with the boundary condition $M_{i,k}(Y = 0) = I_{i,k}$, i.e. the iteration is begun from the unit matrix I. In the next chapter in which the BFKL equation is applied to the calculation of deep inelastic scattering events including two identified forward jets, we shall see that this initial input of the delta function produces difficulties numerically in giving stable results for cross sections when we only require a contribution from the BFKL resummed kernel $\hat{K}$ of (3.23) and not the full BFKL equation of (3.21).

Substituting equations (3.47) and (3.51) into (3.45), we can produce the numerical solution to the BFKL equation of (3.21) at the k_{T_i} nodes. The results are plotted (crosses) in Figure 3.4 for the x range, $10^{-6} < x < 1$, for the k_{T_i} node $i = 10$ which corresponds to a value of $k_T^2 \sim 12$ GeV^2. This solution is for the modified BFKL kernel in which we have treated the unresolved real radiation and virtual radiation on an equal footing. For comparison (solid line in Figure 3.4) is also shown the numerical solution to the original form of the BFKL equation (2.20) in which the kernel has no explicit y dependence over the same x range. For the applicable x range at HERA ($x \gtrsim 10^4$) there is no difference between the two methods of calculating the BFKL equation. At the very small x values ($x \sim 10^{-6}$) differences appear at the 10% level with the resummed BFKL kernel predicting slightly larger magnitudes for the BFKL solution.

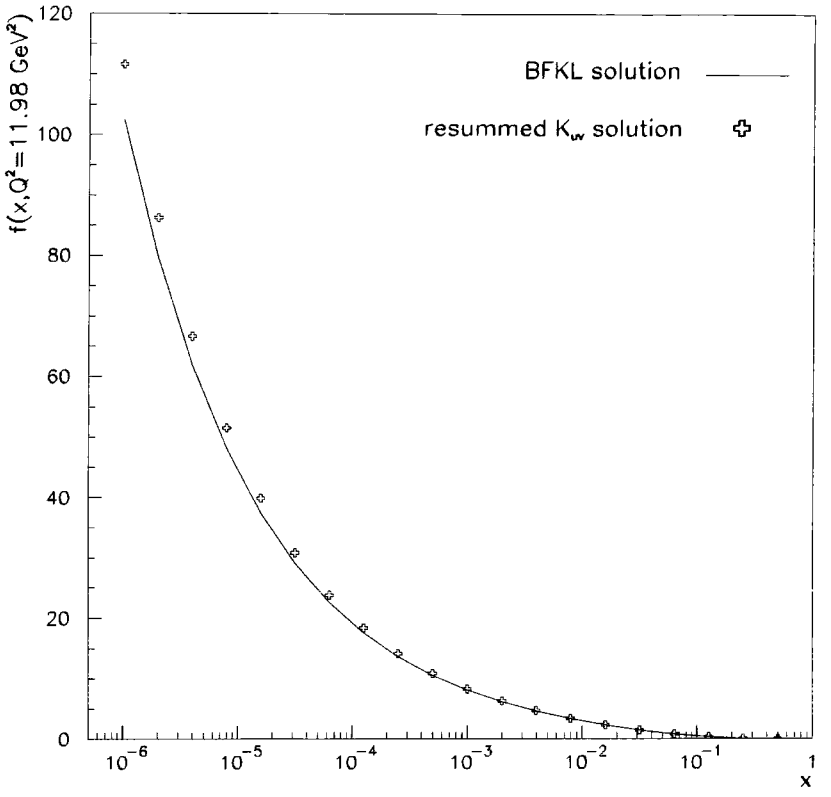

Figure 3.4: Numerical solution of the BFKL equation defined by Eq.(2.20) (solid line) in which the BFKL kernel has no x dependence, and the BFKL equation (3.21) (crosses) in which the unresolved and virtual gluon radiation is resummed producing an explicit x dependence in the modified kernel $\hat{K}$.

3.3.3 Exclusive n-jet iteration

In sections 3.3.1 and 3.3.2 we have seen how to calculate the BFKL equation numerically by treating all gluon emission as unresolved and virtual.

In order to calculate a specific number n real resolved gluon emissions we need to also consider the real resolved terms by reinstating the role of the resolution cutoff parameter, i.e. μ is set to the required physical cutoff (e.g. $\mu = 3.5$ GeV). This now restricts the integration region over q_T^2 in the resummed kernel to $q_T^2 < \mu^2$, with the momentum region $q_T^2 > \mu^2$ integrated separately to give the resolved contributions to the full BFKL kernel

(K_R).

The discretized full kernel of (3.23) is easily obtained by matrix multiplication of the resummed unresolved and virtual contributions with the real resolved kernel

$$\hat{K}_{i,k}(y-y';\mu^2) = \sum_{l=1}^{N} \left[e^{(y-y')K_{UV}}\right]_{i,l} (K_R)_{l,k} \,, \tag{3.52}$$

which is then used to obtain the n-jet contributions to f. The BFKL ladder of Figure 3.2 can be considered as an infinite sum over the n gluon emissions explicitly given in Eq. (3.33), with the 0-jet contribution described by no real resolved gluon emission emitted between the proton and the current jet - $\hat{K}$ is purely the resummed unresolved and virtual terms. For the 1-jet contribution, that is one physical jet is observed in the rapidity region between the proton and current jet, we only allow one real resolved gluon to be emitted, for the 2-jet case, two gluons are emitted with momenta $q_T^2 > \mu^2$ with the radiation between the two emitted jets described by the resummed BFKL kernel and so on. This picture of each real resolved gluon emission producing a jet in the final state naturally leads us to an iterative relation (for the discretized form of the BFKL gluon of (3.41)) between the n^{th} and $(n-1)^{th}$ resolved emitted gluon

$$f_i^n(y\,;\mu^2) = \int_0^y \sum_{k=1}^{N} dy'\, \hat{K}_{i,k}(y-y')\, f_k^{n-1}(y') \tag{3.53}$$

where the 0-jet contribution is described by Eq.(3.47). Equation (3.53) is solved by using the Chebyshev approximation of sections 3.3.1 and 3.3.2, and the n^{th} jet contribution obtained by iteration starting from the input of $\hat{f}^{(0)}$.

Testing the numerics

The recursive relation of the n-jet contributions was tested numerically against a given input to which the analytic solution was known. The aim was to devise a method of testing the full numerical program structure and to obtain an insight into the expected x dependence of the fully calculated exclusive jet contributions to the BFKL equation.

The test function was defined as

$$f(y) = 1 + (K_{UV} + K_R) \int_0^y dy'\; f(y') \tag{3.54}$$

and the y (i.e. x) dependence of f fixed as

$$f(y) = e^{\lambda y} \tag{3.55}$$

where λ is a constant. Similarly we set the BFKL kernel to

$$K = K_{UV} + K_R = \lambda = \lambda_{UV} + \lambda_R \tag{3.56}$$

where λ_{UV} and λ_R define the unresolved & virtual and resolved components respectively.

Writing the differential equation from (3.54) as

$$\frac{\partial f(y)}{\partial y} = \lambda_{UV} f(y) + \lambda_R f(y) \tag{3.57}$$

in which $\lambda_R f(y)$ is regarded as the inhomogeneous term of (3.57), then we can write the solution as

$$f(y) = e^{\lambda_{UV} y} + e^{\lambda_{UV} y} \lambda_R \int_0^y dy'\, e^{-\lambda_{UV} y} f(y') \,. \tag{3.58}$$

Inputting the test form for the driving term $f^{(0)}(y)$ given in (3.55), and using (3.56), then

$$\begin{aligned} f(y) &= e^{\lambda_{UV} y} + e^{\lambda_{UV} y} \lambda_R \int_0^y dy'\, e^{\lambda_R y'} \\ &= e^{\lambda_{UV} y} + e^{\lambda_{UV} y} \lambda_R \left[\frac{e^{\lambda_R y}}{\lambda_R} - \frac{1}{\lambda_R} \right] \\ &= e^{\lambda_{UV} y} e^{\lambda_R y} \,. \end{aligned}$$

We can now write the resolved emission terms as a series expansion for the exponential and identify that the individual n-jet contributions are given by

$$f^n(y) = e^{\lambda_{UV} y} \frac{(\lambda_R y)^n}{n!} \,. \tag{3.59}$$

Thus, we predict that each jet contribution will reach a peak at some value of y and then decrease in magnitude.

The numerical test of the program was performed by defining the kernel as the diagonal matrix in which,

$$\begin{aligned} [K_{UV}]_{ij} &= \lambda_{UV} \delta_{ij} \\ [K_R]_{ij} &= \lambda_R \delta_{ij} \end{aligned} \tag{3.60}$$

so as to reproduce the form (3.56). The diagonal matrix input ensures the results are independent of the Chebyshev nodes i, and allows us to test the full program structure of the n-jet iteration routines. Using (3.60) we can construct the exponentiated unresolved and virtual kernel as

$$\left[e^{K_{UV} y} \right]_{ij} = \left[e^{K_{UV} y} \right] \delta_{ij} \,.$$

The comparison of the numerical solution of (3.54) with the analytic form of (3.59), using the input (3.60) with values

$$\lambda = \lambda_{UV} + \lambda_R = \frac{1}{2}$$

and setting $\lambda_{UV} = -1$ and $\lambda_R = 3/2$, is shown in Figure 3.5 for the first four jet contributions. As we can see there is very good agreement.

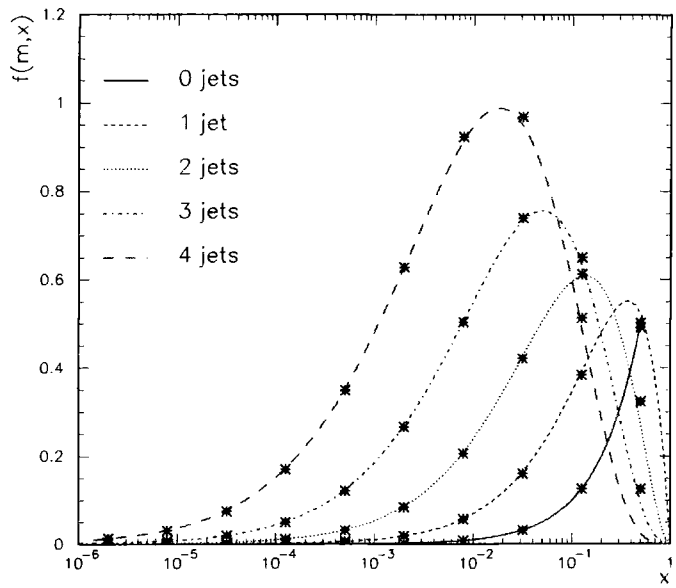

Figure 3.5: Comparison of (3.59) with (3.54) in which the solution is obtained from the input (3.60) to test the numerical program structure. Stars show the accuracy of the numerical solution with the analytic form (lines).

This is only a test function; including the full BFKL kernel will effectively smear the delta function input and have the effect of shifting the peaks of the distributions to smaller x values, especially for the higher jet contributions.

Check of the μ independence of inclusive solution

Each individual jet contribution to the BFKL gluon distribution is dependent on the arbitrary resolution parameter μ. However, the original BFKL equation is independent of any momentum cut, thus, the summation over the jet contributions (3.33) must also

be independent of μ and sum to give the full BFKL solution of (3.21). The accuracy of this μ independence can be seen in Figure 3.6 which shows the summation over 20 jet contributions to the BFKL equation for three different resolution cuts at a scale $k_T^2 = 5$ GeV^2. For resolution cuts as small as $\mu = 1, 2$ GeV a large number of jets was required to obtain the required resolution independence, but nevertheless there is very good agreement over the entire x range spanning six orders of magnitude.

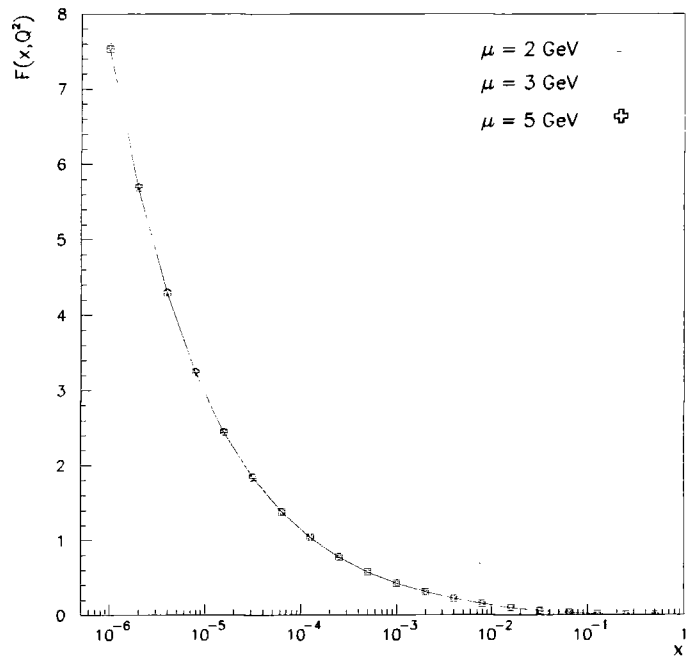

Figure 3.6: μ independence of the summation over $n = 20$ jet contributions to $f(x, k_T^2)$ at the scale $k_T^2 = 5$ GeV^2. Results are plotted for the scaled BFKL solution $F(x, k_T^2) = f(x, k_T^2)/k_T^2$.

3.4 Observable jets from the BFKL chain

We now have all the numerical techniques required for calculation of the exclusive n-jet contributions to the BFKL equation. In this section the results for the jet decomposition of the unintegrated gluon distribution of Eq.(3.21) will be presented, and the extension made to calculations for observable quantities in experiments at HERA.

3.4.1 n-jet components of the BFKL gluon

Using equation (3.53) we can now solve for f_n of (3.34). Although the sum $f(y)$ of (3.33) is independent of μ, as discussed in section (3.3.3), the individual contributions $f_n(y)$ are not. Figures 3.7, 3.8 and 3.9 show the decomposition of $f(y, k_T^2)$ for the scale values $k_T = 2$, 5 and 10 GeV respectively, for three different values of the resolution, namely $\mu = 1$, 2 and 3.5 GeV. As the BFKL gluon density is not a physical observable it is not necessary to restrict ourselves to the higher μ resolution cuts, and we can look at the smaller, non-physical values of the cutoff to gain an insight into the structure of the BFKL gluon. Thus, the low choices of the resolution cuts shown in the following figures are solely to help us gain an insight into the composition of the BFKL gluon from higher jet contributions, with the highest cutoff $\mu = 3.5$ GeV being set at the lowest limit of experimental jet resolution in deep inelastic events at HERA.

The results show the following features:

(i) Gluon jets with $\mu > k_T$ occur; the probability increases as x decreases.

(ii) The lower the value of μ, the greater the number of resolved jets, that is the greater the preponderance of multijet configurations.

(iii) As x decreases, the greater the diffusion in $\ln q_T^2$ so that an n-jet configuration first increases in probability and then decreases as higher jet-configurations take over.

(iv) The higher the value of k_T^2 the sooner in x (as x decreases) will a given multijet configuration go through this rise and fall.

(v) As k_T^2/μ^2 increases the 0-jet contribution drops rapidly to zero.

The most instructive plot for the n-jet decomposition of the BFKL gluon is Figure 3.7 as it shows the n-jet contributions f_n for low values of $k_T = 2$ GeV. Attention should be drawn to the third graph in which the "high" resolution cut of $\mu = 3.5$ GeV is shown. Here we have $\mu > k_T$ and we can clearly see that, even for the HERA x range of $x \lesssim 10^{-2}$, there are contributions arising from the production of higher ($n \geq 1$) gluon emissions. In Figures 3.8 and 3.9, for the experimental μ cut above we also see contributions from $n \geq 1$ jets, but in this case we have the higher scales $k_T = 5$ and 10 GeV; this means $\mu < k_T$ so this resolved gluon emission is not surprising.

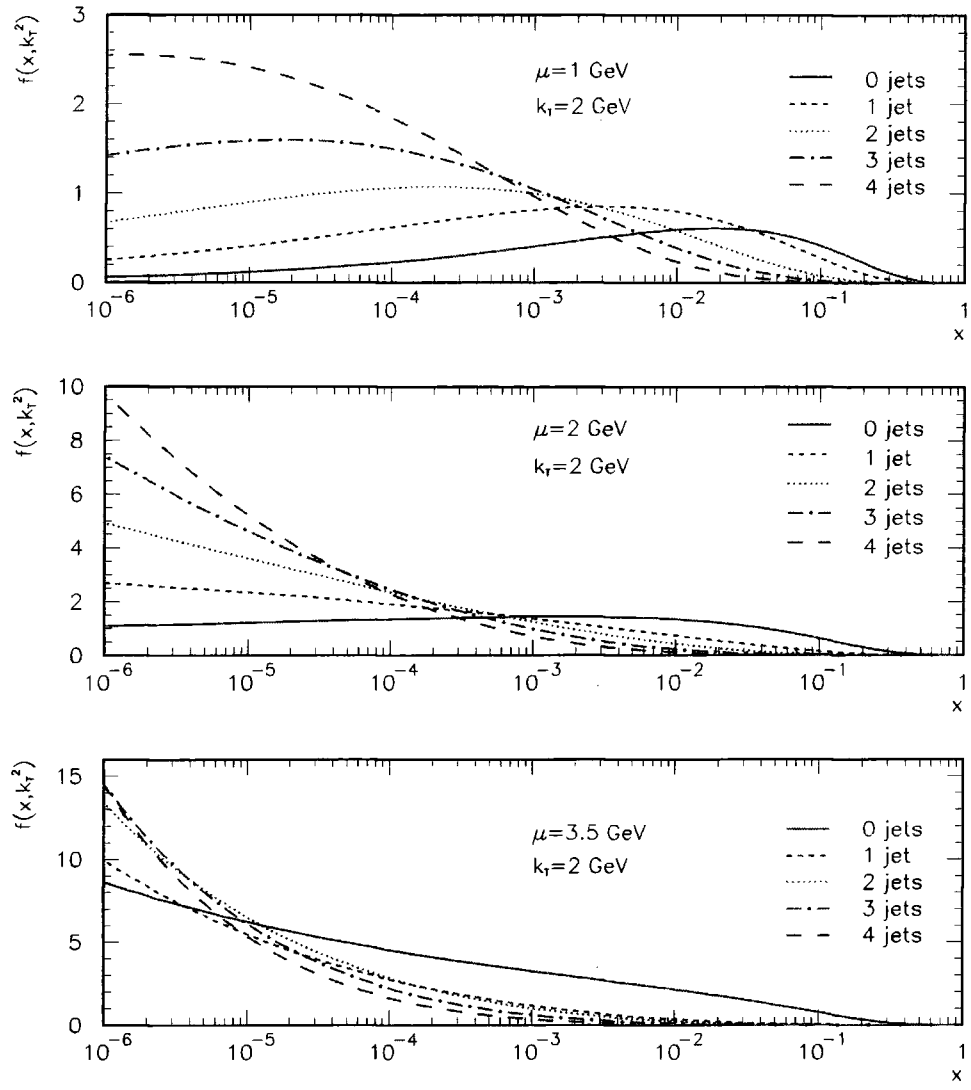

Figure 3.7: The n-jet contributions to the unintegrated gluon distribution $f(x, k_T^2)$ for three different values of the jet resolution parameter μ and for $k_T = 2$ GeV.

For the very low values of μ, eg $\mu = 1$ GeV, we are exposing the role of the virtual corrections in the BFKL kernel as contributions from the unresolved gluon radiation are weakened, whilst the virtual contributions remain unchanged for fixed k_T. The results for low values of the resolution parameter μ show that the functions f_n have a maximum, as predicted analytically (section 3.2.2), which shifts to smaller values of x with increasing n. This maximum is a consequence of the virtual corrections which, in the low μ region, are not entirely compensated by (unresolved) real radiation. The sensitivity of the gluon

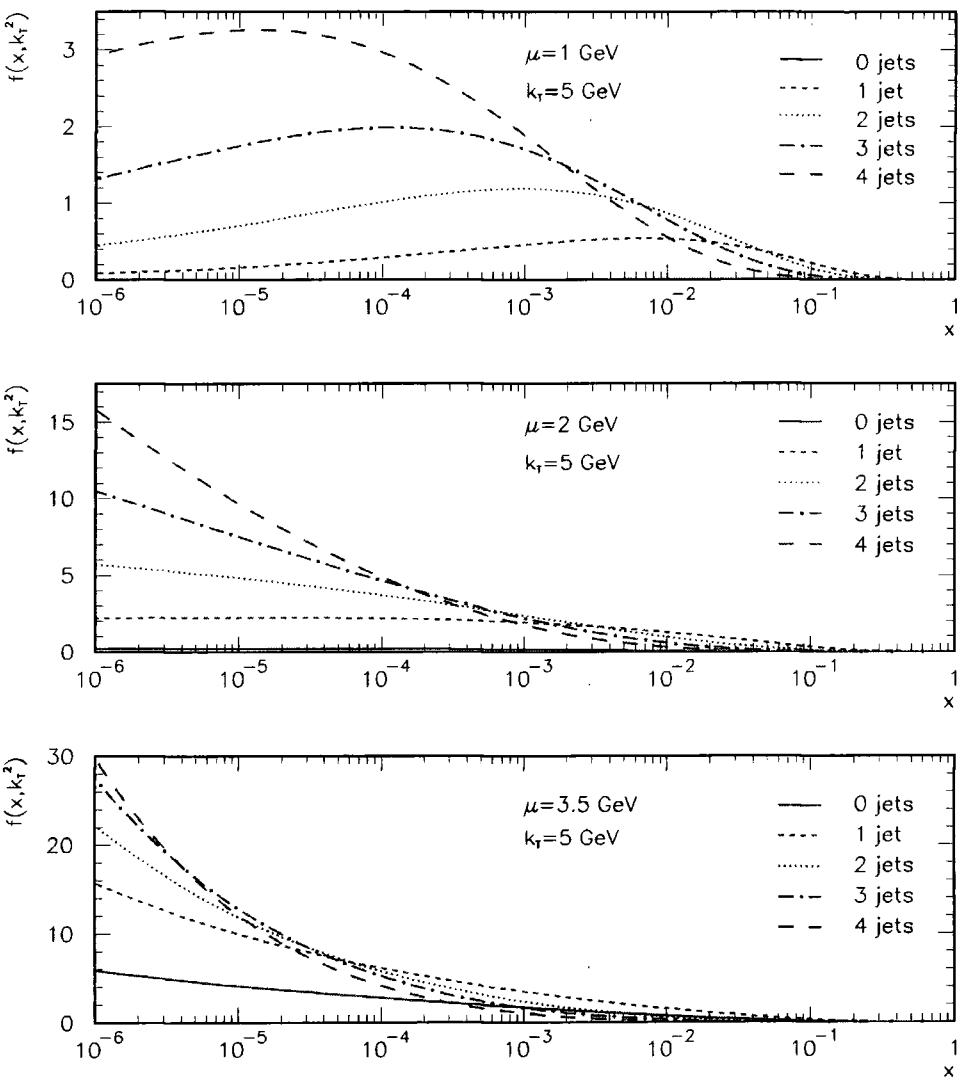

Figure 3.8: The same as Fig. 3.7 but for $k_T = 5$ GeV

structure f_n to this resolution cut is clearly seen - the virtual corrections are only dominant for the small cut of $\mu = 1$ GeV. When we increase this parameter to say $\mu = 2$ GeV, the contributions from the unresolved real radiation are stronger and the maxima disappear.

This structure is the same for all values of k_T with only the 0-jet contribution showing a turn over at $x \sim 10^{-2}$. The higher jet maxima (which are actually very weakly peaked) are delayed to values $x \sim 10^{-5}$ which is outside the HERA experimental kinematic region. For the even larger experimental resolution cut of $\mu = 3.5$ GeV, there are no longer any

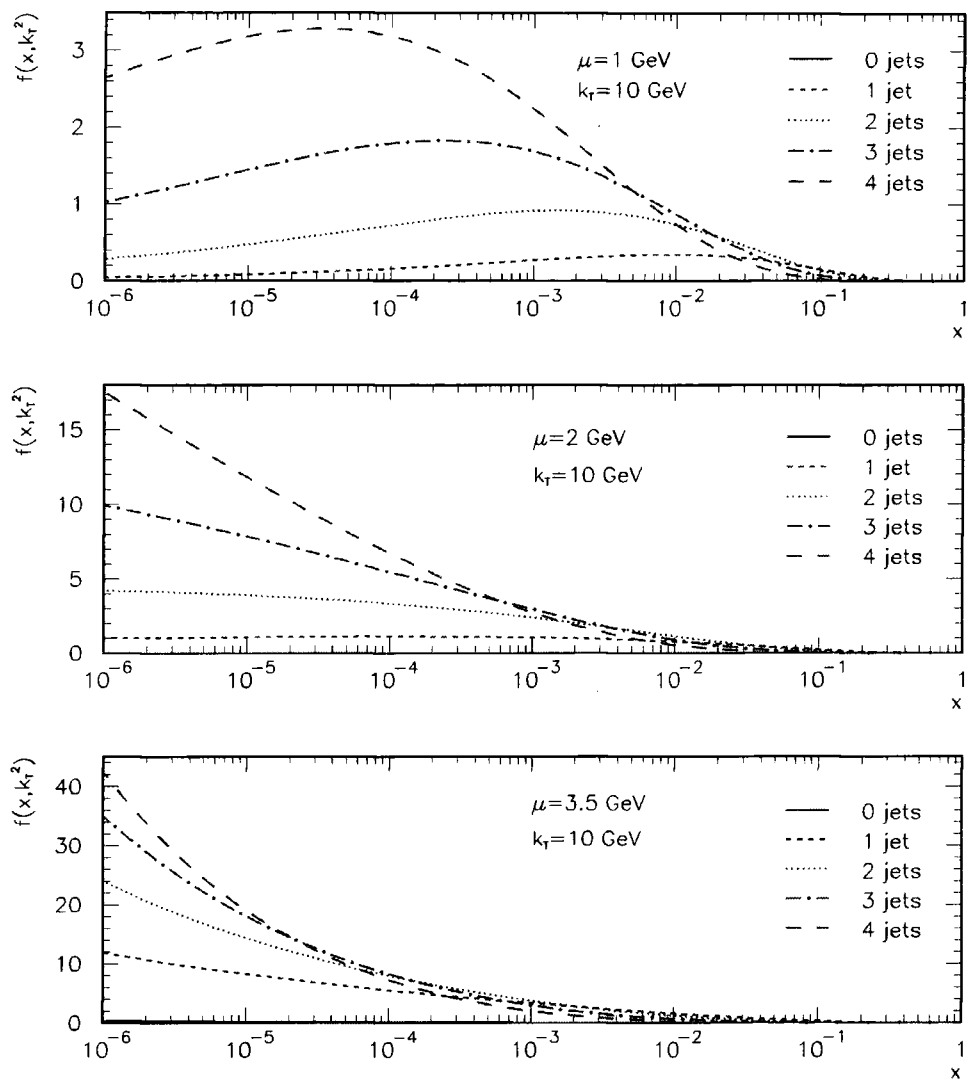

Figure 3.9: The same as Fig. 3.7 but for $k_T = 10$ GeV

maxima to be seen in the jet contributions and, for the entire x range shown, the n-jet contributions are seen to be rising - any maxima are delayed to extremely small values of $x \ll 10^{-6}$.

One interesting feature to note from the above figures is the rapid decrease in the 0-jet contribution for larger k_T^2. Some insight into this behaviour can be obtained from the analytic form presented in section 3.2.2, which applies when μ^2/k_T^2 is small. In this limit the virtual and unresolved real terms lead to a suppression factor

$$\Delta(y) = e^{-Ay} \tag{3.61}$$

where $A \equiv \overline{\alpha}_S \ln(k_T^2/\mu^2)$. Thus from (3.28) we obtain the 0-jet contribution

$$f^0 = \hat{f}^{(0)}(y, k_T^2) = e^{-Ay} \int_0^y dy' \, e^{Ay'} \, 3Ne^{-k_T^2/Q_0^2} \frac{d}{dy'} (1 - e^{-y'})^5 , \tag{3.62}$$

that is the k_T dependence of f^0 is essentially the same as the k_T dependence of the driving term $f^{(0)}$ of (3.5). This exponential suppression ($e^{-k_T^2/Q_0^2}$) explains the origin of feature (v) in which the 0-jet contributions fall to zero with increasing k_T^2. However, this does not mean the 0-jet observable quantities will be negligible as physical quantities can only be obtained through convolution of these theoretical gluon distributions with the hard scattering process $\gamma^* g \to q\overline{q}$ (at the scale Q^2) using the k_T-factorization theorem (3.4.2).

Before applying the n-jet decomposition of the BFKL gluon to make predictions for exclusive jet production in deep inelastic scattering, it just remains to be seen whether the full numerical calculation of the resummation of the unresolved and virtual terms in the BFKL kernel is actually necessary, or, whether we can apply the approximation for $\Delta(y)$ (3.26) calculated in the limit of a small cutoff $\mu \to 0$. Figure 3.10 compares the analytic approximation (3.28) with the full result (3.22) for $\mu^2 = 1$ GeV^2 and $k_T^2 = 4$ GeV^2. As can be seen, in the low μ approximation, the analytic form successfully reproduces the shape of the numerical solution, but it fails in the normalization. There is also a small shift in the position of the peak in the numerical prediction to smaller x. Thus, for physical predictions, the analytical approximation cannot be used as a valid representation for jet contributions, even if we could take the resolution as low as 1 GeV^2 experimentally, and the full numerical calculation of the gluon distribution as discussed in section 3.3 is justified.

We now have predictions for the n resolved gluon emissions from the BFKL chain, but what does this structure imply for the distributions of n observable jets experimentally? The smallest x values probed at HERA are $x \sim 10^{-4}$. For the experimental cut $\mu = 3.5$ GeV, from Figures 3.7, 3.8 and 3.9 it is clear that higher n-jet contributions are non-negligible and arise for as many as four resolved gluons. This would indicate that we can expect to observe a significant number of events in which multiple jets are seen in the central rapidity region between the current jet and the proton remnants in deep inelastic scattering experiments, but, until we perform the integrations over x, Q^2 and k_T^2 (including kinematic constraints for the experiments at HERA) to give the n-jet cross sections, we are not able to determine the actual physical ratios of $0, 1, 2...n$ jet production.

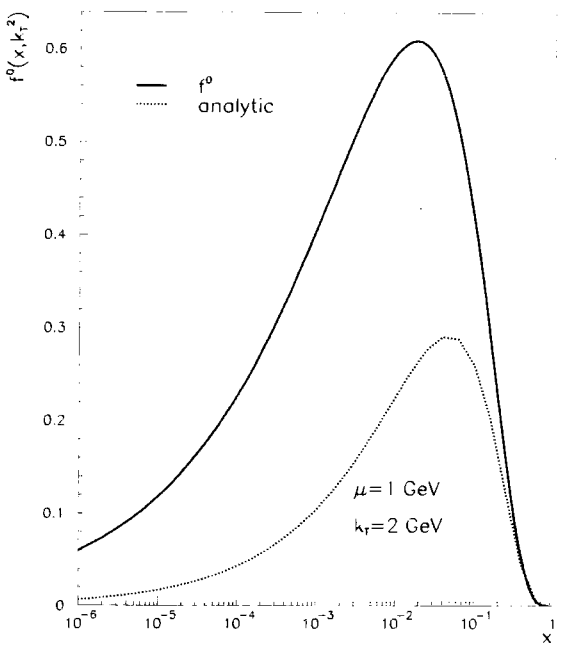

Figure 3.10: The comparison of the analytic and numerical solutions for the 0-jet contribution $f^0(x, k_T^2)$ to the unintegrated gluon distribution.

3.4.2 Numerical results for n-jet observables at small x

We are now in a position to estimate the probability of the different multijet configurations in the small x observables that are driven by the BFKL gluon. The most relevant process to study is deep-inelastic scattering at HERA. Using the results of section 3.4.1, we calculate the jet decomposition of the proton structure functions $F_i(x, Q^2)$. In other words we determine what fraction of events that make up the inclusive measurement of $F_i(x, Q^2)$ contain no-jets, one jet, two jets etc. as a function of x, Q^2 and the jet resolution parameter μ. Recall that our jets are gluons emitted with transverse momentum $q_T > \mu$ and that we do not impose any constraint on the rapidity (η) or azimuthal (φ) separation of the individual jets.

In this study, as we are calculating the gluon emission distributed over the full rapidity gap between the current jet and proton remnant, we do not expect the lack of this η, φ space cut to affect the jet rates drastically. For the majority of jets produced we assume the emitted gluons are well separated, although for large numbers of n-jet emissions we realize this may not hold true. Thus, in the following results we restrict ourselves to the calculation of $n \leq 3$ for the fully integrated cross sections. Theoretically, there are

no such ambiguities when we look at the observable structure functions and it is the decomposition of $F_2(x,Q^2)$ into its different n-jet contributions in which we will look for possible experimental signatures of BFKL dynamics. In chapter 4 in which study of the production of multiple jets in the forward direction of the proton will be made, this separation of the gluons is very important for making reliable predictions to compare with experimental cross sections.

Factorization of the structure functions

From knowledge of the BFKL gluon f we can determine the behaviour of the structure functions via the k_T-factorization theorem. This is shown diagramatically in Figure 3.2 where the lower portion (f^n) describes the perturbatively calculated BFKL gluon ladder as discussed previously, and the upper part ($F^{\gamma g}$) the photon-gluon fusion process in which $\gamma^* g \to q\bar{q}$. In deep inelastic scattering, the photon probing the proton is highly virtual and so we have both longitudinal (L) and transverse (T) polarization contributions to consider for the proton structure functions. These are given by the k_T-factorization formula[58]

$$F_{T,L}(x,Q^2) = \int_x^1 \frac{dx'}{x'} \int \frac{dk_T^2}{k_T^4} f\left(\frac{x}{x'}, k_T^2\right) F_{T,L}^{\gamma g}(x', k_T^2, Q^2) \qquad (3.63)$$

where to lowest order, the photon-gluon fusion $F^{\gamma g}$ (as shown by the box in Figure 3.2) corresponds to the quark box and crossed box contributions shown in Figure 3.11. It is

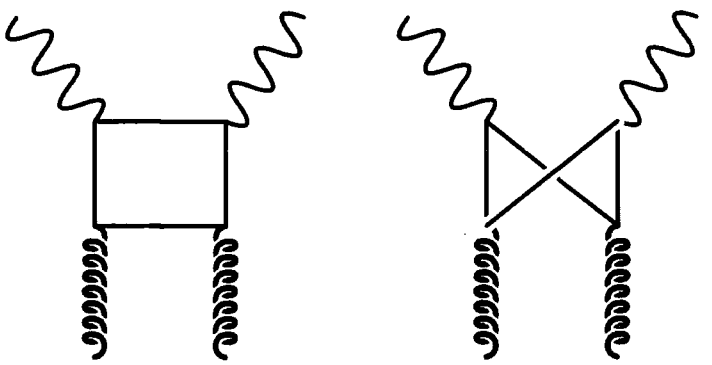

Figure 3.11: The quark box and crossed box diagrams describing photon-gluon fusion, $F^{\gamma g}$ in (3.63).

important to remember that the k_T^2 integration is sensitive to the infrared region (low

k_T^2), thus numerically we prevent the BFKL gluon entering this non-perturbative regime by including a lower cutoff k_0^2 in (3.63). In the following[2] k_0^2 is set to $k_0^2 = 1$ GeV^2. To carry out the integration over the quark line in Figure 3.11 we express its four momenta κ in terms of the Sudakov variables

$$\kappa = \alpha p - \beta q' + \boldsymbol{\kappa}_T$$

where $q' = q + xp$ and p are the basic light-like momenta (q and p are the 4-momenta of the virtual photon and proton respectively). The variable α is fixed by the quark mass-shell constraint, leaving integrations over β and $\boldsymbol{\kappa}_T$. Evaluating the box contributions, equation (3.63) then becomes [24, 25, 59, 60]

$$\begin{aligned} F_T(x,Q^2) &= 2\sum_q e_q^2 \frac{Q^2}{4\pi^2} \int_{k_0^2} \frac{dk_T^2}{k_T^4} \int_0^1 d\beta \int d^2\kappa_T' \, \alpha_S \, f\left(\frac{x}{x'}, k_T^2\right) \\ &\times \left\{ \left[\beta^2 + (1-\beta)^2\right] \left[\frac{\kappa_T^2}{D_1^2} - \frac{\boldsymbol{\kappa}_T \cdot (\boldsymbol{\kappa}_T - \boldsymbol{k}_T)}{D_1 D_2}\right] + \frac{m_q^2}{D_1^2} - \frac{m_q^2}{D_1 D_2} \right\} \quad (3.64) \\ F_L(x,Q^2) &= 2\sum_q e_q^2 \frac{Q^4}{\pi^2} \int_{k_0^2} \frac{dk_T^2}{k_T^4} \int_0^1 d\beta \, \beta^2(1-\beta)^2 \int d^2\kappa_T' \\ &\times \alpha_S \, f\left(\frac{x}{x'}, k_T^2\right) \left\{ \frac{1}{D_1^2} - \frac{1}{D_1 D_2} \right\} \quad (3.65) \end{aligned}$$

where the denominators

$$\begin{aligned} D_1 &= \kappa_T^2 + \beta(1-\beta)Q^2 + m_q^2 \\ D_2 &= |\boldsymbol{\kappa}_T - \boldsymbol{k}_T|^2 + \beta(1-\beta)Q^2 + m_q^2 \end{aligned}$$

and where $\kappa_T' = \kappa_T - (1-\beta)k_T$. The x' integration of (3.63) is implicit in the $d^2\kappa_T'$ and $d\beta$ integrations. Indeed x' is fixed in terms of κ_T' and β

$$x' = \left[1 + \frac{\kappa_T'^2 + m_q^2}{\beta(1-\beta)Q^2} + \frac{k_T^2}{Q^2}\right]^{-1}, \quad (3.66)$$

which ensures that the requirement $0 < x' < 1$ is satisfied. Of course the integration regions of (3.64) and (3.65) must be constrained by the condition

$$x'(\beta, \kappa_T'^2, k_T^2, Q^2) > x \quad (3.67)$$

[2]The magnitude of the BFKL solution is sensitive to the choice of cutoff k_0^2. Increasing the cut from $k_0^2 = 1$ GeV^2 to (say) $k_0^2 = 4$ GeV^2 will produce a decrease in the magnitude of the solution F by a factor ~ 2 for $x \sim 10^{-4}$. The sensitivity of the solution to this cut has been investigated in [27] and an improved treatment of the infrared region i.e. $k^2 < k_0^2$ can be found in [59, 60].

so that the argument $z = x/x'$ of f satisfies the requirement $z < 1$. In (3.64) and (3.65) the sum is over the quark flavours; masses are taken to be $m_q = 0$ for u, d, s quarks, $m_c \simeq 1.5$ GeV and $m_b \simeq 4.3$ GeV for the charm and bottom quarks respectively. The argument of α_S is taken to be $\kappa_T'^2 + m_0^2$, which allows integration over the entire region of $\kappa_T'^2$. The term m_0^2 acts as a regulator and fixes the scale of α_s to prevent $\alpha_s \to \infty$ as $k_T'^2 \to 0$. For the light quarks (u, d, s) $m_0^2 = 1$ GeV^2. The results are found not to be very sensitive [59] to variations of m_0 about this value. For the heavy quark contributions, the regulator would be fixed at the quark masses, ie $m_0^2 = m_c^2, m_b^2$. In the following results, only contributions from the light quarks are shown (this simplifies the forms of (3.64), (3.65) and (3.66)).

The contribution of n-jets to the proton structure function $F_2(x, Q^2)$

The jet decompositions of $F_{L,T}$ are simply obtained by substituting the n-jet unintegrated distribution f^n into (3.64) and (3.65). In this way the observables are broken down into their component n-jet contributions, for example for $F_2 = F_L + F_T$ we have

$$F_2 = \sum_{n=0}^{\infty} F_2^n. \tag{3.68}$$

Figures 3.12 and 3.13 show the components $F_2^n(x, Q^2)$ for deep inelastic events containing n observed jets for the experimental resolution cuts $\mu = 3.5$ GeV (upper plot) and $\mu = 6$ GeV (lower plot). Figures 3.12 and 3.13 correspond to scales of the virtual photon, $Q^2 = 10$ and 20 GeV^2 respectively. For these choices of jet resolution, especially in the HERA x regime, it can be seen that the 0-jet configuration dominates. That is most of the emission from the BFKL ladder is in the form of unresolved and virtual gluon radiation. As expected the n-jet configurations first become important (with decreasing x) for the lower resolution, $\mu = 3.5$ GeV, and the higher Q^2 value, $Q^2 = 20$ GeV^2, and begin to compete with the 0-jet rate for $x \lesssim 10^{-5}$. Indeed this is also true for the lower scale of $Q^2 = 10$ GeV^2. In fact, even the 4-jet rate becomes comparable with the 0-jet rate for $x \sim 10^{-6}$ in Figure 3.13.

Although the 0-jet configuration dominates in the HERA kinematic regime, there is still a non-negligible contribution from resolved jets. For example, for $\mu = 3.5$ GeV at $Q^2 = 10$ GeV^2 and $x = 2 \times 10^{-4}$, the 1- and 2- jet contributions are each approximately $\frac{1}{3}$ of the 0-jet rate, and even the 3- and 4- jet configurations occur at a reasonable rate.

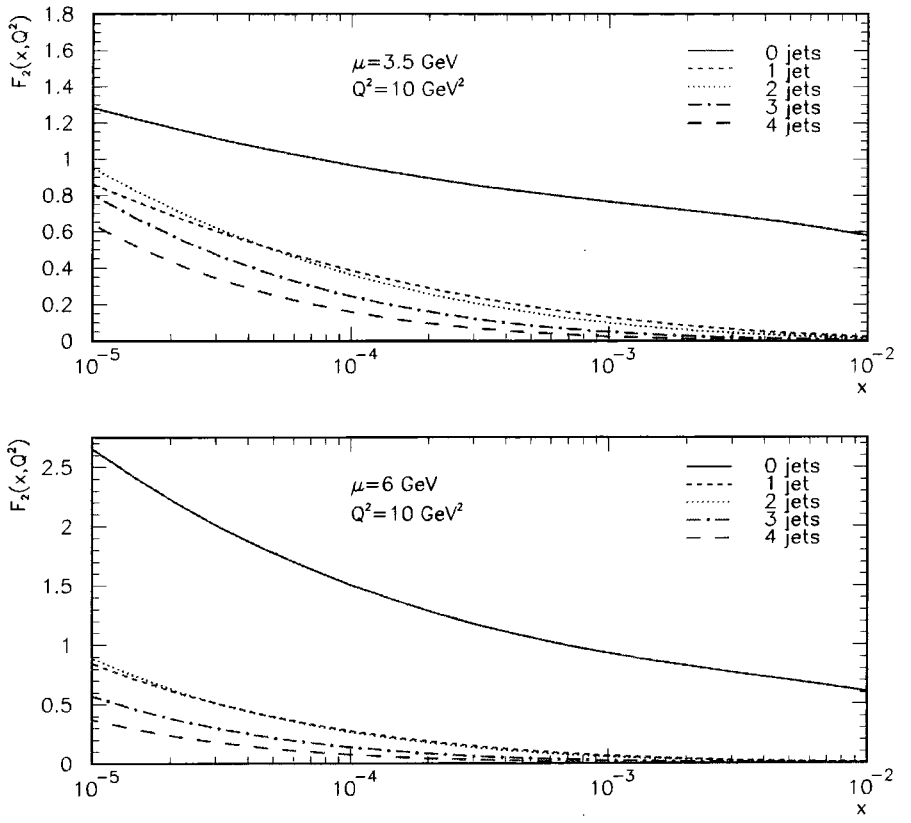

Figure 3.12: The decomposition of the proton structure function $F_2(x, Q^2)$ into contributions coming from different numbers of resolved gluon jets for experimentally accessible values of the resolution parameter $\mu = 3.5$ and 6 GeV. The decomposition is shown as a function of x for $Q^2 = 10$ GeV^2.

This 0-jet contribution is especially dominant when we impose the higher resolution cut of $\mu = 6$ GeV in which we demand the gluon emission to have a high transverse momentum for it to produce a "physical" jet. The important feature to notice in Figures 3.12 and 3.13, for the higher resolution cut, is the production of resolvable jets with $\mu^2 \gtrsim Q^2$. This occurs as a straightforward consequence of diffusion in k_T^2 which as we recall is one of the features of BFKL dynamics.

The experiments at HERA show that the (inclusive) structure function F_2 rises as x decreases (Figure 1.4). How is this rise made up from the various multijet configurations? First we look at the results for the lower jet resolution, $\mu = 3.5$ GeV. Although the 0-jet

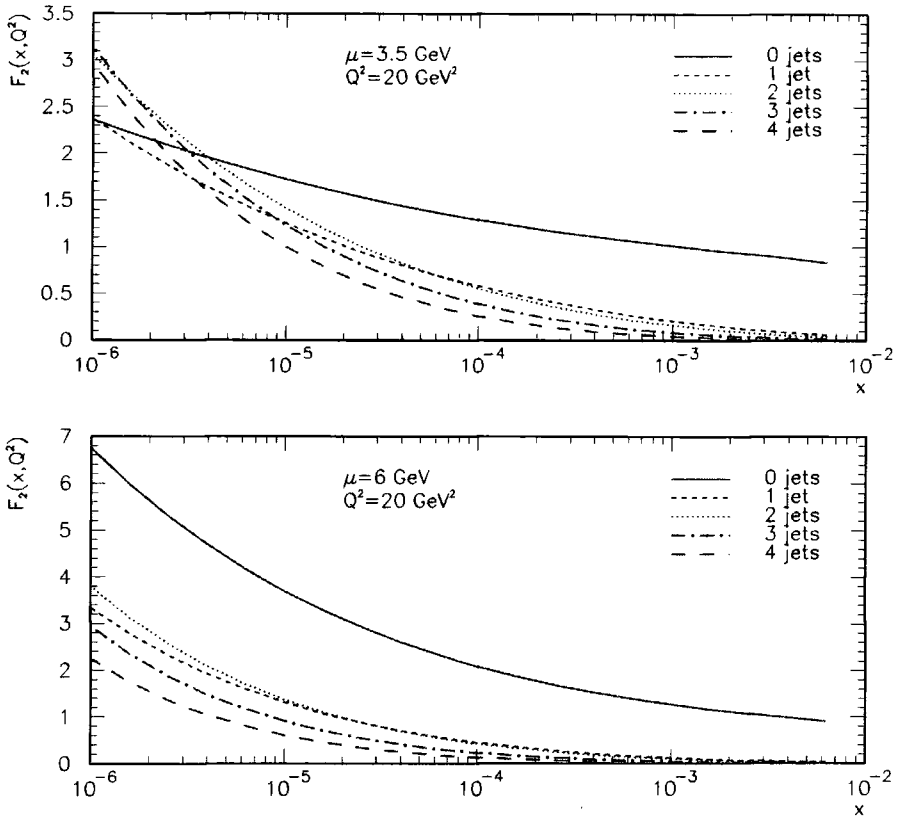

Figure 3.13: The same as Figure 3.12 but for $Q^2 = 20$ GeV^2.

rate dominates, its increase with decreasing x is relatively weak compared to the data. The rise of F_2 comes from the increasing importance of the higher jet configurations. On the other hand at the higher resolution, $\mu = 6$ GeV, the 0-jet configuration is even more dominant and shows a steeper rise over the same x range, as is required for consistency of the results. It is this characteristic difference between the n-jet contributions that could hopefully distinguish BFKL dynamics arising from the momentum diffusion and be seen in the x dependence measurement of individual jet structure functions. However, a word of caution - for the minimum jet resolutions experimentally possible ($\mu = 3.5$ GeV), we are still in the regime of the 0-jet configuration dominating with only small contributions arising from the higher jets at very small values of x. Due to experimental cuts restricting the scattering of the incoming positron we are restricted to x values $x \gtrsim 10^{-4}$ thus we cannot physically look to smaller x to see the domination of these higher jets. Obviously, the smaller the resolution parameter μ, the weaker the 0-jet rate is and we could expect

to see stronger rises in the higher jet contributions. Unfortunately, the value $\mu = 3.5$ GeV is probably as small as experimentalists will be able to go, so even though theoretically we can see a difference in the behaviour of the x dependence of the structure functions (for low μ), experimentally this will be a very difficult measurement to make.

Exclusive n-jet cross sections

Using these predictions for the n-jet contributions to the differential structure functions, we can now obtain numerical results for the exclusive n-jet cross sections at HERA.

The cross section for deep-inelastic scattering is readily calculated from the total structure functions $F_{T,L}$ and is given by (1.9)

$$\sigma = 4\pi\alpha^2 \int \frac{dx}{x} \int \frac{dQ^2}{Q^4} \left\{ y^2\, x\, F_1(x,Q^2) + (1-y)\, F_2(x,Q^2) \right\} \tag{3.69}$$

where as usual $y = Q^2/xs$, $F_T = 2xF_1$ and $F_L = F_2 - 2xF_1$. α is the electromagnetic coupling arising from the γq vertex in Figure 3.2.

As the individual n-jet components of the F_i's were obtained by substitution of the n-jet contributions to the BFKL gluon distribution (f^n) into the equations for F_i, similarly the n-jet contributions for the structure functions F_i^n are substituted into (3.69) to give the individual jet cross sections σ^n. The total inclusive jet cross section at HERA is then given by the summation over the exclusive jet contributions,

$$\sigma = \sum_{n=0}^{\infty} \sigma^n \,. \tag{3.70}$$

The results presented below are for the component cross sections, σ^n, for deep-inelastic events containing n-jets with $q_T > \mu$, again for the two choices of resolution $\mu = 3.5$ and 6 GeV.

First, to approximately reproduce the HERA kinematic domain we take $\sqrt{s} = 300$ GeV and integrate σ over the interval $0.01 < y < 0.5$. The effect of applying tighter kinematical constraints (including cuts on the scattered electron energy and angle) will be investigated in the later part of this section.

Figure 3.14 shows the 0-, 1-, 2- and 3-jet cross sections integrated over x and Q^2 bins of size $\Delta x = 2 \times 10^{-4}$ and $\Delta Q^2 = 10$ GeV^2, where the two entries in each bin correspond to a gluon jet with resolution $\mu = 3.5$ and 6 GeV respectively. The important thing we

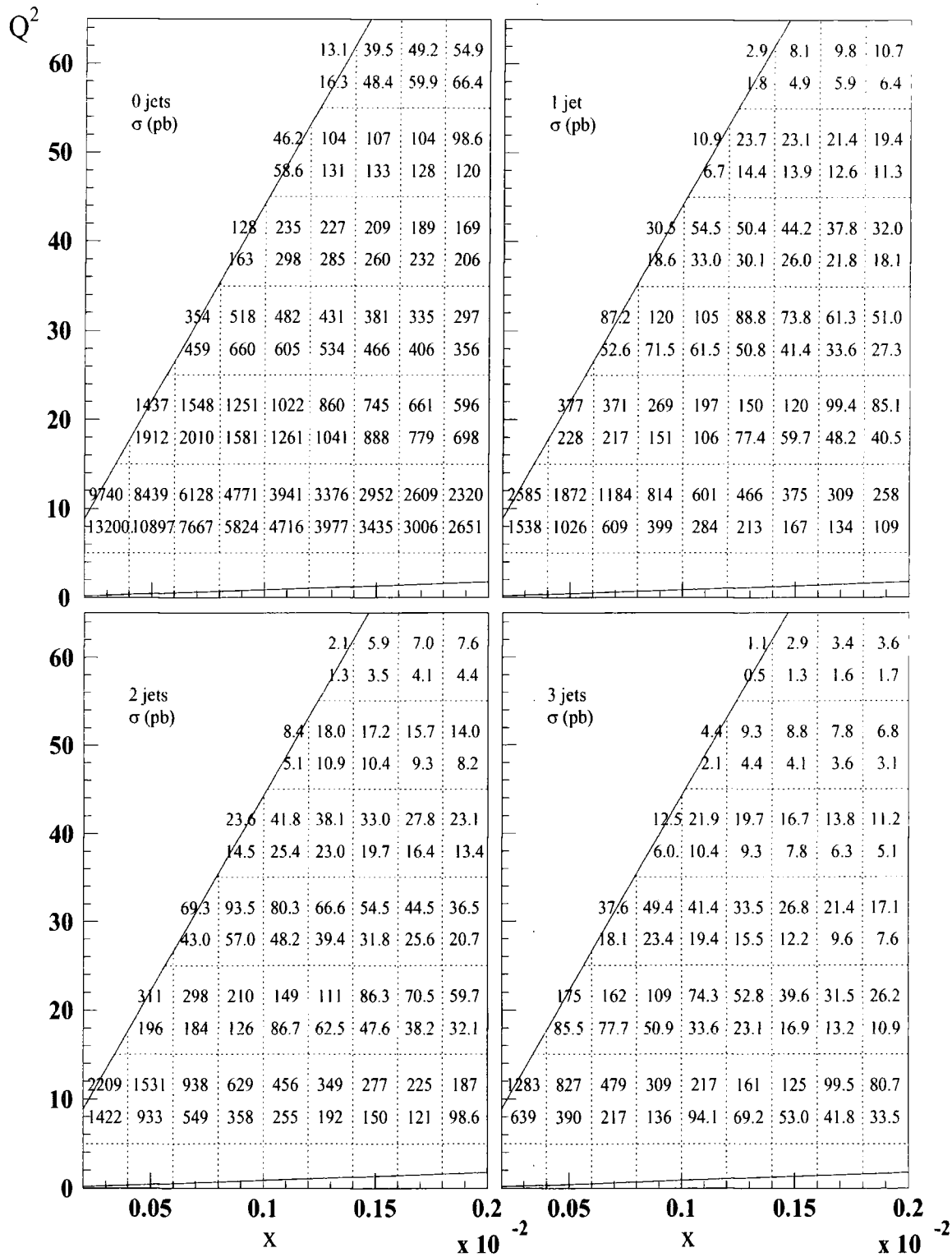

Figure 3.14: The cross-section (in pb) for deep-inelastic scattering in which there are $0-, 1-, 2-, 3-$ resolved gluon jets shown in different x, Q^2 bins in the region accessible at HERA. The width of the bins are $\Delta Q^2 = 10$ GeV^2 and $\Delta x = 2 \times 10^{-4}$ except when modified by the experimental cuts of the accessible HERA domain. The upper and lower values correspond to the resolution parameter $\mu = 3.5$ and 6 GeV respectively.

notice is the presence of an appreciable number of identifiable jets. For example, if we take a resolved jet to be one with $q_T > 3.5$ GeV and an integrated luminosity $\mathcal{L} = 10$ pb^{-1}, then in the bin defined by $0.8 \times 10^{-3} < x < 10^{-3}$ and $15 < Q^2 < 25$ GeV^2 we predict 2686, 2097, 1093 events containing 1-, 2-, 3-jets as compared to 12506 events with no identifiable jet.

Recall that the predictions are obtained by numerically solving the BFKL equation for the gluon. The normalization is dependent on the choice of the cut-off k_0^2. Here we have taken the cut-off to be 1 GeV^2, which was found to give a satisfactory description of the inclusive F_2 [59] distribution. However, the fraction of events containing 0-, 1-, 2-, ...identifiable gluon jets is independent of the choice of the cut-off. For example, for the above $(\Delta x, \Delta Q^2)$ bin and for the lower jet resolution of $\mu = 3.5$ GeV we find 69% of the cross section contains no observable jet and that 1-, 2- and 3-jets occur 14, 10, 5% of the time respectively. Only 2% of the events contain more than 3 jets. For the higher jet resolution of $\mu = 6$ GeV we predict that the BFKL chain will give 88% of the events with no observable jet, leaving only 12% of the total to be split between 1-, 2-, ...jet events.

Because we integrate over k_T^2 in the earlier calculation of the structure functions, and we do not have the explicit dependence of the final state variables in our formalism, it is not a straightforward task to include the experimental kinematic separation criteria between the emitted jets. This will be left to the later calculation of 1- and 2- jet cross sections in deep inelastic scattering including forward jets in the next chapter. However, we can perform a more rigorous calculation of the cross sections by including (approximate) restrictions on the energy and scattering angle of the outgoing electron to see how large a suppression we obtain in the magnitudes of the cross sections for the same x, Q^2 bins above. The cuts selected below are to approximately reproduce the entire kinematic region probed by HERA.

For an incoming electron of $E_e = 27.5$ GeV and proton with energy $E_p = 820$ GeV, we restrict ourselves to the kinematical region of the scattered electron having an outgoing energy, $E_{e'} \geq 5$ GeV lying in the angular region $8° < \theta_{e'} < 172°$ and cut on the y variable using $0.1 < y < 0.5$. The effect of applying these cuts can be seen in Figure 3.15.

Including the above cuts allows more accurate calculation of the outer phase space bins as these regions are affected by the extra constraints. The results of Figure 3.15 show that the kinematical constraints applied do not affect the central bins in which most

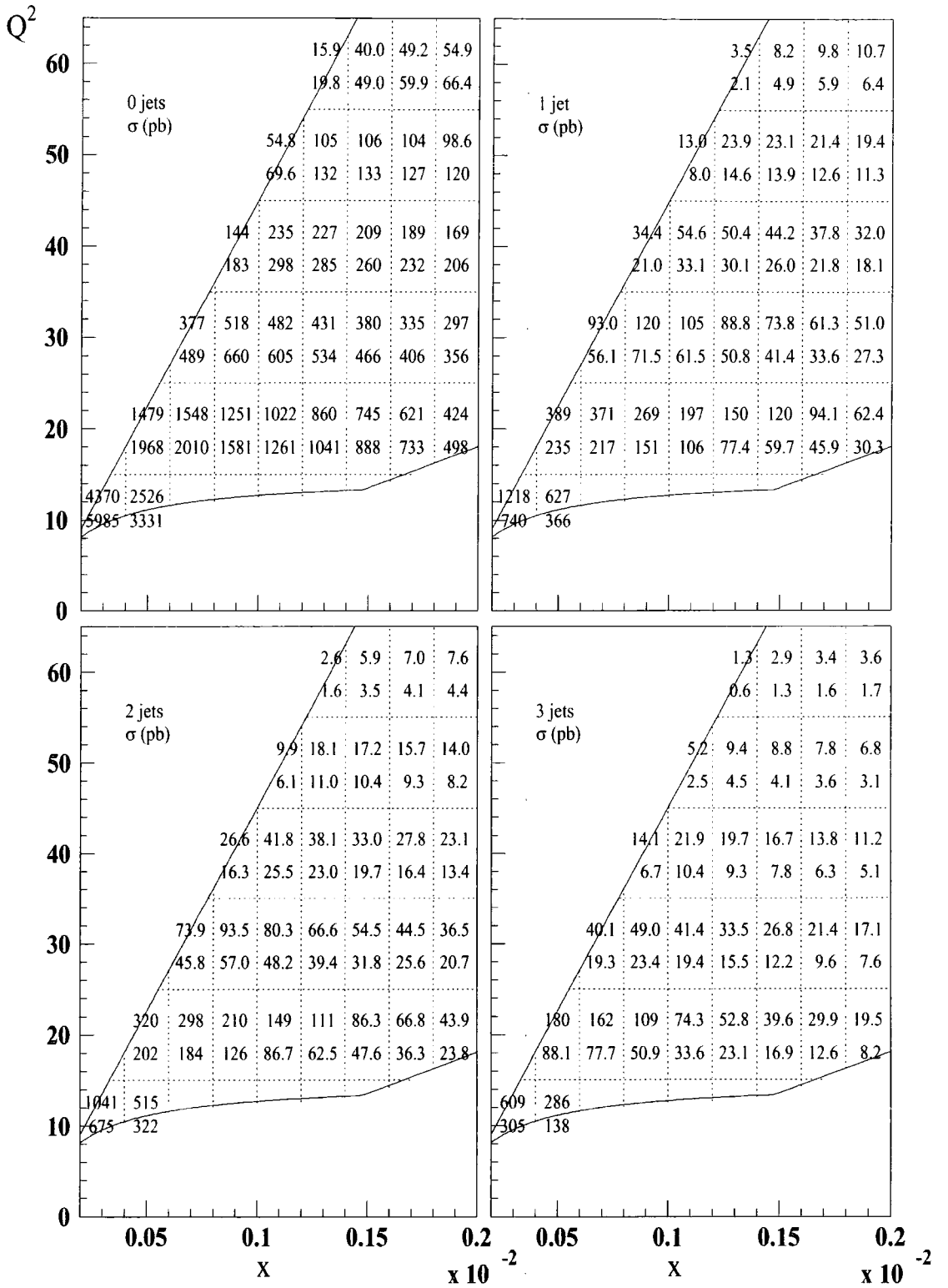

Figure 3.15: The cross-section (in pb) for deep-inelastic scattering in which there are $0-, 1-, 2-, 3-$ resolved gluon jets for the x, Q^2 bins of Figure 3.13 including kinematical cuts on the scattered electron: $E_{e'} \geq 5$ GeV, $8° < \theta_{e'} < 172°$ and $0.1 < y < 0.5$. The upper and lower values correspond to the resolution parameter $\mu = 3.5$ and 6 GeV respectively as before.

experimental data would lie; cross sections in both Figures 3.14 and 3.15 are identical. The effects of the kinematical constraints are only obvious for the "part" bins which are cut by the imposed restrictions. The greatest effect is noticed in the lower Q^2 region where the angular cut $\theta_{e'} < 172^\circ$ dominates the $y > 0.1$ (and also $y > 0.01$ in Figure 3.14) cut. Here we see a dramatic reduction of the cross sections in the $10 \lesssim Q^2 < 15$ GeV^2 region. For the upper Q^2 region, by restricting the upper limit of the Q^2 integration in (3.7), in which the energy, angular and y cuts are determined previously, we obtain more accurate results for the Monte Carlo integrations in the edge of phase space bins - for all n-jet cross sections we observe a slightly increased result than in Figure 3.14.

Thus, the effect of including these extra constraints is that they are not very important for the majority of the phase space covered by the HERA experiments, only in the limiting phase space bins where measurement becomes difficult. If we include a higher cut for the required energy of the scattered electron (say $E_{e'} \geq 11$ GeV as in chapter 4) then this would begin to reduce the magnitudes of the cross sections. However, we can conclude that the approximation of taking the y cut constraint only (as used in [61]) is a good first approximation to the calculated cross section magnitudes.

An interesting point to notice arising from the above results is that the 2-jet rate is comparable with the 1-jet rate. These calculations predict that for any 1-jet event seen at HERA there is $\sim$ 80% probability that a second jet will be found somewhere in the rapidity region between the current jet and proton remnant. Moreover, the 2-jet/1-jet ratio increases with increasing resolution μ as we look to the lower Q^2 bins . For completeness, Figure 3.16 shows the ratio of the 2-jet to 1-jet cross sections. This type of behaviour is consistent with the expectations of the conservation of transverse momentum.

3.5 Kinematic constraints at small x

So far we have calculated physical cross sections for exclusive n-jet production by modifying the BFKL equation to systematically control the cancellation of singularities between the real and virtual gluon emissions. In this formalism, the BFKL equation was written in the form of Eq.(2.20) in which integration is performed over the momenta of the emitted gluon. This formalism has drawbacks for performing realistic calculations of experimental

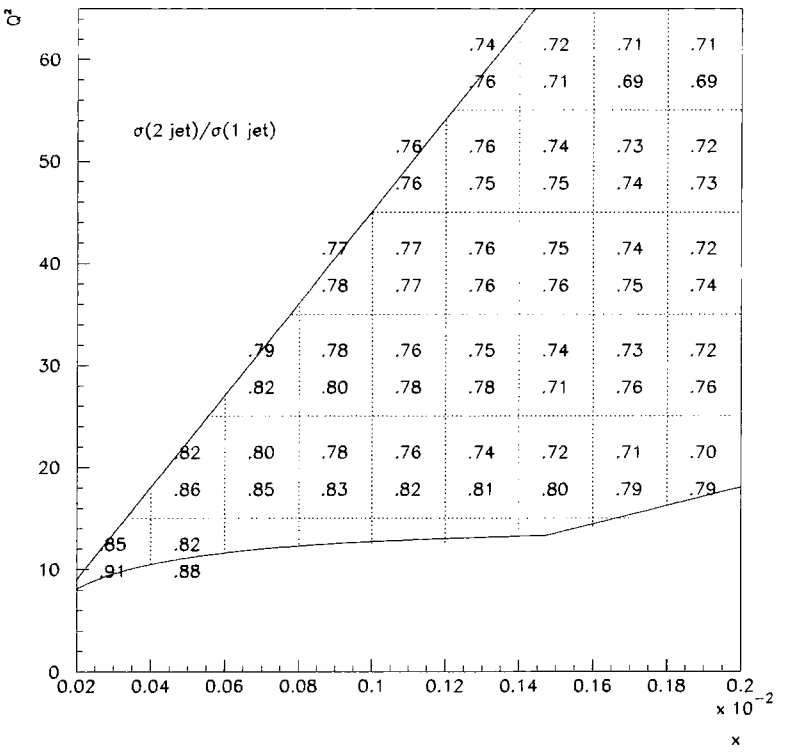

Figure 3.16: Ratio of the 2 to 1 exclusive jet cross sections calculated from Figure 3.15. The upper and lower values correspond to the resolution parameter $\mu = 3.5$ and 6 GeV respectively as before.

observables, in that the application of experimental cuts is difficult. In the above results, there are no cuts on the angular separation of the jets from the beam pipe or cuts on the rapidity-azimuth space of neighbouring jets. Thus, the quoted cross sections should not be compared directly with experiment.

Another drawback is that the BFKL equation above is given only to leading order (LO). That is, it only resums the leading powers of $\alpha_s \ln 1/x$. We still do not know precisely how large an effect subleading $\ln 1/x$ terms will have on predictions made using the BFKL equation. This calculation of the next-to-leading order (NLO) corrections has recently been performed by Lipatov et.al. [19, 35] and Caminci & Ciafaloni[36] and it is only now that the first calculations have been made of the size of these subleading effects. The first indications are that the inclusion of NLO diagrams to the BFKL ladder effectively reduce the value of λ. This would have the result of weakening the steep rise of

the BFKL gluon distribution and so reduce the magnitudes of predictions for observables made using the LO equation (for fixed α_s). It is found however, that the NLO correction (on its own) produces a very large reduction in the value of λ, reducing $\lambda \sim 0.5 \rightarrow 0.2$. As the NLO result is such a large effect, higher order corrections are still required. One part of this NLO correction is a kinematic constraint on the longitudinal momenta of the emitted gluons which indeed *appears* to be a major part of these NLO corrections. However, this kinematic constraint can be performed to *all* orders, which has the effect of increasing the value of λ (above λ_{NLO}), which still lies below λ_{LO} so giving a better description for the exponent (see section 2.4). Thus, this kinematic constraint is an important modification to the LO BFKL formalism and may have a significant impact on the production of higher n-jet rates.

Defining the variable z such that $x' = x/z$ (as shown in Figure 3.17), then we have the constraint [37, 44, 52]

$$k_T^2 > z q_T^2 \,. \tag{3.71}$$

This arises because we require, in the small z region, the virtuality of the exchanged gluons to be dominated by the transverse rather than the longitudinal components of the momentum. That is, for a gluon link of the chain we require

$$|k'|^2 \simeq k_T'^2 \,.$$

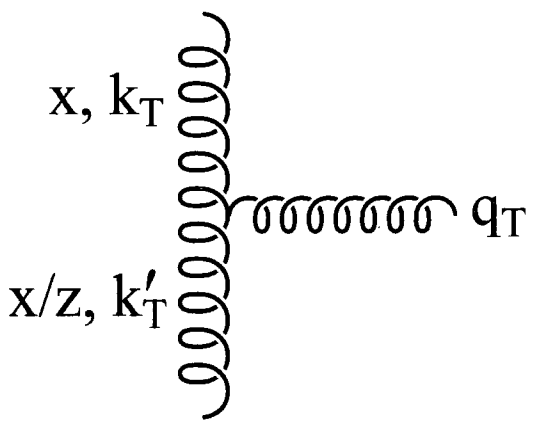

Figure 3.17: Portion of gluon ladder showing kinematic variables relating to the application of the kinematical cut $k_T^2 > z q_T^2$.

So far in the literature, this constraint has been discussed in relation to the BFKL

equation in the framework of the CCFM (Catani-Ciafaloni-Fiorani-Marchesini) formalism. See for example Kwieciński-Martin-Stasto[39] in which this constraint has been studied in detail numerically. This is a unified evolution equation which combines both DGLAP and BFKL equations as solutions in the limits of the respective x, Q^2 kinematic regimes. The CCFM equation is based on the coherent radiation of gluons which leads to angular ordering of these emissions. The above constraint (3.71) dominates over the angular ordering restriction

$$q_T^2 < \frac{Q^2}{z^2}(1-z)^2$$

in the small z regime, i.e. the region in which the CCFM equation reproduces the BFKL limit. Thus, it is natural that we can also apply the same kinematic constraint to the original BFKL formalism. Full details of the CCFM equation can be found for example in [28, 43, 53].

Let us explore the use of cut (3.71) on the BFKL equation for the calculation of exclusive n-jet production.

Defining the notation

$$z = \frac{x}{x'}$$

and recalling that previously we worked with the rapidity variable $y = \ln 1/x$, then we can write

$$\ln \frac{1}{z} = y - y' \,. \tag{3.72}$$

Thus, the kinematic constraint we need to apply to the BFKL equation (written symbolically in (3.12)) becomes

$$e^{y-y'} > \frac{q_T^2}{k_T^2} \,. \tag{3.73}$$

This imposes the extra restriction

$$\Theta(k_T^2 e^{y-y'} - q_T^2) \tag{3.74}$$

on the momentum integration of the real gluon radiation. It is important to note that this constraint does not affect the virtual emissions, but it does the unresolved contribution. Thus, we now need to reformulate the resummation of the unresolved and virtual contributions of (3.14) including the extra constraint (3.74).

Applying (3.74) to (3.3) we have

$$f(y,k_T^2) = f^{(0)}(y,k_T^2) + \overline{\alpha}_S(k_T^2)\int_0^y dy' \int \frac{d^2q_T}{\pi q_T^2} \left[\frac{k_T^2}{k_T'^2} f(y',k_T'^2)\Theta(k_T^2 e^{y-y'} - q_T^2) - f(y',k_T^2)\,\Theta(k_T^2 - q_T^2)\right], \quad (3.75)$$

where we still include the implicit integration limits $\Theta(Q_f^2 - k_T'^2)\Theta(k_T'^2 - Q_0^2)$ of (3.6).

Identifying the kernel components

Splitting the unresolved and resolved components of the real gluon emission as before using (3.13), then we can identify

$$K_R(y) \otimes f(y) = \overline{\alpha}_S(k_T^2)\int_0^y dy' \int \frac{d^2q_T}{\pi q_T^2}\frac{k_T^2}{k_T'^2}\,\Theta(q_T^2 - \mu^2)\Theta(k_T^2 e^{y-y'} - q_T^2) \times f(y',k_T'^2) \quad (3.76)$$

and

$$K_{UV}(y) \otimes f(y) = \overline{\alpha}_S(k_T^2)\int_0^y dy' \int \frac{d^2q_T}{\pi q_T^2}\left[\frac{k_T^2}{k_T'^2}\,\Theta(\mu^2 - q_T^2)\Theta(k_T^2 e^{y-y'} - q_T^2) f(y',k_T'^2) - f(y',k_T^2)\,\Theta(k_T^2 - q_T^2)\right]. \quad (3.77)$$

From (3.76) and (3.77) we notice that the forms of the kernels K_R and K_{UV} now have an explicit y dependence *before* the resummation is performed (c.f. (3.15) and (3.16) from section 3.2.1). Thus, (3.75) can now be written symbolically as

$$f(y,k_T^2) = f^{(0)}(y,k_T^2) + \int dy'\, K_{UV}(y-y')f(y') + \int dy'\, K_R(y-y')f(y'). \quad (3.78)$$

3.5.1 Imposing integration limits on the real radiation

As mentioned above there are no changes to the virtual contributions, thus, the numerical calculation remains the same. Considering the unresolved and real contributions, then from (3.6) using $\boldsymbol{k}_T' = (\boldsymbol{q}_T + \boldsymbol{k}_T)$, we have

$$Q_0^2 < q_T^2 + k_T^2 + 2k_T q_T \cos\varphi < Q_f^2$$

where φ is the azimuthal angle between the vectors $\boldsymbol{q}_T$ and $\boldsymbol{k}_T$. By considering the limits on the azimuthal integration then,

$$\frac{Q_0^2 - q_T^2 - k_T^2}{2q_T k_T} < \cos\varphi < \frac{Q_f^2 - q_T^2 - k_T^2}{2q_T k_T} . \tag{3.79}$$

From (3.79) the limits are identified using

$$\frac{Q_0^2 - q_T^2 - k_T^2}{2q_T k_T} > -1$$

and

$$\frac{Q_f^2 - q_T^2 - k_T^2}{2q_T k_T} < 1,$$

leading to the integration restriction

$$q_T^2 \;<\; (Q_f + k_T)^2 .$$

Including cuts from the resolution μ and the kinematical cut (3.74), then the unresolved real momentum integration is constrained by the condition

$$Q_0^2 < q_T^2 < \min\left[\mu^2,\; k_T^2 e^{y-y'},\; (Q_f + k_T)^2\right] . \tag{3.80}$$

Similarly for the real resolved radiation we find that the condition

$$\mu^2 < q_T^2 < \min\left[k_T^2 e^{y-y'},\; (Q_f + k_T)^2\right] \tag{3.81}$$

must be satisfied, subject to the restriction $\mu^2 < k_T^2 e^{y-y'}$.

3.5.2 Resumming the BFKL kernel including kinematical constraint

The resummation of the unresolved and virtual terms is performed as in section 3.2.1. Rearranging (3.78) we have

$$\begin{aligned} f(y) &= f^{(0)}(y) + \int_0^y dy' \; [K_{UV}(y-y') + K_R(y-y')]\, f(y') \\ &= f^{(0)}(y) + \hat{K} \otimes f(y) \end{aligned}$$

where the convolution $\otimes$ is over the integral y' and $\hat{K}$ is the combined resummed $K_{UV} + K_R$ terms. Defining the moment equation as

$$f^m = \int_o^\infty dy \; f(y) e^{-my}$$

then we can take the moments of the kernel to give

$$\begin{aligned} f^m &= f^{(0)m} + (K^m_{UV} + K^m_R) f^m \\ &= (f^{(0)m} + K^m_R f^m) + K^m_{UV} f^m \\ &= \frac{f^{(0)m}}{(1 - K^m_{UV})} + \frac{K^m_R}{(1 - K^m_{UV})} f^m \ . \end{aligned} \tag{3.82}$$

Multiplying (3.82) by m/m and defining the resummed kernel as

$$\Delta = \frac{1}{(1 - K^m_{UV})m} \tag{3.83}$$

then the moment equation becomes

$$f^m = \Delta m f^{(0)m} + \Delta m K^m_R f^m \ . \tag{3.84}$$

The significance of multiplying by m/m removes the necessity of having to numerically model Δ from the input $\delta(y)$ which is very unstable to the Chebyshev expansion method. After rearrangement and conversion to y space of the moment equation for Δ, (3.83) is constructed from

$$\Delta = I + \int_0^y dy' \ K_{UV}(y - y')\Delta(y')$$

using the driving term of the unit matrix I.

Converting (3.84) back to y space, then

$$f(y) = \int_0^y dy' \ \Delta(y - y') \frac{\partial f^{(0)}(y')}{\partial y'} + \int_0^y dy' dy'' \ \Delta(y - y') \frac{\partial K_R(y' - y'')}{\partial y''} f(y'')$$

from which we identify the new driving term

$$\hat{f}^{(0)}(y) = \int_0^y dy' \ \Delta(y - y') \frac{\partial f^{(0)}(y')}{\partial y'} \ , \tag{3.85}$$

and the full resummed kernel

$$\hat{K}(y - y'') = \int_0^y dy' \ \Delta(y - y') \frac{\partial K_R(y' - y'')}{\partial y''} \ . \tag{3.86}$$

Differentiating the real resolved kernel

From (3.86) it is obvious that the new form of the BFKL kernel including the kinematical restriction of (3.71) is much more complicated than before due to the extra differentiation of the real resolved kernel term. Writing

$$\overline{K}(Y) = \frac{\partial K_R(Y)}{\partial Y} = \frac{\partial K_R(y - y'')}{\partial (y - y'')}$$

then we have from (3.76) and (3.86),

$$\overline{K}_R(Y) = \frac{\partial}{\partial Y}\left[\overline{\alpha}_s(k_T^2)\int \frac{d^2q_T}{\pi q_T^2}\frac{k_T^2}{k_T'^2}\Theta(k_T^2e^Y - q_T^2)\Theta(q_T^2-\mu^2)\Theta((Q_f+k_T)^2-q_T^2)\Theta(Y)\right] \quad (3.87)$$

where the extra theta function, $\Theta(Y)$, is inserted due to the implicit constraint $Y > 0$. Rearrangement of $\Theta(k_T^2e^Y - q_T^2) \rightarrow \Theta(Y - \ln(q_T^2/k_T^2))$, and using $d\Theta(y)/dy = \delta(Y)$, allows differentiation of (3.87) giving

$$\begin{aligned}\overline{K}(Y) &= \overline{\alpha}_s(k_T^2)\left[\delta(Y)\int \frac{d^2q_T}{\pi q_T^2}\frac{k_T^2}{k_T'^2}\Theta(k_T^2e^{Y=0} - q_T^2)\Theta(q_T^2-\mu^2)\Theta((Q_f+k_T)^2-q_T^2)\right. \\ &+ \\ &\left.\int \frac{d^2q_T}{\pi q_T^2}\frac{k_T^2}{k_T'^2}\Theta(Y)\Theta(q_T^2-\mu^2)\Theta((Q_f+k_T)^2-q_T^2)\delta(Y-\ln q_T^2/k_T^2)\right] . \quad (3.88)\end{aligned}$$

Substituting (3.88) into (3.86) and performing the y' integration using the δ functions, gives the resummed full kernel as

$$\begin{aligned}\hat{K}(y-y'') &= \Delta(y-y'')\overline{\alpha}_s(k_T^2)\int \frac{d^2q_T}{\pi q_T^2}\frac{k_T^2}{k_T'^2} \\ &\quad\times \left[\Theta(k_T^2-q_T^2)\Theta(q_T^2-\mu^2)\Theta((Q_f+k_T)^2-q_T^2)\right] \\ &+ \quad (3.89) \\ &\quad \overline{\alpha}_s(k_T^2)\int \frac{d^2q_T}{\pi q_T^2}\frac{k_T^2}{k_T'^2}\Delta(y-y''-\ln q_T^2/k_T^2) \\ &\quad\times \left[\Theta(q_T^2-k_T^2)\Theta(q_T^2-\mu^2)\Theta((Q_f+k_T)^2-q_T^2)\Theta(k_T^2e^{y-y''}-q_T^2)\right] ,\end{aligned}$$

where $\Theta(q_T^2 - k_T^2)$ of the second term is from rearrangement of $\Theta(\ln q_T^2/k_T^2)$.

Equations (3.85) and (3.89) are combined to give the full BFKL equation incorporating the kinematical constraint and are solved under the restrictions of section 3.5.1.

The effects of solving the BFKL equation including (3.71) are shown in Figure 3.18 for the first four jet contributions. As we see, the cut reduces the amount of higher jet emissions as we go to smaller x. Thus, the cross sections of the exclusive n-jet emission would be reduced in respect to the results of Figures 3.14 and 3.15. It should be noted that the numerical calculation of the BFKL gluon, including the kinematical constraint, was made with N=10 Chebyshev nodes (c.f. N=20 in section 3.4). This was purely to give practical running times for the numerics due to the more complex discretized kernel structure. The effect of reducing the number of Chebyshev nodes in the discretized approximation gives a ~5% difference in the BFKL solutions at the very small x values of $\sim 10^{-6}$. These differences reduce as we move to higher Bjorken x.

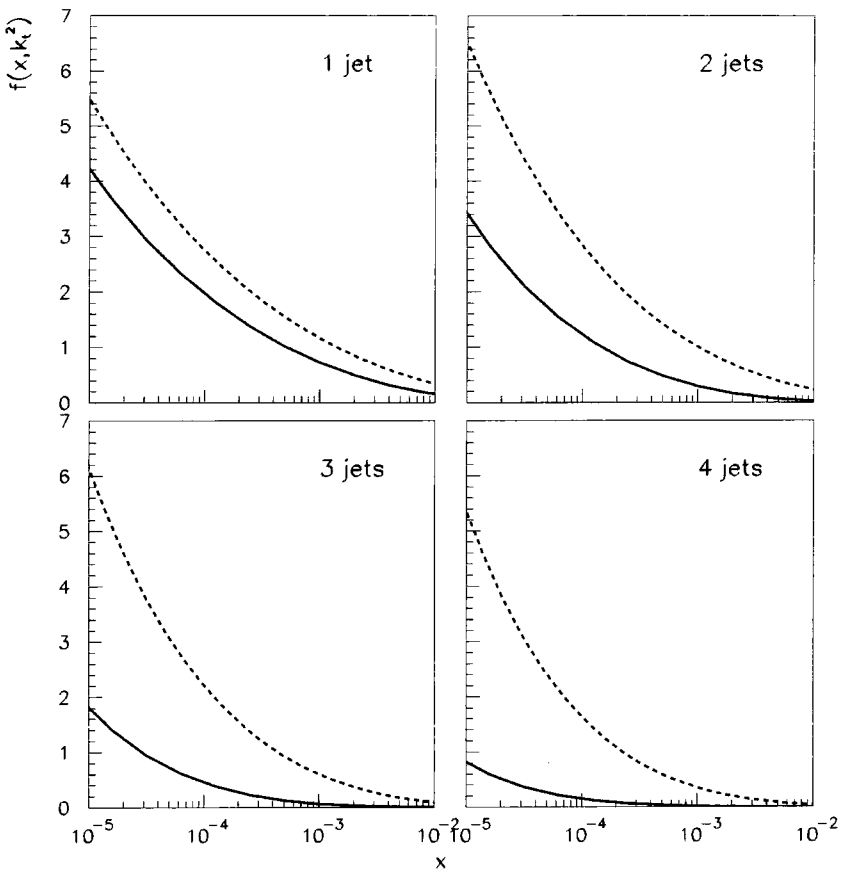

Figure 3.18: BFKL unintegrated gluon distributions for the exclusive $n = 1, 2, 3$ & 4-jet contributions showing the effect of including the kinematic constraint of equation (3.71) to the BFKL equation. Results are given for a resolution cut $\mu = 3.5$ GeV and $k_T = 2$ GeV. Solid lines show the solution for BFKL + kinematic cut. Dashed lines show the original BFKL solution.

3.5.3 n-jet cross sections including kinematical constraint

Figure (3.18) shows the reduction of the higher jet contributions to the BFKL gluon distribution under the constraint that we require the gluons to have a large transverse momentum component. As we can see, the constraint is more restrictive for the higher jet emissions.

Using the BFKL gluon of (3.75), the resulting n-jet cross sections are shown in Figure 3.19 for the lower transverse momentum cut $\mu = 3.5$ GeV with the HERA phase space and kinematical jet cuts of 3.4.2. These are compared with the corresponding $\mu = 3.5$ GeV cross sections of Figure 3.15.

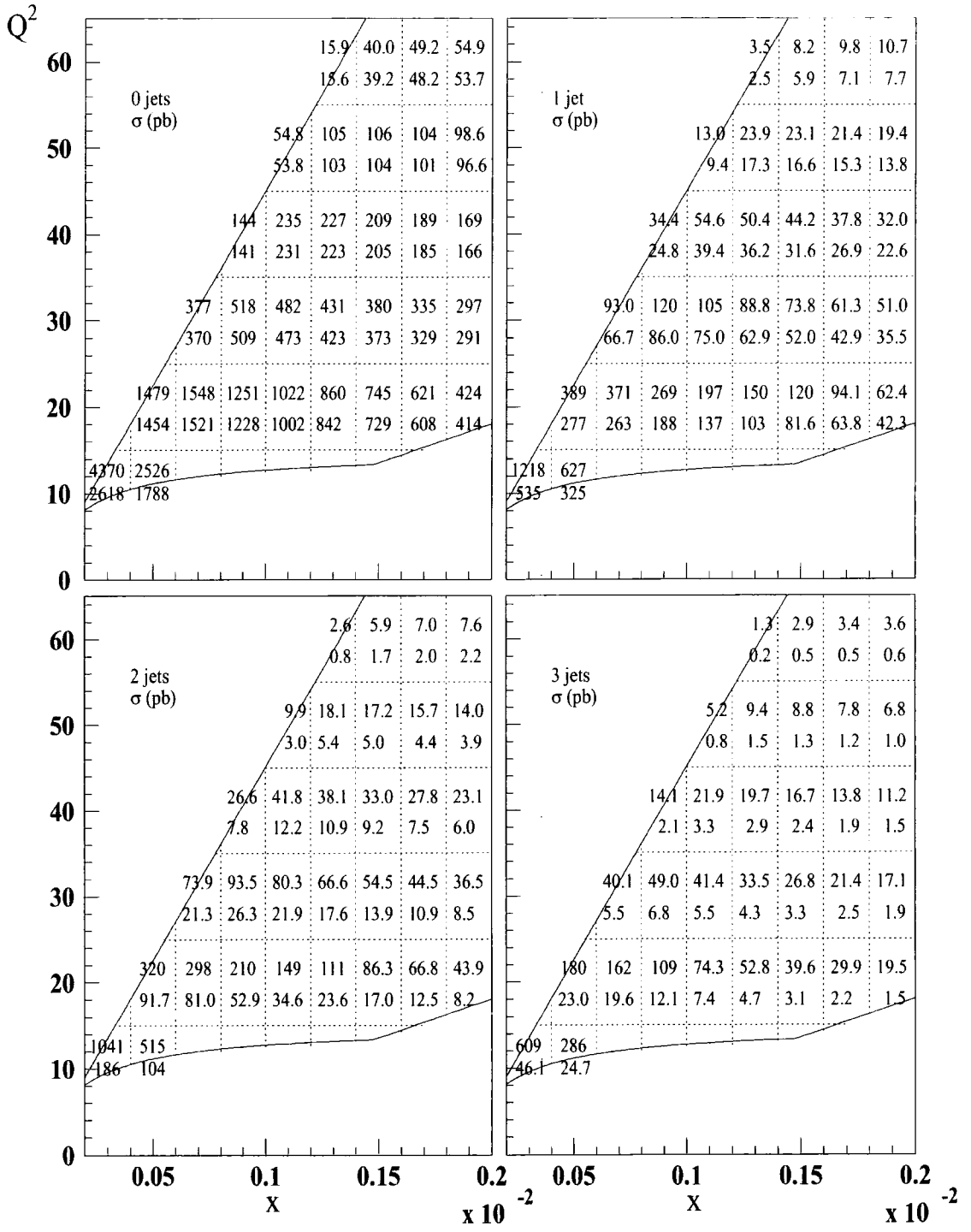

Figure 3.19: The cross-section (in pb) for deep-inelastic scattering in which there are 0-, 1-, 2-, 3- resolved gluon jets for the x, Q^2 bins of Figure 3.15 for $\mu = 3.5$ GeV. The upper value corresponds to the cross section of Figure 3.15 with the lower value the corresponding n-jet cross section calculated including the kinematical constraint of (3.71).

Obviously the effect of including the kinematic constraint (3.71) is significant for the higher jet rates, with all $n > 1$ jet cross sections reduced. The 0-jet cross section remains unchanged under the imposition of cut (3.71) as essentially the 0-jet contribution, for relatively small resolution parameter μ, is the resummed virtual gluon contributions which remain unaffected by the cut on the longitudinal momentum. The small deviations between the numbers in the first plot of Figure 3.19 are due to the numerical computation being performed with $N = 10$ Chebyshev nodes instead of $N = 20$ for the cross sections without kinematic constraint. The reduction of the cross sections increases for higher n, producing a greater suppression of the n-jet rates. For the 1-jet cross section, we observe a factor of 1.4 between the cross sections calculated with only the HERA phase space and kinematic cuts compared to those with the inclusion of the extra kinematic constraint. This factor increases to ~ 3.5 for the 2-jet cross section, and higher still to a factor ranging between $\sim 6 - 13$ for the $n = 3$ rate. This introduces an interesting point; the effect of including the kinematic constraint becomes dependent on the x, Q^2 bin studied (the factor 1.4 is constant between the 1-jet rates) for the higher jet emissions. This dependence is especially marked in the x, Q^2 bins bordered by the phase space cuts. See for example the bin $x = 0.0002 - 0.0004, Q^2 \sim 10 - 15$ GeV^2 which has a factor 13.2 between the calculated cross sections, compared to a factor 6 in the bin of the top right hand corner of the plot for the 3-jet rates.

We can now make a similar comparison to that of Figure 3.16 to see if we still observe similar emission rates for the 1- and 2- jet cross sections when we include the cut of (3.71). The ratio of the 2-jet to 1-jet cross section including kinematical constraint is shown in Figure 3.20.

Recall, from Figure 3.16 we observe that the 2 jet/1 jet ratio is $\sim .75 - .80$; there are a substantial amount of 1-jet events that will contain a 2nd jet somewhere in the detector. In Figure 3.20, this ratio falls to $\sim 30\%$ for the percentage of 2:1 exclusive jet events at HERA. Thus, in this analysis, the imposition of the kinematical constraint produces a significant impact on the exclusive jet production rates. One interesting test would be to see experimentally the rate of 2:1 exclusive jet cross sections. This would show whether the imposition of this kinematical cut is required, or, whether we really do see a high proportion of 2:1 jet rates experimentally.

From other analyses including the kinematic constraint on the unified DGLAP and

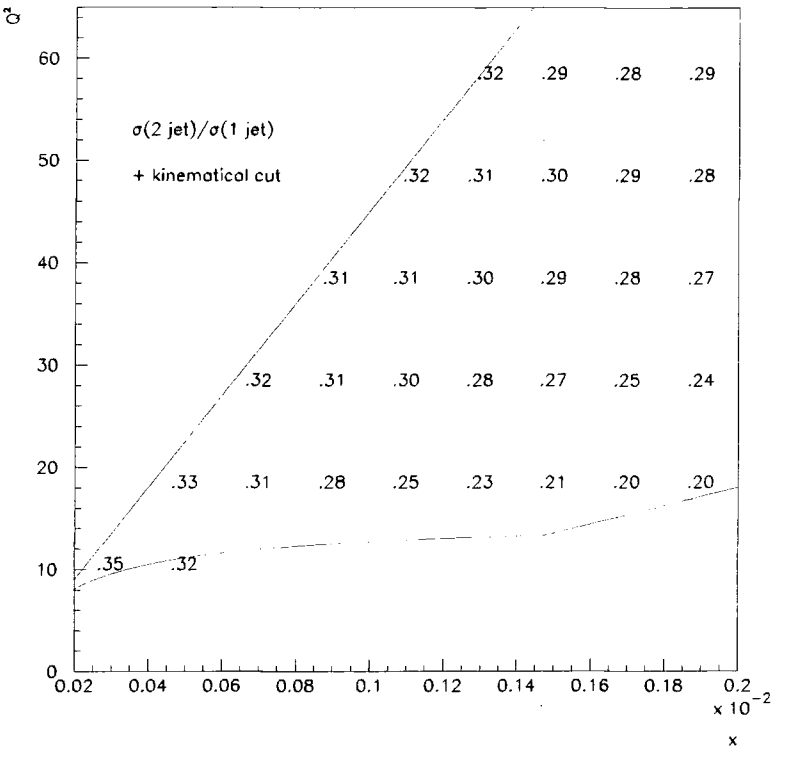

Figure 3.20: Ratio of the 2 to 1 exclusive jet cross sections including the kinematical constraint of (3.71).

BFKL equation, the inclusive unintegrated gluon [39] shows a significant reduction under the inclusion of the above cut which has been compared, favourably, at the structure function level with experiment. Thus, the observed reduction in the above n-jet cross sections is consistent with our understanding of this subleading effect.

3.6 Summary

In this chapter we have made a theoretical study of the BFKL equation to give an insight into its structure and to give a first exploration of the interesting effects that can be observed when application is made to the small x kinematic regime at HERA. Explicitly we have formulated a modified form of the BFKL equation which allows an exclusive analysis of the multijet yields in deep-inelastic lepton scattering in the small x regime. The jets are defined as gluon emissions from the BFKL chain which have transverse

momenta q_T greater than a specified resolution μ. First the modified BFKL equation was solved to determine the jet decomposition of the unintegrated gluon distribution $f(x, k_T^2)$ and then the k_T-factorization theorem used to determine the jet decomposition of the structure function $F_2(x, Q^2)$ (hence also the total deep-inelastic electron-proton scattering cross section) in the HERA small x regime. The jet decompositions were presented as a function of the kinematic variables and for different choices of the jet resolution parameter μ.

The modified BFKL equation is shown symbolically in (3.21) and the kernel $\hat{K}$ in (3.23). The equation embodies a resummation of the virtual contributions together with the *unresolved* real gluon emissions with $q_T < \mu$. As a consequence the kernel $\hat{K}$ has an explicit $y = \ln 1/x$ dependence, which depends on the amount of unresolved radiation and so is a function of μ. Indeed for unrealistically low values of μ, for pedagogic purposes, the analytic form of the y dependence of the kernel was derived, see (3.26). For the more realistic numerical solutions presented, the correlation between the x dependence of the n-jet cross sections and the resolution parameter μ is apparent.

The behaviour of the n-jet contribution to the gluon f, or to F_2, exhibits a characteristic behaviour as x decreases, rising to a maximum and then falling back to zero. The higher the value of n the lower the value of x at which the maximum occurs. In the HERA small x regime the behaviour is only apparent for low choices of the parameter μ, for example $\mu \sim 1$ GeV, see Figures 3.7, 3.8 and 3.9. For experimentally realistic values of the resolution parameter (say $\mu = 3.5$ or 6 GeV) the maxima shift to very small values of x and lie below the minimum experimental x limit available. The dominant contribution in the HERA range then comes from events with no resolved gluon jets emitted from the BFKL chain. Nevertheless the 1-, 2-, 3-, ...jet rates are still significant. An interesting feature of the multijet cross sections is that they are non-negligible even if $\mu > Q$. The existence of such jets with $q_T > Q$ is a straightforward consequence of the characteristic $\ln k_T^2$ diffusion along the BFKL gluon chain.

In summary, an exploratory study of a form of the BFKL equation which allows the final state jet configurations to be determined in a consistent manner has been made. The equation was solved and a selection of results presented to illustrate the properties of these gluon jets which occur in deep inelastic scattering at small x as a result of BFKL dynamics. Of course the normalization is dependent on the choice of input $f^{(0)}$

and the cut-off Q_0^2. Our choice is such that the predictions for the totally inclusive F_2 are compatible with the measurements at HERA. On the other hand the shape in x of the individual jet contributions, and the predicted values of the jet ratios are much less sensitive to the input. In addition there are $\ln 1/x$ and fixed-order QCD jet contributions to consider. These may modify the predictions in the HERA regime, but with decreasing x the BFKL behaviour should become increasingly dominant. One non-leading effect, is the imposition of the constraint $q_{nT}^2 < x_n k_T^2/x$ (in the notation of Figure 4.13) which follows from the requirement that the virtuality of the gluon links is dominated by $-k_T^2$ [37, 44]. This constraint is very important as initial studies of the NLO BFKL corrections indicate that this cut is a major contribution of the full NLO calculation. This means that in applying the constraint of (3.71) to the LO BFKL equation as used in this thesis provides a good (first) insight into the effects of higher order corrections. This constraint is also important as it can be done to all orders within the BFKL formalism and not just to NLO which provides a much better solution to the BFKL equation (see section 2.4). In applying this cut, the available phase space for multijet production is limited and, as a consequence, applying the kinematically constrained BFKL gluon distributions (3.75) to calculate fully integrated exclusive jet cross sections, reduces the yield of multijet events. The effect of applying the constraint to the BFKL gluon is shown in Figure 3.18 and the resulting decrease in the observable n-jet cross sections in Figure 3.19. The application of (3.71) to the real gluon emission has the effect of dramatically reducing the emission of higher numbers of jets compared to the results without the constraint (see Figure 3.15). Thus, this exploratory study is of importance for a full experimental analysis of exclusive jet production at HERA, and also has applications to $p\overline{p}$ and pp collisions with further modification.

In the next chapter we will further the study of this modified BFKL equation, which enables us to make calculations of final state jets, and apply it to the process of deep inelastic scattering including identified forward jet emission in an attempt to isolate signatures of BFKL dynamics at HERA.

Chapter 4

The BFKL formalism of forward jets

4.1 Introduction

The HERA kinematic range covers the region of small Bjorken x, and it is precisely at small x (i.e. high energies) where we would expect the BFKL equation to be valid. However, problems arise when we wish to observe signatures of these dynamics experimentally as the measured observables such as the rise of the proton structure function $F_2(x, Q^2)$ can be described satisfactorily by both BFKL evolution in $\ln 1/x$ and, by using a suitable choice of input at the scale Q_0^2, DGLAP evolution in $\ln Q^2$ of the gluon distribution. This leads to the conclusion that the structure function F_2 is too inclusive to act as a discriminator of the underlying small x dynamics.

One focus of recent studies at HERA has been to look for less inclusive quantities in which to distinguish, one way or another, whether the BFKL or the DGLAP description is the correct picture to apply in the kinematic regime of HERA. In particular, attention is being focused on final state physics as it is expected that hadronic final states will provide additional information and be more sensitive to the parton distributions.

In the previous chapter, we have discussed the process of exclusive jet production in DIS to try to find observables sensitive to BFKL dynamics and thus to provide signatures that could be observed experimentally. In this chapter, the focus will be shifted to another less inclusive quantity - the production of an extra jet in the forward region of the detector accompanying DIS events.

The small x region at HERA is the range $10^{-4} \lesssim x \lesssim 10^{-2}$. Here, $\ln 1/x$ terms are large, and, as these are precisely the terms summed by the LO BFKL equation, we would expect it to give a valid description of physical observables in this region.

BFKL dynamics are characterized by the absence of transverse momentum ordering of the emitted gluons and its $x^{-\lambda}$ behaviour where λ has an effective value[1] ~ 0.5 in the small x deep inelastic regime accessible at HERA. Thus, we would expect to see evidence of these in the experimental data. However, there are some ambiguities in the BFKL formalism which need to be considered before we can conclusively prove that BFKL dynamics have been observed. Firstly, the BFKL equation of (2.20) requires a non-perturbative input, $f^{(0)}(x, k_T^2)$, from which the Lipatov $\ln 1/x$ evolution is started. This introduces uncertainties from our lack of knowledge of the non-perturbative regime into any quantitative predictions we make. Secondly, the absence of transverse momentum ordering along the gluon chain leads to a diffusion in k_T^2, allowing the unintegrated gluon distribution $f(x, k_T^2)$ to enter the non-perturbative region during its evolution. This makes it difficult to distinguish whether the steep rise of the structure functions as predicted by the BFKL equation, are due to the Lipatov behaviour or to evolution of the non-perturbative input.

The solution to these problems has been known for some time. In 1990, the measurement of the less inclusive quantity of DIS events plus an energetic forward jet (Figure 4.1) was proposed by Mueller [45, 49, 62] as a method for eliminating these uncertainties. In this scenario, jet production is studied in the phase space region away from the struck parton such that the current jet, arising from the interaction of the photon with the gluon through the $q\overline{q}$ box of Figure 3.11, is well separated from the forward jet of interest which travels in the direction of the proton remnant. Thus, experimentally this is observed as a 2 $(1 + 1)$ jet process.

Recent work on jet production in DIS events [63] provides compelling evidence of the observation of BFKL dynamics in forward jet measurements. Full $\mathcal{O}(\alpha_s^2)$ calculations of NLO QCD forward jet production, when compared to the expected BFKL cross sections are much smaller. On comparison of these fixed order predictions with preliminary HERA forward jet results [64], the fixed-order QCD prediction falls well below the data, whereas, BFKL predictions successfully reproduce the observed magnitudes of the cross sections.

[1]For fixed α_s the exponent λ has the value $\lambda = \overline{\alpha}_s 4 \ln 2$, where $\overline{\alpha}_s \equiv 3\alpha_s/\pi$

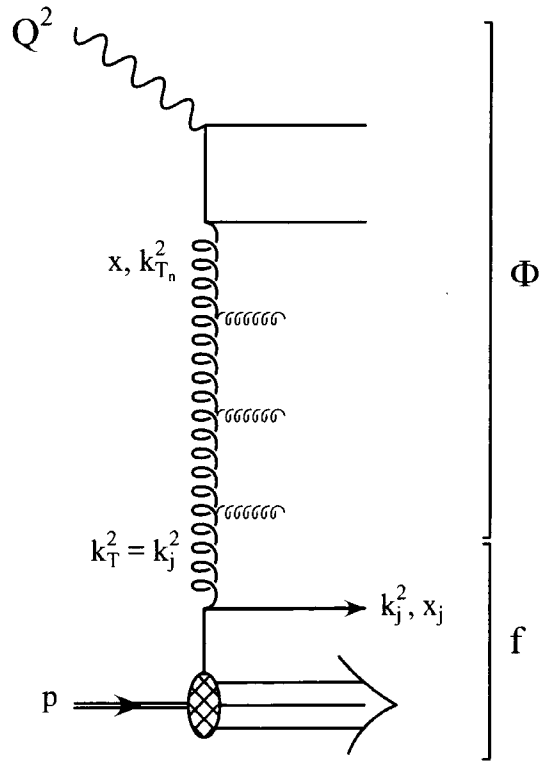

Figure 4.1: Diagramatic representation of a deep-inelastic event containing an identified forward jet, carrying longitudinal momentum $x_j P$ and transverse momentum k_j^2. The photon scatters from the gluon chain described by the BFKL equation which resums all soft gluon radiation (indicated by thin, horizontal gluons). The forward jet can originate from either a quark or gluon within the proton.

However, we should be careful. The identification of BFKL dynamics at HERA has not been conclusively proved - this evidence of BFKL dynamics is observed via an enhancement of the forward jet cross sections over the NLO expectations, but additional data, especially for harder forward, i.e. larger transverse momentum, jets is still required before more reliable comparisons can be made.

We will now consider these DIS including forward jet processes in greater detail.

In DIS events, as discussed in chapter 1, the virtual photon acts as a probe of the proton (Figure 1.1). However, if we require that an identified jet with kinematic variables x_j, the longitudinal momentum fraction, and k_j^2, its transverse momentum, have $x_j \gg x$ with $x_j \sim \mathcal{O}(1)$ such that it does not lie in the small x region, and $k_j^2 \simeq Q^2$, then the photon now probes a specific parton within the proton. The evolution of the gluon

density now corresponds to the cascade of partons (gluons) which may be emitted before interaction with the virtual photon probe. This cascade can be described by either the DGLAP or BFKL evolution equation, although as we shall see, the measurement of DIS events including a forward jet is a clean method of neutralizing the Q^2 DGLAP evolution.

From experiment, for large x, the parton distributions of the proton are well known, see for example[12, 65]. Thus, for $x_j \sim \mathcal{O}(1)$ we no longer have to start evolution of the BFKL equation from an unknown non-perturbative driving term. Also, due to strong ordering at the lower gluon-parton vertex (Figure 4.1), the exchanged gluon and jet have approximately the same transverse momentum i.e. $k_T^2 = k_j^2$. Because DGLAP evolution is characterized by the strong ordering of the transverse momenta of the emitted gluons, the selection of events with $k_T^2 \simeq Q^2$ will suppress the phase space available for jet production arising from DGLAP dynamics. This allows us to focus directly on the small x/x_j behaviour of the forward jets. In principle this provides a clean test of BFKL dynamics, and, recently data for the process DIS plus an identified forward jet has been published [66, 67] allowing direct comparison of BFKL predictions with the experimental cross sections.

Neutralizing the BFKL k_T diffusion into the IR region

One of the main features of BFKL dynamics is the diffusion in k_T Eq.(2.15) along the gluon ladder, that is, there is a random walk in the transverse momentum of the emitted gluons where

$$k_{T_i} \sim k_{T_{i-1}}$$

and k_{T_i} can be both larger and smaller than the momentum of the previous rung. It is this diffusion which causes problems. The k_T integration phase space can enter the infra red (IR) region which is described by non-perturbative physics. This is shown in Figure 4.2(a) in which the evolution of the parton distribution is started at the input scales x_0 and k_0^2. As we evolve to smaller values of x, the momentum changes from the input scale $k_0^2 \rightarrow k_{box}^2$, the scale set by the upper part of the diagram in Figure 4.1. During this evolution, for an input scale k_0^2 not very large, it is possible that the k_T diffusion will enter the IR region introducing contributions from non-perturbative physics which are unknown. However, if we consider the process of DIS plus a forward jet (Figure 4.2(b)), because the momentum of the gluon-parton vertex is restricted to $k_T^2 \simeq Q^2$, for large

virtualities of the photon where $Q^2 \gtrsim$ few GeV^2, then the diffusion in k_T as we evolve towards smaller x no longer enters the non-perturbative region. The measurement of forward jet processes removes ambiguities arising from the effects of unknown physics.

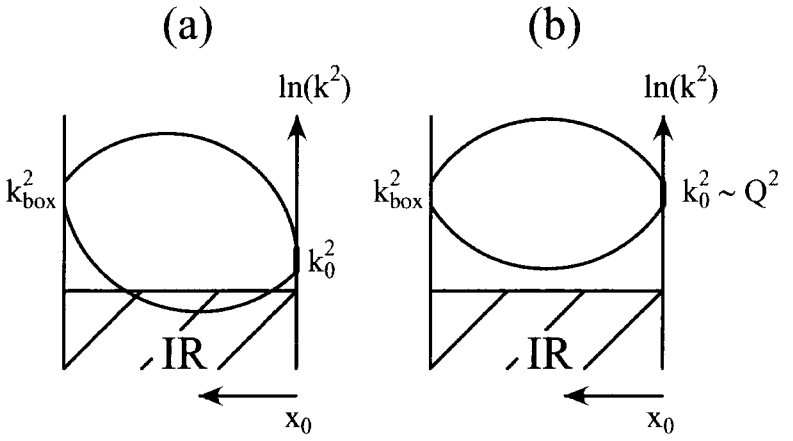

Figure 4.2: Representation of the diffusion in k_T during BFKL evolution. Figure (a) shows the k_T of the gluons entering the non-perturbative IR region through diffusion during evolution from an input scale of k_0^2 to k_{box}^2. Figure (b) shows the diffusion in k_T for the process of DIS including a forward jet. Due to a higher input scale, k_0^2, there is no longer diffusion into the IR region, removing uncertainties arising from unknown physics. These diagrams are known as "Bartels Cigar"[68].

2 jet events in the forward region

As well as identifying the DIS including a single forward jet process, experimentalists have observed a few events in which two jets have been identified as being emitted in the forward direction. For the 1993 H1 and ZEUS data, the ratio of processes involving two forward jets to those involving only one, is approximately 4% [67].

The BFKL formalism can readily be extended to include emission of a second jet when we allow an emitted gluon rung from the chain of Figure 4.1 to have a transverse momentum greater than some minimum cutoff $p_{Tjet}^2 > p_{Tmin}^2$. In the language of the previous chapter, we allow the gluon to be *resolved* as an identified jet.

The aim of this chapter is to study the process of DIS including 2 identified forward jets within the BFKL description, and to predict the ratio of 2:1 jet events in the forward

direction at HERA.

4.2 Forward jets in deep inelastic scattering

We are interested in the DIS process including an identified forward jet, $e+p \longrightarrow jet+X$ shown in Figure 4.1, where the emitted jet originates from either a quark or gluon within the proton.

In this process we wish to expose the dependence of the final state jet variables, thus, the cross section of (1.11) is written as the differential with respect to x_j and k_j^2 as

$$\frac{d\sigma}{dxdQ^2dx_jdk_j^2} = \frac{4\pi\alpha^2}{xQ^4}\left[(1-y)\frac{\partial F_2}{\partial x_j \partial k_j^2} + \frac{1}{2}y^2\frac{\partial F_T}{\partial x_j \partial k_j^2}\right], \tag{4.1}$$

where the variables x, Q^2, y and s are the usual DIS quantities of chapter 1. We have chosen to use the transverse (F_T) and longitudinal (F_L; $F_2 = F_T + F_L$) structure functions as these are calculable from the $\gamma^* g \rightarrow q\overline{q}$ fusion process of the quark box in the upper part of Figure 4.1, see (3.64) and (3.65).

The above differential structure functions have the leading small $z = x/x_j$ behaviour described by the Mueller formalism. Writing the convolution equation for the structure function i

$$F_i(x, Q^2, x_j, k_j^2) = \Phi_i \otimes f\ , \tag{4.2}$$

then Φ_i represents the photon-gluon process and f the momentum distribution of the partons dependent on the jet variables. These contributions are shown in Figure 4.1. It is useful to note, in this formalism the BFKL evolution of the gluon is contained in the term Φ, in which evolution is considered to start from the driving term ($\Phi^{(0)}$) of the box at the top of the diagram. This is essentially "upside down" compared with the description used in chapter 3. Here, the gluon evolution was considered to originate from the proton using the driving term $f^{(0)}$ derived from non-pertubative considerations of the parton distributions inside the proton (see section 3.2).

Formally (4.2) is written [45, 62]

$$F_i(x, Q^2, x_j, k_j^2) = \int \frac{dk_j^2}{k_j^2}\int \frac{dx_j}{x_j}\ \frac{N_c\alpha_s}{\pi}\ \sum_a x_j f_a(x_j, k_j^2)\frac{\Phi_i(x/x_j, k_j^2, Q^2)}{k_j^2}\ ,$$

giving the differential structure function

$$x_j \frac{\partial F_i(x,Q^2,x_j,k_j^2)}{\partial x_j \partial k_j^2} = \frac{3\alpha_s}{\pi k_j^4} \sum_a x_j f_a(x_j,k_j^2)\ \Phi_i\left(\frac{x}{x_j},k_j^2,Q^2\right) . \tag{4.3}$$

The term $1/k_j^4$ arises from the gluon propagators giving the k^{-4} behaviour associated with single jet production. The term Φ_i/k_j^2 is identified with the gluon structure function integrated over the longitudinal momentum of the gluon and explicitly Φ_i has dimensions of k^2. The differential structure function (4.3) contains an "extra" factor α_s to the formalism of chapters 1 & 3, because the above process involving an identified jet is $\mathcal{O}(\alpha_s)$ with respect to the inclusive DIS structure functions F_i of (1.27).

What does equation (4.3) imply for the observable structure function F_2? For the proton structure function, using the naive parton model of (1.27) we have

$$F_2 = x \sum_q e_q^2 q(x,Q^2)$$

where the partons at small x are dominated by the gluon distribution. From the BFKL equation(section 2.2.2), the gluon distribution has the behaviour

$$xg(x,Q^2) \sim Cx^{-\lambda} ,$$

thus, the expected dependence of the differential structure function for DIS including a forward jet is

$$x_j k_j^2 \frac{\partial F_2}{\partial x_j \partial k_j^2} \sim \frac{3\alpha_s}{\pi} \sum_a x_j f_a(x_j,k_j^2)\ \left(\frac{x}{x_j}\right)^{-\lambda} , \tag{4.4}$$

i.e. we expect to be able to study the (x/x_j) behaviour of the structure functions.

For a forward jet carrying a momentum fraction $x_j \sim \mathcal{O}(1)$, the parton distributions $f_a(x_j,k_j^2)$ of the proton are well known from data, and the sum over the parton distributions, $\sum f_a$ of (4.3), is shown below to have the effective form

$$\sum_a f_a = g + \frac{4}{9}(q+\bar{q}) , \tag{4.5}$$

see (4.9), where g is the gluon distribution and q, $\bar{q}$ the sum of individual quark and antiquark distributions respectively. In the results presented later for DIS events including a forward jet, the index a runs over u, d, s, c flavoured quarks and antiquarks which are obtained using the MRS(A) parton distributions [12] with a value $\Lambda_{QCD} = 230 MeV$.

Effective parton distribution assuming t-channel pole dominance

The effective form for the sum of the parton distributions quoted in (4.5), holds only in the limit of t-channel pole dominance for scattering processes. For completeness, a discussion will be presented here on the origin of this form.

Consider the 2-2 scattering process $A + B \rightarrow C + D$, shown in Figure 4.3(a), where the Mandelstam variables are given by the usual definitions

$$\begin{aligned} s &= (P_A + P_B)^2 \\ t &= (P_A - P_C)^2 \\ u &= (P_A - P_D)^2 \,. \end{aligned} \tag{4.6}$$

For scattering processes with parton exchange in the t-channel, the pole structure has

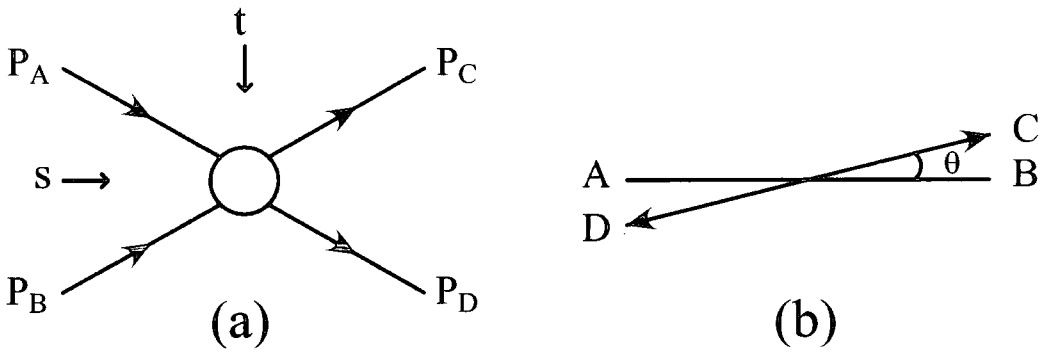

Figure 4.3: (a) 2-2 scattering for the process $A+B \rightarrow C+D$ showing the different scattering channels. The u channel corresponds to $(P_A - P_D)$. (b) For t-channel dominance, scattering of final state particles is at very small angles θ.

the form (Halzen & Martin[2] chapter 6)

$$t_{pole} \sim \frac{1}{t^2} \,,$$

which will dominate the scattering amplitude in the limit $t \rightarrow 0$, i.e. for scattering of particles C & D into very small angles θ, Figure 4.3(b). The scattering process of quarks and gluons, via gluon exchange, has three t-channel processes (labelled qq, qg and gg) shown in diagrams (a), (b) and (c) of Figure 4.4 respectively.

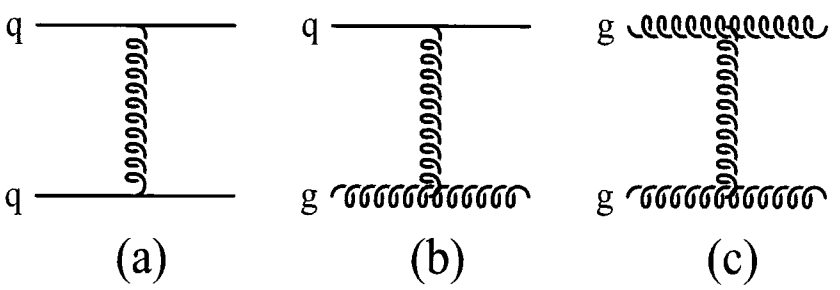

Figure 4.4: Contribution to the scattering of partons via gluon exchange in the t-channel.

The cross sections of these parton subprocesses are proportional to the matrix elements squared, which in the small t limit have the approximate forms

$$\begin{aligned} |\mathcal{M}|^2_{qq} &\sim \frac{C_F^2}{t^2} \\ |\mathcal{M}|^2_{qg} &\sim \frac{C_F C_A}{t^2} \\ |\mathcal{M}|^2_{gg} &\sim \frac{C_A^2}{t^2}\,, \end{aligned} \tag{4.7}$$

where C_F and C_A are the colour factors with values $C_F = 4/3$ and $C_A = 3$ for QCD.

The total cross section for the scattering process is the sum over the contributions of Figure 4.4 where

$$\sigma \sim \sum |\mathcal{M}|^2 \,.$$

Labelling the individual quark and antiquark flavour distributions which can take part in the scattering as, $u, d, ...\overline{u}, \overline{d}, ...$ etc. and the gluon distribution g, then the total cross section for 2-2 scattering is the sum over all possible $q_i q_j, q_i g, gg$ combinations and becomes

$$\begin{aligned} \sigma \;\sim\; \Big[&(uu + dd + ud + \overline{u}u + ...)\frac{C_F^2}{t^2} \;+\; (u + d + ...)g\frac{C_F C_A}{t^2} \\ &+\; g(u + d + ...)\frac{C_F C_A}{t^2} \;+\; gg\frac{C_A^2}{t^2}\Big] \,, \end{aligned}$$

which factorizes as

$$\begin{aligned} \sigma \;\sim\; \frac{C_A^2}{t^2}\Big[&gg \;+\; g(u + d + ...)\frac{C_F}{C_A} \;+\; (u + d + ...)g\frac{C_F}{C_A} \\ &+(uu + dd + ud + \overline{u}u + ...)\frac{C_F^2}{C_A^2}\Big] \end{aligned}$$

$$\sim \frac{C_A^2}{t^2}\left[g + \frac{C_F}{C_A}(u+d+...)\right]\left[g + \frac{C_F}{C_A}(u+d+...)\right] . \tag{4.8}$$

Using the notation

$$q = u + d + ... \quad \text{and} \quad \overline{q} = \overline{u} + \overline{d} + ...$$

to describe the sum over all flavours of quarks and antiquarks respectively, then (4.8) can be written as

$$\sigma \sim \frac{C_A^2}{t^2}\left[g + \frac{C_F}{C_A}(q+\overline{q})\right]\left[g + \frac{C_F}{C_A}(q+\overline{q})\right]$$

from which we identify that the sum over all parton distributions, in the limit $t \to 0$, is given by

$$\begin{aligned} \sum_a f_a &= \left[g + \frac{C_F}{C_A}(q+\overline{q})\right] \\ &= \left[g + \frac{4}{9}(q+\overline{q})\right] , \end{aligned} \tag{4.9}$$

(from the explicit numerical values of C_F and C_A), giving the form as quoted in (4.5).

The approximate forms for $|\mathcal{M}|^2$ of (4.7) only hold in the limit $t \to 0$, thus $\sum f_a$ of (4.9) gives the asymptotic sum of the parton distributions.

Gluon distributions at small z

We are interested in the small $z = x/x_j$ behaviour of the gluon chain in Figure 4.1. This is given by the term $\Phi_i(z, k_j^2, Q^2)$ of (4.3), which for fixed α_s satisfies the BFKL equation of (2.20)

$$\begin{aligned} \Phi_i(z, k_T^2, Q^2) &= \Phi_i^{(0)}(z, k_T^2, Q^2) + \overline{\alpha}_s \int_z^1 \frac{dz'}{z'} \int \frac{d^2 q_T}{\pi q_T^2} \\ &\left[\frac{k_T^2}{k_T'^2}\Phi_i(z', k_T'^2) - \Phi_i(z', k_T^2)\Theta(k_T^2 - q_T^2)\right] , \end{aligned} \tag{4.10}$$

where the label i represents the longitudinal(L) and transverse(T) contributions to the quark box driving term and $\overline{\alpha}_s = 3\alpha_s/\pi$. Equation (4.10) is written in the form as used in chapter 3, in which the integral is over the momentum of the emitted gluon and where the singularities as $q_T^2 \to 0$ cancel between the real (1st term under the integral in (4.10)), and virtual, gluon (2nd term under the integral in (4.10)) contributions of the BFKL kernel. The vector $k_T'^2$ is as usual given by $k_T'^2 = (\boldsymbol{k}_T + \boldsymbol{q}_T)^2$.

4.2.1 Structure functions of DIS + forward jet processes

As mentioned above, the driving term $\Phi^{(0)}_{L,T}(z, k_T^2, Q^2)$ is given by the respective longitudinal and transverse contributions of the quark (and crossed) box of Figure 3.11. It is important to note that the driving term for the quark box, for small z, is independent of z i.e. $\Phi^{(0)}_{L,T}(z, k_T^2, Q^2) \simeq \Phi^{(0)}_{L,T}(k_T^2, Q^2)$ [27].

The explicit forms for the polarization contributions of the driving term $\Phi^{(0)}_i$ are given by [27][2]

$$\Phi^{(0)}_T(k_T^2, Q^2) = 2\sum_q e_q^2 \frac{Q^2}{4\pi^2}\alpha_s(k_T^2)\int_0^1 d\beta \int_{\kappa_0^2}^{\infty} d^2\boldsymbol{\kappa}[\beta^2 + (1-\beta)^2]\left(\frac{\kappa^2}{D_1^2} - \frac{\boldsymbol{\kappa}\cdot(\boldsymbol{\kappa} - \boldsymbol{k}_T)}{D_1 D_2}\right) \tag{4.11}$$

$$\Phi^{(0)}_L(k_T^2, Q^2) = 2\sum_q e_q^2 \frac{Q^4}{\pi^2}\alpha_s(k_T^2)\int_0^1 d\beta \int_{\kappa_0^2}^{\infty} d^2\boldsymbol{\kappa}[\beta^2(1-\beta)^2]\left(\frac{1}{D_1^2} - \frac{1}{D_1 D_2}\right),$$

where, assuming massless quarks

$$D_1 = \kappa^2 + \beta(1-\beta)Q^2$$
$$D_2 = (\boldsymbol{\kappa} - \boldsymbol{k}_T)^2 + \beta(1-\beta)Q^2 .$$

Again β and $\boldsymbol{\kappa}$ arise from the Sudakov decomposition of the four momentum of the quark line of the box diagrams of Figure 3.11. These should be compared with the form of (3.65) in which the quark box is convoluted with the already x dependent BFKL gluon density $f(x, k_T^2)$.

However, for the results presented below, the azimuthal integration of (4.11) between $\boldsymbol{\kappa}$ and $\boldsymbol{k}_T$ was removed by the introduction of the Feynman parameter λ, which after some algebraic manipulation, allows us to write

$$\Phi^{(0)}_T(k_T^2, Q^2) = \sum_q e_q^2 \frac{\alpha_s(k_T^2)}{\pi} k_T^2 Q^2 \int_0^1 d\beta \int_0^1 d\lambda \int_{\kappa_0'^2}^{\infty} d\kappa'^2 \left[\beta^2 + (1-\beta)^2\right]\lambda$$
$$\times \frac{(2\lambda - 1)\kappa'^2 + (1-\lambda)\left[\lambda(1-\lambda)k^2 + \beta(1-\beta)Q^2\right]}{\left[\kappa'^2 + \lambda(1-\lambda)k^2 + \beta(1-\beta)Q^2\right]^3} \tag{4.12}$$

and

[2]The integration κ is over the momentum of the quark line of the box diagrams (Figure 3.11). The lower cut κ_0^2 is explicitly included in this integral since, as one cuts on the gluon virtuality then one ought to do the same for the quark. However, there is no need for this cut on the integral of the quark transverse momentum i.e. we can set $\kappa_0^2 = 0$ (and also $\kappa_0'^2 = 0$ in (4.12) & (4.13)) . The importance of this cut will be observed in the discussion relating to the normalization of the BFKL gluon in section 4.2.3.

$$\Phi_L^{(0)}(k_T^2, Q^2) = \sum_q e_q^2 \frac{\alpha_s(k_T^2)}{\pi^2} Q^4 \int_0^1 d\beta \int_0^1 d\lambda \int_{\kappa_0'^2}^{\infty} d\kappa'^2 \, \beta(1-\beta)^2 \times \left[\frac{1}{2} \frac{6\lambda(1-\lambda)\left[4\pi\kappa'^2 k^2 + 2\pi k^4(1-2\lambda)^2\right]}{\left[\kappa'^2 + k^2\lambda(1-\lambda) + \beta(1-\beta)Q^2\right]^4} \right] . \quad (4.13)$$

To arrive at the above results we make the change of variable $\boldsymbol{\kappa} = \boldsymbol{\kappa}' + k(1-\lambda)$. These equations are then numerically solved with the integration over κ'^2 regulated by the cut $\kappa_0'^2 = 1$ GeV^2.

In reality, the contribution from F_L to the structure function F_2 is only a small amount, with $F_L \sim 2F_T/9$. It is often omitted in earlier work on the calculations of F_2 [27, 69]. For the results of DIS including forward jet cross sections presented below (sections 4.2.4 & 4.4), the longitudinal component is included in the description of F_2.

As before, we will solve for the BFKL equation using the running coupling $\alpha_s(k^2)$. In this formalism, we will use the "full" BFKL solution of chapter 3 in which all gluon radiation of the gluon chain is treated as soft and is resummed with the virtual contributions. The full BFKL kernel is given by the exponential of the unresolved and virtual emissions, K_{UV} of (3.19), i.e. the resolution parameter μ of chapter 3 is effectively $\mu = \infty$.

To include running α_s in (4.10), it is convenient to work with the function

$$H(z, k_T^2, Q^2) = \overline{\alpha}_s(k_T^2)\Phi(z, k_T^2, Q^2) \quad (4.14)$$

where $\overline{\alpha}_s = 3\alpha_s/\pi$. This is to remove the necessity of having two different scales of α_s for the real and virtual terms ($\alpha_s(k_T'^2)$ & $\alpha_s(k_T^2)$) in the [ ] term of (4.10). By using the variable H we only have one scale to deal with during computation. Thus, rewriting (4.10) gives

$$H(z, k_T^2, Q^2) = H^{(0)}(k_T^2, Q^2) + \overline{\alpha}_s(k_T^2) \int_z^1 \frac{dz'}{z'} \int \frac{d^2 q_T}{\pi q_T^2} \left[\frac{k_T^2}{k_T'^2} H(z', k_T'^2) - H(z', k_T^2)\Theta(k_T^2 - q_T^2) \right] . \quad (4.15)$$

Symbolically this is written as

$$H = H^{(0)} + K \otimes H , \quad (4.16)$$

where the kernel is given by $K = \Delta = \exp(K_{UV} y)$ of (3.19), and $H^{(0)} = H_T^{(0)}, H_L^{(0)}$ is obtained by applying (4.14) to (4.12) and (4.13).

In the following, (4.15) was solved using the numerical techniques of section 3.3 with $N = 10$ Chebyshev nodes for the k_T^2 dependence.

The Lipatov effect

Is it possible to observe signatures of BFKL dynamics in the structure functions at HERA?

We can observe the effect of the Lipatov dynamics if we compare the structure function F_2 when we use the full form of (4.15) in which we allow evolution of the gluon, to that in which the struck parton interacts directly with the photon probe and couples directly through the $\Phi = \Phi_{box}^{(0)}$ term only. This comparison is shown in Figure 4.5 for the differential structure function (4.3) as a function of the jet longitudinal momentum fraction. This is shown for the kinematic choice, $k^2 = Q^2 = 5$ GeV^2 for three choices of Bjorken $x = 0.01$, 0.001 and 0.0001. The solid line shows the F_2 structure function if we allow no gluon radiation from the struck parton. Obviously, the effect of including the BFKL gluon summation is to increase the magnitude of the proton structure function.

The results of Figure 4.5 are calculated using the resummed BFKL kernel $\Delta = \exp(K_{UV}y)$ as derived in chapter 3, and the MRS(A) parton distributions. This plot reproduces the form of the differential structure functions presented in [27] providing a check of the numerical methods used. The magnitude here is larger due to a higher choice of Λ_{QCD} in α_s of the BFKL gluon calculation, and the use of different parton distributions to those in [27]. The numerical calculation is a direct modification of the *full* BFKL gluon distribution from the previous chapter, in which, evolution is now started from the top of the ladder chain instead of the bottom.

In (4.15) we have the integration $\int_z^{z_0} dz'/z'$, in which the upper limit is restricted via a cut $z_0 \neq 1$, such that we restrict $x_j > x$. The restriction $z < z_0$ ensures we will probe the small z region. z_0 determines the point, at which the evolution in $\ln 1/z$ starts, i.e. the point at which the gluon chain is matched to the quark box $\Phi_i^{(0)}$. In the above, $z_0 = 0.1$. Essentially z_0 is a free parameter which will be fixed to match the BFKL result to the DIS plus 1 forward jet cross section data. This will then be used to make predictions for different kinematical cuts and the 2 forward jet production rate. Of course, this normalization is dependent on how rigorous a calculation is made of the quark box, subject to how many quark flavours are included and how many flavours are summed over

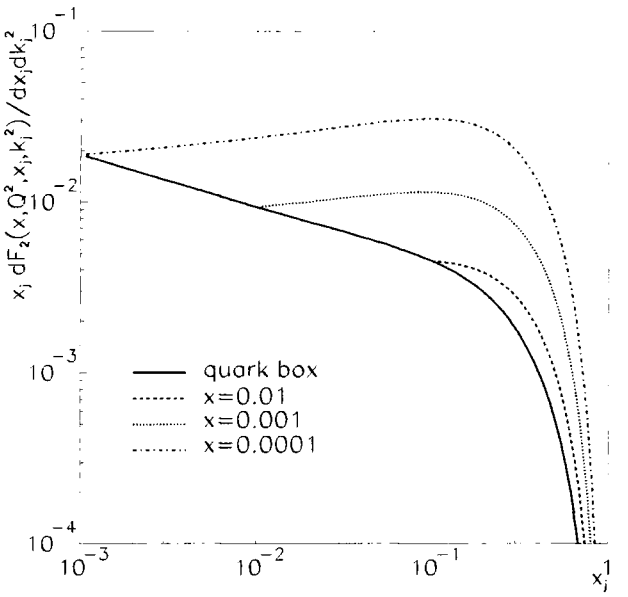

Figure 4.5: Differential structure function F_2 as a function of jet momentum fraction x_j. Solid line shows the contributions from the quark box only - that is for no gluon radiation from the probed gluon before interaction with the photon. Dot/dash lines show the increase of the structure function when we include contributions from the BFKL resummed soft gluon radiation. This is shown for three choices of fixed Bjorken x for the kinematic choices, $k_T^2 = Q^2 = 5$ GeV^2, with a lower cut $\kappa_0^2 = 1$ GeV^2 in the integrations of (4.12) and (4.13). MRS(A) parton distributions are used with $\Lambda_{QCD} = 230$ MeV.

in the identified jet. A more detailed discussion of the normalization chosen for the final results presented later is discussed in section 4.2.3.

4.2.2 DIS + 1 forward jet - experimental cuts

The fully integrated cross section is readily obtained by inserting the solved BFKL equation of (4.15) into (4.1). To make a valid comparison of the DIS including 1 forward jet cross section with the data, we need to include the experimental kinematical cuts to the integration phase space. These essentially are the same as those discussed in section 1.2.1, although the forward jet region has a very large cut on the allowed scattering angles of the final state electron compared to those listed in (1.8).

Unless otherwise stated, the following analysis imposes the constraints as used by the H1 collaboration for forward jet event selection [66]. We are constrained to the x, Q^2 phase space, such that, for an incoming electron with energy $E_e = 27.5$ GeV and proton energy $E_p = 820$ GeV, we restrict the energy of the scattered electron to be $E_{e'} > 11$ GeV and its angle with respect to the proton direction to be $160° < \theta_{e'} < 173°$. The allowed electron acceptance region is shown in Figure 4.6 for two upper restrictions on the kinematic variable y Eq.(1.1). That is, we impose

$$0.1 < y < 0.5 \ (1.0)$$

where the smaller and larger upper limits are shown by the solid and dashed lines respectively. The importance of this upper limit cut on y will be discussed in section 4.2.4.

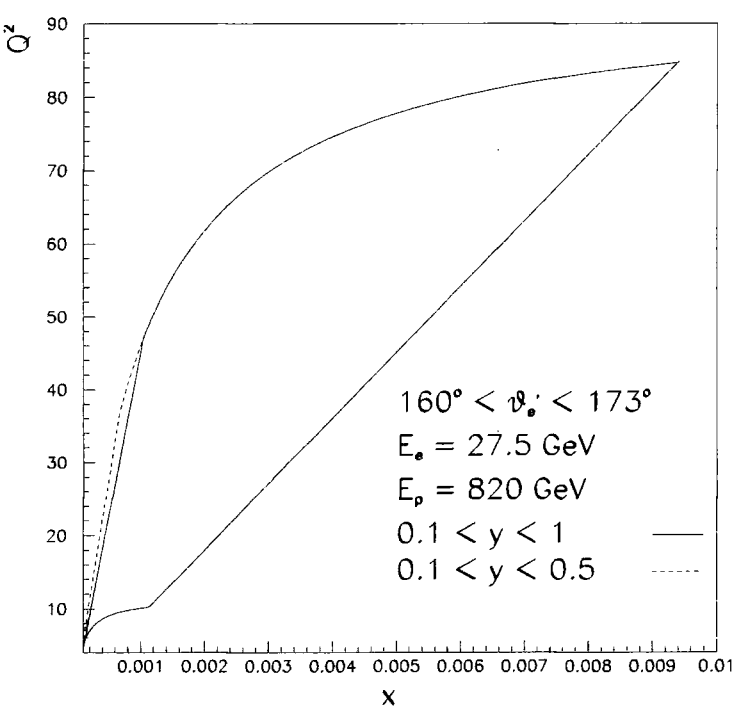

Figure 4.6: Electron acceptance region for forward jet identification using H1 experimental cuts from [66] .

Comparing Figure 4.6 with Figure 1.3 showing the "full" phase space of HERA, we see that the most restrictive cut is from the lower electron angle limit of 160°. This dominates

the y_{cut} restriction. In fact, the limit $\theta_{e'} > 163°$ restricts the available x region for forward jets to $10^{-4} \lesssim x \lesssim 10^{-2}$.

As well as cuts for the scattered electron, we require that the forward jet itself have a minimum transverse momentum $p_{Tjet} > \mu$. H1 have published data for the cuts $\mu = 3.5$, 5 and 6 GeV. It must also have a minimum energy set by $E_{jet} > 28.7$ GeV and lie within $7° < \theta_j < 20°$ with respect to the proton (see Figure 1.2). The restriction on $E_{jet} > E_{min}$ forces the integration of the jet longitudinal momentum fraction to $x_j > 0.035$, through the relation $E_j \simeq x_j E_p$. This also gives $x_{j'} > 0.035$ for the 2 forward jet calculation of section 4.3.

One other important kinematical cut, especially for the 2 forward jet production, is the restriction on the allowed momentum of the emitted jets. We restrict $p_{Tjet} \sim Q^2$ and set

$$\max[\mu^2, Q^2/2] < p_{Tjet}^2 < 2Q^2 \, .$$

This is implemented to minimize DGLAP $\ln(Q^2)$ evolution and to prevent background from one of the $q\overline{q}$ constituents of box contribution being identified as an individual jet in the forward detector region. We assume the $q\overline{q}$ pair are close enough together to be observed as one current jet.

To implement these cuts on the jet kinematics, they are translated to the integration limits for the DIS variables x, Q^2, x_j, k_j and azimuth through the manipulation of the energy/angle forms of the variables in (1.1).

4.2.3 Normalizing the BFKL gluon

Before we look at the BFKL predictions for cross sections of DIS including a forward jet, we should consider the normalization of the BFKL gluon and the stability of the results obtained.

There are two main contributions to the integrals of the box driving term which will affect the normalization of the 1 forward jet cross section. These are:

(i) the number of quark flavours in the $q\overline{q}$ box diagram contribution to $\Phi_i^{(0)}$, and less significantly, the number of heavy quarks we allow in the summation $\sum f_a$.

(ii) The integration cutoff $\kappa_0'^2$ of (4.12) and (4.13).

However, once the normalization is fixed, this is not changed throughout for the results of the next sections.

As mentioned above, the normalization is determined by the point at which the starting scale of the $\ln 1/z$ evolution is fixed. The upper limit is set to z_0 where we define

$$z_0 = \frac{x}{x_0}$$

with x_0 the minimum value of the jet momentum fraction. The larger the value of z_0, the longer the evolution length in $\ln 1/x$, thus producing a greater contribution from the BFKL growth.

Let us consider the two contributions affecting the normalization.

The aim of the work in this chapter is to ultimately calculate the ratio of 2:1 DIS event cross sections including forward jets at HERA, thus, since contributions from the input $\Phi_i^{(0)}$ of (4.11) will essentially cancel between the two jet rates, we can make some approximations to allow practical numerical computation which should not affect the accuracy of the final results. To this end, explicit heavy quark (c, b) contributions were neglected in the equations of the quark box as the inclusion of these essentially doubles the computation running time. Only massless quarks are included.

Another component affecting the normalization is the inclusion of heavy charm in the forward jet. However, this produces an increase in the cross sections for the smallest x bins of only a few pb and as such is not very important in fixing the normalization. Charm contributions in the forward jet are included in the $\sum f_a$ term for the parton distributions in the following results.

Using a lower integration cut $\kappa_0'^2 = 1$ GeV^2 in (4.12) and (4.13), normalizing the 1 forward jet results to the H1 data of [66] we obtain the starting value $z_0 = 0.5$ (see Figure 4.7(a)). This can be compared to the inclusion of an explicit charm contribution to the input quark box. Charm provides an approximate 20% contribution to the structure function F_2, increasing the overall cross section and reducing the starting input to a value $z_0 \sim 0.1$ for accurate description of the magnitude of the cross section data.

The resulting magnitude of the BFKL solution (Φ) is also sensitive to the cut $\kappa_0'^2$ of the box integration. The above normalization $z_0 = 0.5$ is set using the lower cut $\kappa_0'^2 = 1$

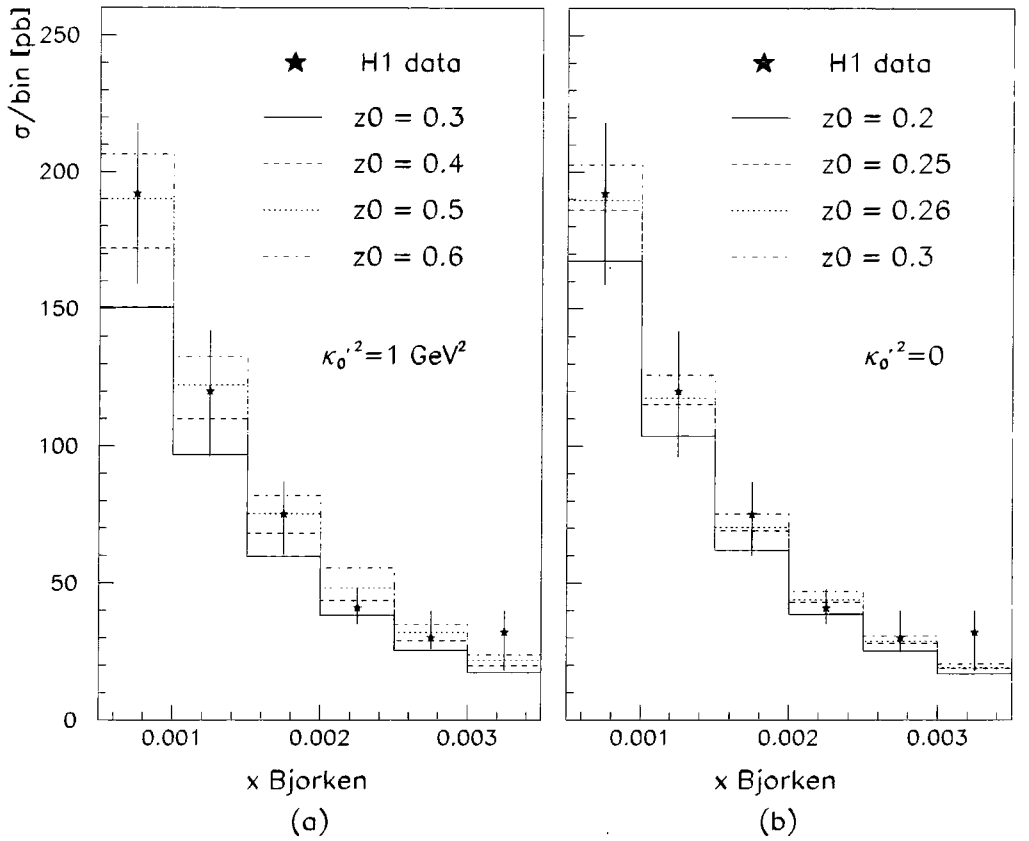

Figure 4.7: Fitting the BFKL DIS + 1 forward jet cross section to experimental data for no heavy quark masses in the box diagram of Figure 3.11. (a) Shows the normalization required to obtain the correct magnitude when the integration limit is set to $\kappa_0'^2 = 1$ GeV^2 and (b) the reduction of the normalization z_0 when the integration limit is set to $\kappa_0'^2 = 0$.

GeV^2 as used in [27]. If instead $\kappa_0'^2 = 0$, there is approximately a factor of two increase in the the overall DIS plus 1 forward jet cross section at $x \sim 10^{-4}$; the higher x bins are less sensitive to changes of the normalization parameter. The results for the 1 jet cross section using the cut $\kappa_0'^2 = 0$ are shown in Figure 4.7(b) for a range of starting values $z_0 = 0.2 - 0.3$.

Choosing $z_0 = 0.26$ to give the "best" fit with the data, we can compare the cross sections for the two choices of normalization: $\kappa_0'^2 = 1$ GeV^2 & $z_0 = 0.5$, and, $\kappa_0'^2 = 0$ & $z_0 = 0.26$. These are shown in Figure 4.8 and we can conclude that, within experimental data errors there is no "best" choice of normalization - one choice is as valid as the other.

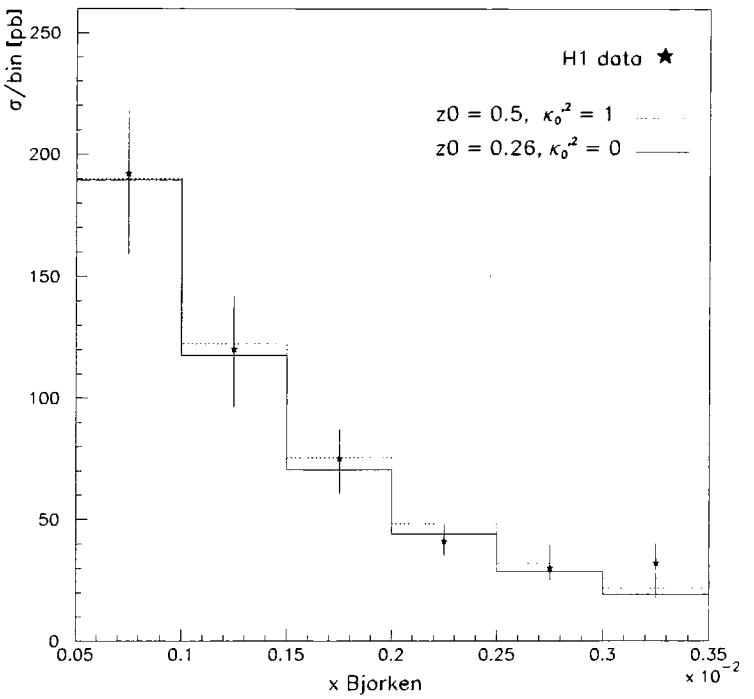

Figure 4.8: Comparison of the two choices of normalization for the BFKL result with the H1 data of [66].

The question we should ask is, how stable are our results to calculations of the BFKL solution with different choices of normalization? From Figure 4.8 we see that the experimental data has relatively large error bars allowing some flexibility in choosing the "best" normalization, and there is a possibility the data points for the 1 jet cross section will shift [70] when the newest experimental data sets are published. Obviously the absolute magnitudes of the 1 and 2 forward jet cross sections will be dependent on the explicit choice of normalization used. To fix the "correct" normalization to give predictions for magnitudes of absolute cross sections would require the inclusion of heavy quark masses in the box integrations. However, we are interested in the ratio of 2:1 jet cross sections, providing the motivation for the above mentioned approximation. Thus, if the experimental cross section data were to be reduced, and so shift the normalization to smaller values of z_0, how would this change of normalization affect the predictions for the 2:1 jet cross section ratios?

To show the stability of the calculated results, we will jump ahead of ourselves and

look at the dependence of the 2:1 jet ratios[3] on the choice of normalization z_0. For an x bin corresponding to the range $0.0001 < x < 0.004$, minimum transverse momentum of the jet $p_{Tmin} = 3.5$ GeV, kinematic cut $p_t^2/Q^2 < 2$, and using an integration cutoff $\kappa_0'^2 = 1$ GeV^2, then for three choices of normalization $z_0 = 0.5,\ 0.4,\ \&\ 0.35$ we find, for a separation $R_{cut} = 1.7$, the ratio of 2:1 forward jet cross sections is 3.3% for all z_0 values. Similarly, for a second choice of jet separation $R_{cut} = 2.0$ we find the ratio is, again for all z_0, 2.9%. The value R_{cut} determines the minimum separation required in pseudo rapidity(η)-azimuth(φ) space between the two emitted jets for them to be resolved as individual objects (see section 4.3.2). Thus as expected, we see that the ratio of the two jet rates is independent of the normalization used, and we can assume the approximations made above will not determine the final results. To a first approximation, we can neglect the effects of the box contributions to the cross sections as the information required, at least for the ratios of the jet rates, is contained in the bottom half of the diagram of Figures 4.1 and 4.12.

From the above discussion it is clear that the absolute normalization of the BFKL equation is still much of an unknown quantity and there are certain ambiguities that arise through theoretical computation such as; what are the "correct" integration limits in the box calculation to take or, which observable (F_2, σ) should we use to determine the best values of z_0? At present there is no answer to the normalization problem, although the latest calculation of the NLO $\ln 1/x$ effects of the BFKL equation may go some way to answering this question in the future.

The ambiguity of the normalization prompted this study of jet ratios rather than calculation of absolute magnitudes of the cross sections in order to remove, as fully as possible, these problems. However, by essentially fitting the DIS plus 1 forward jet data, the normalization is fixed and we can now make predictions for other quantities such as cross sections of the 2 forward jet rate. To a first approximation, allowing for the simplifications made above, this should provide a good indication of the magnitudes of the cross sections.

In summary, for this study there is no one answer as to which normalization is the best, and the choice of normalization that will be used throughout in the following sections is

$$\kappa_0'^2 = 1 \text{ GeV}^2 \text{ and } z_0 = 0.5\ . \tag{4.17}$$

[3]For calculation and results of DIS + 2 forward jet cross sections, see section 4.3. A discussion of the stability of the 2:1 forward jet cross sections will be given in greater detail in section 4.5.

4.2.4 BFKL predictions versus experiment

In the previous sections we have seen the cuts required to define the allowed experimental phase space for forward jet production at HERA (section 4.2.2) and the choice of normalization that will be used (section 4.2.3), thus, we can now present the DIS + 1 forward jet cross section results using the BFKL formalism.

Recall that the fully integrated cross section is obtained by substitution of the solved BFKL equation (4.15) into (4.3) and (4.1) with the integration limits subject to the restrictions of section 4.2.2. The resulting cross sections for one forward jet events, comparing the theoretical results with the published H1 data are shown in Figures 4.9 and 4.10.

Figure 4.9 shows the cross section for integrated x bins of size 5 x10^{-4} and a minimum transverse momentum cut $\mu = 3.5$ GeV of the forward jet. It also indicates the importance of the experimental phase space cuts on the measured cross sections.

It is worth exploring here the importance of the kinematical cut y of (1.1) on the cross sections in the very small x regions. The upper cut on y is imposed to remove background arising from radiative corrections and electron resolution, and so is quite often chosen conservatively. Using the cut $y < 0.5$, as used in section 3.4.2 for the exclusive jet cross sections, and the normalization $z_0 = 0.5$ (solid curve) gives a good description of the data, but we notice a deficiency in the cross section for the smallest x bin, $0.0005 < x < 0.001$ compared with the central data point. The importance of this upper phase space cut can now be seen. This deficiency is removed if we allow a slightly larger phase space bounded by $y < 1$ (Figure 4.6), as shown by the dashed line. It is this larger $y < 1$ cut that is shown in Figure 4.8 to fix the normalization for the smallest x bin of section 4.2.3. However, if we move to the next smaller x bin, $0.0001 < x < 0.0005$, this depletion in the cross section is observed even for the larger y cut value; we see a turnover in the production rates. The importance of these phase space cuts on the very small x region can be seen more clearly for the DIS including 2 forward jet cross sections, see section 4.4, where the lower constraint ($y < 0.5$) actually produces a turnover in the cross section for the small x bin (0.0005-0.001). For the 1-jet case this bin still shows an increase in the cross section. The DIS + 2 forward jet cross sections will be discussed in detail from section 4.3 onwards.

Figure 4.10 also shows the DIS + 1 forward jet cross section but for the larger integra-

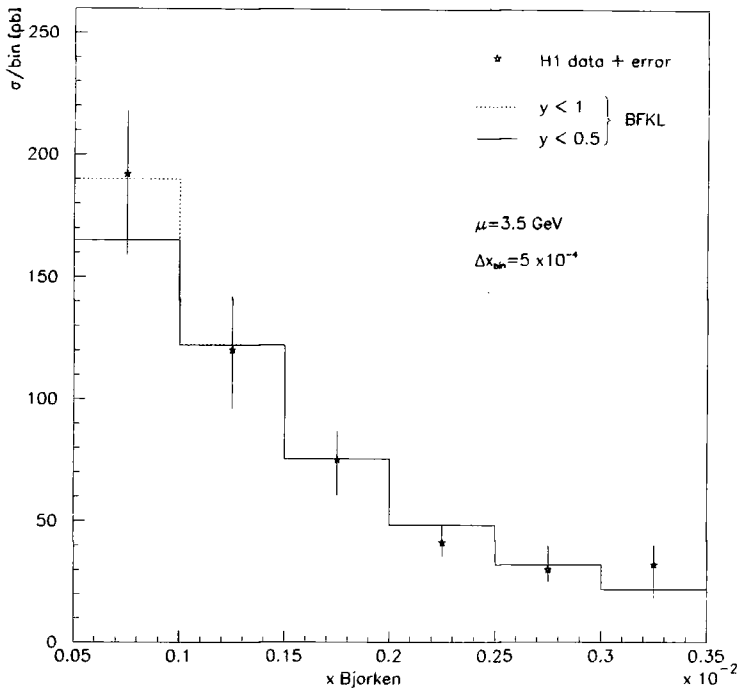

Figure 4.9: DIS + 1 forward jet cross section calculated for a minimum transverse momentum of emitted jet $p_{Tjet} > 3.5$ GeV, and x bin size $\Delta x5$ x10^{-4}, in comparison with H1 experimental DIS + 1 forward jet data. The resummed (unresolved and virtual radiation) BFKL kernel is normalized with $z_0 = 0.5$, for $y < 0.5$ (solid line) and $y < 1$ (dotted line).

tion x bins of size 1.5 x10^{-3} for different choices of the minimum transverse momentum cuts; $p_{Tjet} > \mu = 3.5$, 5 and 6 GeV. These are shown for the cut $y < 0.5$. The horizontal lines show the experimental data error bands with the BFKL result given by the solid star. The results for the larger x bins $(0.002 - 0.0035)$ show very good agreement with experiment for all momentum cuts. For the lower cut $\mu = 3.5$ GeV, the results in the smaller x bin $(0.0005 - 0.002)$ agree well with the central data values. Recall, the normalization was fixed for the kinematic cut $\mu = 3.5$, in section 4.2.3, so we would expect good agreement, but, for the higher cuts $\mu = 5$ and 6 GeV in the smallest x bins, the calculated cross sections are rising with the prediction for $\mu = 6$ GeV lying above the data error bars. However, it is this very small x region in which the normalization is so difficult to fix. Here the BFKL solution rises steeply and is very sensitive to the phase space cuts imposed. Applying the larger phase space cut of $y < 1$ increases the cross sections in the smaller x bin by approximately 25, 20 and 10 pb for the cuts $\mu = 3.5$, 5

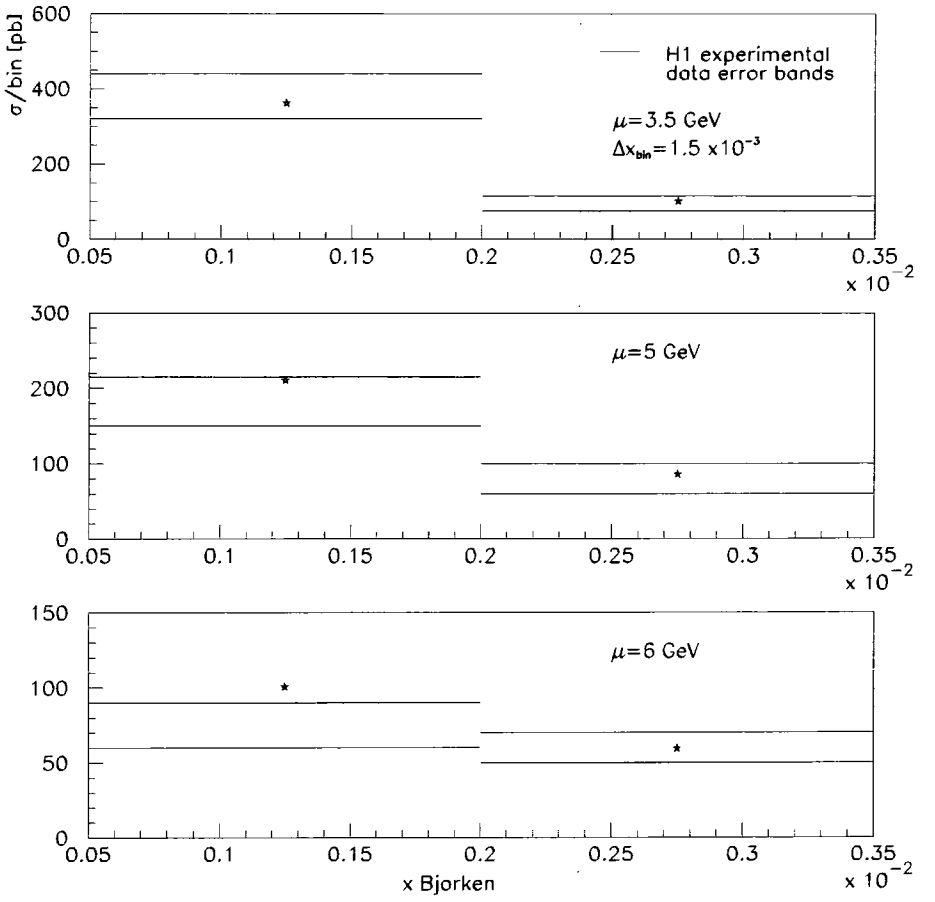

Figure 4.10: Same as Figure 4.9 but for different values of minimum transverse momentum of the forward jet, ($p_{Tjet} > 3.5,\ 5,\ 6$ GeV), and for larger integrated integrated x bins of size $1.5\text{x}10^{-3}$ with cut $y < 0.5$.

and 6 GeV respectively, which is still in reasonable agreement with experiment.

Using the slightly different kinematical cuts for forward jet event selection as presented in [67], we can again compare the BFKL prediction with the data. This is shown in Figure 4.11 for the explicit cuts

initial state energies :	$E_e = 26.7$ GeV and $E_p = 820$ GeV
scattered electron cuts :	$160° < \theta_{e'} < 173°$
	$E_{e'} > 12$ GeV
	$0.1 < y < 1$
forward jet cuts :	$6° < \theta_j < 20°$

$$\begin{aligned} p_{Tjet} &> 5 \text{ GeV} \\ x_{jet} &> 0.025 \\ 0.5 &< p_T^2/Q^2 < 4 . \end{aligned} \tag{4.18}$$

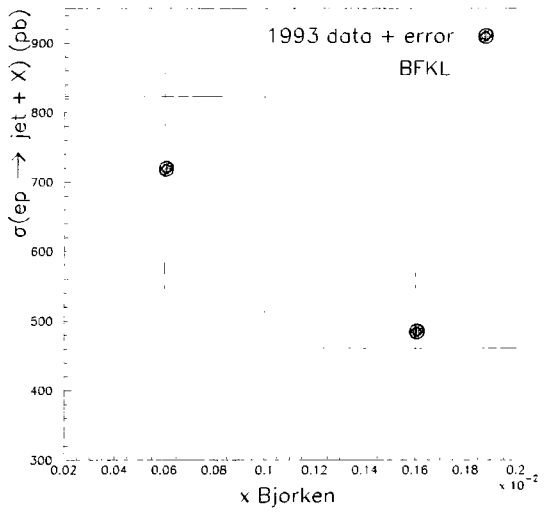

Figure 4.11: DIS + 1 forward jet cross sections showing the 1993 HERA data with the kinematic and phase space cuts of (4.18) for the two x bins $\Delta x = (0.0002 - 0.001)$ and $(0.001 - 0.002)$. The solid line shows the corresponding BFKL prediction using the normalization $z_0 = 0.5$ of section 4.2.3.

Within the large experimental errors we again see good agreement of the data with the BFKL expectation for the cross sections.

Overall, we can conclude that there is good agreement of theory with experiment for different kinematical cuts. In the next section, we will use the the basis of this calculation, with the inclusion of an extra resolved gluon jet and our normalization of (4.17), to predict the production of DIS events including two forward jets at HERA.

4.3 Two forward jet production at HERA

In the previous section we have seen that equations (4.3) and (4.15) using the BFKL resummation of soft gluon emission successfully describe the data for DIS + 1 forward jet

production. We now want to modify this by extending the BFKL formalism to include emission of an extra jet in the forward direction. The kinematics of the process $\gamma^* + p \longrightarrow jet_1 + jet_2 + X$ is illustrated in Figure 4.12, where the second jet is identified as real *resolved* gluon emission from the BFKL ladder chain. By resolved we require that the emitted gluon

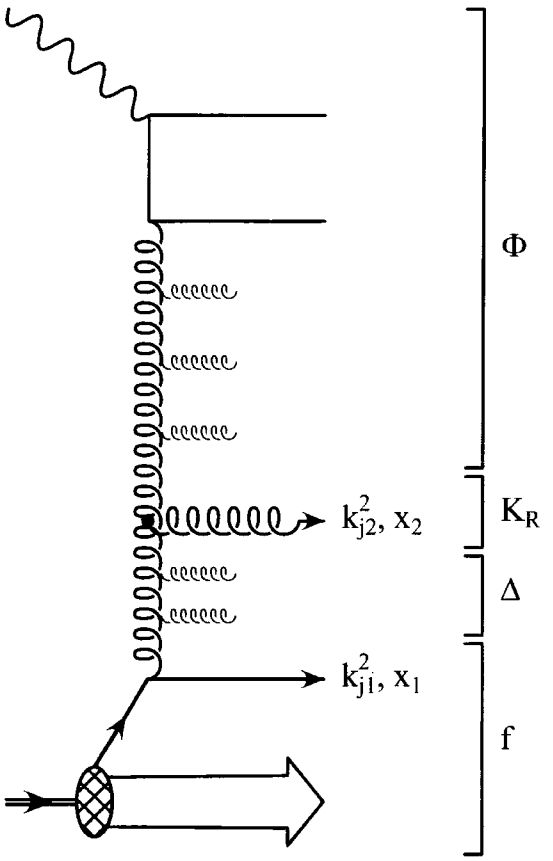

Figure 4.12: Diagramatic representation of a deep-inelastic event containing 2 forward jets. The first forward jet is as for Figure 4.1, carrying longitudinal and transverse momenta $x_1 P$ and k_{j1}^2 respectively. The second forward jet originates from a resolved ($p_{Tjet} > \mu$) gluon from the BFKL chain, carrying momenta $x_2 P$ and k_{j2}^2. Soft gluon radiation is represented by the thin gluon lines. Here we also allow soft gluon radiation between the two forward jets described by the resummed BFKL kernel Δ of (3.19).

has a transverse momentum greater than some minimum cut, i.e. $k_{j2}^2 > p_{T_{min}}^2 = \mu^2$. This is exactly the same as for the 1 forward jet case. Labelling the kinematic variables of the forward jets as 1 and 2, with the 2nd jet referring to that of the real gluon emission from the BFKL ladder, then the differential cross section for two forward jet production

is obtained from the cross section of (1.9) as

$$\frac{d\sigma}{dxdQ^2dx_1dk_{j1}^2dx_2dk_{j2}^2} =$$

$$\frac{4\pi\alpha^2}{xQ^4}\left[(1-y)\frac{\partial F_2}{\partial x_1\partial k_{j1}^2\partial x_2\partial k_{j2}^2}+\frac{1}{2}y^2\frac{\partial F_T}{\partial x_1\partial k_{j1}^2\partial x_2\partial k_{j2}^2}\right]. \qquad (4.19)$$

4.3.1 Differential structure functions for 2 forward jets

Figure 4.12 diagramatically shows how the differential structure functions for 2 forward jet production are built from the components of the 1 jet structure function with modifications arising from the emission of a single real gluon from the BFKL ladder.

Symbolically, by identifying the individual contributions, we can write for the structure functions i

$$F_i = \Phi_i \otimes K_R \otimes \Delta \otimes f \qquad (4.20)$$

where as before for the one forward jet emission, Φ_i contains knowledge of the BFKL soft gluon radiation in which evolution is started from the driving term of the box diagram; this takes the same form as (4.10). Again f describes the ("first") emitted jet arising from a parton; $q, \overline{q}$ or g, within the proton which is given by the effective sum of all parton momenta of (4.5).

The presence of a second forward jet arises when we emit a real gluon from the BFKL ladder of Figure 4.12. The 2-jet structure function is then obtained by the modification of the one jet differential structure function by the inclusion of a real emission kernel term, K_R, as shown in the diagram. The requirement that this real gluon have some minimum transverse momentum for it to be resolved as a jet in the final state will be implemented through kinematic cuts on the phase space limits of the integrals for the integrated cross section in the numerical computation. The second forward jet need not be emitted from the bottom of the gluon ladder, there can still be more soft gluon radiation emitted between the two forward jets. This is the origin of the Δ term shown in Figure 4.12 which resums the unresolved and virtual gluon emissions. However, as we shall see in section 4.3.4, this "extra" BFKL summation is not necessary and will be omitted for the final DIS + 2 forward jet results presented in this thesis. In the following sections we will study the inclusion of this resummed gluon emission between the two forward jets, and by physical considerations of the allowed phase space argue that it is not required. This

is fortunate, as the inclusion of this extra BFKL term produces numerical computation problems when the $\ln 1/x$ evolution is started from the initial boundary condition of the delta function $\Delta^{(0)} = \delta(k_1^2 - k_2^2)$. This will be discussed in sections 4.3.4 & 4.3.5.

Notation for 2 forward jet variables

Before presenting the explicit mathematical form for the 2 forward jet structure functions it is useful to define the notation that will be used in this section. This is summarized in Figure 4.13.

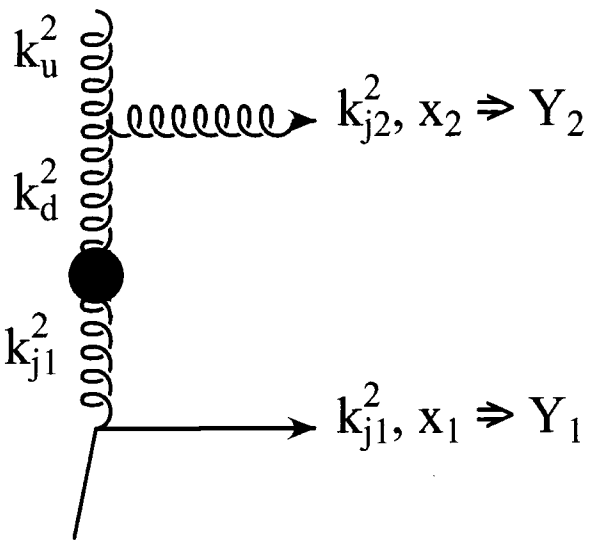

Figure 4.13: Kinematic variable definitions for DIS + 2 forward jets.

Figure 4.13 shows the emission of the two forward jets. The first jet originates from the proton and is labelled by its transverse momentum k_{j1}^2 and the longitudinal momentum fraction x_1. Similarly, the second jet is labelled by k_{j2}^2 and x_2.

We will again work with the rapidity variable Y defined as

$$Y_1 = \ln\left(\frac{x_1}{x}\right) \quad \text{and} \quad Y_2 = \ln\left(\frac{x_2}{x}\right) \tag{4.21}$$

such that the difference

$$Y_1 - Y_2 = \ln\left(\frac{x_1}{x_2}\right) .$$

It is important to remember that the quantity $Y_1 - Y_2$ is not the rapidity gap between the two emitted jets as the full expression for rapidity also includes the jet transverse momentum.

In Figure 4.13 the black dot represents the resummation of the soft real, and virtual gluon emissions from the gluon propagator between the two jets. This is described in our notation by Δ in Figure 4.12. Δ is dependent on the momenta of the gluons spanning the blob, and the rapidity variable difference between the two jets, i.e.

$$\Delta = \Delta(k_{j1}^2, Y_1 - Y_2, k_d^2) \, .$$

In the presence of soft gluon emission between the 2 forward jets then $k_d^2 \neq k_{j1}^2$.

The labels k_d^2 and k_u^2 refer to the t-channel gluon transverse momentum, below (down) and above (up) the real emitted gluon producing the second jet. We have the relation

$$k_u^2 = (\boldsymbol{k}_d + \boldsymbol{k}_{j2})^2 \, , \tag{4.22}$$

which, due to the angular dependence between the vectors $\boldsymbol{k}_d$ and $\boldsymbol{k}_{j2}$ means the angular integrations of the structure functions are non-trivial.

Note: In the following the individual transverse momenta of the forward jets are labelled k_{j1}^2 and k_{j2}^2. For discussions applying to either jet or both jets, e.g. kinematic cuts which apply equally to both jets, then the general term p_T^2 will be used.

Angular definitions

For completeness, the definitions of the azimuthal angles of the jets are shown in Figure 4.14, where we define the first forward jet to lie along the x-axis.

The individual momentum vectors have the azimuthal angles φ_1, φ_2 and φ_d for the 1st jet, 2nd jet and down momentum vectors respectively. However, not all of these angles are independent and we have the following relations

$$\begin{aligned} \varphi_{1d} &= |\varphi_1 - \varphi_d| \\ \varphi_{2d} &= |\varphi_2 - \varphi_d| \\ \varphi_{12} &= |\varphi_2 - \varphi_1| \, , \end{aligned} \tag{4.23}$$

and

$$\varphi_{12} = \varphi_{1d} + \varphi_{2d} \, . \tag{4.24}$$

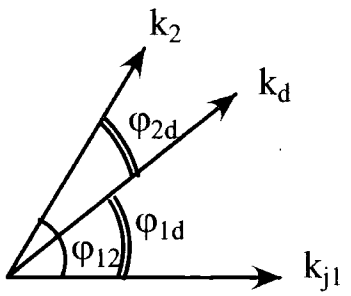

Figure 4.14: Azimuthal angles of the emitted jets.

2-jet differential structure functions including soft gluon radiation

From the identification of the different components of the structure function as shown in Figure 4.12, and using the notation of Figure 4.13, we can write down the explicit form for the 2 forward jet structure function as

$$\frac{\partial F_i}{\partial Y_1 \partial Y_2 \frac{\partial^2 k_{j1}}{\pi} \frac{\partial^2 k_{j2}}{\pi}} = \overline{\alpha}_s(k_{j1}^2) \sum_a x_1 f_a(x_1, k_{j1}^2) \frac{1}{k_{j1}^4} \int \frac{d^2 k_d}{\pi} \left[\Delta(k_{j1}^2, Y_1 - Y_2, k_d^2) \right.$$
$$\left. \times \quad \overline{\alpha}_s(k_{j2}^2) \frac{k_d^2}{k_u^2 k_{j2}^2} \Phi_i(k_u^2, Y_2, Q^2) \right] . \qquad (4.25)$$

The running scale dependence of α_s is taken as the transverse momenta of the emitted jets and the $1/k^4$ behaviour associated with jet emission is clearly seen for the first jet in the $1/k_{j1}^4$ term. The ratio of the BFKL vertex function, $k_d^2/k_u^2 k_{j2}^2$, is just the real gluon BFKL emission kernel denoted by K_R in Figure 4.12. We again see here the $1/k^4$ behaviour, this time for the 2nd jet emission. (4.25) is written using the variable Y where we have used the replacement

$$x \frac{\partial}{\partial x} \rightarrow \frac{\partial}{\partial Y}$$

in (4.19).

Explicitly showing the azimuthal dependence of (4.25) then

$$\frac{\partial F_i}{\partial Y_1 \partial Y_2} = \int \frac{d^2 k_{j1}}{\pi} \frac{d^2 k_{j2}}{\pi} \frac{d^2 k_d}{\pi} \left[\overline{\alpha}_s(k_{j1}^2) \sum_a x_1 f_a(x_1, k_{j1}^2) \right.$$
$$\left. \Delta(k_{j1}^2, Y_1 - Y_2, k_d^2) \frac{\overline{\alpha}_s(k_{j2}^2)\ k_d^2}{k_{j1}^4 \cdot k_u^2\ k_{j2}^2} \Phi_i(k_u^2, Y_2, Q^2) \right] , \qquad (4.26)$$

and using

$$\int d^2 k \rightarrow \frac{1}{2} \int dk^2 \int_0^{2\pi} d\varphi ,$$

we can write

$$\frac{\partial F_i}{\partial Y_1 \partial Y_2} = \frac{1}{(2\pi)^3} \int dk_{j1}^2 dk_{j2}^2 dk_d^2 d\varphi_1 d\varphi_{12} d\varphi_{2d} \left[\overline{\alpha}_s(k_{j1}^2) \sum_a x_1 f_a(x_1, k_{j1}^2) \right.$$
$$\left. \Delta(k_{j1}^2, Y_1 - Y_2, k_d^2) \frac{\overline{\alpha}_s(k_{j2}^2)\ k_d^2}{k_{j1}^4\ k_u^2\ k_{j2}^2} \Phi_i(k_u^2, Y_2, Q^2) \right] \quad (4.27)$$

where the angles are defined in Figure 4.14. From (4.27) we see the azimuthal dependence on φ_1, and also φ_{12}, is trivial and we lose a factor $(2\pi)^2$ on integration in the above. However, due to the presence of the term $k_u^2 = (\boldsymbol{k}_d + \boldsymbol{k}_{j2})^2$, which brings in a dependence on φ_{2d}, the azimuthal integration over this variable is non-trivial and we obtain the differential structure function for the 2 forward jet process

$$\frac{\partial F_i}{\partial Y_1 \partial Y_2 \partial k_{j1}^2 \partial k_{j2}^2} = \frac{1}{2\pi} \int dk_d^2 \int_0^{2\pi} d\varphi_{2d} \left[\frac{\overline{\alpha}_s(k_{j1}^2) \sum_a x_1 f_a(x_1, k_{j1}^2)\ \overline{\alpha}_s(k_{j2}^2)}{k_{j1}^4\ (k_d^2 + k_{j2}^2 + 2k_d k_{j2} \cos(\varphi_{2d}))\ k_{j2}^2} \times \right.$$
$$\left. \Delta(k_{j1}^2, Y_1 - Y_2, k_d^2)\ \Phi_i((k_d^2 + k_{j2}^2 + 2k_d k_{j2} \cos(\varphi_{2d})), Y_2, Q^2) \right] \quad (4.28)$$

The differential structure function (4.26) has a trivial dependence on the angles φ_1 and φ_{12}. However, the calculation of the fully integrated cross section imposing all kinematical and phase space cuts will generate a non-trivial dependence on φ_{12}. This is due to the requirement of a separation cut in η, φ space of the two emitted jets which will allow them to be resolved as individual objects in the detector (see Equations (4.31) and (4.32)).

4.3.2 DIS + 2 forward jet cross sections

The two forward jet cross section is readily obtained by the substitution of (4.26) into (4.19) which gives

$$\sigma_{2jet} = \int dx \int dQ^2 \int dY_1 \int dY_2 \frac{4\pi\alpha^2}{xQ^4} \left[(1-y) \frac{\partial F_2}{\partial Y_1 \partial Y_2} + \frac{1}{2} y^2 \frac{\partial F_T}{\partial Y_1 \partial Y_2} \right]$$
$$= \int \frac{dx}{x} \frac{dQ^2}{Q^4} dY_1\ dY_2 \frac{dk_{j1}^2}{k_{j1}^4} \frac{dk_{j2}^2}{k_{j2}^2} dk_d^2\ d\varphi_1\ d\varphi_{12}\ d\varphi_{2d} \frac{4\pi\alpha^2}{(2\pi)^3}$$
$$\times \left\{ \overline{\alpha}_s(k_{j1}^2) \sum_a x_1 f_a(x_1, k_{j1}^2)\ \overline{\alpha}_s(k_{j2}^2) \frac{k_d^2}{k_u^2} \Delta(k_{j1}^2, Y_1 - Y_2, k_d^2) \right.$$
$$\left. \times \left[(1-y) F_2(Y_2, k_u^2, Q^2) + \frac{1}{2} y^2 F_T(Y_2, k_u^2, Q^2) \right] \right\} . \quad (4.29)$$

Equation (4.29) gives the explicit form of the DIS + 2 forward jet cross section. This will be used as the master equation to which we will apply different cuts and approximations and will lead to the equation for the 2-jet cross section of (4.37) from which we will obtain the final 2-jet, and ultimately the ratio of 2:1, forward jet cross sections.

Kinematic cuts for the 2 forward jet cross sections

The integrated cross section of (4.29) is obtained subject to the imposition of the experimental cuts required for forward jet event selection. These are identical to those imposed on the DIS + 1 forward jet cross section as discussed in 4.2.2, with the addition that the kinematic cuts on the forward jet are also applied identically to the 2nd jet. Thus, we have the extra restrictions

$$\begin{aligned} & E_{jet2} > 28.7 \text{ GeV} \\ & 7^\circ < \theta_{j2} < 20^\circ \\ & p_{Tjet2} > \mu = 3.5,\ 5 \text{ or } 6 \text{ GeV} \\ & \max[\mu^2, Q^2/2] < p^2_{Tjet} < 2Q^2 \\ & x_2 > 0.035\ . \end{aligned} \tag{4.30}$$

By imposing these constraints on the 2nd jet, which must be satisfied simultaneously with the 1 forward jet cuts, we drastically limit the available phase space for jet production. This will suppress 2 forward jet emissions and we would expect to see only small cross sections for the DIS + 2 forward jet process.

The identification of a 2nd jet in the forward region of the detector requires one other cut. We have to ensure that the two emitted jets are sufficiently separated in the detector for them to be resolved as individual objects and not combined experimentally to form one broad jet. If we only impose the cuts of section 4.2.2 with the additional restrictions of (4.30), this gives the "absolute" DIS + 2 forward jet cross section. In the following results this will be calculated and compared with the cross sections where we impose a cut on the separation of the jets to observe the effect of this experimental resolution.

Experimentally an observed jet will lie in a cone of certain radius R, defined in pseudo rapidity-azimuth (η, φ) space as

$$R = \sqrt{\left[(\Delta\eta^2) + (\Delta\varphi^2)\right]}\ . \tag{4.31}$$

Typically $R = 0.7$ or 1, with the larger the cut, the smaller the observed rate of higher numbers of jets. Conversely, the smaller the value of R, the more likely it is that an event will contain multiple jets. For the identification of 2 forward jets, the angular separation between them is defined in terms of the variable R, such that we place a cut on the

minimum separation of the axes of the two jet cones. This requires the cut

$$R_{cut} \geq 2R \tag{4.32}$$

for successful detection of two individual objects. This can be seen diagramatically in Figure 4.15. Experimentally, $R_{cut} \gtrsim 1.7$[71].

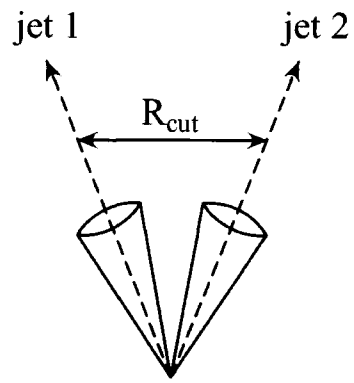

Figure 4.15: Schematic diagram of the separation cut between two emitted jets for identification of individual objects. R_{cut} is required to be greater than $2R$ where R is the radius of the jet cone.

For the theoretical cross section calculations we will cut on the η, φ space of the two partons producing the forward jets, where the pseudo-rapidity is obtained from

$$\eta = -\log\left(\tan\frac{\theta}{2}\right)$$

and θ is the angle of the jet with respect to the proton direction. Recall that we have the restriction $7° < \theta < 20°$ for the identification of forward jets at HERA. The value of θ for a given jet configuration can be calculated from the relations of (1.1), (1.6) and (1.7) for a given set of kinematic variables under the integration of (4.29).

In the following we will show results for the DIS + 2 forward jet cross sections for values of $R_{cut} = 0,\ 1,\ 1.5,\ 1.7$ and 2.

4.3.3 2 Forward jets including BFKL gluon resummation

We will now use the master equation of (4.29) to obtain an expression for the DIS + 2 forward jet cross section including the presence of soft gluon radiation between the two forward jets.

If we neglect imposing a cut on the separation of the emitted jets, then the azimuthal dependences of φ_1 and φ_{12} are both trivial and we can perform the two azimuthal integrations to produce a factor $4\pi^2$. However, if we include the cut (4.32) on the separation of the two jets, then the quantity $\Delta\varphi$ of (4.31) is just given by φ_{12}. Thus, this integration in (4.29) becomes non-trivial. We still have the integration over φ_1 producing a factor 2π.

We can write the explicit form for the 2-jet cross section, including kinematic cuts (4.30) and (4.32) as

$$\begin{aligned}\sigma_{2jet} &= \frac{4\pi\alpha^2}{(2\pi)^2}\int_{xbin}\frac{dx}{x}\,\frac{dQ^2}{Q^4}\,dY_1\,dY_2\,dk_{j1}^2\,dk_{j2}^2\,dk_d^2\int_0^{2\pi}d\varphi_{12}\,d\varphi_{2d} \\ &\times \left\{\overline{\alpha}_s(k_{j1}^2)\sum_a x_1 f_a(x_1,k_{j1}^2)\,\overline{\alpha}_s(k_{j2}^2)\,\frac{k_d^2}{k_{j1}^4 k_{j2}^2 k_u^2}\,\Delta(k_{j1}^2, Y_1 - Y_2, k_d^2)\right. \\ &\times \left.\left[(1-y)F_2(Y_2,k_u^2,Q^2) + \frac{1}{2}y^2 F_T(Y_2,k_u^2,Q^2)\right]\right\}\,, \qquad (4.33)\end{aligned}$$

where the integration limits of the kinematic variables are determined by the specific x_{bin} studied, i.e. we have $Q^2(x), Y_i(x), k_i^2(Q^2(x))$. The dependence on φ_{12} appears in the restrictions for the allowed kinematic phase space and φ_{2d} is contained in

$$k_u^2 = k_d^2 + k_{j2}^2 + 2k_d k_{j2}\cos(\varphi_{2d})\,.$$

The BFKL resummed gluon radiation is contained in $\Delta(k_{j1}^2, \tilde{Y}, k_d^2)$ which is given by the operator Δ of (3.19) acting on the delta function i.e.

$$\Delta = e^{(\tilde{Y}K_{UV})} \otimes \delta^2(k_{j1} - k_d)\,.$$

Equation (4.33) is solved numerically using the methods of section 3.3.

4.3.4 Omitting the BFKL kernel

If we consider what the production of two jets in the forward direction of the proton at HERA implies, then we can make an approximation which will simplify the 2-jet cross section of (4.29). The presence of 2 forward jets will require that the longitudinal momentum fraction of *both* jets satisfy the relation

$$x_2 \leq x_1 \sim \mathcal{O}(1)\,, \qquad (4.34)$$

such that neither jet enters the small x region and ensures that we do not enter the strongly ordered configuration of $x_2 \ll x_1 \sim \mathcal{O}(1)$. We impose soft ordering of the jets

$x_2 < x_1$. Essentially, through the tight restrictions which require that both jets be emitted into a very small phase space region (4.30), and from (4.34) we do not expect that there will be a large rapidity difference between the emitted jets, then we can assume that there will be little opportunity for the emission of a significant amount (if any) of gluon radiation. Thus, we can neglect (soft) gluon radiation between the jets and approximate the Δ term of (4.29) by the two dimensional delta function

$$\Delta = \delta^2(\boldsymbol{k}_{j_1} - \boldsymbol{k}_d) \, . \tag{4.35}$$

This is equivalent to the removal of the black blob in Figure 4.13, i.e. we have that $\boldsymbol{k}_{j_1} = \boldsymbol{k}_d$.

Thus, in the absence of gluon radiation between the jets we can write (4.29) as

$$\begin{aligned} \sigma_{2jet} \;=\; & \frac{4\pi\alpha^2}{(2\pi)^2} \int_{xbin} \frac{dx}{x} \frac{dQ^2}{Q^4} \, dY_1 \, dY_2 \, dk_{j1}^2 \, dk_{j2}^2 \, d^2k_d \int_0^{2\pi} d\varphi_1 \, d\varphi_{12} \\ & \times \left\{ \overline{\alpha}_s(k_{j1}^2) \sum_a x_1 f_a(x_1, k_{j1}^2) \, \overline{\alpha}_s(k_{j2}^2) \, \frac{k_d^2}{k_{j1}^4 k_{j2}^2 k_u^2} \, \delta^2(\boldsymbol{k}_{j_1} - \boldsymbol{k}_d) \right. \\ & \times \left. \left[(1-y) F_2(Y_2, k_u^2, Q^2) + \frac{1}{2} y^2 F_T(Y_2, k_u^2, Q^2) \right] \right\} \, , \end{aligned} \tag{4.36}$$

in which we can perform the implicit integrals over k_d^2 and φ_{2d} through the presence of the two dimensional delta function. This gives the result

$$\begin{aligned} \sigma_{2jet} \;=\; & \frac{4\pi\alpha^2}{2\pi} \int_{xbin} \frac{dx}{x} \frac{dQ^2}{Q^4} \, dY_1 \, dY_2 \, dk_{j1}^2 \, dk_{j2}^2 \int_0^{2\pi} d\varphi_{12} \\ & \times \left\{ \overline{\alpha}_s(k_{j1}^2) \sum_a x_1 f_a(x_1, k_{j1}^2) \, \overline{\alpha}_s(k_{j2}^2) \, \frac{1}{k_{j1}^2 k_{j2}^2 k_u^2} \right. \\ & \times \left. \left[(1-y) F_2(Y_2, k_u^2, Q^2) + \frac{1}{2} y^2 F_T(Y_2, k_u^2, Q^2) \right] \right\} \, , \end{aligned} \tag{4.37}$$

where now

$$k_u^2 = k_{j1}^2 + k_{j2}^2 + 2k_{j1}k_{j2}\cos(\varphi_{12}) \, .$$

Equation (4.37) is also evaluated numerically using the Chebyshev approximation methods of section 3.3.

Numerical predictions - with and without the BFKL kernel Δ

The numerical predictions of the DIS + 2 forward jet cross sections, using both methods for the inclusion and omission of the soft gluon radiation are shown in Figure 4.16 for two

choices of kinematic cut $p_T^2/Q^2 < 2,\ 5$. The minimum transverse momentum of the jets is set to $\mu = 3.5$ GeV.

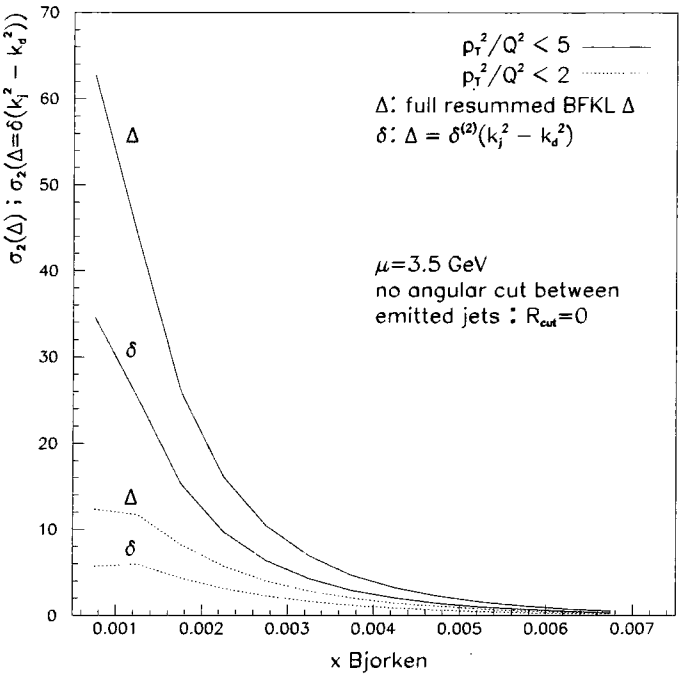

Figure 4.16: DIS + 2 forward jet cross sections for two choices of kinematic cut $p_T^2/Q^2 < 2, 5$ shown by the dotted and dashed lines respectively. The increase of the cross sections can be seen when we include soft gluon radiation between the two emitted jets (Δ) when we solve (4.33) above the approximation when we allow no radiation between the jets (δ) for the solution of (4.37). These are shown for the minimum transverse momentum cut $\mu = 3.5$ GeV and $y < 0.5$ and for no separation between the jets - i.e we show the "absolute" 2 forward jet predictions.

In both cases we see that the relaxation of the kinematic constraint $p_T^2/Q^2 < 2 \rightarrow 5$ produces a large rise in the 2 jet cross section (see section 4.4.1). However, the surprising feature is the large increase in the cross sections between the results with and without the inclusion of the extra gluon radiation. The ratio between the two cross sections $(\sigma(\Delta)/\sigma(\delta))$, for both kinematic cuts, is ~ 1.5 for $x \sim 10^{-3} - 10^{-2}$, but is actually larger with a factor of two difference in the small x region of $\sim 10^{-4}$. Since we would expect very little gluon radiation between the emitted jets, we would expect the resummed BFKL kernel to produce a much smaller increase of the cross section over the approximation in which we allow no gluon radiation between the jets.

4.3.5 Choosing the "correct" DIS + 2 forward jet description

As mentioned previously, we do not expect a substantial amount of gluon radiation to be emitted between the two forward jets due to tight restrictions of the allowed rapidity phase space. But we are observing at least a factor 2 increase in the cross sections when we include the BFKL kernel Δ, as given by (4.33), over the numerical result when we omit the gluon radiation, as given by (4.37) - see Figure 4.16. Which description do we believe gives the correct result?

Recall, for the two jets to both be emitted in the forward direction of the proton then rapidity differences between them $(Y_1 - Y_2)$ may be small. The formalism of the BFKL equation as used in this thesis holds for the approximation of large Y. That is, if we consider the *full* (analytic) form of the BFKL equation then we have[23, 62]

$$f = \frac{1}{2\pi}\sum_m e^{im\varphi}\frac{1}{2\pi}\int_{-\infty}^{\infty}\frac{d\nu}{\nu^2+\frac{1}{4}}\exp\left[\frac{2\alpha_s C_A}{\pi}\Re e\left(\Psi(1)-\Psi((m+1)/2+i\nu)\right)\right] \qquad (4.38)$$

from which we see that the *full* azimuthal dependence of the BFKL equation is given by the summation over all azimuthal projections m in the exponential $\exp(im\varphi)$. For large rapidity values of Y then the BFKL equation is, to good approximation, given by the first azimuthal projection $m = 0$. This gives us the BFKL equation as discussed in chapter 2.

For one forward jet emission then we have large rapidities and the equation of (4.10), as used in this analysis, gives a good description of the BFKL gluon. However, we require two jets to be emitted in a very small rapidity phase space, $x_2 \lesssim x_1 \sim \mathcal{O}(1)$, which would imply that the rapidity variable difference $Y_1 - Y_2$ (related to x_i through (4.21)) can be small. Thus, the approximation of using only the $m = 0$ term in the above may not hold true when we deal with the insertion of the BFKL gluon radiation term Δ between the forward jets of (4.33). To give the full azimuthal dependence of the BFKL kernel in our formalism we would need to make the modification that the BFKL kernel of (3.19) becomes

$$\Delta = \sum_m \Delta^m(k_1^2, k_2^2)e^{im\varphi_{12}} \qquad (4.39)$$

where the notation refers to general momentum vectors 1 and 2 spanning the blob (Δ) of Figure 4.13. That is, the $\exp(im\varphi_{12})$ introduces an extra $\cos(\varphi_{12})$ term (from considering the real parts only) into the computation of the BFKL kernel. However, initial studies including this extra azimuthal dependence appear to produce only very small reductions in the magnitude of the BFKL solution which cannot explain the large (factors of 2)

differences we are seeing. This inclusion of the extra φ dependence does however solve one of the numerical mysteries we encountered during this analysis, in that the kernel solution Δ at first (for small Y values) decreases before the onset of the expected BFKL increase of the gluon distribution with decreasing x. With the inclusion of say $m = 10$ terms in the summation of (4.39), this decrease at small Y is removed.

Thus, the inclusion of the extra azimuthal projections does not appear to explain the large increase of the 2 forward jet cross sections when we include soft gluon radiation between the jets.

Other serious problems were encounterd in the numerical computation of equation (4.33). For the 1 forward jet cross section the BFKL gluon evolution is started from the input of the quark box of the $\gamma^* g \rightarrow q\bar{q}$ fusion process and is contained in the term Φ_i. However, when we wish to insert an extra BFKL kernel corresponding to the resummation of soft gluon radiation between the two forward jets, to numerically compute this term we have to start evolution from an input of the delta function $\delta(k_1^2 - k_2^2)$. This makes the Chebyshev expansion of the k^2 dependence of the BFKL solution unstable. We observe large oscillating tails away from the delta function peak $k_1^2 = k_2^2$ which can make the final results dependent on the number (N) of Chebyshev nodes used in the approximation (e.g. for small values of $N \sim 10 - 20$). To remove the above problem and to obtain results for the numerical computation of (4.33) we note that the momentum vector k_d does not appear in the final state and we can approximate the integration $\int dk_d^2$ as a summation over the Chebyshev nodes. This produces the stable result as shown in Figure 4.16. However, these problems were also encountered when we made an initial investigation of two forward jet production at the TEVATRON in $p\overline{p}$ collisions[49, 72]. This also requires the insertion between the two jets of the BFKL gluon Φ numerically solved from the delta function input. In this case we still have not been able to control the stability of the cross section solutions as the variables of integration are those of the jets in the final state. Here the problem is also enhanced due to the large energy scale ($\sqrt{s} = 1.8$ TeV) allowing jets to have larger transverse momenta than those at HERA. We are required to model a larger range of k^2 values for $\Delta(k_1^2, Y, k_2^2)$ which enhances the problems of the oscillating tails away from the delta function equality $k_1^2 = k_2^2$ using the Chebyshev approximation.

In conclusion, the modelling of the BFKL gluon distribution when we only have evolution from an input of the delta function is very difficult to achieve numerically using

the Chebyshev techniques of this thesis. For the deep inelastic scattering case at HERA this problem has been overcome and stable results achieved. However, we feel that the magnitudes of the two jet cross section as shown in Figure 4.16 for the inclusion of the extra BFKL soft gluon radiation is too large - we see a *very* large enhancement over the delta function contribution. In the above discussions it has not been possible to pinpoint the cause of the large increase we are observing between the 2 forward jet cross sections when we include gluon radiation between the jets and when we omit this radiation (in the limit $Y \to 0$ the two results should be equal!). The discrepancy is probably due to some problem in the numerical calculation which we have been unable to detect. However, the argument that we do not expect much gluon radiation between the two jets from the phase space considerations is perfectly valid, thus, this is the form we will assume gives the "correct" description of the DIS + 2 forward jet structure function and cross section. We will now use this to predict the ratios of 2:1 jet production in the forward region at HERA.

4.4 Numerical predictions for DIS + 2 forward jets at HERA

We will now present predictions for DIS events including 2 forward jets for the kinematic phase space at HERA using the BFKL formalism to describe the gluon distributions but neglecting emission of soft gluon radiation between the two forward jets. The cross section results for 2 forward jet rates, using Equation (4.37), are shown in Figures 4.17 and 4.20.

In this section we will explore the sensitivity of the 2 forward jet cross section to changes of the phase space and kinematical constraints. That is, we will study the effect of the cut y on the magnitudes of the cross section in the very small x region and the increase of the cross section when we relax the constraint $p_T^2/Q^2 < 2$ in the definition of a forward jet. Here we will observe the effect of these cuts. In the following section (4.5) we will make a closer examination of these cuts and discuss their validity in relation to (preliminary) experimental observation.

Figure 4.17 shows the fully integrated cross section (in pb) for x bins of size $\Delta x = 5\times10^{-4}$ and $\mu = 3.5$ GeV with $y < 0.5$ for the two choices of cut $p_T^2/Q^2 < 2$ and $p_T^2/Q^2 < 5$

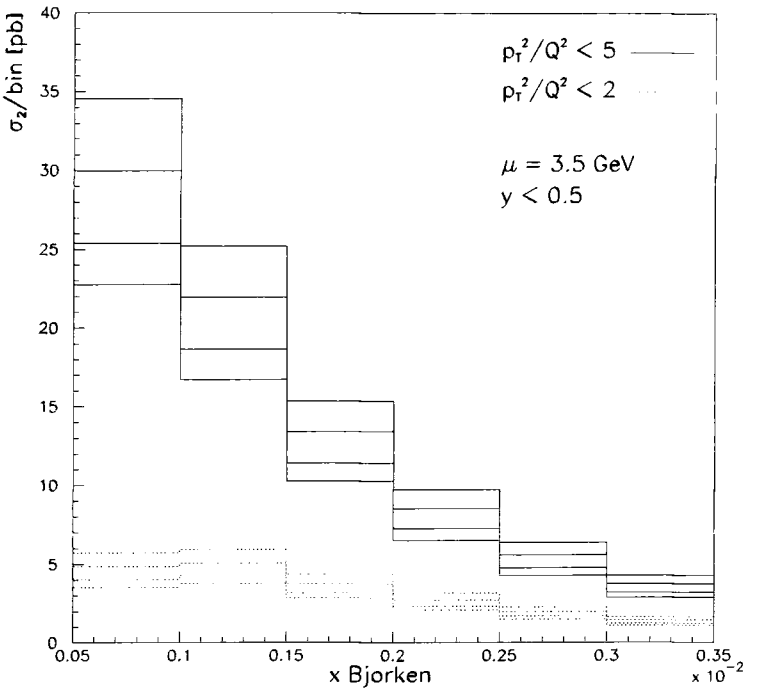

Figure 4.17: DIS + 2 forward jet fully integrated cross sections using the same x bins as for the DIS + 1 forward jet results. σ_2 is plotted for $p_{Tjet} > 3.5$ GeV for two choices of upper cut on the transverse momenta; $p_T^2/Q^2 < 2$ and $p_T^2/Q^2 < 5$ (dashed and solid sets of curves respectively), for four different cuts on the minimum separation between the 2 forward jets i.e. $(R > \sqrt{[(\Delta\eta^2) + (\Delta\varphi^2)]})$, for R=0, R=1, R=1.7 and R=2 with $y < 0.5$. The smaller the separation cut, the higher the cross section.

for cone separations[4]; $R = 0$, 1, 1.7 and 2. Two striking effects can be seen here. First, for the lower curves which have the cut $p_T^2/Q^2 < 2$, there is a turnover in the cross section for the smallest x bin. This effect has two origins; a) The allowed momenta of the two jets can only vary between $\max[\mu^2, Q^2/2]$ and $p_T^2/Q^2 < 2$ thus restricting the p_T^2 of the jet to low values of Q^2. The effect is removed when we relax the constraint to say, $p_T^2/Q^2 < 5$ and b) the cut $y < 0.5$. When the larger x, Q^2 phase space is implemented allowing $y < 1$, the reduction in the cross section at very small x is also eliminated. Increasing the phase space to $y < 1$ produces a corresponding increase in the cross sections for the higher kinematic constraint $p_T^2/Q^2 < 5$. This dependence of the DIS + 2 forward jet cross section for the small x bin $0.0005 - 0.001$ on the phase space cut y can be found in Table 4.1.

[4]For simplicity we will use the notation $R_{cut} = R$ for the separation of the jets in the following

	σ_2 in pb			
	$p_T^2/Q^2 < 2$		$p_T^2/Q^2 < 5$	
R	$y < 0.5$	$y < 1$	$y < 0.5$	$y < 1$
0	5.7	7.2	34.6	39.6
1	4.9	6.2	30.0	34.5
1.7	4.0	5.1	25.4	29.0
2	3.6	4.6	22.8	26.2

Table 4.1: Dependence on phase space cut y for the DIS + 2 forward jet cross section with $\mu = 3.5$ GeV and small x bin=$\Delta x = 0.0005 - 0.001$.

The second interesting feature is that for the higher kinematical cut, $p_T^2/Q^2 < 5$, we observe a significant increase in the cross section over the result for the lower cut. For the DIS + 1 forward jet process, when we relax the above kinematical constraint we obtain an increase in the cross section by a factor of ~ 2.5 for the small x bin $0.0005 - 0.001$, which is reduced to a factor of ~ 1.5 for the largest x bin. Similarly for the DIS + 2 forward jets cross section we would expect some increase as we allow a larger range of jet momentum values to be identified as a forward jet, however, we would expect this increase to be balanced by the fall off in higher jet multiplicities as we allow larger p_T^2 of the jets. For the 2 forward jet case, the predicted increase is by a factor ~ 5.5 for the bin $\Delta x = 0.0005 - 0.001$, and ~ 2.5 for $\Delta x = 0.003 - 0.0035$. An explanation for this large increase can be found if we inspect Figure 4.18.

4.4.1 Relaxing the kinematic cuts

Figure 4.18 shows the differential DIS + 2 forward jet p_T^2 spectrum, where we constrain $k_{j1}^2 = k_{j2}^2$ for an integrated x bin $= 0.001 - 0.0015$. The plot shows the differential 2-jet cross section with respect to dk_{j1}^2 and dk_{j2}^2 for fixed Q^2 versus p_T^2/Q^2 for $\mu = 3.5$ GeV. The Q^2 dependence is indicated by the different curves. When we make the cut $p_T^2/Q^2 < 2$, i.e. we essentially draw a vertical line at $p_T^2/Q^2 = 2$ and remove all contributions to the right of this line, then we remove a substantial contribution to the cross section from the low Q^2 region. By cutting at $p_T^2/Q^2 = 5$ we immediatly see that there are large contributions now included to the fully integrated cross section from the low Q^2 region. This effect is enhanced by the jet resolution cut $p_T^2 > \mu^2$, which requires the cross section to be zero when $\mu^2/Q^2 < 2$ as indicated by the vertical arrows in the bottom

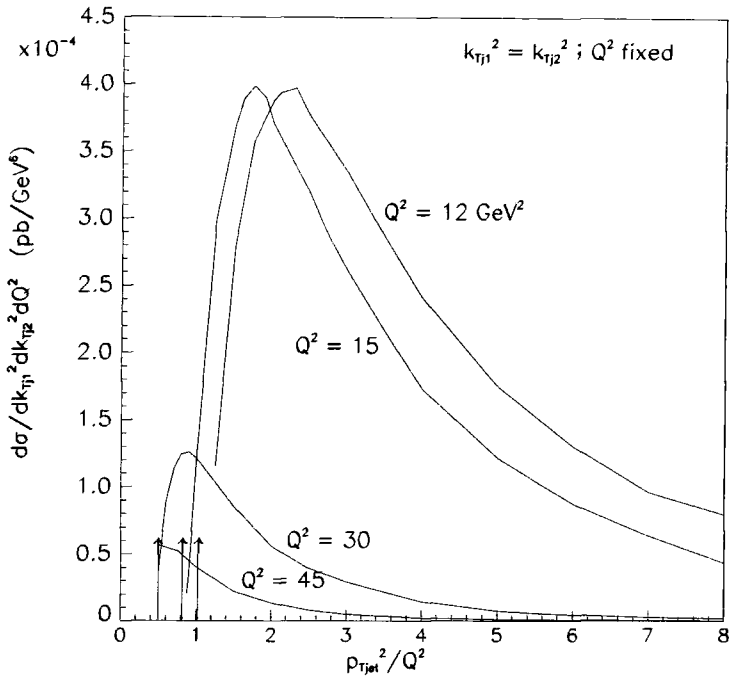

Figure 4.18: p_{Tjet} spectrum for DIS + 2 forward jets. The differential cross section, for fixed Q^2, is plotted versus p_T^2/Q^2 for $k_{j1}^2 = k_{j2}^2$, for a single x bin $(0.001 - 0.0015)$, $R = 0$ and $p_{Tjet} > 3.5$ GeV. Lower momentum cutoffs are indicated by the vertical arrows in the bottom left hand corner of the plot.

left hand corner of the plot. These limits occur above the lower bound $p_T^2/Q^2 = 1/2$ for both $Q^2 = 15$ and 12 GeV^2 for $\mu = 3.5$ GeV. Thus the resolution constraint has significant impact at the lower values of Q^2. This, together with the large contribution from the low Q^2 region, causes the large increase in the cross sections between the lower and higher kinematical cuts $p_T^2/Q^2 < 2$ and $p_T^2/Q^2 < 5$. It is interesting to note that the peak for the p_T^2 distribution of the low Q^2 contribution occurs for $p_T^2/Q^2 \sim 2$. Thus, in relaxing the constraint from $p_T^2/Q^2 < 2$ (the experimental cut), to say $p_T^2/Q^2 < 3$ or 4 should also produce a significant increase in the 2 forward jet cross section, and correspondingly an increase in the ratio of the 2:1 forward jets. This dependence of the DIS + 2 forward jet cross section on the kinematical constraint can be seen in Figure 4.19 for x bins of size $\Delta x = 0.0005$ for no separation cut between the jets ($R = 0$), and $y < 1$. The decrease in cross section due to phase space cuts is clearly seen in the lowest x bin $0.0001 - 0.0005$ for all kinematic cuts (c.f. DIS + 1 forward jet results). By increasing the upper limit $p_T^2/Q^2 < 2 \rightarrow n$ the momentum phase space of the jets becomes asymmetric.

However, calculation of cross sections for different lower cuts Q^2/n, where $n = p_T^2/Q^2$, shows this asymmetry does not have a large effect on the cross section. This is due to the lower momentum constraint being dependent also on the minimum transverse cut μ, ie $p_T^2 > \max[\mu^2, Q^2/n]$. It is important to remind ourselves that these large increases for the cross sections are calculated at the parton level. Experimentally corrections to the data are required at both the hadron and parton levels for accurate comparison of theory and experiment. Unfortunately, losses due to hadronization effects are strongly dependent on the Monte Carlo models used which may produce difficulties in measuring the large increases we predict in the cross sections. This will be discussed in section 4.5.

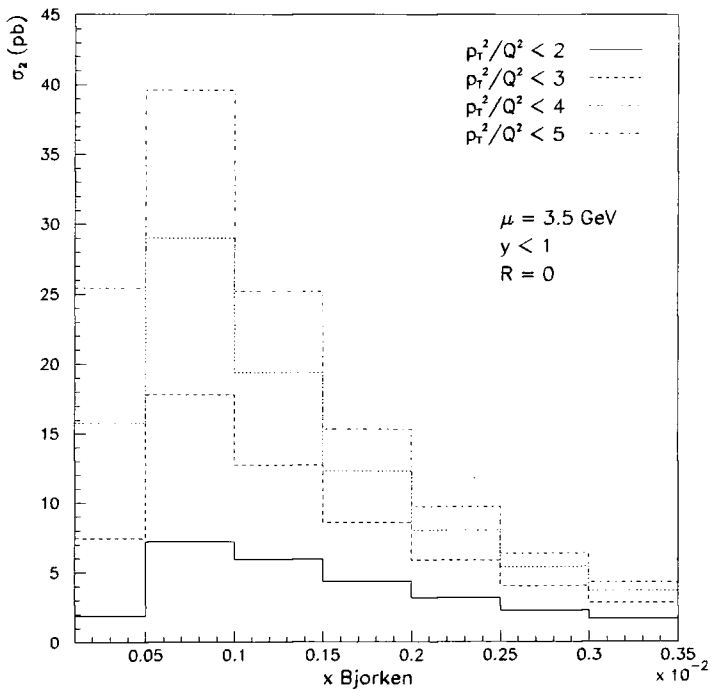

Figure 4.19: DIS + 2 forward jet cross section (in pb) dependence on kinematical constraint $p_T^2/Q^2 < n$, for no separation constraint between the two jets and $y < 1$.

The 2-jet cross sections, this time for larger integrated x bins and different values of the minimum transverse jet momentum μ, are shown in Figure 4.20 for both $p_T^2/Q^2 < 2$ (Fig.(a)) and $p_T^2/Q^2 < 5$ (Fig.(b)). The large increase in the cross section with change of kinematic constraint is readily observed, e.g. for the cut $\mu = 3.5$ GeV, $y < 0.5$ and an experimental cone separation $R = 1.7$, the cross section increases from 11.5 to 55.6 pb in

the lowest x bin, and from 5.3 to 15.3 pb for the higher x bin - similar effects are observed for all $p_{Tjet} > \mu$ cuts. However, as we have larger x bins than in Figure 4.17, the increase in cross section is less marked when the y cut is loosened to $y < 1$, with the cross sections for the x bin $0.0005 - 0.002$ rising by approximately $1pb$ and $3pb$ for the cuts $\mu = 3.5$ & 5 GeV respectively for both $p_T^2/Q^2 < 2,\ 5$. For the larger transverse jet momentum $\mu = 6$ GeV this increase falls to $\sim$ 0.5 & $1pb$ for the respective kinematic cuts p_T^2/Q^2. Figure 4.20 also shows the dependence on the 2 forward jet cross section when we vary the cone separation from a value of $R = 0$ (the "absolute" 2 forward jet cross section) to $R = 2$. As we expect, the larger the cone separation cut, the greater the reduction in magnitude

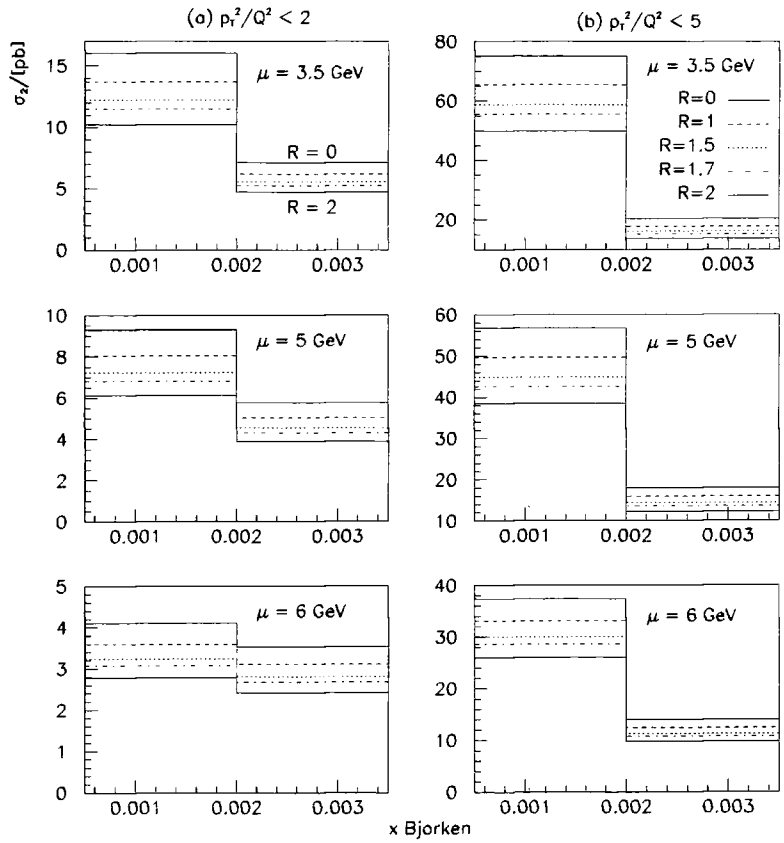

Figure 4.20: Same as for Figure 4.17 but for larger x bins and different minimum p_{Tjet} cuts with $y < 0.5$.

of the 2 forward jet cross section in relation to the absolute cross section. However, it is interesting to note that these predictions show that the relaxation of the kinematic cut $p_T^2/Q^2 < n$ should produce a greater increase of the observed 2-jet cross sections than in trying to resolve jets with smaller and smaller cone radii which is experimentally difficult.

Ratio of 2:1 forward jet cross sections at HERA

Recall, to calculate the DIS + 2 forward jet cross section we first fitted the BFKL solution of the DIS + 1 forward jet cross section to H1 forward jet data (section 4.2.3) and used the parameter z_0 to make predictions for the 2 jet cross section; thus, an interesting quantity to study is the ratio of the 2:1 DIS + forward jet rates in which any ambiguities through approximations we have made will be reduced. Because the BFKL functions Φ_i are common to both the single and two jet cross sections, taking the ratio of the $\sigma_{2\text{jet}}/\sigma_{1\text{jet}}$ rate in which the Φ_i's will essentially cancel, gives us a measure of the BFKL vertex function (K_R of Figure 4.12). Figures 4.21 and 4.22 plot the 2:1 forward jet cross sections for the two choices of kinematical constraint as earlier, for four choices of the experimental cone separation R = 0, 1, 1.7 & 2 (Figure 4.21), and for a larger range including R = 1.5 in Figure 4.22. Figure 4.22 also shows the dependence of the ratio

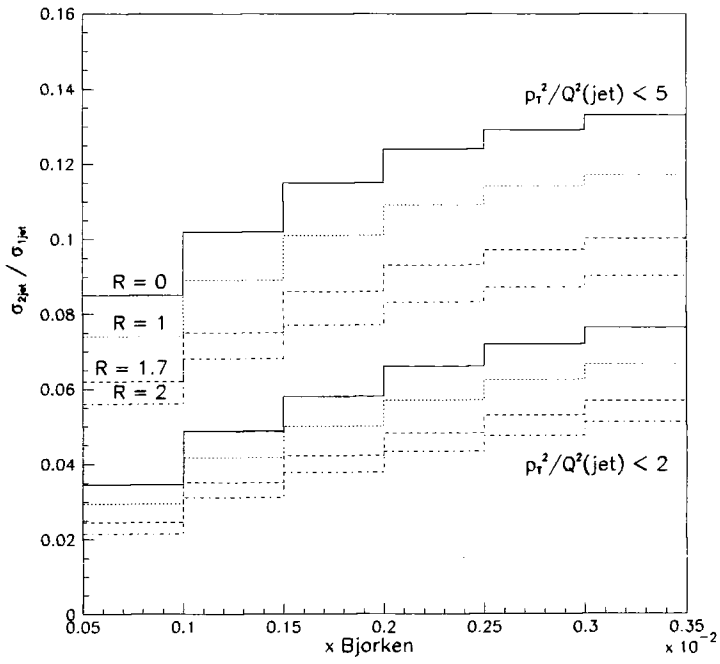

Figure 4.21: Ratio of the 2:1 DIS + forward jet cross sections for x bins of size 0.0005, and $p_{Tjet} > 3.5$ GeV for the four selected cone separation cuts as in Figure 4.17 and $y < 0.5$. Shown for two choices of upper momentum cut, $p_T^2/Q^2 < 2$ (lower four curves) and $p_T^2/Q^2 < 5$ (upper four curves).

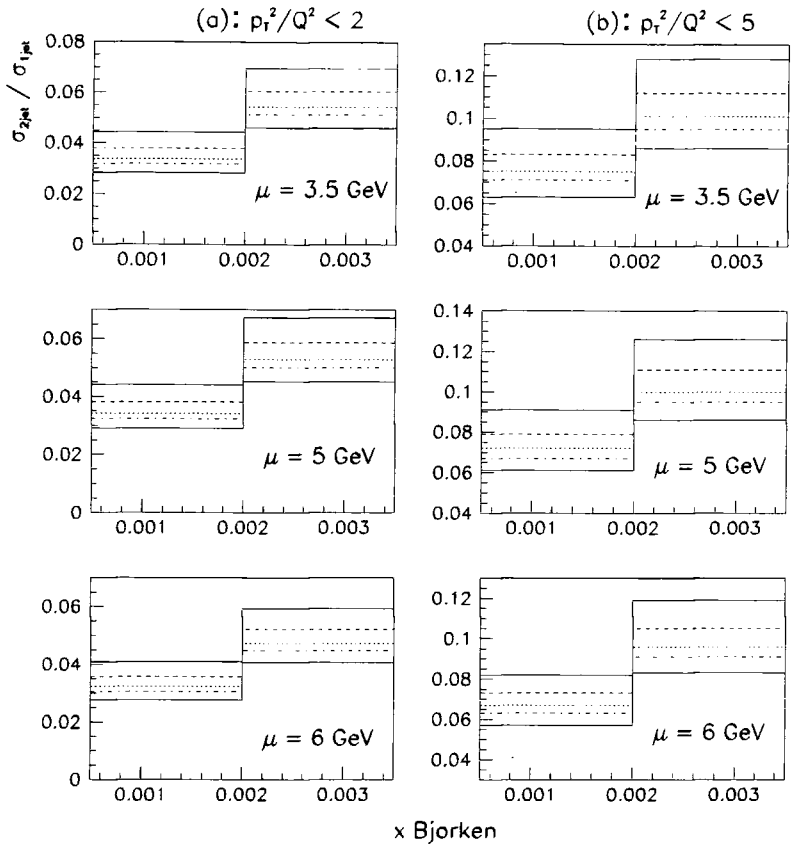

Figure 4.22: Ratio of the 2:1 DIS + forward jet cross sections for x bins of size 0.0015, and for different values of $p_{Tjet} > 3.5$, 5, 6 GeV with $y < 0.5$. Ratios are given for cone separations of $R > 0$ (upper solid curve), $R > 1$, $R > 1.5$, $R > 1.7$ and $R > 2$ (lower solid curve), and two choices of upper transverse momentum cuts, $p_T^2/Q^2 < 2$ given in column (a), and $p_T^2/Q^2 < 5$, column (b).

on the jet resolution parameter μ (but using larger x bins). We note that the fraction is rather insensitive to the value of the jet resolution μ, see Figure 4.22(a). These plots allow us to investigate the effect of the experimental kinematic and phase space cuts on the observed jet rates.

The 2-jet cross section increased significantly with the relaxation of the cut $p_T^2/Q^2 < 2$ to $p_T^2/Q^2 < 5$ (Figures 4.17 and 4.20). In the case of the 2:1 forward jet ratio of the cross sections we observe an increase by a factor of $\sim 2 - 2.5$ for the smallest integrated x bins (dependent on the x integration range), and ~ 1.8 for larger x bins. We also see that the ratio shows an increase as we move from lower to higher values of x. This results from the imposition of the ordering $x_2 < x_1$ of the two emitted jets which means that

the reduction of the cross section due to decreasing evolution length is less for 2 forward jets than for single jet production. The effect of increasing the phase space cut $y < 0.5$ to $y < 1$ produced a rise in the magnitudes of the DIS + 2 jet cross section for the small x bin $0.0005 - 0.001$. When we take the ratio of the 2:1 jet rates this corresponds to an increase of only $\sim 1\%$ for the cut $p_T^2/Q^2 < 2$ and falls to $\sim 1/10\%$ with the cut $p_T^2/Q^2 < 5$, i.e. we find the ratio is insensitive to changes in phase space cuts. For completeness, the dependence on y for the small x region is shown in Table 4.2 for the HERA experimental jet separation cuts $R = 1.7$ & 2.

	R = 1.7				R = 2			
μ	$p_T^2/Q^2 < 2$		$p_T^2/Q^2 < 5$		$p_T^2/Q^2 < 2$		$p_T^2/Q^2 < 5$	
GeV	y $\leq .5$	y ≤ 1	y $\leq .5$	y ≤ 1	y $\leq .5$	y ≤ 1	y $\leq .5$	y ≤ 1
3.5	3.2	3.5	7.1	7.1	2.8	3.1	6.3	6.4
5	3.2	3.6	6.7	6.9	2.9	3.2	6.1	6.2
6	3.1	3.4	6.3	6.4	2.7	3.1	5.7	5.8

Table 4.2: Kinematic (p_T^2/Q^2) and phase space (y) dependence on the ratio of 2:1 forward jets in the small x bin $\Delta x = 0.0005 - 0.002$.

Azimuthal signatures of BFKL dynamics in 2 forward jet processes

A characteristic feature of the BFKL chain is that soft gluon emission produces an angular decorrelation of jets, such that, two jets which would normally be produced "back-to-back" in azimuth space will be emitted at some angle $\neq 180°$. This has been of interest for some time, especially for jet production in collisions at the $p\overline{p}$ collider the TEVATRON as well as at HERA (see for example [47, 49, 72]), as a method of searching for signatures of BFKL dynamics. Thus, it is interesting to look at the azimuthal dependence of the two forward jets at HERA arising through the term $\Phi_i(k_u^2(\varphi), Y_2, Q^2)$ in the description of the structure functions. Due to the lack of k_T-ordering the k_u gluon of Figure 4.13 can bring significant transverse momentum into the two jet system and hence considerably broaden the back-to-back peak in the azimuthal distribution $\Delta\varphi = \varphi_1 - \varphi_2$.

Here we present results for the azimuthal dependence of the DIS + 2 forward jet cross section. The differential cross section with respect to $d\Delta\varphi$ is shown in Figure 4.23 for both choices of kinematical cuts p_T^2/Q^2 and a minimum transverse momentum $\mu = 3.5$ GeV.

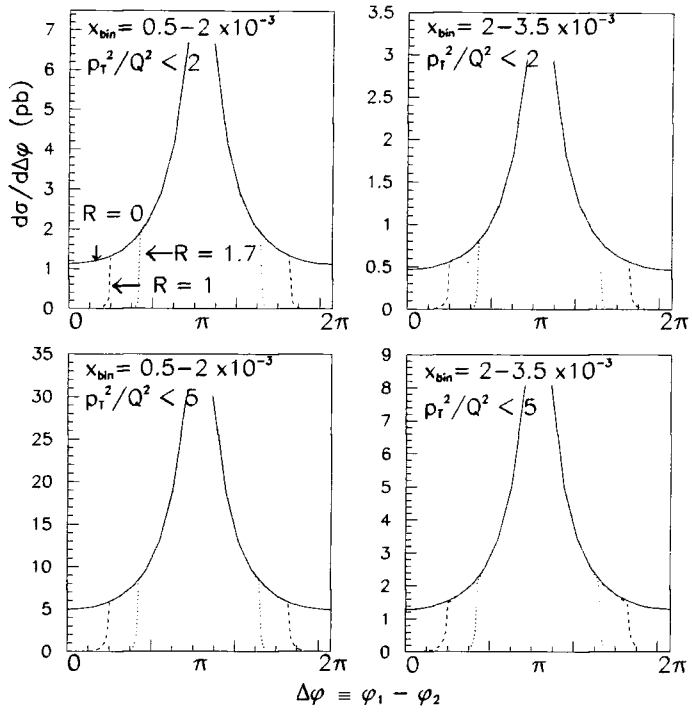

Figure 4.23: Azimuthal dependence of DIS + 2 forward jet cross section plotted for two choices of x bin for each $p_T^2/Q^2 < 2,5$ cut and $y < 0.5$. The dependence on the minimum cone separation is given for R=0, R=1 and R=1.7.

We predict a peak in the distribution at $\Delta\varphi = \pi$. However, in order to remove the infrared $k_T^2 \to 0$ infinities in the BFKL equation we impose the cut $k_T^2 = k_{j1}^2 + k_{j2}^2 > 1$ GeV^2. This, together with the ambiguity due to hadronization, means that the distributions near the back-to-back configuration cannot be predicted. Rather it is the tails of the distribution which will charaterize the lack of k_T ordering.

We impose the separation cuts $R = 0,\ 1\ \&\ 1.7$, the effects of which are clearly noticeable as a cut-off of the tails of the distributions. Unfortunately this jet separation cut, which is likely to be $R \gtrsim 1.7$, will effectively remove the whole of the tail of the distribution (see Figure 4.23). The azimuthal decorrelation is thus unlikely to be a way of identifying the small x dynamics.

4.5 Accuracy of the theoretical predictions

Let us now return to the discussion of DIS + 2 forward jet cross sections and see if we can obtain a feeling for the accuracy of the predictions that were presented in section 4.4. Recall that the unintegrated BFKL gluon distribution has no constraint on its normalization other than the magnitude of the DIS including 1 forward jet cross section was fixed to agree with the experimental data. The normalization chosen was a cut-off $\kappa_0'^2 = 1$ GeV^2 in the box integration and a matching point $z_0 = 0.5$. However, a different choice of cuts can reproduce the same 1 forward jet cross section magnitude (see Figure 4.8). With the present accuracy of experimetal errors, no one choice of normalization is better than another.

In our formalism, the magnitude of the 2 forward jet cross section is directly dependent on the magnitude of the 1 forward jet cross section, and so affected by the choice of normalization used. Unfortunately, at present there is no published DIS + 2 forward jet cross sectional data that the above predictions can be compared with to give a straightforward check of the accuracy of our calculations. Although below in section 4.5.2 a discussion of the validity of these results will be given in the light of initial studies of the 2 forward jet rates observed at HERA.

4.5.1 Stability of numerical results with change of normalization

The BFKL functions Φ_i are common to both the single and two forward jet rates, see (4.3) and (4.25). Thus the ambiguities in our calculation due to numerical approximations should be reduced in the prediction of the ratio $\sigma_{2jet}/\sigma_{1jet}$. Before discussing further the results of the calculation it is useful to first check how sensitive the individual cross sections are to variations of the normalization z_0, and more importantly, how insensitive the ratio of the jet cross sections is to these changes. The following ratios were presented in section 4.2.3 in the discussion of the normalization of the BFKL gluon. Here we will split the contributions to the ratio into the individual 1 and 2 forward jet cross section components to observe the variations in the magnitudes of the cross sections for each quantity.

The magnitude of the two forward jet cross section is also dependent on the separation

cut between the jets as well as the choice of normalization for the BFKL gluon distribution. In table 4.3 the ratios of the 2:1 forward jet cross sections at HERA are shown for two choices of experimental separation cuts $R = 1.7$ and $R = 2$, for a selection of normalization parameters z_0. The integrated x range corresponds to the region $\Delta x = 0.0001 - 0.004$ for a momentum cut $\mu = 3.5$ GeV and $p_T^2/Q^2 < 2$ with the smallest $Q^2(x)$ values constrained by $0.1 < y < 1$. See (4.40) for a list of the full kinematic cuts.

	σ(1jet) *pb*	σ(2jet) *pb*		σ(1jet)/σ(2jet)	
z_0		R = 1.7	R = 2	R = 1.7	R = 2
0.35	520	16.9	15.1	0.033	0.029
0.4	553	18.0	16.1	0.033	0.029
0.5	611	20.1	17.9	0.033	0.029

Table 4.3: Ratio of 2:1 forward jet cross sections in DIS events at HERA to show its sensitivity to changes in the normalization of the BFKL gluon distribution. See text for exact phase space parameters used.

As expected we observe an increase in the magnitudes of the individual jet cross sections with increasing z_0, i.e. we allow a longer evolution length for the BFKL equation. In changing from a starting point $z_0 = 0.35$ to $z_0 = 0.4$ there is an approximate 6.5% increase in the DIS + 1 forward jet cross section, and approximately a 10% increase in changing from $z_0 = 0.4$ to $z_0 = 0.5$. However, this increase in the 1 forward jet cross section is exactly matched by a corresponding increase in the 2 forward jet cross section, thus proving that the 2 forward jet rate in our formulation is directly controlled by the BFKL contribution to the 1 forward jet cross section. This is a good check of the numerics since we have omitted any soft gluon radiation between the two forward jets. The result is that the ratio of the 2:1 forward jet cross section is independent of the choice of normalization used (see columns 5 & 6 of Table 4.3) as expected. Thus, the results for the cross sectional ratios are stable to any ambiguities in our normalization of the BFKL gluon and will not be affected even if the experimental data for the 1-jet cross section, to which we fixed the normalization, is modified at some later date.

This stability of the ratios allows us to assume the approximation made of not including charm contributions to the quark boxes of Figures 4.1 and 4.12, is to first order valid, as the "interesting" information for forward jet production in ep scattering is contained at the "proton end" of the diagrams. Of course, for reliable predictions of the absolute

magnitudes of cross sections the inclusion of heavy quarks to the box diagrams is important. Thus, we can assume the values for the calculated ratios of 2:1 DIS + forward jet cross sections presented in section 4.4 and 4.5.2 are accurate even with our numerical simplifications.

4.5.2 Comparison of forward jet events with data

In the publication of forward jet rates in DIS events at HERA [67], the first experimental estimates of the ratio have been made, but so far only to give an indication of the size of the effect. A value of approximately 4% is quoted for the ratio of 2-jet/1-jet events for the slightly different choice of kinematic cuts than those in section 4.2.2. The DIS including 1 forward jet data has already been compared with our cross section calculation (see Figure 4.11) for the relevant experimental cuts of (4.18). We observe good agreement of the one forward jet cross sections for the different x bins. Applying the same phase space and kinematic cuts to the 2 forward jet cross section we obtain the results $\sigma_{2\text{jet}} = 45.7\ pb$ for an x bin $\Delta x = 0.0002 - 0.001$ and, $\sigma_{2\text{jet}} = 38.9\ pb$ for the bin $\Delta x = 0.001 - 0.002$. This gives, for each x bin, a ratio for the 2:1 forward jet cross sections of $\sigma_{2\text{jet}}/\sigma_{1\text{jet}} = 0.055,\ 0.084$ respectively. These are calculated for a jet separation cut $R = 2$. Thus, for the forward jet phase space region at HERA, for the kinematic cuts of (4.18) we find that $\sim 6.6\%$ of DIS events including a forward jet should contain 2 jets in the forward region. This is in the "ball park" of the experimental observation and provides encouragement for the validity of our 2 forward jet calculation presented for the different experimental cuts of section 4.2.2 in which we predict that the ratio of 2:1 forward jet cross sections lie in the range $\sim 2 \rightarrow 4\%$ with increasing Bjorken x for the experimental cut $R = 2$ and kinematical constraint $p_T^2/Q^2 < 2$ (see Figure 4.21).

We have also seen in section 4.4.1 a large increase in the magnitude of the 2 forward jet cross section when we relax the kinematic constraint p_T^2/Q^2 from $2 \rightarrow 5$ (see Figures 4.17 and 4.19). This would indicate that experimentally a relaxed cut of $p_T^2/Q^2 < 5$ should greatly increase the observed 2 forward jet cross sections.

In the previous sections a large sample of numerical predictions for forward jet production at HERA has been presented. This was to investigate the effects of the many different phase space and kinematical cuts and to investigate the x dependence of the observable quantities in order to see possible signatures of BFKL dynamics. Unfortunately,

the measurement of 2 forward jets at HERA is difficult due to very low statistics, thus, the observation of a dependence on the kinematic variables x and Q^2 is, at the present time, not practical. For a possible comparison of our results with experiment at some later date, we should look at the forward jet region of HERA as a whole.

Jet cross sections in the forward region at HERA

Let us consider the full experimental forward jet region as measured by H1 and calculate the ratio of 2:1 forward jets. We will consider the experimental phase space bounded by the explicit parameters

$$\begin{aligned}
\text{initial state energies :} \quad & E_e = 27.5 \text{ GeV and } E_p = 820 \text{ GeV} \\
\text{scattered electron cuts :} \quad & 160^\circ < \theta_{e'} < 173^\circ \\
& E_{e'} > 11 \text{ GeV} \\
& 0.1 < y < 1 \\
\text{forward jet cuts :} \quad & 7^\circ < \theta_j < 20^\circ \\
& p_{T\,jet} > 3.5 \text{ GeV} \\
& x_{jet} > 0.035 \\
& 0.5 < p_T^2/Q^2 < 2 \,. \qquad (4.40)
\end{aligned}$$

Using these constraints we obtain the cross section for the DIS + 2 forward jet process for the single x bin $\Delta x = 0.0001 - 0.004$ as

$$\begin{aligned}
\sigma_{\text{2jet}} &= 20.1 \; pb \text{ for } R = 1.7 \\
\sigma_{\text{2jet}} &= 17.9 \; pb \text{ for } R = 2 \,. \qquad (4.41)
\end{aligned}$$

The DIS + 1 forward jet cross section for the same cuts is

$$\sigma_{\text{1jet}} = 611 \; pb \,. \qquad (4.42)$$

This gives the ratio of 2:1 forward jet events at HERA as 3.3% for the jet separation cut $R = 1.7$, and 2.9% for $R = 2$. First indications from experiment would appear to show the ratio will be less than a couple of percent for the same kinematic cuts at the hadronic level[73]. However, we must remember that statistics for the 2 forward jet cross sections will be extremely small.

We can also look at the increase in the 2-jet cross section for the relaxed kinematic cut $p_T^2/Q^2 < 5$. In section 4.4 we predict that by increasing this constraint we should observe a significant increase in the cross sections. This gives the results

$$\begin{aligned} \sigma_{1\text{jet}} &= 1479\ pb \\ \sigma_{2\text{jet}} &= 95.2\ pb \text{ for } R = 1.7 \\ \sigma_{2\text{jet}} &= 85.5\ pb \text{ for } R = 2\ , \end{aligned} \tag{4.43}$$

from which we observe an increase by a factor ~ 5 between the $\sigma_{2\text{jet}}$ results of (4.41) and (4.43). However, preliminary experimental analysis does not show such a large increase. The results of (4.43) give a ratio for the 2:1 jet cross sections for the kinematic cut $p_T^2/Q^2 < 5$ as: 6.4% for $R = 1.7$ and 5.8% for $R = 2$. Thus, we predict that by relaxing the kinematic cut p_T^2/Q^2 from the experimental cut of $2 \rightarrow 5$ then there should be an increase of approximately a factor 2 in the statistics for the ratio of the cross sections.

Between preliminary experimental observation[73] and our theoretical calculations for the 2:1 DIS + forward jet cross sections there may be at least a factor 2 discrepancy. This factor may even increase for the absolute magnitudes of the cross sections for the relaxed kinematic constraint $p_T^2/Q^2 < 5$. However, for a direct comparison of experiment with theory, measurements need to be corrected from the hadron to the parton level. Unfortunately, preliminary studies of the corrections required show that the corrections in changing from hadron $\rightarrow$ parton level results are very sensitive to the Monte Carlo model used. Also, these hadronization corrections appear to be of greater significance to the 2 forward jet measured cross section than for the 1 forward jet. At present, depending on the Monte Carlo model used, for the relaxed kinematic cut $p_T^2/Q^2 < 5$ where the correction factor is actually greater than for the lower cut $p_T^2/Q^2 < 2$, the correction factor for the number of parton jets / number of hadron jets ranges between the values 0.36(MEPS)[5]and 2.2(CDM)[6]! This would indicate that a direct comparison with experimental observations will be difficult until these corrections can be more fully understood.

Thus, our first analysis for the ratio of the 2 forward jet cross section to the 1 forward

[5]MEPS - Matrix Elements + Parton Shower Monte Carlo in which the parton evolution is based on the DGLAP scheme.

[6]CDM - Colour Dipole Model Monte Carlo in which there is no p_T ordering. Both CDM and MEPS use JETSET hadronization models to calculate the hadron $\rightarrow$ parton corrections, thus, the difference in the factors between the two Monte Carlos cannot be caused by differences in hadronization. [70]

jet cross section in DIS events is encouraging. However, at the level of the absolute magnitudes of the cross sections there are indications we may see somewhat large disagreement between observation and theory, especially for forward jets with minimum transverse momentum $p_{Tjet} > 3.5$ GeV and relaxed kinematic constraint[7] $p_T^2/Q^2 < n$ for $n > 2$. At the present time however, decisive conclusions about the accuracy of the predictions for the absolute magnitudes cannot be made due to the large uncertainties (e.g. the approximation in neglecting heavy quarks and the ambiguity of the normalization) in the theoretical calculations of the cross sections. For details of the experimental measurement for the DIS + 2 forward jet cross sections at HERA see [73].

4.6 Summary

The measurement of DIS scattering events (x, Q^2) containing a very forward energetic jet (x_j, k_{Tj}^2), with $x_j \gg x$ and $k_{Tj}^2 \sim Q^2$, has long been advocated as a favourable way of investigating the dynamics which underlie small x physics. In this chapter we have studied these forward jets using the BFKL formalism presented in chapter 3 in which we have performed a resummation of the real and virtual gluon emissions to give a modified expression for the BFKL equation (Eqs. (3.21) and (3.23)). This provides a method of calculating exclusive jet rates in the final state allowing us to extend the picture to include the production of an extra jet in the forward direction. The aim of this work was to calculate the cross section of 2 forward jet emissions in ep collisions at HERA, and also the ratio of 2:1 forward jet rates. Theoretically we are allowed to include gluon radiation between the two forward jets. This was studied in detail with the 2 forward jet cross section given by (4.33). However, due to experimental selection cuts for forward jet identification the available phase space for gluon radiation between the jets is very limited and we expect only a small enhancement of the 2 forward jet cross section when we include gluon radiation between the jets compared to when we omit it (see sections 4.3.4 & 4.3.5). The simplified form for the cross section, which is used for the numerical predictions presented in section 4.4, is given by Eq.(4.37).

The forward region is defined by cuts of the type given in (1.8), with large restrictions imposed on the minimum allowed angle of the scattered electron ($\theta_{e'} \gtrsim 160°$) in the

[7]See Figures 4.10 and 4.11 which show the BFKL prediction for the 1 forward jet cross section to be somewhat larger than the experimental data in the very small x region $x \sim 10^{-4} - 10^{-3}$. We can expect this "excess" to feed into the result for the 2 forward jet cross sections.

detector. Jet events are collected which typically lie in the region

$$\frac{1}{2}Q^2 < k_{Tj}^2 < 2Q^2 \tag{4.44}$$

subject also to the jet resolution cut, $k_{Tj}^2 > \mu^2$. To obtain sufficient statistics the first measurements take $\mu = 3.5$ GeV for a series of small x bins of size 0.0005, but ideally as the integrated luminosity at HERA improves, it will be preferable to obtain a DIS sample restricted to jets with higher transverse momentum. At present, forward jet cross sections for a higher minimum transverse momentum $\mu = 5,\ 6$ GeV are presented only for two large x bins of size 0.0015.

The DIS + forward jet data sample contains a small fraction of events with two identified jets[71]. For the set of kinematic cuts given in (4.40), H1 quote[67] a value of approximately 4% for the ratio of 2:1 forward jet cross sections in DIS events at HERA.

The main purpose of this chapter is to predict the fraction of these events. Our results for the above cuts (4.18), in comparison with the experimental observation, gives the ratio in an x bin $\Delta x = 0.0002 - 0.002$ of $\sim 6.6\%$. For the slightly different phase space cuts for forward jet observation as described in section 4.2.2 [66], our results are shown by the lower set of histograms in Figure 4.21 for $\mu = 3.5$ GeV, and in Figure 4.22(a) for three different values of μ. We see that the fraction of 2 jet events for $R = 1.7$ is about 2.5% for the x interval $0.0005 - 0.001$ rising to about 5% for $\Delta x = 0.0025 - 0.003$, see Figure 4.21. The fraction is rather insensitive (i) to the value of the jet resolution parameter μ, see Figure 4.22(a), and (ii) to ambiguities in the function Φ_i describing the BFKL gluon chain since it is common to both the 1-jet and 2-jet predictions and tends to cancel in the ratio. The experimental confirmation of the predicted 2-jet fractions will therefore serve as a check on the BFKL vertex function which occurs in (4.25).

We have also investigated the effect of the experimental kinematic and phase space cuts on the magnitude of the forward jet cross sections to observe the sensitivity of the predictions to changes in jet event selection criteria. The analysis shows that the absolute magnitudes are extremely sensitive to these cuts - especially in the small x region ($x \sim 10^{-4}$) where we would hope to observe signatures of the BFKL dynamics. In fact our studies show the magnitudes of the cross sections in the very small x region are controlled primarily through the phase space $y < 0.5, 1$ cut and the kinematic cut $k_{Tj}^2 \sim Q^2$. The sensitivity of the magnitudes of the cross sections to these cuts has been traced to the importance of the low Q^2 region which provides a large contribution to

the fully integrated cross section (see Figure 4.18). Applying experimental jet selection cuts essentially restricts the low Q^2 region. The kinematic domain (4.44) as used in this chapter is chosen such that $k_{Tj}^2 \sim Q^2$ so as to suppress DGLAP gluon emission. The results for the larger domain $Q^2/2 < k_{Tj}^2 < 5Q^2$ were presented simply to gain insight into the behaviour of the DIS + two forward jet cross section. These can be seen in the upper histograms of Figure 4.21 and Figures 4.20(b) & 4.22(b). The interesting result is that the analysis indicates that a substantial increase in the two forward jet cross section statistics should be observed by relaxing this experimental kinematic cut, and consequently also in the ratio of the 2:1 forward jets. This is useful as the 2 forward jet experimental measurement will be restricted by very low statistics - it is easier to relax the contraint $p_T^2/Q^2 < n$ in the selection criteria of forward jets, than to separate smaller and smaller jet cone resolutions to increase statistics.

Chapter 5

Summary and Conclusions

The electron-proton collider HERA is now accumulating large luminosity allowing high precision tests of QCD at very small values of Bjorken x. As we have seen, the description of the observables measured at HERA is (usually) obtained through evolution of the parton densities of the proton with respect to one or other of the independent variables: x, the fraction of momentum carried by the struck parton within the proton, or Q^2, the virtuality of the photon. The DGLAP evolution equation which gives a resummation of the $\ln Q^2/Q_0^2$ terms (and which is known to NLO) successfully predicts the rise of the structure function F_2 and the rise of the cross sections as seen experimentally, providing we choose the input carefully at some starting scale for the evolution Q_0^2.

HERA probes the small x region to values as low as $x \sim 10^{-4}$. Here the dominant parton distribution of the proton is the gluon. For values of x this small then logarithms of the form $\ln 1/x$ are large and have to be resummed. This resummation is performed (to LO) by the BFKL equation, thus, we can also look at the evolution of the gluon density with respect to x. This formalism, with its predicted $x^{-\lambda}$ ($\lambda \sim 0.5$) behaviour, also successfully reproduces the observed rise of the structure functions and cross sections. The ambiguity lies in the fact that the observable quantities that were first measured by HERA, the total structure function F_2, and the total deep inelastic ep scattering cross section σ, are too inclusive quantites with which to distinguish the relevant underlying dynamics. In this thesis the aim has been to look for less inclusive quantities which are observable at HERA and which will neutralize, as far as possible, evolution in Q^2 (the DGLAP formalism), and concentrate on exposing the role of the small x (BFKL) dynamics. To this end we have made a theoretical study of the BFKL equation giving an insight into its

structure and have applied the resulting gluon distribution to physical processes applicable at HERA - specifically exclusive jet production and forward jet production in deep inelastic ep scattering.

In chapter 3 the process of exclusive jet production was studied with the aim of using the BFKL formalism to make quantitative predictions for the number of 0-, 1-, 2- ...n-jet emissions which should be seen experimentally. The BFKL gluon is considered as a gluon ladder with real gluon emissions forming the rungs[23]. This picture lends itself nicely to the concept of exclusive jet production where we consider each real gluon emission, providing its transverse momenta q_T is greater than a resolution parameter μ, to form a jet in the final state. However, gluon emissions with $q_T < \mu$, the unresolved jets, have to be treated equally with the virtual gluon emissions in order to ensure cancellation of infrared divergences as $q_T^2 \to 0$. Thus, first we modified the BFKL kernel ($\hat{K}$) based on the method discussed in [28, 56] in which the unresolved emissions were resummed with the virtual emissions. Normally the BFKL kernel K of Eq.(2.6) is a function of k_T and k'_T only, i.e. of the transverse momenta of the t-channel gluon. In performing the above resummation, the consequence is that the kernel $\hat{K}$ obtains an explicit $y = \ln 1/x$ dependence which is determined by the amount of unresolved radiation and thus is also a function of the resolution μ. For physical jets observable in the detectors at HERA then the resolution μ is reasonably large e.g. $\mu \sim 3.5 - 6$ GeV.

The resumming of the unresolved and virtual gluons to give the modified kernel $\hat{K}$ allowed decomposition of the total gluon distribution $f(x, k_T^2)$ into its individual n-jet components, $f^n(x, k_T^2)$. The characteristic behaviour obtained as x decreases is a rise in f to a maximum and then a decrease back to zero. The higher the n^{th} jet emission, the lower the value of x for which the maximum occurs. Unfortunately, for the HERA small x regime this behaviour is only apparent for very small values of $\mu \sim 1$ GeV. For realistically large resolutions, $\mu \sim 3.5 - 6$ GeV, the maxima shift to very small x values lying well below the x range possible for study at HERA. For the physical observables F_2^n and σ^n our analysis shows the 0-jet contribution to be dominant, with the steep rise of the (inclusive) structure function with decreasing x arising due to the onset of higher jet emissions, especially for the lower value $\mu = 3.5$ GeV. However, we do see significant amounts of 1-, 2-, 3-jet production, with the x dependence of the exclusive jet structure functions F_2^n (the flatness of the 0-jet contribution in relation to the steep increase of the higher jet contributions) being enhanced for lower jet resolutions and higher Q^2. An

important observation of the analysis is that we predict a non-negligible amount of $n > 1$ jets arising for $\mu > Q$, i.e. jets with momenta $q_T > Q$, which arises as a direct consequence of the characteristic $\ln k_T^2$ diffusion of BFKL dynamics. In fact, the production of jets with $q_T > Q$ is disallowed by DGLAP dynamics due to strong ordering in the transverse momenta.

The second process considered was DIS events including the production of 2 forward jets as discussed in chapter 4. The measurement of the DIS + 1 forward jet process has long been advocated[49, 62] as a method of investigating the underlying small x dynamics as it effectively neutralizes all Q^2 evolution of the gluon distribution. These experimental measurements have shown a small fraction of events to contain 2 forward jets in the direction of the proton. The modification of the BFKL kernel to allow for exclusive jet production enabled us to easily write down an expression for the cross section of DIS + 2 forward jet events by identifying the second jet as arising from the emission of a real gluon from the BFKL chain.

The interesting observations of this study arose from the inclusion of "extra" BFKL radiation between the two forward jets. As there is very little rapidity phase space between the two jets we expect little or no radiation to be present. However, we found that we predicted too much enhancement of the 2 forward jet cross section when we included this radiation over the prediction when we neglected radiation between the jets. Thus, this analysis has allowed an insight into the numerical practicalities of modelling the BFKL gluon using the Chebyshev methods described in this thesis. We found that in modelling the gluon from a starting distribution of the delta function $\delta(k_1^2 - k_2^2)$, instead of say to the parton distributions of the proton or the photon gluon fusion process of the quark box diagrams, then the solution becomes unstable and difficult to work with. This has direct consequences if we wish to apply the (numerically modelled) BFKL equation to other processes such as $p\overline{p}$ collisions at the TEVATRON or pp collisions at the future LHC collider - exclusive jet and forward jet production from the BFKL gluon may not be so easily modelled here using exactly the same numerical techniques as in this thesis as the input for the 0-jet production is the above delta function. However, this instability was observed mainly through problems in the normalization of the resulting cross sections rather than the predicted shapes thus, with more study of the numerical techniques required these problems probably can be overcome.

For the DIS + forward jet processes measured at HERA we have successfully reproduced the observed x dependence and normalization of the 1 forward jet cross section. For the two forward jet production, when we omit any BFKL radiation between the forward jets, we predict a ratio of $\sim 2.5\%$ for 2:1 forward jet production in the small x region $x \sim 5 \times 10^{-4}$ which rises with increasing x to $\sim 5\%$ at $x \sim 3 \times 10^{-3}$, for the selection cuts of section 4.2.2 with $\mu = 3.5$ GeV and $p_T^2/Q^2 < 2$. The ratios of 2:1 jet production presented in chapter 4 are rather insensitive to the value of the resolution parameter μ and also to ambiguities in the modelling of the BFKL gluon distribution. On the other hand, the absolute magnitudes of the 1 and especially the 2 forward jet cross section are found to be very sensitive to changes in the parameters of the BFKL calculation. Interestingly we observe that for the very small x region $x \sim 10^{-4}$, the magnitude of the cross section is controlled by the explicit phase space and kinematic cuts applied. Also we predict a dramatic increase, by approximately a factor of 5 in the 2-jet cross section in relaxing the kinematic constraint $p_T^2/Q^2 < 2$ to $p_T^2/Q^2 < 5$. All these noticeable effects in the small x region have been traced to the importance of the low Q^2 region providing large contributions to the fully integrated cross section.

Thus in conclusion, this initial theoretical study of the BFKL equation to calculate exclusive observable quantites in ep scattering indicates that there are possible signatures of small x dynamics to be seen. Unfortunately, for the HERA x range and with present experimental jet resolutions these will be very difficult measurements to make as the interesting behaviour is visible only for very small jet resolutions or very small x, e.g. the onset of high $n = 3, 4..$ jet production for jets with large p_T which have resolution values of $\mu \sim 5, 6$ GeV will not easily be observed except for x values smaller than those which can be reached by HERA. However, the exploratory study made here for ep collsions at HERA is of importance for making full experimental exclusive jet cross section measurements. This also applies to exclusive measurements at the TEVATRON and LHC which may allow us to see small x (BFKL) characteristics with their higher energies.

This analysis has been made at LO but also including the modifications of running coupling and a first look at applying the kinematic constraint[39] on the longitudinal momenta of emitted gluons to exclusive jet production - these are NLO effects. Noticeably the kinematic constraint reduces the amount of higher jet emissions. Thus the inclusion of the full NLO and higher order effects to the BFKL equation are essential before we will have a fully accurate description of the BFKL gluon, with these corrections hopefully

removing many of the ambiguities encountered in calculating the LO approximation, such as the gluon normalization. Thus with the calculation of the NLO contributions of the BFKL equation just finished, deep inelastic scattering at HERA described using the BFKL formalism, and other closely related areas, remains a very interesting topic of study and will continue to be so for years to come.

Appendix A

Solution of the BFKL kernel

In this appendix the solution of the BFKL kernel is obtained following the method described in the PhD thesis of A.J.Askew[25], and is included here for completeness. The solution can also be found in [24] for the BFKL equation containing the full azimuthal dependence φ, which has the general result

$$\chi_n(\nu) = 2\left(-\gamma_E - \Re e\left[\Psi((n-1)/2 + i\nu)\right]\right)$$

where n refers to the azimuthal projection $\exp(in\varphi)$. For the BFKL equation used in this thesis, we use the approximation that the $n = 0$ projection gives an adequate description of f for large rapidities. The standard integrals used in these appendices are performed using Gradshteyn and Ryzhik[17] unless otherwise stated.

The integral BFKL kernel is only dependent on k^2 and is scale invariant such that, under the transformation $k \to \lambda k$, for λ a number, then (A.1) remains unchanged. This allows us to obtain the solution of the BFKL equation (for fixed α_s) using Mellin transform techniques. Applying the definition of moments, Eq.(2.11), to the BFKL equation of (2.3), then we have

$$\begin{aligned}\frac{\partial \tilde{f}(x,\omega)}{\partial \ln 1/x} &= \int_0^\infty (k^2)^{-\omega-1} dk^2 \overline{\alpha}_s k^2 \int_0^\infty \frac{dk'^2}{k'^2} f(x,k^2)\left[\frac{\frac{f(x,k'^2)}{f(x,k^2)} - 1}{\mid k'^2 - k^2 \mid} + \frac{1}{(4k'^4 + k^4)^{\frac{1}{2}}}\right] \\ &= \tilde{K}(\omega)\tilde{f}(x,\omega)\,, \end{aligned} \tag{A.1}$$

where $\overline{\alpha}_s = N_c\alpha_s/\pi$ and $\tilde{K}(\omega)$ is the Lipatov kernel equation in moment space. Rearranging (2.11) we can write

$$f(x,k^2) = (k^2)^{\omega+1}\frac{\partial \tilde{f}}{\partial k^2},$$

and by making the change of variables $u = k'^2/k^2$ such that

$$\frac{f(x,k'^2)}{f(x,k^2)} = \frac{f(x,uk^2)}{f(x,k^2)} = u^\omega,$$

then

$$\tilde{K}(\omega) = \overline{\alpha}_s \int_0^\infty \frac{du}{u}\left[\frac{u^\omega - 1}{|\,u-1\,|} + \frac{1}{(4u^2+1)^{\frac{1}{2}}}\right]. \tag{A.2}$$

The above integral can be performed by splitting (A.2) into two regions, $[0:1]$ and $[1:\infty]$, which define the contributions $\tilde{K}_a$ and $\tilde{K}_b$ to the full kernel $\tilde{K}$, where

$$\tilde{K} = \tilde{K}_a + \tilde{K}_b. \tag{A.3}$$

Explicitly these are given by

$$\tilde{K}_a(\omega) = \int_1^\infty \frac{du}{u}\frac{u^\omega - 1}{u-1} \tag{A.4}$$

and

$$\tilde{K}_b(\omega) = \lim_{\epsilon,\delta\to 0}\left[\int_0^1 \frac{du}{u^{1-\epsilon}}\frac{u^\omega}{(1-u)^{1-\delta}} - \int_0^1 \frac{du}{u^{1-\epsilon}}\frac{1}{(1-u)^{1-\delta}} + \int_0^\infty \frac{du}{u^{1-\epsilon}}\frac{1}{(4u^2+1)^{\frac{1}{2}}}\right], \tag{A.5}$$

where to remove any divergences in the region $x \to 0, 1$ we have introduced the regulators ϵ and δ.

$\tilde{K}_a(\omega)$ of (A.4) is simply evaluated by first making the change of variables,

$$v = \frac{1}{u}$$

and recalling that the logarithmic derivative of the Gamma function[17]

$$\Psi(z) = \int_0^1 dt \frac{t^{z-1}-1}{t-1} - \gamma_E\,; \quad \gamma_E = -\Psi(1),$$

where $\gamma_E = 0.577215...$ is the Euler-Mascheroni constant, we then obtain the solution,

$$\tilde{K}_a(\omega) = \Psi(1) - \Psi(1-\omega). \tag{A.6}$$

$\tilde{K}_b(\omega)$ of (A.5) is evaluated using the standard integrals for the β-function

$$\beta(x,y) = \int_0^1 dt\, t^{x-1}(1-t)^{y-1}dt\,;\ \Re e(x), \Re e(y) > 0$$

$$\frac{1}{\nu}\beta\left(\frac{\mu}{\nu}, \frac{\nu-\mu}{\nu}\right) = \int_0^\infty dx \frac{x^{\mu-1}}{1+x^\nu}\,;\ \Re e(\nu), \Re e(\mu) > 0$$

which gives, evaluating each integral seperately,

$$\tilde{K}_b(\omega) = \lim_{\epsilon,\delta\to 0}\left[\beta(\omega+\epsilon,\,\delta)-\beta(\epsilon,\,\delta)+\beta(\epsilon/2,\,1/2-\epsilon/2)\frac{2^\epsilon}{2}\right]. \tag{A.7}$$

Rewriting (A.7) in the gamma function representation, we obtain the solution for $\tilde{K}_b(\omega)$ as

$$\tilde{K}_b(\omega) = \lim_{\epsilon,\delta\to 0}\left[2^{-\epsilon}\frac{\Gamma(\epsilon/2+1)\Gamma(1/2-\epsilon/2)}{\Gamma(1/2)}\,\frac{1}{\epsilon}+\frac{\Gamma(\delta+1)\Gamma(\omega+\epsilon)}{\Gamma(\omega+\epsilon+\delta)}\,\frac{1}{\delta}\right. \tag{A.8}$$

$$\left.-\frac{\Gamma(1+\epsilon)\Gamma(1+\delta)}{\Gamma(1+\epsilon+\delta)}\,\frac{\epsilon+\delta}{\delta}\right].$$

We can then use the Taylor expansion,

$$\Gamma(1+z)\simeq 1+\gamma_E z+O(z^2)+...$$

to take the limits $\epsilon,\delta\to 0$, producing,

$$\tilde{K}_b(\omega)=\Psi(1)-\Psi(\omega). \tag{A.9}$$

This only leaves us to substitute the results of (A.6) and (A.9) into (A.3), including the prefactor $\overline{\alpha}_s$, to give the solution for the BFKL kernel of equation (2.6)

$$\tilde{K}(\omega)=\overline{\alpha}_s[2\Psi(1)-\Psi(\omega)-\Psi(1-\omega)].$$

Appendix B

Asymptotic solution of the BFKL equation

Here we obtain the analytic solution of the BFKL equation (2.3) for fixed α_s using the method outlined in[10]. Taking the symbolic form for the derivative of the BFKL equation in moment space,

$$\frac{\partial \tilde{f}(x,\omega)}{\partial \ln(1/x)} = \tilde{K}(\omega)\tilde{f}(x,\omega) \tag{B.1}$$

where the kernel $\tilde{K}(\omega)$ has the solution (Appendix A),

$$\tilde{K}(\omega) = \overline{\alpha}_s[2\Psi(1) - \Psi(\omega) - \Psi(1-\omega)], \tag{B.2}$$

then the solution to (B.1) is of the form,

$$\tilde{f}(x,\omega) = \tilde{f}(x_0,\omega)\left(\frac{x}{x_0}\right)^{\tilde{K}(\omega)}. \tag{B.3}$$

The scale x_0 is some input starting value from which we will begin the $\ln(1/x)$ evolution, and $\overline{\alpha}_s$ the usual notation for $N_c\alpha_s/\pi$. Both x and x_0 are small enough so that the approximation in which the Lipatov equation is derived is valid and $x \ll x_0$.

The unintegrated gluon distribution $f(x,k^2)$ is then obtained by taking the inverse transform of (B.3),

$$f(x,k^2) = \frac{1}{2\pi i}\int_{c-i\infty}^{c+i\infty} d\omega\ (k^2)^{\omega}\tilde{f}(x_0,\omega)\left(\frac{x}{x_0}\right)^{\tilde{K}(\omega)}, \tag{B.4}$$

which is solved by noting that the point $\omega = 1/2$ is a saddle point for the integration, thus for $x \ll x_0$, the integral obtains a maximal contribution from the region $\nu \sim 0$ around

$\omega = 1/2$. This allows the function $\tilde{f}(x_0,\omega)$ to be evaluated by first making a Taylor series expansion of the relevant quantities about this point. Making the change of variable,

$$i\nu = \omega - \frac{1}{2}\,, \tag{B.5}$$

then for the ω dependent terms in (B.4) we obtain:

$$\begin{aligned} (k^2)^\omega &= (k^2)^{\frac{1}{2}}\, e^{i\nu \ln(k^2)} \\ \tilde{K}(\omega) &= \tilde{K}(1/2 + i\nu) \\ \tilde{f}(x_0,\omega) &\simeq \tilde{f}(x_0,1/2)\left[1 - i\nu \ln \overline{k}^2 - \frac{\nu^2}{2} A\right] \end{aligned} \tag{B.6}$$

where we have defined

$$A \equiv \frac{1}{\tilde{f}}\,\frac{d^2\tilde{f}}{d\omega^2}.$$

Letting λ be an eigenvalue of the kernel such that

$$\tilde{K}(1/2) = \lambda,$$

and from (B.5) we have $\omega = 1/2 + i\nu$, we can make the expansion

$$\begin{aligned} \tilde{K}(1/2 + i\nu) &= \tilde{K}(1/2) + i\nu\,\frac{d\tilde{K}(1/2)}{d\omega} + \frac{(i\nu)^2}{2}\,\frac{d^2\tilde{K}(1/2)}{d\omega^2} + \ldots \\ &\simeq \lambda + i\nu\lambda' - \frac{\nu^2}{2}\,\lambda''. \end{aligned}$$

Thus by keeping only the real terms we get the result,

$$\Re e\,[\tilde{K}(\omega)] = \lambda - \frac{\lambda''\nu^2}{2}. \tag{B.7}$$

But from (B.2) we already know the eigenvalues of the kernel in terms of Ψ functions, thus, expanding (B.2) about the point $\omega = 1/2$,

$$\begin{aligned} \tilde{K}(1/2 + i\nu) &= \overline{\alpha}_s[2\Psi(1) - \Psi(1/2 + i\nu) - \Psi(1/2 - i\nu)] \\ &\simeq \overline{\alpha}_s\left[2\Psi(1) - [\Psi(1/2) + i\nu\Psi'(1/2) - \frac{\nu^2}{2}\Psi''(1/2)] - \right. \\ &\qquad \left. [\Psi(1/2) - i\nu\Psi'(1/2) - \frac{\nu^2}{2}\Psi''(1/2)]\right], \end{aligned} \tag{B.8}$$

and by keeping the real parts

$$\Re e\left[\tilde{K}(\omega)\right] = \overline{\alpha}_s[2\Psi(1) - 2\Psi(1/2) + \nu^2\Psi''(1/2)], \tag{B.9}$$

we can equate (B.9) with (B.7), recalling $\lambda = \Psi(1/2)$, to get the famous value for the BFKL slope,

$$\begin{aligned} \lambda &= \overline{\alpha}_s 4\ln(2) \\ \lambda'' &= -\overline{\alpha}_s 2\Psi''(1/2) = \overline{\alpha}_s 28\zeta(3). \end{aligned} \tag{B.10}$$

Thus the kernel $\hat{K}(\omega)$ has its maximal value at $\hat{K}(1/2) = 4\ln 2$ along the contour $\omega = 1/2 + i\nu$. After substitution of (B.6) and (B.7) into (B.4) we now solve for $f(x,k^2)$ using the saddle point method of integration where the integration contour in (B.4) is taken as $c = 1/2$, to give:

$$\begin{aligned} f(x,k^2) &= \frac{1}{2\pi}\int_{-\infty}^{\infty} d\nu \left\{ (k^2)^{\frac{1}{2}} e^{i\nu\ln(k^2)}\, \tilde{f}(x_0,1/2) \left[1 - i\nu\ln(\bar{k}^2) - \frac{\nu^2 A}{2}\right] \right. \\ &\qquad \left. \times \left(\frac{x}{x_0}\right)^{-\lambda+\lambda''\nu^2/2} \right\} \\ &= \frac{1}{2\pi}(k^2)^{\frac{1}{2}} \tilde{f}(x_0,1/2) \left(\frac{x}{x_0}\right)^{-\lambda} \times \\ &\qquad \int_{-\infty}^{\infty} d\nu\, e^{i\nu\ln(k^2)} \left[1 - i\nu\ln(\bar{k}^2) - \frac{\nu^2}{2}A\right] e^{\lambda''\nu^2\ln(x/x_0)/2} \end{aligned} \tag{B.11}$$

where we have recognised that,

$$e^{-\lambda\ln(x/x_0)}\, e^{\lambda''\nu^2\ln(x/x_0)/2} = \left(\frac{x}{x_0}\right)^{-\lambda+\lambda''\nu^2/2}.$$

Using the series expansion of e^t and the standard integral

$$\int_{-\infty}^{\infty} e^{-at^2+ibt} dt = \left(\frac{\pi}{a}\right)^{\frac{1}{2}} e^{-b^2/4a}$$

we arrive at the solution of the BFKL equation (2.3),

$$f(x,k^2) = \left(\frac{x}{x_0}\right)^{-\lambda} \frac{\tilde{f}(x_0,1/2)\,(k^2)^{\frac{1}{2}}}{[2\pi\,(\lambda''\ln(x/x_0) + A)]^{\frac{1}{2}}} \exp\left(\frac{-\ln^2(k^2/\bar{k}^2)}{2\lambda''\ln(x_0/x) + 2A}\right) \tag{B.12}$$

as quoted in Eq.(2.15).

Bibliography

[1] M. Gell-Mann, Phys. Lett. **8** (1964) 214; G. Zweig, CERN preprints 8182/TH.401 and 8419/TH.412 (1964).

[2] A.D. Martin and F. Halzen, *Quarks & Leptons*, Wiley, (1984) .

[3] F. Close, *The Cosmic Onion*, Academic Press, (1979) ;
A. Besier, *Concepts of Modern Physics*, McGraw-Hill, (1987) ;
B.R. Martin and G. Shaw, *Particle Physics*, Wiley, (1992) .

[4] A.D. Martin, Contemporary Physics, **36** No.5 (1995) 335.

[5] R. Basu, Preprint IMSC-97/05/16 (May 97), Talk presented at X11DAE Symposium on High Energy Physics, Dec 1996, Guwahati, India.

[6] D.P. Roy, Preprint TIFR/TH/97-24 (May 97) .

[7] M. Klein, Proceedings of the Workshop. Vol.**1** on *Physics at* HERA, Hamburg, October 29-30 (1991) 71, Ed. W. Buchmüller and G. Ingelman.

[8] DESY internet homepage http://info.desy.de

[9] J.D. Bjorken, Proceedings of *"Enrico Fermi" International School of Physics*, Course XLI, Ed. J. Steinberger (New York Academic Press).

[10] A.D. Martin in Proceedings from *Addendum to the 1993 European School of High-Energy Physics*, Zakopane, Poland 12-25 Sep. (1993), Eds. N. Ellis, M.B. Gavela CERN **94-04**.

[11] F_2 results obtained from HEPDATA with references:
BCDMS, Benvenuti et al, Phys. Lett. 223B (1989) 485; NMC, Arneodo et al, Phys.

Lett. 364B (1995) 107; H1, Aid et al, DESY 96-039 March 1996; ZEUS, Derrick et al, DESY-96-076, June 1996 .

[12] A.D. Martin, R.G. Roberts and W.J. Stirling, Phys. Rev. **D50** (1994) 6734; Phys. Lett. **354** (1995) 155.

[13] See for example, P. Söding, B. Wiik, G. Wolf and S.L. Wu, Proceedings of *Int. Europhysics Conf. on High Energy Physics*, Brussels Augues (1995). (World Scientific, Singapore 1995), p.3

[14] R.K. Ellis, W.J. Stirling and B.R. Webber, *QCD and Collider Physics*, Cambridge University Press (1996).

[15] G. Altarelli and G. Parisi, Nucl. Phys. **126** (1997) 298; V.N. Gribov and L.N. Lipatov, Sov. J. Nucl. Phys. **15** (1972) 438.

[16] Yu.I. Dokshitzer, Sov. Phys. JETP **46** (1977) 641;
Yu.I. Dokshitzer, V.A. Khoze, A.H. Mueller and S.I. Troyan, *Basics of Perturbative QCD*, (1991), (Gif-sur-Yvette: Editions Frontierès), Chapter 1.

[17] Gradshteyn and Ryzhik, *Table of integrals, series and products*, Fourth edition.

[18] G. Curci, W. Furmanski and R. Petronzio; W. Furmanski and R. Petronzio: Nucl. Phys. **B175** (1980) 27; Phys. Lett. **B97** (1980) 437; Z. Phys. **C11** (1982) 293;
R.G. Roberts, *The structure of the proton*, Cambridge University Press (1990).

[19] V.S. Fadin, M.I. Kotsky, L.N. Lipatov, preprint BUDKERINP/96-02 April (1997);
V.S. Fadin, L.N. Lipatov, Nucl. Phys. **B477** (1996) 767.

[20] C.R. Schmidt, preprint hep-ph/9612454 Dec. 1996.

[21] G. Marchesini and B. Webber, Nucl. Phys. **B386** (1992) 215.

[22] S. Catani, F. Fiorani, G. Marchesini and G. Oriani, Nucl. Phys. **B361** (1991) 645; S. Catani, M. Ciafaloni and F. Hautmann, Phys. Lett. **B242** (1990) 97; Nucl. Phys. **B366** (1991) 135; G. Marchesini, Nucl. Phys. **B445** (1995) 49.

[23] E.A. Kuraev, L.N. Lipatov and V.S. Fadin, Phys. Lett. **B60** (1975) 50; Sov. Phys. JETP **44** (1976) 443; Sov. Phys. JETP **45** (1977) 199.
Ya. Ya. Balitsky and L.N. Lipatov, Sov. J. Nucl. Phys. **28** (1978) 822.

L.N. Lipatov, in *Perturbative QCD*, edited by A.H. Mueller, (World Scientific, Singapore, 1989), p.441;
J.B. Bronzan and R.L. Sugar, Phys. Rev. **D17** (1978) 585.

[24] J.R. Forshaw and D.A. Ross *Quantum Chromodynamics and the Pomeron*, Cambridge University Press, 1997.

[25] A.J. Askew, Durham University, PhD Thesis July 1995.

[26] A.J. Askew, J. Kwieciński, A.D.Martin and P.J. Sutton, Phys. Rev. **D49** (1994) 4402.

[27] J. Kwieciński, A.D.Martin and P.J. Sutton, Phys. Rev. **D46** (1992) 921.

[28] J. Kwieciński, A.D. Martin and P.J. Sutton, Phys. Rev. **D52** (1995) 1445.

[29] J.R. Forshaw, P.N. Harriman and P.J. Sutton, J. Phys. **G19**: 1616 (1993).

[30] L.V. Gribov, E.M. Levin and M.G. Ryskin, Phys. Rep. **100**, 1, (1983);
A. H. Mueller and J. Qui, Nucl. Phys. **B268** (1986) 427;
V.N. Gribov, Sov. Phys. JETP **26** (1968) 414.

[31] J. Kwieciński, A.D.Martin and P.J. Sutton, Phys. Rev. **D44** (1991) 44;
A.J. Askew, K. Golec-Biernat, J. Kwieciński, A.D.Martin and P.J. Sutton, Phys. Lett. **B325** (1994) 212.

[32] A.L. Ayala F°, M.B. Gay Ducati and E.M. Levin, Phys. Lett. **B388** (1996) 188.

[33] J. Bartels, Nucl. Phys **B175** (1980) 365; Z.Phys. **C60** (1993) 471; Phys. Lett. **B298** (1993) 204;
J. Bartels and M. Wüsthoff, Z.Phys. **C66** (1995) 157;
J. Bartels and M. Wüsthoff and L.N. Lipatov, Nucl. Phys **B464** (1995).

[34] L.N. Lipatov and V.S. Fadin, Sov. J. Nucl. Phys. **50** (1989) 712; JETP Lett. **49** (1989) 352;
V.S. Fadin and R. Fiore, Phys. Lett. **B294** (1992) 286;
V.S. Fadin and L.N. Lipatov, Nucl. Phys. **B**, (Proc. suppl.) **29A** (1992) 93; Nucl. Phys. **B406** (1993) 259;
V.S. Fadin, R. Fiore and A. Quartarolo, Phys. Rev. **D50** (1994) 2265; Phys. Rev. **D50** (1994) 5893; Phys. Rev. **D53** (1996) 2729.

[35] V. Del Duca, Talk presented at 10^{th} Les Rencontres de Physique de la Vallee d´Aoste, *Results and Perspectives in Particle Physics*, La Thuile, Italy, March (1996) 463-478; Phys. Rev. **D54** (1996) 989; Phys. Rev. **D54** (1996) 4474.

[36] G. Caminci, M. Ciafaloni, Ringberg Conf. June (1996).

[37] J. Kwieciński, A.D. Martin, P.J. Sutton, Z.Phys. **C71** (1996) 585.

[38] Private communication L.N. Lipatov.

[39] J. Kwieciński, A.D. Martin and A.M. Stasto, DTP/97/18 March (1997).

[40] H1 collaboration: S. Aid *et al.*, DESY report 96-039, Z. Phys. **C** (in press).

[41] ZEUS collaboration: M. Derrick *et al.*, Z. Phys. **C69** (1996) 607, DESY report 96-076, Z. Phys. **C** (in press).

[42] M. Glück, E. Reya and A. Vogt, Z.Phys. **C67** (1995) 433.

[43] J. Kwieciński, A.D.Martin and P.J. Sutton, Phys. Rev. **D53** (1996) 6094.

[44] B. Andersson, G. Gustafson and J. Samuelsson, Lund preprint LU TP 95-13.

[45] A.H. Mueller, Nucl. Phys. **B**, Proc. Suppl. **18 C** (1991) 125;
W.K. Tang, Phys. Lett. **B278** (1991) 363;
J. Bartels et al. Z.Phys. **C54** (1992) 635; Phys. Lett. **B309** (1993) 400; Phys. Lett. **B384** (1996) 300;
J. Kwieciński, A.D.Martin and P.J. Sutton, Phys. Rev. **D46** (1992) 921; J. Kwieciński, A.D.Martin and P.J. Sutton, Nucl. Phys. **B**, Proc. Suppl. **29A** (1992) 67;

[46] J. Kwieciński, Nucl. Phys. **B**, Proc. Suppl. **39 C** (1995) 58;
M. Kuhlen, Proc. of DIS95 Workshop, Paris 1995, eds. J.F. Laporte and Y. Sirois, p.345.

[47] A.J. Askew, J. Kwieciński, A.D.Martin and P.J. Sutton, Phys. Lett. **B338** (1994) 92; J. Bartels, V. Del Duca and M. Wusthoff DESY-96-220 (hep-ph/9610450).

[48] M. Kuhlen, Phys. Lett. **B382** (1996) 441.

[49] A.H. Mueller and H. Navelet, Nucl. Phys. **B282** (1987) 727;

[50] V. Del Duca and C.R. Schmidt, Phys. Rev. **D49** (1994) 4510; **D51** (1995) 2150;
W.J. Stirling, Nucl. Phys **B423** (1994) 56;
K. Golec-Biernat, J. Kwieciński, A.D. Martin and P.J. Sutton, Phys. Lett. **B335** (1994) 220; Phys. Rev. **D50** (1994) 217;
V.T. Kim and G.B. Pivovarov, Phys. Rev **D53** (1996) R6.

[51] G. Marchesini, Nucl. Phys. **B445** (1995) 49.

[52] M. Ciafaloni, Nucl. Phys. **B296** (1988) 49.

[53] S. Catani, F. Fiorani and G. Marchesini; Phys. Lett. **B234** (1990) 339; Nucl. Phys. **B336** (1990) 18;
G. Marchesini, Proceedings of the Workshop *QCD at 200 TeV*, Erice, Italy (1990), edited by L. Cifarelli and Yu. L. Dokshitzer (Plenum Press, New York, 1992) p183.

[54] A.D. Martin, Acta Phys. Polon. **25** (1994) 265.

[55] J. Kwieciński, D. Strozik-Kotlorz; Z.Phys. **C48** (1990) 315; A.D. Martin, R.G. Roberts and W.J. Stirling, Phys. Rev. **D47** (1993);

[56] T. Jaroszewicz, Acta. Phys. Polon. **B11** (1980) 965.

[57] Numerical Recipies in Fortran, The Art of Scientific Computing, 2nd edition, Cambridge Press.

[58] S. Catani, M. Ciafaloni and F. Hautmann, Phys. Lett. **B242** (1990) 97; Nucl. Phys. **B366** (1991) 657;
J.C. Collins and R.K. Ellis, Phys. Lett. **B360** (1991) 3;
E.M. Levin, M.G. Ryskin and A.G. Shuvaev, Sov. J. Nucl. Phys. **53** (1991) 657.

[59] A.J. Askew, J. Kwieciński, A.D. Martin and P.J. Sutton, Mod. Phys. Lett. **A8**:3813-3822, 1993.

[60] A.J. Askew, J. Kwieciński, A.D. Martin and P.J. Sutton, Phys. Rev. **D47** (1993) 3775.

[61] J. Kwieciński, C.A.M. Lewis and A.D. Martin, Phys. Rev. **D54** (1996) 6664.

[62] A.H. Mueller, J. Phys. **G17** 1443 (1991).

[63] E. Mirkes and D. Zeppenfeld, Talk given by D.Z. at *5th International Workshop on Deep Inelastic Scattering and QCD*, Chicago, Illinois, 14-18 April (1997); Phys. Rev. Lett **78** (1997) 428; Proceedings of *Workshop on Furture Physics at HERA*, Hamburg, Germany, 25-26 Sep (1996), 588-593.

[64] M. Wobish for the H1 collaboration. Proceedings of *5th International Workshop on Deep Inelastic Scattering and QCD*, Chicago, Illinois, 14-18 April (1997)

[65] H.L. Lai, J. Huston, S. Kuhlmann, F. Olness, J. Owens, D. Soper, W.K. Tung and H. Weerts, Phys. Rev. **D55** (1997) 1280;
H.L. Lai and W.K. Tung, Z.Phys. **C74** (1997) 463.

[66] H1 Collaboration: C. Adloff *et al.*, contributed paper pa 03-049 to 28th International Conference on High Energy Physics, ICHEP'96, Warsaw, Poland, July 1996.

[67] A. de Roeck et al. for H1 and ZEUS collaborations. Presented at Workshop on *Deep Inelastic Scattering and QCD (DIS 95)*, Paris, France, 24-28 April 1995, editors J.F. Laporte and Y. Sirois (Ecole Poly.), Published Paris DIS(1995): 309-314 QCD 162: **D41** (1995),

[68] J. Bartels and H. Lotter, Phys. Lett. **B309** (1993)400.

[69] J. Kwieciński, A.D.Martin and P.J. Sutton, Phys. Lett. **B287** (1992) 254.

[70] Private communication E. Mroczko.

[71] H1 collaboration: A. De Roeck, private communication.

[72] W.J. Stirling, Nuc. Phys. **B423** (1994)56-79; L.H. Orr and W.J. Stirling, Durham preprint DTP/97/48 June (1997);
V. Del Duca, Proceedings of International Workshop on *Deep Inelastic Scattering and Related Phenomena*, (DIS96) Rome, Italy 15-19 April (1996):DIS 1996 491-494;
V. Del Duca and C.R. Schmidt, Phys. Rev. **D49** (1994)4510; **D51** (1995)2150;
A.J. Askew, D. Graudenz, J. Kwieciński and A.D. Martin, Phys. Lett. **B338** (1994)92;
J.R. Forshaw and R.G. Roberts, Phys. Lett. **B335** (1994) 494.

[73] Private communication E. Mroczko, Krakòw, Institute of Nuclear Physics, PhD thesis - July 97.